Imperial College London
Department of Chemical Engineering

Computational Analysis of Hemodynamics and Thrombosis in Aortic Dissection for Clinical Applications

Author: Chlöe Harriet Armour *Supervisor:* Prof. Xiao Yun Xu

A thesis submitted in fulfilment of the requirements for the degree of
Doctor of Philosophy and Diploma of Imperial College London, 2021

Copyright

Declaration of originality

I hereby declare that this thesis and the work presented in it are my own as the result of my own investigation except where otherwise stated. This thesis has not been submitted in whole or in part to another university for the award of any other degree or professional qualification.

September 2021

Chlöe Harriet Armour

Acknowledgements

My greatest thanks to my supervisor Prof. Yun Xu, who inspired me to undertake my PhD and has been the most influential person in getting me to this point. Thank you for your guidance on my work, for giving me so many incredible opportunities to learn and develop over the last 4 years, and for being so caring and understanding in difficult times.

I am grateful to the UK Engineering and Physical Sciences Research Council for granting my scholarship, and to the Department of Chemical Engineering for hosting my PhD. A great thanks goes to my clinical collaborators Dr Baolei Guo, Dr Yifan Liu, Prof Zhihui Dong, Dr Lydia Hanna, and Mr Richard Gibbs for providing the data on which my studies have been based, and also for guiding me through the work and providing invaluable clinical knowledge.

Thank you to all those who I have worked with and who have helped me throughout my PhD. Thank you to Rocky – from rig building to FSI simulations, you have been a fountain of knowledge I've had the privilege of learning from. A huge thanks goes to Claudia and Simone – I'm extremely lucky to have had the opportunity to work alongside and learn from you both. Most significantly thank you to Selene. Thank you for always being open to my endless questions, for the uncountable hours you have spent helping me, for teaching me so much I can't begin to list it all, and for being a wonderful friend.

To Katie Carpani, it is safe to say you have seen all the ups and downs throughout the past 4 years (plus the 3 years before that getting through undergrad). Your support, reality checks, and friendship have meant so much to me over the past 7 years. Thank you for getting me through it all, one step at a time.

Thank you to Prof. Nigel Wood for always providing valuable insight on my work. To 1M17B, Selene, Emily, Sam, Xioaxin, Boram, Claudia, Simone, Nasrul, Yu, Howard, Moath, George, Mei Yan, Serena, Alessandra, thank you for making time in the office (and on teams meetings) so enjoyable, for sharing so much knowledge with me, and for being great friends.

I have been fortunate to call a few different places home over the past four years. Thank you to Becky and Adam for keeping me happy and sane at home in Selkirk. To Dave, your friendship and support were the bedrock of home-life outside of the office, and I can't thank you enough. Thank you to Nixon and Anisha for sharing a shorter than hoped for but nevertheless wonderful

time in Prothero.

Thank you to Isy and Tim for always being there for me, for making wonderful memories together in London, and for making a bizarre and challenging lockdown a happy and joyful time to look back on. To Simon and Michèle, thank you for giving me a truly special home, and loving and supporting me throughout it all. I will forever cherish memories of the past year.

The past four years have been immeasurably impacted by Oliver Watson, Emily Manchester, Hannah Moran, Nixon Sunny, Seb Green, Brett Parkinson and Anton Firth. Nimmt, muffins, lunches, catan evenings, home karaoke, The Slug, weekends away, excessively long calls, and even card throwing and fireworks have got me through it all smiling. I couldn't have asked for better friends to share this time with.

None of this would have been possible without the endless support and love of my family. To Ailsa and Murray, I am very grateful for you (hand clasp). I love you to the moon and back. Can't say much more than that. Thank you to Amy and Fred for being so excited and supportive at every stage, and to Alexander for bringing so much happiness in the final few weeks of writing. To Louis, thank you for going to the moon with me, teaching me to wear the right size of socks even in the most challenging of times, and for always keeping me peaceful and grounded.

Grampa, when you surprised me all those years when I got into Imperial I would never have guessed that 8 years later I would be finishing my PhD. And yet, here we are heading for the Royal Albert Hall again! Gran, I wish you were here to celebrate this moment with me. While my new graduation picture will be up in the hallway, I'll always be with you in Grampa's study. Thank you both for loving me endlessly.

To Mum and Dad, I don't think it's possible to write a big enough thank you in a paragraph here. I couldn't have dreamt of better parents who have loved me so much and truly have made me who I am today. I am forever grateful for every minute I have with you, in person or on endless phone calls. Thank you for everything.

Finally, to Tom. You have been the centre of my life since starting at Imperial 8 years ago, and I can't imagine going through any of it without you. Thank you for always loving me and making me the happiest I can be. I can't wait to keep bumbling along with you forever, 10/10.

Abstract

Type B aortic dissection is a potentially devastating disease of the aorta initiated by a tear in the inner lining of the aortic wall. Blood flow through this tear causes the aortic wall layers to separate and a secondary channel of blood flow know as the 'false lumen' forms. Complete thrombosis (clotting) of the false lumen, is the desired outcome of either medical or endovascular (TEVAR) treatment. However, it is currently unclear at the time of diagnosis how a specific dissection will progress with either treatment option.

Anatomical studies have identified a range of morphological factors that may be influential in disease progression, though no single parameter has been found to be independently predictive of patient prognosis. Computational fluid dynamics (CFD) studies have aimed to assess the hemodynamic state of dissection, however, studies have generally been limited due to simplified geometries and unphysiological boundary conditions due to the lack of patient-specific *in vivo* flow data. Thanks to recent developments in imaging technologies, *in vivo* flow data can now be acquired through 4D-flow magnetic resonance imaging (MRI), though detailed evaluation of dissection flow fields is limited due to poor image quality. CFD has the potential to be a useful tool in clinical practice for predicting disease progression, as long as the results are physiological to specific patients. 4D-flow MRI data could provide the patient-specific details required to build detailed and accurate CFD models.

The primary objective of this thesis is to develop clinically applicable computational models to accurately simulate hemodynamics and thrombus formation in type B dissection patients. A 4D-flow MRI based CFD workflow was developed and key model inputs were assessed in detail. The use of a patient-specific 3D inlet velocity profile was compared to commonly used idealised profiles, with the 3D profile producing results which agreed best with *in vivo* data. The importance of major and minor aortic branches in geometry segmentation was assessed, and results showed that exclusion of such branches can significantly impact predicted hemodynamics and thrombus formation. The finalised CFD workflow was evaluated against *in vivo* data and was shown to be able to faithfully reproduce dissection hemodynamics in a study of 5 patients. A hemodynamics-based thrombus predicting model was evaluated and simplified in order to improve computational efficiency for clinical application. Finally, the CFD workflow and thrombus model were utilised in studies on the influence of re-entry tears both pre- and post-TEVAR.

Contents

Acknowledgements **iv**

Abstract **vi**

1 Introduction **1**

1.1 Research Objectives 3

1.2 Thesis Outline 5

2 Literature Review **7**

2.1 The Cardiovascular System 7

2.2 The Aorta 9

2.3 Aortic Dissection 10

2.3.1 Diagnosis 13

2.3.2 Treatment 15

2.4 Thrombosis 16

2.4.1 Modelling Thrombosis 19

2.5 Evaluation of Aortic Hemodynamics 24

2.5.1 Computational Fluid Dynamics 24

2.5.2 4D-flow MRI Analysis 29

2.6 Morphological Parameters That Influence the Progression of Type B Aortic Dissection 31

2.7 Summary and Research Objectives 37

3 Methodology **39**

3.1 General Governing Flow Equations 39

3.2 Modelling Thrombosis 42

3.3 Numerical Methods 46

3.4 Geometry Reconstruction 48

3.5 Meshing 51

3.6 Boundary Conditions 54

3.7 Analysing Results 57

3.8 Processing 4D-flow MRI Data 58

4 The Influence of Inlet Boundary Condition on Aortic Hemodynamics[†] **61**

4.1 Methodology 62

4.2 Results 68

4.2.1 Flow patterns 68

4.2.2 Wall shear stress 69

4.2.3 Pressure 73

4.3 Discussion 74

4.4 Summary 78

5 The Effect of Side Branches on Aortic Hemodynamics and Thrombus Formation 79

5.1 Methodology 80

5.2 Results 84

5.2.1 Major aortic branches 84

5.2.2 FL perfused minor aortic branches 92

5.3 Discussion 95

5.4 Summary 103

6 Evaluation and Verification of Patient-Specific Modelling of Type B Aortic Dissection 105

6.1 Methodology 106

6.2 Results 109

6.2.1 Geometric features 109

6.2.2 Inlet flow waveforms and measured pressure 110

6.2.3 3-element Windkessel parameters 111

6.2.4 Flow patterns 112

6.2.5 Pressure 116

6.3 Discussion 118

6.4 Summary 124

7 Evaluation of Thrombosis Model for Clinical Application 127

7.1 Methodology . . . 128

7.2 Results . . . 131

7.2.1 Idealised geometry . . . 131

7.2.2 Patient-specific geometry . . . 135

7.3 Discussion . . . 137

7.4 Summary . . . 142

8 Application 1: The Influence of Re-entry Tears on Hemodynamics and Progression of Aortic Dissection 143

8.1 Methodology . . . 144

8.2 Results . . . 147

8.2.1 Morphological Changes . . . 147

8.2.2 MRI-based Flow Analysis . . . 149

8.2.3 Computational Flow Analysis . . . 149

8.3 Discussion . . . 154

8.4 Summary . . . 161

9 Application 2: Location of Reentry Tears Affects False Lumen Thrombosis Following TEVAR† 163

9.1 Methodology . . . 164

9.2 Results . . . 167

9.2.1 Anatomical Characteristics . . . 167

9.2.2 Flow Patterns and Related Parameters 167

9.2.3 Thrombus Formation in the False Lumen 172

9.3 Discussion 174

9.4 Summary 180

10 Conclusions and Future Work **181**

10.1 Summary of Main Contributions 181

10.2 Limitations and Future Work 183

10.2.1 Rigid Wall Assumption 183

10.2.2 Laminar Flow Assumption 188

10.2.3 Blood Properties 190

10.2.4 Cohort Size 190

Bibliography **191**

A Mesh Sensitivity Test Results **215**

A.1 Chapter 4 216

A.2 Chapter 5 220

A.3 Chapter 6 223

A.4 Chapter 7 228

A.5 Chapter 8 230

A.6 Chapter 9 233

B Chapter 6 supplementary material **237**

C Publications and Presentations **249**

C.1 Peer-Reviewed Publications 249

C.2 Presentations 250

D Copyright Permissions **253**

List of Tables

3.1 Values of parameters used in the Quemada model for blood viscosity. 46

3.2 Total lumen volume segmented by user A on day 1, 2 and 3, and by users B and C. 50

4.1 Top: P1 measured average pressures at each aortic side branch, used to calculate 3EWK parameters for P1, P2 and P2P. Bottom: Flow splits for each aortic side branch used to calculate 3EWK parameters for P1, P2 and P2P. Branches include brachiocephalic (BRAC), left common carotid (LCCA) and left subclavian (LSA) artery, celiac trunk (CEL), superior mesentric artery (SMA), right (RR) and left (LR) renal, and right (RI) and left (LI) iliac. 66

4.2 Key flow parameters of the inlet flow waveform for patients P1, P2 and P2P. Re - Reynolds number; $\mathrm{Re_c}$ - critical Re, equal to 250α (Kousera et al. 2012); α - Womersley number. 66

4.3 Cross-lumen pressure difference (ΔP) for each patient with simulated inlet profiles. FL: false lumen, TL: true lumen. (Armour et al. 2020) 74

5.1 A: Pre-TEVAR and B: Post-TEVAR percentage of inlet flow and total volume (cm^3) reporting to each side branch for all models. *LSA was occluded by the stent graft in post-TEVAR models. 82

5.2 Proportion of descending aorta (DA) flow reporting to the TL and FL, and mean and maxmimum velocity through the primary entry tear (PET) in all pre-TEVAR models. 84

5.3 Time averaged wall shear stress (TAWSS) in the thoracic (Thor) and abdominal (Abd) aorta for all pre and post-TEVAR models. 88

5.4 Cardiac cycle mean and peak systolic pressures throughout the TL and FL in all pre-TEVAR models, on planes P1-P6, the location of which are shown in Figure 5.1. 89

5.5 Cardiac cycle mean and peak systolic pressures throughout the TL and FL in all post-TEVAR models, on planes P1-P6, the location of which are shown in Figure 5.1. 90

5.6 Percentage change in FL volume by region between the baseline and 1-year follow-up CT scan for PI and PII. Thoracic: above celiac trunk; abdominal: below celiac trunk. 101

6.1 Key flow parameters of the inlet flow waveform for patients P1-P5. Re - Reynolds number; Re_c - critical Re, equal to 250α (Kousera et al. 2012); α - Womersley number. 107

6.2 Geometric features of patients P1-P5. [a]Ascending aorta (AAo) diameter calculated based on inlet area. [b]Maximum descending aorta (DAo) diameter measured on the axial slices of the CT scans. [c]Primary entry tear (PET) measured as the maximum axial diameter of the tear. [d]Start and end point of dissection; LSA - distal to the left subclavian artery; BIF - aortic bifurcation; SMA - superior mesentric artery; CEL - celiac trunk; LR - left renal artery. [e]Length of dissection measured along the centreline of each 3D model. [f]Tortuosity calculated as the length of dissection along the centreline divided by the straight verticle distance between the start and end of dissection. 109

6.3 Diameter of each aortic side branch for all patients. Standard branch diameters reported by Du et al. (2015) and Uberoi et al. (2011) are also given. Branches include brachiocephalic (BRAC), left common carotid (LCCA) and left subclavian (LSA) artery, celiac trunk (CEL), superior mesentric artery (SMA), right (RR) and left (LR) renal, and right (RI) and left (LI) iliac. 109

6.4 3-element Windkessel parameters for all branches in patients P1-P5. Branches include brachiocephalic (BRAC), left common carotid (LCCA) and left subclavian (LSA) artery, celiac trunk (CEL), superior mesentric artery (SMA), right (RR) and left (LR) renal, and right (RI) and left (LI) iliac. Reported parameters are proximal resistance (R1), distal resistance (R2) and compliance (C). 111

6.5 Pearson correlation coefficient (R) and mean absolute error for each velocity component u_x, u_y and u_z in the 5 regions of the aorta shown in Figure 6.2 for all patients. 114

6.6 Maximum peak systolic primary entry tear (PET) velocity and false lumen ejection fraction (FLEF, defined in Equation 6.2 measured from 4D-flow MRI scan and predicted from CFD simulation for each patient. 115

6.7 Volume averaged peak systolic kinetic energy in 5 regions the location of which are shown in Figure 6.2 (AAo - ascending aorta; AA - aortic arch; Prox-DAo - proximal descending aorta; Mid-DAo - mid descending aorta; Dis-DAo - distal descending aorta) for patients P1-P5. 116

6.8 Doppler-wire (DW) measured and CFD predicted systolic, diastolic and average pressures throughout the aorta. Ascending aorta (AA); true (TL) and false (FL) lumen; primary entry tear (PET); spine vertebrae locations (T9/T12/L1). DW pressure curves were not available for P3 AA, P4 TL-PET and P4 FL-L1 to determine average pressures; the dissection in P5 did not extend to L1. 117

7.1 Number of hours taken for idealised and patient-specific simulations to reach a plateau in thrombus volume. All simulations were run in parallel with the idealised geometry using 12 cores and the patient-specific geometry using 16 cores. 137

8.1 Information on model development: date and state of model at each scan point. 145

8.2 Top – True (TL) and false (FL) volume percentage changes between follow up scans. Middle – maximum axial diameter of entry and naturally formed distal re-entry tear on scans S0-S3. Bottom - maximum sagittal diameter of created re-entry tear 1 and re-entry 2 two on scans S2 and S3. 147

8.3 Percentage of inlet flow reporting to each outlet, measured from 4D MRI data. . 148

9.1 Anatomical measurements for each model. 167

10.1 Peak systolic pressure difference between the true (TL) and false lumen (FL) on 4 planes throughout the dissection, the location of which is shown in Figure 10.2B for the rigid and FSI model. 188

A.1 Number of elements for three meshes (M1, M2, M3) used for mesh sensitivity analysis for models P1, P2 and P2P in Chapter 4. 216

A.2 Mean and maximum velocity and time average wall shear stress (TAWSS) on analysis planes (shown in Figure A.1 in each mesh for P1 in Chapter 4. |%E|: Absolute percentage change in value between noted meshes. 217

A.3 Mean and maximum velocity and time average wall shear stress (TAWSS) on analysis planes (shown in Figure A.1) in each mesh for P2 in Chapter 4. |%E|: Absolute percentage change in value between noted meshes. 218

A.4 Mean and maximum velocity and time average wall shear stress (TAWSS) on analysis planes (shown in Figure A.1) in each mesh for P2P in Chapter 4. |%E|: Absolute percentage change in value between noted meshes. 219

A.5 Number of elements for three meshes (M1, M2, M3) used for mesh sensitivity analysis for models PI and PII in Chapter 5. 220

A.6 Mean and maximum velocity and time average wall shear stress (TAWSS) on analysis planes (shown in Figure A.2) in each mesh for PI in Chapter 5. |%E|: Absolute percentage change in value between noted meshes. 221

A.7 Mean and maximum velocity and time average wall shear stress (TAWSS) on analysis planes (shown in Figure A.2) in each mesh for PII in Chapter 5. |%E|: Absolute percentage change in value between noted meshes. 222

A.8 Number of elements for three meshes (M1, M2, M3) used for mesh sensitivity analysis for models P1, P2, P4 and P5 in Chapter 6. 223

A.9 Mean and maximum velocity and time average wall shear stress (TAWSS) on analysis planes (shown in Figure A.3) in each mesh for P1 in Chapter 6. |%E|: Absolute percentage change in value between noted meshes. 224

A.10 Mean and maximum velocity and time average wall shear stress (TAWSS) on analysis planes (shown in Figure A.3) in each mesh for P2 in Chapter 6. |%E|: Absolute percentage change in value between noted meshes. 225

A.11 Mean and maximum velocity and time average wall shear stress (TAWSS) on analysis planes (shown in Figure A.3) in each mesh for P4 in Chapter 6. |%E|: Absolute percentage change in value between noted meshes. 226

A.12 Mean and maximum velocity and time average wall shear stress (TAWSS) on analysis planes (shown in Figure A.3) in each mesh for P5 in Chapter 6. |%E|: Absolute percentage change in value between noted meshes. 227

A.13 Number of elements for three meshes (M1, M2, M3) used for mesh sensitivity analysis for the idealised geometry in Chapter 7. 228

A.14 Mean and maximum velocity and time average wall shear stress (TAWSS) on analysis planes (shown in Figure A.4) for the idealised geometry used in Chapter 7. |%E|: Absolute percentage change in value between noted meshes. 229

A.15 Number of elements for three meshes (M1, M2, M3) used for mesh sensitivity analysis for models S1 and S2 in Chapter 8. 230

A.16 Mean and maximum velocity and wall shear stress (WSS) on analysis planes (shown in Figure A.5) in each mesh for S1 in Chapter 8. |%E|: Absolute percentage change in value between noted meshes. 231

A.17 Mean and maximum velocity and wall shear stress (WSS) on analysis planes (shown in Figure A.5) in each mesh for S2 in Chapter 8. |%E|: Absolute percentage change in value between noted meshes. 232

A.18 Number of elements for three meshes (M1, M2, M3) used for mesh sensitivity analysis for models P2 and P3 in Chapter 9. 233

A.19 Mean and maximum velocity and time average wall shear stress (TAWSS) on analysis planes (shown in Figure A.6) in each mesh for P2 in Chapter 9. |%E|: Absolute percentage change in value between noted meshes. 234

A.20 Mean and maximum velocity and time average wall shear stress (TAWSS) on analysis planes (shown in Figure A.6) in each mesh for P3 in Chapter 9. |%E|: Absolute percentage change in value between noted meshes. 235

D.1 Figure copyright permissions. 255

List of Figures

1.1 Left: healthy aorta. Right: dissected aorta with green arrows indicating blood flow to and from the false lumen. Available at: https://iradonline.org/about.html (International Registry of Acute Aortic Dissection) 2

2.1 Simplistic diagram of the cardiovascular system: the systemic system transports oxygen-rich blood; the pulmonary system transports oxygen-poor blood. Available at: https://www.ncbi.nlm.nih.gov/books/NBK279250/ (Institute for Quality and Efficiency in Health Care) 8

2.2 Diagram of the aorta, and a selection of the major branches that extended from the aorta. Available at: https://iradonline.org/about.html (International Registry of Acute Aortic Dissection) 10

2.3 Left: Diagram showing an aortic dissection - a tear in the intima allows blood to flow within the layers of the aorta wall creating a false lumen. Available at: https://iradonline.org/about.html (International Registry of Acute Aortic Dissection). Right: Diagrams showing dissection classification under the Debakey and Stanford naming systems Salameh & Ratchford (2016). 12

2.4 Left: Surgical treatment on Type A dissection - a graft replaces the damaged aortic wall. Available at: https://www.saintlukeskc.org/health-library/aortic-dissection-repair (Saint Luke's). Right: Endovascular repair (TEVAR) of a Type B dissection - a stent is inserted into the aorta to cover the primary tear and provide structure (Krol & Panneton 2017) 15

2.5 Diagram showing the process of platelet activation and adhesion in high and low shear conditions (McMichael 2005) 18

2.6 Simplistic schematic of the coagulation cascade. Solid black arrows represent the previous species acting as a catalyst for the activation of the following species. Solid coloured arrows represent the transformation of one species into the next. Dotted arrows represent negative feedback loops to control the coagulation cascade. 20

2.7 a) T1-T3 predicted thrombus growth alongside observed thrombus growth on follow up CT scan (S6). b) In plane velocity reducing to zero during the simulation in regions where thrombus growth was observed on follow up CT scans (S5 and S7), presented by Menichini et al. (2016). 23

2.8 Velocity streamlines modelled by CFD simulation presented by Cheng et al. (2014). 26

2.9 Velocity streamlines derived from 4D-flow MRI data throughout the cardiac cycle presented by François et al. (2013). 30

2.10 Diagram showing the locations used to calculate the fusiform dialation index (FI). A is the maximum diameter of the descendingaorta, B is the diameter of the distal aortic arch, and C is the diameter of the descending aorta at the level of the origin of the main pulmonary artery (Marui et al. 2007) 34

2.11 Diagram showing the measurement of the circumferential extend of the false lumen (CEFL). A-C shows the mobility of the intimal flap throughout the cardiac cycle. D demonstrates that the CEFL stays constant while the intimal flap moves, presented by Sailer et al. (2017). 35

3.1 Feedback loop regulating thrombus formation (Menichini et al. 2016) 45

3.2 The steps of creating a 3D model from CT scans in Mimics. A: A CT scan is imported - here one axial slice is shown. B: Thresholding is carried out as the first step of creating a mask. C: The mask is refined through masking splitting, region growing and manual segmentation. D: A 3D model is created. E: Automatic and manual smoothing is carried out. 49

3.3 Computed mesh using densities in areas that require local refinement. 51

3.4 Axial cut-plane of the aorta which show volume meshes created using the Octree (left) and Delaunay (right) method. 52

3.5 An electric circuit representing the aorta and circulatory system. R_1 and R_2 represent the proximal and distal resistances of the aorta and downstream branches respectively. C represents the compliance of the branches, Q(t) the blood flow and P(t) the pressure drop across the aorta. 55

3.6 Workflow to process and analysis 4D flow MRI scans to extract flow data. Flowrate shown as an example is extracted from 4D-flow MRI scan of swine model presented in Chapter 8. 59

4.1 Geometries of P1, P2 and P2P used for simulation. The primary entry tear (PET) in each model is indicated, as well as planes on which pressure readings were taken (A1-5, B1-2 and C1-2) (Armour et al. 2020). 62

4.2 Workflow to extract 3D inlet velocity profile from 4D-flow MRI data. 63

4.3 Top: Flowrate of inlet velocity profiles derived from 4D-flow MRI scans of P1 and P2, studied in each geometry. Bottom: 3D, TP and flat inlet velocity profiles for P1 and P2 at time points (T1 – T5) throughout the cardiac cycle. Time points are indicated by red circles and squares for P1 and P2, respectively, on flowrate curves (adapted from Armour et al. 2020). 65

4.4 Peak systolic streamlines for A: P1 with a 3D, TP and Flat inlet velocity profile (IVP), B: P2 with a 3D, TP, Flat, Flat75% and FlatP1 IVP, with 4D-flow MRI derived streamlines for comparison (Armour et al. 2020). 67

4.5 Peak systolic streamlines for P2P with a 3D, TP and Flat inlet velocity profile (Armour et al. 2020). 69

4.6 A: P1 TAWSS values with a 3D, TP and Flat inlet velocity profile (IVP). B: Absolute difference in TAWSS values between the 3D IVP and the two other IVPs (Armour et al. 2020). 70

4.7 A: P2 TAWSS values with a 3D, TP, Flat, Flat75% and FlatP1 inlet velocity profile (IVP). B: Absolute difference in TAWSS values between the 3D IVP and the four other IVPs (adapted from Armour et al. 2020). 71

4.8 A: P2P TAWSS values with a 3D, TP and Flat inlet velocity profile (IVP). B: Absolute difference in TAWSS values between the 3D IVP and the two other IVPs (Armour et al. 2020). 72

4.9 Average pressure within the true (TL) and false lumen (FL) at peak systole for P1, P2 and P2P, for all inlet velocity profiles applied (Armour et al. 2020). . . . 73

4.10 Predicted thrombus formation (shown in red) in P2 with a 3D, TP and Flat inlet velocity profile, alongside partially thrombosed (highlighted in red circle) geometry of P2 segmented from CT scan (Armour et al. 2020). 76

5.1 Pre and post-TEVAR geometries used for simulation. 'All' - including all major side branches; 'Arch' - including only supra-aortic branches; 'None' - including no side branches. Planes P1-P6 used to analyse pressure are shown for example in 'All' models. 80

5.2 Geometric models used for simulations: (left) PI geometry without and with 11 FL fed intercostal arteries (ICA); (right) PII geometry without and with the false lumen (FL) fed inferior mesenteric artery (IMA). Planes A-I used for analysis shown in each patient. 83

5.3 Peak systolic velocity streamlines. A: Pre-TEVAR models. B: Post-TEVAR models. 85

5.4 Proportion of flow report from the A: FL to TL in pre-TEVAR models and B: TL to FL in the post-TEVAR models through four re-entry tears. 86

5.5 Time averaged wall shear stress (TAWSS). A: Pre-TEVAR models. B: Post-TEVAR models 87

5.6 Mean cardiac cycle and peak systolic pressure difference ($\Delta P(P_{TL} - P_{FL})$) on planes P1-P6, the location of which are shown in Figure 5.1, for all pre and post-TEVAR models. 91

5.7 Velocity streamlines throughout the systolic phase for PI and PI+IMA. 92

5.8 Velocity streamlines throughout the systolic phase for PII and PII+IMA. 93

5.9 Time-averaged wall shear stress (TAWSS) for models PI, PI+ICA, PII and PII+IMA. 94

5.10 Peak systolic cross-lumen pressure difference ($\Delta P(P_{TL} - P_{FL})$) on planes A-I, the location of which is shown in Figure 5.2, for PI and PII. 95

5.11 Predicted thrombus formation after 16 cycles for PII and PII+IMA alongside actual observed thrombus formation from 1-year follow up CT scan 96

5.12 A small intercostal artery branching from the false lumen near the aortic arch is identified in the red circle. 102

6.1 Patient-specific geometric models reconstructed from CT scans. 106

6.2 Definition of regions of the aorta (1-5) used for analysis of kinetic energy. Locations of lumbar spinal points T9, T12, L1, used for analysis of pressure, are also indicated. 108

6.3 Inlet flow waveforms for patients P1-P5 derived from 4D-flow MRI scans and imposed in CFD simulations. 110

6.4 Mid-systolic, peak systole and mid-systolic deceleration velocity fields for P1, P2 and P3. For each patient at each time point the 4D-flow MRI derived velocity field is shown on the left alongside the CFD predicted velocity field on the right. 112

6.5 Mid-systolic, peak systole and mid-systolic deceleration velocity fields for P4 and P5. For each patient at each time point the 4D-flow MRI derived velocity field is shown on the left alongside the CFD predicted velocity field on the right. . . . 113

6.6 Motion artefact visible due to flap motion on the axial view of the descending aorta on the CT scan for P2. Red arrows indicate the intimal flap (darker line in the middle of the aorta). 122

7.1 A: Idealised geometric model. Diameters of the ascending aorta (AA), true (TL) and false lumen (FL), dissection length and distance between tears are indicated. B: Inlet flowrate used in simulation of the idealised geometry (Chong et al. 2020).128

7.2 Thrombus (shown in red) growth patterns with the original model after T1: 6, T2: 10, T3: 13, T4: 14, T5: 16 and T6: 20 cycles. For each time point the central aorta x-y plane is shown on the left and the central FL y-z plane is shown on the right. 130

7.3 Total thrombus volume as a function of time for the original model (Model-original), model without activated and resting platelets (Model(BP,C,RT)), and model without activated and resting platelets and residence time (Model(BP,C)) in the idealised geometry. 131

7.4 A: Thrombus growth (shown in red) after 20 cycles without activated and resting platelets modelled and no adjustment to kinetic constants k_{BP}, k_C and k_{C2}. The central aorta x-y plane is shown on the left and the central FL y-z plane is shown on the right. B: Average AP distribution over cycle 3 in the original model. AP is modelled relative to the inlet concentration hence it is dimensionless. 132

7.5 Thrombus (shown in red) growth patterns without activated and resting platelets modelled (Model(BP,C,RT)) after T1: 6, T2: 10, T3: 13, T4: 14, T5: 16 and T6: 20 cycles. For each time point the central aorta x-y plane is shown on the left and the central FL y-z plane is shown on the right. 133

7.6 Thrombus (shown in red) growth patterns without activated and resting platelets and residence time modelled (Model(BP,C)) after T1: 6, T2: 10, T3: 13, T4: 14 and T5: 16 cycles. For each time point the central aorta x-y plane is shown on the left and the central FL y-z plane is shown on the right. 134

7.7 Total thrombus volume as a function of time for the original model (Model-original) and model without activated and resting platelets (Model(BP,C,RT)) in the patient-specific geometry. 135

7.8 Evolution of PII false lumen surface after T1: 6, T2: 10, T3: 13, T4: 14 and T5: 16 cycles for the original model and Model(BP,C,RT). 136

7.9 Central aorta x-y plane showing top: cycle average shear rate and bottom relative residence time (RRT) after T1: 6, T2: 10, T5: 16 and T6: 20 cycles. 140

8.1 A – Geometry of S1, S2 and S2mod used for CFD. Analysis planes (P1-7) are indicated on S1. B – 3D inlet velocity profile for S1, S2 and S2mod, extracted from the 4D-flow MRI data of S1 and S2. 144

8.2 A - Inlet flowrate extracted from 4D MRI scan of S1 and S2. B - True (TL) and false (FL) lumen flowrates extracted from 4D MRI data of S1. C – TL and FL lumen flowrates extracted from 4D MRI data of S2. TL and FL flowrates in B and C were evaluated on plane 2, the location of which is shown in Figure 8.1. . 148

8.3 A - Peak systolic velocity magnitude derived from 4D MRI data of S1 and S2. B - Peak systolic velocity from CFD simulations of S1 and S2. C - MRI and CFD data on planes P1, P2 and P3 (the location of which is shown in Figure 8.1A) and across the entry tear for S1. R - linear correlation value between MRI and CFD. 150

8.4 A - Distribution of descending aorta flow between the TL and FL, measured on each plane within the dissection (P2-P6) shown in Figure 8.1A for models S1, S2 and S2mod. B - Reverse flow index, calculated on each plane (P1-P7) shown in Figure 8.1A, for models S1, S2 and S2mod. 151

8.5 A – Peak systolic velocity contours on each plane shown in Figure 8.1A, for models S1, S2 and S2mod. B – maximum velocity on each plane shown in Figure 8.1A at peak systole, for models S1, S2 and S2mod. Values in the true (TL) and false (FL) lumen are reported on separate graphs. 152

8.6 A – Time averaged wall shear stress (TAWSS) for models S1, S2 and S2mod. B – TAWSS around re-entry tears in models S2 and S2mod. 153

8.7 FL pressure on each plane (P2-P6) within the dissection shown in Figure 8.1A, at mid-systolic acceleration, peak systole and mid-systolic deceleration for models S1, S2 and S2mod. B – Pressure distribution throughout the aorta, on planes P2-P6, at mid-systolic acceleration, peak systole and mid-systolic deceleration for models S1, S2 and S2mod. 155

8.8 A - calcification (shown in black) throughout the dissection in scans S1, S2 and S3. B – areas of calcification (high intensity white pixels) within the intimal flap identified in scans S1, S2 and S3. C – velocities extracted from 4D MRI data in the upper thoracic aorta, proximal to the dissection at different time points throughout the systolic phase. D – velocities extracted from 4D MRI data within the dissection at different time points throughout the systolic phase. 160

9.1 (a) P1, first post-procedure geometry; (b) P1-mod, modified geometry of P1 with the first post-stent reentry tear artificially moved proximally by 30 mm; (c) P2, first post-procedure geometry; (d) P2-mod, modified geometry of P2 with 2 proximal entry tears artificially occluded; and (e) P3, first post-procedure geometry (Armour et al. 2020). 165

9.2 Instantaneous velocity streamlines at (A) mid-systolic acceleration, (B) peak systole, and (C) mid-systolic deceleration in P1, P2, and P3 (Armour et al. 2020).168

9.3 A: Time-averaged wall shear stress (TAWSS) distribution and B: Temporal average wall pressure normalised by the spatial average in patients P1, P2, and P3. Adapted from (Armour et al. 2020). 169

9.4 Instantaneous velocity streamlines at mid-systolic acceleration, peak systole and mid-systolic deceleration, time-averaged wall shear stress (TAWSS), and temporal average wall pressure normalised by the spatial average for P1-mod and P2-mod. Adapted from (Armour et al. 2020). 170

9.5 Evolution of false lumen (FL) surface in P1 following thrombus growth. (a) Reconstructed lumen surface based on the first post-procedure scan for P1 and predicted FL surface following thrombus growth at (b) 8, (c) 15, and (d) 26 seconds in comparison with (e) the reconstructed lumen surface based on follow-up scans acquired at 3 years post-procedure. Over-prediction of thrombus growth due to the exclusion of minor branches is highlighted in the red circles (Armour et al. 2020). 172

9.6 Evolution of false lumen (FL) surface in P2 following thrombus growth. (a) Reconstructed lumen surface based on the first post-procedure scan in P2 and predicted FL surface following thrombus growth at (b) 15, (c) 22, and (d) 28 seconds in comparison with the reconstructed lumen surface based on follow-up scans acquired at (e) 1 year and (f) 2 years post-procedure. This simulation shows under-prediction of thrombus growth due to the exclusion of minor branches (Armour et al. 2020). 173

9.7 Evolution of false lumen (FL) surface in P3 following thrombus growth. (a) Reconstructed lumen surface based on the first post-procedure scan in P3 and predicted FL surface following thrombus growth at (b) 8, (c) 15, and (d) 26 seconds in comparison with (e) the reconstructed lumen surface based on follow-up scans acquired at 1 year post-procedure (Armour et al. 2020). 174

9.8 (a) Reconstructed postprocedure geometry of P1. Predicted thrombus formation for P1 in (b) the original geometry and (c) the modified geometry. The difference in predictions due to modified reentry tear position is highlighted (Armour et al. 2020). 175

9.9 Evolution of P2 and P2-mod false lumen surface following thrombus growth compared throughout the simulation at (a) 15, (b) 22, and (c) 28 seconds (Armour et al. 2020) 176

10.1 Peak systolic displacement contours in the FSI model for the left: wall and right: flap. 185

10.2 A: Peak systolic pressure distributions in the rigid and FSI model. B: Location of analysis planes in the dissection. C: Average aortic pressure over the cardiac cycle in the rigid and FSI model. 186

10.3 Velocity fields at peak systole (T = 0.2 s) in the rigid model, and at peak systole and into systolic deceleration in the FSI model. 187

10.4 A: Helical flow visualised throughout the cardiac cycle. B: Magnified images show a high velocity jet through the entry-tear resulting in turbulence (Takahashi et al. 2021). 189

A.1 Analysis planes used for mesh sensitivity tests for models P1, P2 and P2P in Chapter 4. 216

A.2 Analysis planes used for mesh sensitivity tests for models PI and PII in Chapter 5.220

A.3 Analysis planes used for mesh sensitivity tests for models P1, P2, P4 and P5 in Chapter 6. 223

A.4 Analysis planes used for mesh sensitivity tests for idealised geometry in Chapter 7.228

A.5 Analysis planes used for mesh sensitivity tests for models S1 and P2 in Chapter 8.230

A.6 Analysis planes used for mesh sensitivity tests for models P2 and P3 in Chapter 9.233

Nomenclature

Abbreviations

3EWK 3-element Windkessel

AA Aortic arch

AAo Ascending aorta

AP Activated platelets

AWSS Average wall shear stress

BMT Best medical therapy

BP Bound platelets

BRAC Braciocephalic artery

C Coagulant

CEFL circumferential extent of the false lumen

CEL Celicac artery

CFD Computational fluid dynamics

CT Computed tomography

DA Descending aorta

Dis-DAo Distal descending aorta

DW Doppler wire

FI Fusiform dilation index

FL False lumen

FLEF False lumen ejection fraction

FRT First post-stent re-entry tear

FSI Fluid-structure interaction

GCI Grid convergence index

ICA Intercostal arteries

IMA Inferior mesenteric artery

IVP Inlet velocity profile

KE Kinetic energy

LCCA Left common carotid artery

LI Left iliac artery

LR Left renal artery

LSA Left subclavian artery

MAE Mean absolute error

Mid-DAo Mid-descending aorta

MRI Magnetic resonance imaging

OSI Oscillatory shear index

PET Primary entry tear

Prox-DAo Proximal descending aorta

RBC Red blood cell

RFI Reverse flow index

RI Right iliac artery

RMS Root-mean-square

RP Resting platelets

RR Right renal artery

RRT Relative residence time

RT Residence time

SG-FRT Stent-graft to first post-stent re-entry tear distance

SINE Stent-graft induced new entry tear

SMA Superior mesenteric artery

TAWSR Time-average wall shear rate

TAWSS Time-average wall shear stress

TBAD Type B aortic dissection

TEE Transesophageal echogradiography

TEVAR Thoracic endovascular aortic repair

TL True lumen

TP Through-plane

TTE Transthoracic echocardiography

VENC Velocity encoding

vWF von Willebrand factor

WBC White blood cell

Greek symbols

α Womersley number

$\dot{\gamma}_c$ Critical shear-rate

$\dot{\gamma}_t$ Shear-rate threshold

$\dot{\gamma}$ Shear-rate

ϵ Clot porosity

μ Viscosity

$\mu)P$ Plasma viscosity

ϕ Hematocrit

$\phi_{\dot{\gamma}}$ Shear-rate switching function

ϕ_i switching function for species i

ρ Density

τ Stress Tensor

τ_t Time-constant of exponential diastolic pressure fall

τ_w Wall shear stress

Roman symbols

$\widehat{\boldsymbol{i}}$ Velocity component i

$\widehat{\boldsymbol{j}}$ Velocity component j

$\widehat{\boldsymbol{k}}$ Velocity component k

AP_t Activated platelet threshold

BP_t Bound platelet threshold

c Pulse wave speed

c_i	Concentration of species i
C_T	Vessel compliance
C_t	Coagulant threshold
d	branch diameter
$D_{C_{eff}}$	Effective coagulant diffusivity
D_C	Coagulant diffusivity
D_{Pt}	Platelet thermal diffusivity
D_P	Platelet diffusivity
D_{RT}	Self-diffusivity of blood
k_0	Intrinsic blood viscosity
k_1	Kinetic constant 1 for activated and resting platelet reaction
k_2	Kinetic constant 2 for resting platelet reaction
k_C	Kinetic constant for coagulant reaction
k_{inf}	Intrinsic blood viscosity
k_{BP}	Kinetic constant for coagulant reaction
k_{C2}	Kinetic constant 2 for coagulant reaction
RT_t	Residence time threshold
S	Surface
S_i	Source term for species i
t	Time
V	Volume
n	Normal unit vector
u	Velocity
v	Velocity
$\mathbf{F}$	Body forces
p, P	Pressure
Q	Volumetric flowrate
R	Pearson correlation coefficient
R_1	Proximal resistance

R_2 Distal resistance

R_T Total resistance

Re Reynolds number

Re_c Critical reynolds number

Chapter 1

Introduction

In 2019, cardiovascular diseases accounted for 32% of deaths worldwide (World Health Organisation, 2021). With a growing global population research into the biomechanics of cardiovascular diseases, diagnosis procedures and treatment methods is critical. At the centre of the arterial branch of the cardiovascular system is the aorta, which protrudes from the left ventricle of the heart and is the primary and largest artery that transports oxygenated blood throughout the body. Aortic dissection is the most common catastrophic disease of the aorta (McMahon & Squirrell 2010), affecting 3-5 per 100,000 individuals every year. For those aged 65-75, who are at higher risk, this rate may be as high as 35 per 100,000 individuals (Nienaber et al. 2016). A dissection occurs when the inner most layer of the aortic wall tears. Blood flow through this tears causes the wall layers to separate and a secondary channel of blood flow known as the false lumen (FL) forms (Figure 1.1). In cases where the ascending aorta is dissected (Type A) and blood flow to the brain is compromised mortality rates are high at 1-2% per hour and emergency surgical intervention is usually required. Dissection of the descending aorta (Type B) presents lower but still troubling mortality rates of 10% in the first 30 days (and up to 70% for high risk patients). For these cases medical management or minimally invasive endovascular treatments (involving the insertion of a stent-graft to cover the tear and provide structure to the aorta) are generally adopted, provided there are no other complications presenting at the same time.

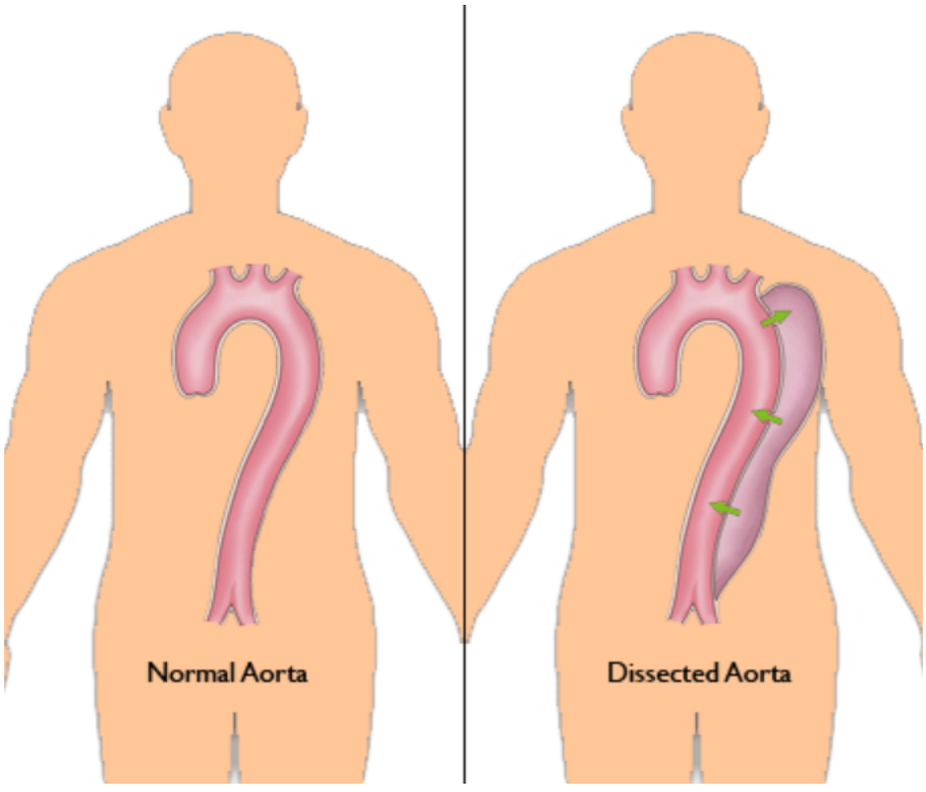

Figure 1.1: Left: healthy aorta. Right: dissected aorta with green arrows indicating blood flow to and from the false lumen. Available at: https://iradonline.org/about.html (International Registry of Acute Aortic Dissection)

For uncomplicated Type B aortic dissection (TBAD) where immediate emergency treatment is not necessary, and multiple treatment options are available, there is uncertainty over which patients should be selected for endovascular treatment and which patients can safely be medically managed. A dissection can develop in multiple ways. The FL can continue to be perfused with blood and remain stable, decrease in volume, or continue to grow, or thrombosis (clotting) can occur to varying levels, with patient prognosis linked to the extent of thrombosis (Trimarchi et al. 2013, Tsai et al. 2007, Qin et al. 2012). With a range of potential outcomes, it is desirable to be able to predict how a specific dissection may develop at the time of diagnosis. Many anatomical studies have aimed to do just this and parameters such as tear number and size, aortic diameter and FL perfusion of aortic side branches have been identified as influential in disease progression (Qin et al. 2012, Kotelis et al. 2016, Tolenaar et al. 2013, Kim et al. 2014, Ge et al. 2017). However, no single parameter has been found to be independently predictive, and morphological analysis alone neglects the complex hemodynamic environment of the dissection.

Computational fluid dynamics (CFD) methodologies have been continuously developed and

modified over the past few decades for biomedical applications. CFD studies of TBAD have been able to show flow patterns, wall shear stress distributions and pressure gradients are closely intertwined with the geometric complexities of a dissection, and have aimed to uncover the fluid dynamic factors at play which drive disease progression (Chen et al. 2013, Cheng et al. 2010, Karmonik et al. 2008, Tse et al. 2011). Significantly, hemodynamic analysis is the base of a model developed by Menichini & Xu (2016) to predict thrombus formation which in patient-specific geometries has been shown to have good agreement between predicted and observed thrombosis (Menichini et al. 2016, 2018). While providing valuable insight into the hemodynamic state of a general dissection, CFD studies have been limited in their physiological accuracy due to the lack of access to patient-specific flow details required to build a CFD model. Physiologically accurate results are critical for computational methods to be used in the clinical setting. Advancements in imaging technologies have meant that 4D-flow magnetic resonance imaging (MRI) which captures velocities in a 3D volume at multiple points in a cardiac cycle has allowed for *in vivo* hemodynamics to be assessed in a way not previously possible. However, 4D-flow MRI still has limitations primarily related to spatial and temporal resolution which creates challenges particularly in TBAD where geometries are complex and vessels sometimes small (Zilber et al. 2021). The combination of 4D-flow MRI and CFD methodologies presents an opportunity for high-quality computational analysis of aortic dissection hemodynamics.

1.1 Research Objectives

The primary aim of this thesis is to fully develop and evaluate a 4D-flow MRI based CFD workflow for patient-specific simulation of TBAD. The secondary aim is to then utilise these CFD methodologies to address clinically important questions.

Key CFD model inputs which can be derived from CT and 4D-flow MRI patient scans are geometry and inlet velocity profile (IVP). Advancing on from idealised geometries, many TBAD CFD studies have incorporated patient-specific geometries of the aorta and the dissection, but have varied in terms of which aortic side branches, if any, were included in the models.

Jiang et al. (2019) utilised two post-TEVAR models to study the influence of excluding major abdominal branches in one case and excluding aortic arch branches in another. While this study highlighted the potential impact of branch exclusion in two scenarios, there remains unanswered important questions surrounding side branches. The influence of branch exclusion on pre-TEVAR geometries has not been assessed - this is important as any CFD tool used in a clinical setting for treatment planning will be modelling the pre-TEVAR state. Additionally, some studies in the literature have not included any branches, and have not adjusted the aortic flowrate to account for excluded branches - the effect of both of these practices has yet to be evaluated. Finally, many minor side branches are present along the aorta and are nearly never included in CFD TBAD studies - the effect of their exclusion is currently also unknown.

The choice of IVP has been studied in non-dissected aortas (Chandra et al. 2013, Morbiducci et al. 2013, Pirola et al. 2018, Youssefi et al. 2018), with patient-specific 2D and 3D IVPs compared to idealised profiles including flat, parabolic and Womersley. However, no study has yet been conducted to assess the influence of IVP on TBAD hemodynamics specifically, which may having differing results due to the more complex morphologies that arise with dissection. It has also been common practice for inlet flowrates to be set based on literature values in TBAD CFD studies if patient-specific flow details are not available. However, the volume of blood ejected by the heart into the aorta (stroke volume) can vary significantly between patients (Maceira et al. 2006) and the effect of such non-patient-specific stroke volume on simulated hemodynamics has not been assessed.

Pirola et al. (2019) presented a comprehensive TBAD CFD study, in which all major side branches were included, the IVP was derived from 4D-flow MRI, and outlet boundary conditions were tuned using 4D-flow MRI flowrates and invasively measured pressures. The use of 4D-flow MRI data to tune CFD boundary conditions was shown to produce physiological results, with strong agreement between CFD and *in vivo* hemodynamics. There were however limitations including the inlet boundary condition being a 2D through-plane rather than fully patient-specific 3D IVP, and the study being of a single subject. Thus, a fully patient-specific workflow implementing a 3D IVP alongside outlet boundary conditions tuned with *in vivo* flow data has yet to be presented. A comprehensive evaluation of such a workflow using multiple data

sets would ensure that the model is validated across a range of dissection morphologies and hemodynamic states, and would provide a vast data set of model parameters for use in future studies without access to patient-specific flow data.

As well as accurately modelling hemodynamics, predicting thrombus formation at the time of diagnosis would be hugely advantageous for clinicians to plan treatment. The hemodyanmic based thrombus formation model developed by Menichini & Xu (2016) can accurately predict thrombus patterns in patient-specific geometries (Menichini et al. 2016, 2018). However, for computational models to be useful in the clinical setting, the time taken for the simulation to run has to be appropriate, and currently the thrombus model takes 1-2 weeks to complete a simulation. Evaluation of the model parameters to simplify the model and reduce computational time is desirable for clinical applicability.

1.2 Thesis Outline

Chapter 2 of this thesis first presents medical background on the cardiovascular system, aortic dissection, and current diagnostic and treatment methods. A review of current literature is then presented, covering thrombosis modelling, evaluation of hemodynamics through CFD and 4D-flow MRI analysis, and anatomical studies to identify important morphological features of TBAD. Chapter 3 lays out the methodologies used throughout the thesis, including the fundamentals of CFD and numerical methods, a detailed description of the hemodynamic-based model for thrombus prediction developed by Menichini & Xu (2016) which is used in this PhD project, and 4D-flow MRI data analysis methods. In Chapter 4, a detailed study on inlet velocity profiles (IVPs) is presented, where the use and accuracy of various 4D-flow MRI derived patient-specific and idealised generic IVPs is evaluated. Chapter 5 then presents a study on the influence of both major and minor aortic side branches on hemodynamic and thrombosis predictions. The methodologies discussed in Chapter 3 and the best practices based on the results of Chapter 4 and 5 are then utilised to conduct a fully patient-specific CFD analysis of five TBAD patients in Chapter 6. The CFD workflow is evaluated through comprehensive

qualitative and quantitative comparison to *in vivo* hemodynamics derived from 4D-flow MRI data. The thrombus model is then evaluated in Chapter 7, where the importance of modelled species is investigated and the model is simplified in order to increase computational efficiency. The methodologies developed and evaluated throughout Chapters 3-7 are then implemented in two application studies. Chapter 8 presents a study on the influence of re-entry tears on aortic hemodynamics in a non-thrombosed dissection through a longitudinal study of a controlled swine model. Chapter 9 then considers the influence of re-entry tears on thrombosis in post-TEVAR models through a study on the distance between the first post-stent re-entry tear and distal end of the stent-graft. Finally, conclusions, recommendations and future work is presented in Chapter 10.

Chapter 2

Literature Review

2.1 The Cardiovascular System

The cardiovascular system is a critical component in the body and is pivotal in keeping the body functional and healthy. The cardiovascular system is responsible for transporting blood throughout the body, and is primarily made up of two parts: the heart and the vasculature.

The heart is an organ that controls the flow of blood throughout the vasculature. It functions as two pumps, each controlling the two main blood circuits of the body: the pulmonary and systemic circuits. The pulmonary circuit takes oxygen depleted blood, taken into the heart through the right atrium, and pumps it to the lungs, from the right ventricle, to re-oxygenate the blood before it recirculates through the body. This re-oxygenated blood leaves the lungs and enters the systemic system, where it enters the left atrium of the heart. The left ventricle of the heart then pumps this blood to the body. Figure 2.1 shows a simplistic diagram of the pulmonary and systemic circuits, the four chambers of the heart, and where the blood enters and leaves the heart.

The circulation of blood is controlled by the electrical system of the heart, which self regulates the speed at which the heart pumps depending on the requirement the body has for oxygenated blood. At rest, the heart will pump between 60 and 100 times every minute in a healthy human,

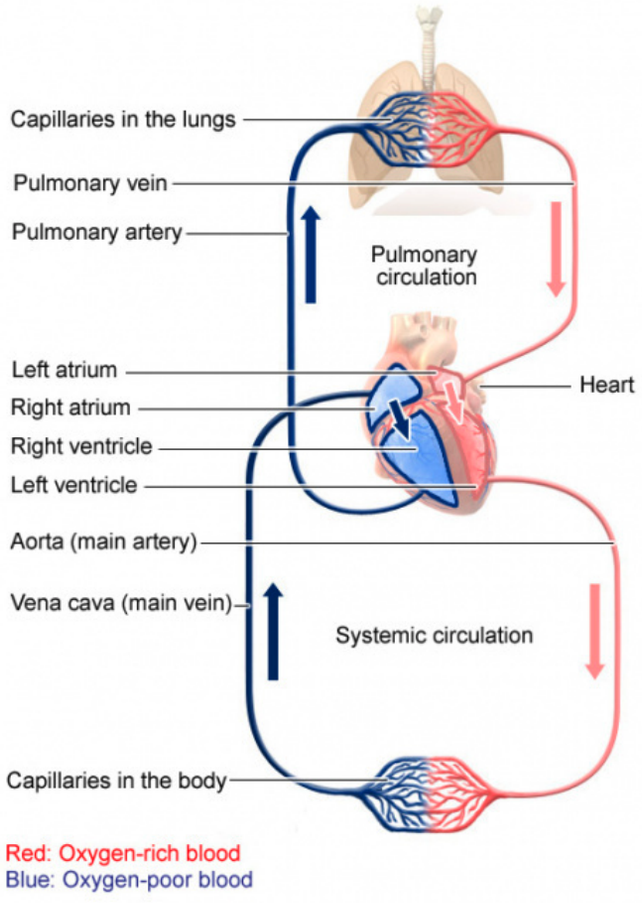

Figure 2.1: Simplistic diagram of the cardiovascular system: the systemic system transports oxygen-rich blood; the pulmonary system transports oxygen-poor blood. Available at: https://www.ncbi.nlm.nih.gov/books/NBK279250/ (Institute for Quality and Efficiency in Health Care)

and this can be lower for those that exercise at lot. Normally, the heart beats occur at regular intervals. The time for one heart beat to occur is known as a cardiac cycle. During a cardiac cycle the heart contracts and dilates, producing the pumping motion required to transport the blood. The period during which the heart contracts is known as systole, and within this period there will be a maximum pressure within the blood vessels - this is known as systolic pressure. Conversely, the period during which the heart dilates and relaxes is known as diastole. The minimum pressure which is experienced in this period is known as diastolic pressure. A healthy human would be expected to have a systolic pressure of 90-120 mmHg and a diastolic pressure of 60-80 mmHg.

All vessels through which blood flows, apart from the heart, make up the vasculature. Oxygenated blood leaving the heart flows through large vessels known as arteries. These branch

into smaller vessels, called arterioles, which in turn branch into the smallest of vessels, known as capillaries. The pulmonary and umbilical arteries are exceptions to this as oxygen-depleted blood is transported through them. Within the capillaries the vast majority of mass transfer between the blood and the surrounding tissue occurs. Once the mass transfer is completed and the blood is oxygen depleted, the capillaries join together to branch into larger vessels, venules. These then branch into larger vessels, known as veins, which connect back to the heart. Again, the pulmonary and umbilical veins are exceptions to this as they carry oxygen rich blood (Ethier & Simmons 2007).

2.2 The Aorta

The aorta is the largest artery and is the beginning of the systemic circuit, protruding from the left ventricle of the heart. Blood flow from the heart into the aorta is controlled by the aortic valve. The aorta is typically split into 3 regions: the ascending aorta, the aortic arch and the descending aorta. The ascending aorta stretches from the aortic valve up towards the head. The coronary arteries branch from the aortic root to supply the heart itself with blood. The aorta then curves around the heart and this section is known as the aortic arch. From the arch, three major vessels branch off to supply blood to the arms and head: the brachiocephalic artery (BRAC), the left common carotid artery (LCCA) and the left subclavian artery (LSA). The aorta then stretches down the body, in line with the spine - this section is known as the descending aorta. The descending aorta can be split into two regions, the thoracic and abdominal aorta. The split is defined as the point where the aorta passes below the diaphragm (Salameh & Ratchford 2016). Minor intercostal arteries branch from the descending aorta to provide blood to the intercostal spaces in the spine, while major branches originate from the abdominal aorta to supply blood to vital organs - these abdominal branches include the celiac trunk (CEL), superior mesenteric artery (SMA), and left (LR) and right renal (RR) arteries. At the bottom of the abdominal section, the aorta bifurcates into the left (LI) and right iliac (RI) arteries which supply blood to the legs. Figure 2.2 shows the sections of the aorta and some of the major branches that extend from the aorta.

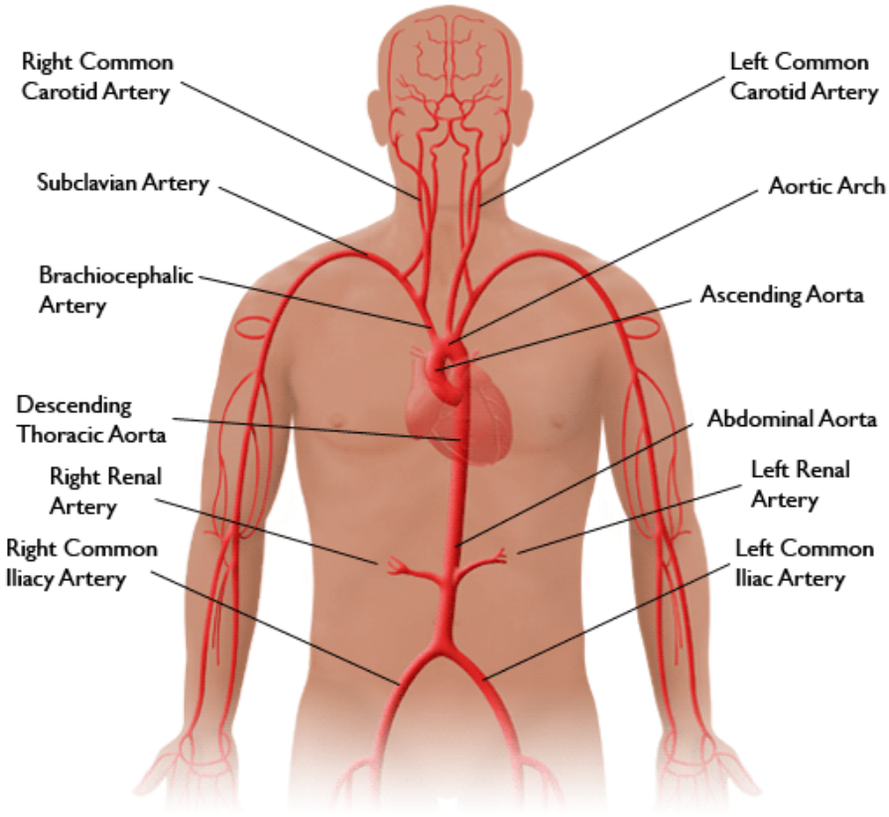

Figure 2.2: Diagram of the aorta, and a selection of the major branches that extended from the aorta. Available at: https://iradonline.org/about.html (International Registry of Acute Aortic Dissection)

The aorta wall is made up of three layers. The intima is a thin smooth surface of endothelial cells and is the inner most layer of the aorta, in contact with the flowing blood. The middle layer, the media, is made up of smooth muscle cells and elastic fibres and provides the elasticity of the aorta required to adsorb the energy of pulsatile flow created by the pumping heart. Finally, the adventitia, the outer most layer provides additional structural support to the aorta (Salameh & Ratchford 2016).

2.3 Aortic Dissection

Aortic dissection is the most common catastrophic disease the aorta can experience (McMahon & Squirrell 2010). It has been reported that 3-5 per 100,000 individuals are affected every year, and for those aged 65-75, who are at higher risk, this rate may be as high as 35 per 100,000 individuals (Nienaber et al. 2016). A dissection occurs when a tear forms in the intima of the

aorta wall, allowing blood to flow between into the media which in turn causes a separation of the wall layers. Thus, a secondary channel of blood is created, known as the false lumen (FL), as opposed to the true lumen (TL) (Salameh & Ratchford 2016). The creation of the false lumen also results in the creation of what is known as the intimal flap - this is the section of the intima that separates the true and false lumen. Figure 2.3 shows a diagram of a dissection. The initial tear that forms is known as the primary entry tear, and it is common for additional tears to be present throughout the rest of the aorta - these are known as re-entry tears.

There are two main naming systems for classifying dissections, primarily based on the position of the primary tear and false lumen. The DeBakey system and the Stanford system are both systems used to classify dissections based on morphological features of the dissection. The DeBakey system defines a dissection as Type I if the primary tear occurs in the ascending aorta, and the dissection propagates past the arch and into the descending aorta. A Type II dissection is one in which the tear occurs in the ascending aorta and the false lumen is present only in the ascending aorta. The final category, Type III, are dissections where the primary tear is in the descending aorta, meaning the ascending aorta and aortic arch are unaffected (Salameh & Ratchford 2016). The Type III category is sometimes broken down further to Type IIIa, where only the descending thoracic is affected, and Type IIIb, where the dissection propagates down into the abdominal aorta (Clough & Nienaber 2015).

The Stanford classification system distinguishes dissections into two categories. Type A dissections are those with a primary tear in the ascending aorta (the dissection may propagate down to the descending aorta under this classification). The second category, Type B, are dissections that have a primary tear in the descending aorta (leaving the ascending aorta and aortic arch unaffected) (Salameh & Ratchford 2016). The Stanford classification system will be used throughout this thesis. Figure 2.3 shows these various geometric features that define a dissection under each naming scheme. A further classification of dissections is defined by the time elapsed from the onset of symptoms. A dissection is described as acute in the first 14 days from the onset of symptoms. After 14 days the dissection is then described as chronic (McMahon & Squirrell 2010).

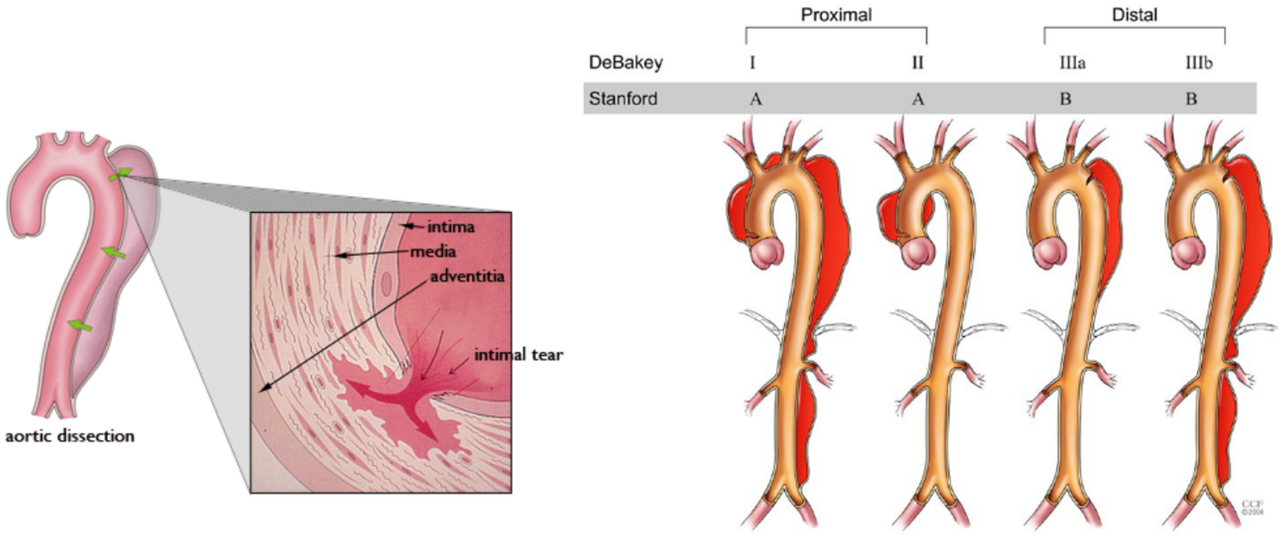

Figure 2.3: Left: Diagram showing an aortic dissection - a tear in the intima allows blood to flow within the layers of the aorta wall creating a false lumen. Available at: https://iradonline.org/about.html (International Registry of Acute Aortic Dissection). Right: Diagrams showing dissection classification under the Debakey and Stanford naming systems Salameh & Ratchford (2016).

The presence of the false lumen results in reduced blood flow in the true lumen, which can lead to devastating complications. A patient may exhibit malperfusion of distal vessels within the circulatory system, which can result in ischemia (reduced blood supply to the organs) and ultimately major organ failure (Salameh & Ratchford 2016). The weakened vessel wall in combination with the pressure in the false lumen can lead to aneurysms or aortic rupture (Pape et al. 2015).

The importance of a functional aorta and the potential for such severe complications leads to high mortality rates. Acute Type A dissections have a mortality rate of 1-2% per hour for the first 24 hours, which can reach up to 50% if no medical intervention is made. Acute Type B dissections have a lower morality rate of 10% in the first 30 days, however this can be up to 70% for high risk patients (Salameh & Ratchford 2016, Frank J. Criado 2011). Approximately two-thirds of dissections are Type A (Nienaber et al. 2016).

While the exact mechanism by which an aortic dissection occurs is unknown, several risk factors have been identified. A key risk factor is hypertension (high blood pressure) - roughly 80% of patients with aortic dissection have hypertension (Nienaber et al. 2016). Other factors reported

to place patients at a high risk of developing a dissection are pre-existing aortic anyeurysms, a bicuspid aortic valve (where the aortic valve has two flaps instead of three), connective tissue disorders (such as Marfan and Ehlers-Danlos syndrome), previous cardiac surgery, age and sex (one study of over 30,000 patients showed 65.7% of patients to be male (Landenhed et al. 2015)) (McMahon & Squirrell 2010, Nienaber et al. 2016).

Finally, a Type B patient is said to have a complicated dissection if any complication, such as those listed above, are present along side the dissection. Patients that exhibit only a dissection with fairly stable conditions are said to be uncomplicated (Frank J. Criado 2011).

2.3.1 Diagnosis

Typical symptoms that patients experience with aortic dissection include sudden and sharp chest and back pains, uncontrollable high blood pressure, and a variety of symptoms resulting from malperfusion to vital organs (Pape et al. 2015, Salameh & Ratchford 2016). As these symptoms are present in a variety of diseases more common than aortic dissection, the diagnosis of patients is challenging (Nienaber et al. 2016, Hagan et al. 2000, Salameh & Ratchford 2016), and patients can be diagnosed incorrectly - often patients can be diagnosed as having acute coronary syndrome (Pape et al. 2015). Due to these difficulties, incorrect initial diagnosis has been reported to occur in more than 30% of cases (Nienaber et al. 2016).

Various methods are used to diagnose aortic dissection. When comparing such methods, their sensitivity and specificity are used to evaluate the accuracy a specific method has at diagnosing a disease. Sensitivity indicates the ability for a method to correctly diagnose patients who have the relevant disease - 100% sensitivity indicates all patients with the disease were identified to have the disease. Specificity indicates the ability for a method to correctly identify patients who do not have the disease - as before, 100% specificity indicates all patients without the disease were identified as so (Lalkhen & McCluskey 2008).

One of the most common methods of diagnosis is computed tomography (CT). CT scans are often favoured as a diagnosis method as they are easily accessible, results are obtained quickly,

and they can be accurate in identifying the location and extend of the dissection while also giving a wide view of the surrounding systems that may also be affected by the dissection (Nienaber et al. 2016, Salameh & Ratchford 2016). CT has a high sensitivity and specificity of 100% and 98% respectively (McMahon & Squirrell 2010). However, CT scans do carry disadvantages including the exposition of patients to radiation, and sometimes the need for intravenous dyes which some patients cannot have due to other health problems (Nienaber et al. 2016, Salameh & Ratchford 2016).

Another method often used is echocardiography. This method involves using ultrasound waves to image the heart. Transthoracic echocardiography (TTE) is a simple form of the method where the chest is scanned. Only the ascending aorta can reliably be examined with this method, resulting in a lower sensitivity (78.3%) and specificity (83%) compared to other methods (Thrumurthy et al. 2012). Transesophageal echocardiography (TEE) involves the insertion of a camera into the esophagus to scan a larger area of the aorta, including the aortic valve and descending aorta (Salameh & Ratchford 2016). TEE has higher sensitivity and specificity values - 98% and 95%, respectively (Thrumurthy et al. 2012). TTE can be a favourable first-step method as it can be completed easily for immobile patients. However, for accuracy, an additional diagnosis method is often required for confirmation. TEE is an invasive process that carries risks and thus a different non-invasive method is often preferable. (Nienaber et al. 2016).

Finally, magnetic resonance imaging (MRI) is a reliable method of diagnosis. MRI scans create images through the reaction of protons in the body when the body is exposed to a strong magnetic field. The sensitivity (98%) and specificity (98%) for MRI is high. This is a non invasive, non harmful (due to there being no radiation exposure) method, that can provide accurate, highly detailed images of the body. However, the process itself and the time taken to get results is slow. Additionally, MRI scanners are not widely available. For this reason, MRI scans are often used in chronic patients to dictate treatment, rather than in the diagnosis stages (Thrumurthy et al. 2012).

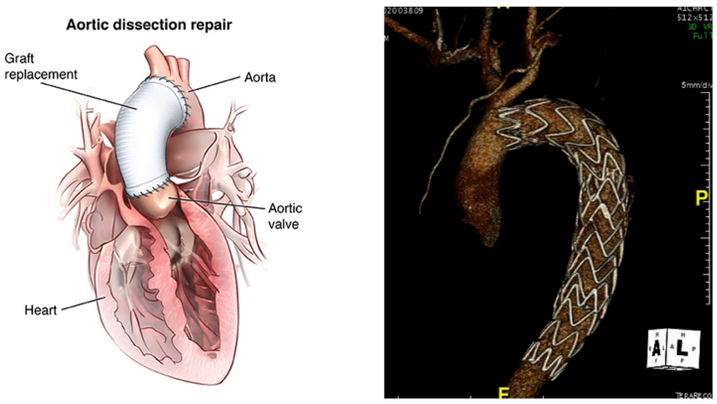

Figure 2.4: Left: Surgical treatment on Type A dissection - a graft replaces the damaged aortic wall. Available at: https://www.saintlukeskc.org/health-library/aortic-dissection-repair (Saint Luke's). Right: Endovascular repair (TEVAR) of a Type B dissection - a stent is inserted into the aorta to cover the primary tear and provide structure (Krol & Panneton 2017)

2.3.2 Treatment

A patient with a Type A dissection is susceptible to much higher risks than a Type B patient. There is often an urgent need for intervention to reduce the potentially fatal effect a limited supply of blood to the brain can have. As such, Type A dissections are often treated through open heart surgery. This involves removing the section of the aorta that is dissected and replacing it with an intraluminal graft (see figure 2.4) (Salameh & Ratchford 2016). This method of treatment carries several risks, including infection and occurrence of heart attacks. Given the risks this method of treatment carries, and the development of new technologies, there has been a decrease in the number of Type B dissection patients treated in this way (Pape et al. 2015). However, surgical techniques including the frozen elephant trunk method, which involves replacing the aortic arch with an intraluminal graft which is attached to a stent-graft inserted into the thoracic descending aorta, are still considered in complicated Type B cases (Kreibich et al. 2018, Matsuzaki et al. 2019).

Medical management of a patient involves the administration of antihypertensive drugs in order to attempt to control the blood pressure within the aorta and reduce the stress on the damaged vessel (Brunkwall et al. 2014). Medical management will be referred to as best medical therapy (BMT) throughout this thesis. If a patient is stable, and responds well to the given medication, this is often a favoured initial treatment as there are no highly invasive procedures required.

Over the past 25 years, endovascular treatment has been developing. As the technology has been refined there has been a shift towards the use of this treatment for Type B patients. Thoracic endovascular aortic repair (TEVAR) involves the placement of a stent graft into the vessel to cover the primary entry tear and to provide structure and support to the damaged wall (figure 2.4). This is a minimally invasive surgery, and recent studies have shown its efficacy for the treatment of Type B aortic dissection (Brunkwall et al. 2014, Nienaber et al. 2014). However, there remains a debate as to which patients should receive TEVAR, and within what time frame the treatment should be administered.

One study that demonstrated the efficacy of TEVAR was the ADSORB trial (Brunkwall et al. 2014). The ADSORB trial (Aortic Dissection: Stent Graft OR Best Medical Therapy) was the first randomized trial for acute, uncomplicated Type B aortic dissection, and was conducted throughout Europe. 61 patients were randomly assigned to be treated with TEVAR or BMT, and were followed up for at least 1 year, and in some cases, longer. Results from the one-year review of the ADSORB trial concluded that the use of TEVAR promoted positive remodelling of the aorta.

2.4 Thrombosis

The objective of any treatment is to achieve complete thrombosis (clotting) of the false lumen, thus stopping all blood flow through the false lumen. Several studies have found that patient prognosis is linked to the thrombosis status of the false lumen, with complete thrombosis being associated with the greatest positive prognosis (Trimarchi et al. 2013). A patent (no thrombosis) false lumen has been found to show similar trends to complete thrombosis (Tsai et al. 2007), while a partially thrombosed false lumen has been found to be linked to a higher risk of late-on set complications and mortality (Qin et al. 2012, Girish et al. 2016). Partial thrombosis has been defined as the concurrence of flow and thrombus in the FL (Qin et al. 2012, Tsai et al. 2007). However, current literature is lacking a quantitative definition for the extreme cases towards both ends of the patent/complete thrombus scale where there may be a

very small amount of thrombus or blood flow.

In order to provide appropriate treatment to patients it is important to understand what influences the formation of thrombus. A variety of morphological parameters have been found to influence the progression of aortic dissection (and FL thormbosis) and these are discussed in section 2.6. However, the reason for why such parameters induce or prohibit thrombus formation is not so clear, and the underlying chemical processes through which thrombus forms need to be understood, and related back to these morphological parameters.

While blood may look like a continuous fluid to the eye, it contains a variety of particles suspended in a fluid. The fluid is called plasma, and constitutes roughly 60% of the blood. Plasma is mainly made of water, but it contains important species such as proteins used in the clotting process, along with other proteins, sugars and fats. The remaining 40% of blood is made up of red blood cells (RBCs), making up the majority of this 40%, white blood cells (WBCs) and platelets. These cells all have vital functions in the body. Red blood cells carry oxygen to supply all cells in the body; white blood cells are important part of the immune system; and platelets are vital for the hemostasis and blood clotting process (Dean 2005).

Hemostasis, the process of stopping blood flow, can be generalised into two stages, primary and secondary hemostasis. Primary hemostasis involves the recruitment, adhesion and activation of platelets at the site of an injured vessel. As platelets flow through the blood in a healthy vessel there will be no interaction between or activation of platelets. This is due to the production of anticoagulant agents by the endothelium cells exposed to the blood flow that inhibit the activation of platelets. However, when a vessel wall is damaged, the subendothelium extracellular matrix is exposed to the blood flow and the primary hemostasis process begins. Within this extracellular matrix are a variety of substances, such as collagen and von Willebrand factor (vWF) that promote platelet adhesion and activation. The initial adhesion of platelets is due to the contact of platelets with such substances (Austin 2013).

Under high shear platelets bind to vWF, and then begin to activate. The activation process in general involves the platelets changing shape, resulting in the expression of surface receptors (GP Ibα, GPIIb-IIIa) and glycoproteins, that are used to further propagate platelet activation.

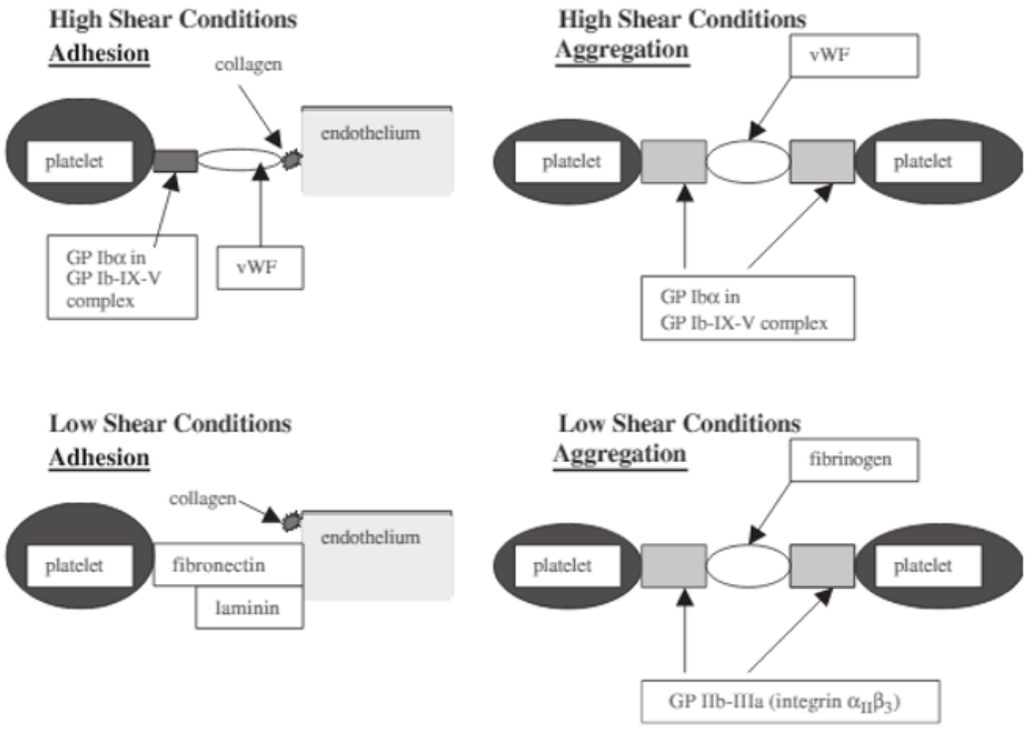

Figure 2.5: Diagram showing the process of platelet activation and adhesion in high and low shear conditions (McMichael 2005)

Under low shear, platelets adhere to the wall by connecting with collagen (McMichael 2005). The adhesion process for high and low shear conditions is summarised in Figure 2.5. As the number of platelets activated and bound to the vessel wall increases, resting platelets circulating come into contact with the activated platelets and bind - this is the process of aggregation. The platelet-platelet binding action is controlled by fibrinogen present on the activated platelets which is able to 'catch' resting platelets. Once bound, these platelets then activate and the cycle continues (Austin 2013).

Secondary hemostasis (also known as the coagulation cascade) involves the eventual production of fibrin, which is the primary substance used in the cross-linking of the platelets to form a strong and stable blood clot. The coagulation cascade is a combination of two pathways: the extrinsic and intrinsic pathway. The extrinsic pathway is the first pathway that is activated when subendothelium cells are exposed. Tissue factor (also known as factor III) is a protein within the subendothelium cells. Tissue factor activates factor VII, which activates factor X. It is important to clarify that when one factor activates another, there is no transformation of one factor to another. Factor III activating factor VII simply means that factor III acts a catalyst

for the change of factor VII from its resting state to its activated state. Factor X aids in the activation of prothrombin to thrombin (factor II). Thrombin is a key species in the coagulation cascade as it is responsible for the conversion of fibrinogen to fibrin. The intrinsic pathway involves the activation of factor XII, due to college exposure, which then leads to a cascade of activation of factors XI, IX and X. Factors VIII and V are also involved in the intrinsic pathway, and these are activated by thrombin, along with factors VII, XI and XIII. Finally, factor XIII aids in the cross linking of fibrin strands which provide the blood clots (thrombus) stability and strength (Austin 2013, Khan Academy 2014).

As this is a cascade with many feedback loops, without any form of self regulation and control there would be a never ending production of blood clots. Thus the mechanism has two key points of negative feedback to control production rates. The production of thrombin results in the conversion of plasmin from plasminogen - plasmin will react with strands of fibrin to break them down. Thrombin also creates a species known as antithrombin, which impedes the conversion of prothrombin to thrombin, and also impedes the activation of factor X. Figure 2.6 gives a simplified view of the coagulation cascade.

2.4.1 Modelling Thrombosis

It can be seen from the discussion throughout section 2.4 that the process through which thrombus forms involves many species in multiple complex biological processes. These processes also evolve over varying time and length scales, from the large scale flow of platelets within the blood, to the small scale activation of various coagulation factors. Hence, to model the formation of thrombus presents significant challenges. Existing models in the literature are based on varying principals and use a range of assumptions to simplify the process.

A variety of models are kinetics based, and range in the number of species that are modelled. A simple model proposed by Wootton et al. (2001) describes thrombus formation in stenosed vessel. The only species modelled are platelets, which are modelled as a dilute species through a convection-(shear-enhanced) diffusion-reaction process. The reaction and adhesion of platelets to the wall was modelled through a first order reaction, where a constant adhesion rate was

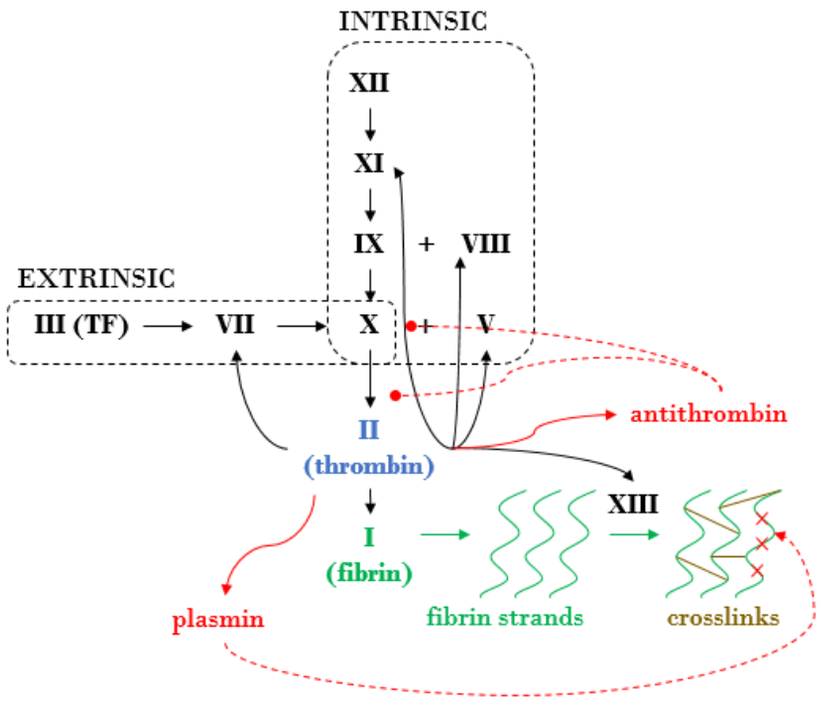

Figure 2.6: Simplistic schematic of the coagulation cascade. Solid black arrows represent the previous species acting as a catalyst for the activation of the following species. Solid coloured arrows represent the transformation of one species into the next. Dotted arrows represent negative feedback loops to control the coagulation cascade.

assumed. With such a simplistic model, differences were observed when model results were compared to experimental results.

A model including a larger number of species was proposed by Sorensen et al. (1999*a*). The model used a set of convection-diffusion-reaction equations to describe the transport of resting and activated platelets, platelet-released and platelet-synthesised agonists, prothrombin, thrombin and ATIII (which inhibits thrombin). This range of species is much more representative of the thrombosis process as a whole. The activation of platelets is modelled as a first order reaction, and platelet adhesion to both other platelets and the surface is modelled through surface-flux boundary conditions. The model was applied to a rectangular microdomain and the model results showed good general agreement with experimental results. However, differences were observed between the model and experiment as the model did not account for the interactions between the fluid flow and platelets (Sorensen et al. 1999*b*).

A comprehensive model, in terms of inclusion of species, was presented by Anand et al. (2006),

who modelled the extrinsic pathway of the coagulation cascade. Their model included the transport of resting and activated platelets, fibrinogen and fibrin, prothrombin and thrombin, as well as a number of coagulant factors in their resting and activated forms: 29 species in total. Convection-diffusion-reaction equations governed the transport of all species, and a shear activation mechanism for platelets was included as well as biological activation. This study was a comprehensive model of the extrinsic pathway, but neglected the intrinsic pathway which is known to play a major role in the coagulation process. Additional, the study was limited to a simplistic 2D geometry.

Goodman et al. (2005) presented a model that described the transport of resting and activated platelets, platelet cohesion agonists, thrombin, prothrombin and antithrombin. Again, both shear induced and biological activation of platelets were included in the model. Differing to the previous models discussed, Goodman et al. (2005) included in the model the influence of thrombus formation on flow, by adjusting velocity patterns at each time step to account for thrombus formation. This was done by increasing the viscosity 100,000 fold in regions defined as thrombus, and applying surface flux boundary conditions to neighbouring regions. Leiderman & Fogelson (2011) also presented a model that included the influence thrombus growth has on flow. Platelets were modelled in four states (mobile and resting, mobile and activated, bound and activated, and subendothelial bound and activated), and the momentum equation was modified to include a negative source term which represented the friction flow experiences due to the presence of thrombus.

Kinetic based models may be beneficial in that the transport of many of the species involved in the thrombosis process can be modelled. However, due to the complexity and shear volume of equations that are required to simulate these biological processes the computational cost can be very high. Hemodynamic based models can be much more efficient in terms of computational cost, and many hemodynamic factors have been identified to be linked to the thrombosis process.

Karino et al. (1987) investigated the adhesion of platelets to collagen fibres downstream of a sudden expansion, which created an annular vortex. They found that the adhesion peaks were

influenced by the curvature of the streamlines carrying the platelets, and these streamlines were dependant on the geometry in which the fluid flows. Schoephoerster et al. (1993) also examined the influence of geometry and local fluid dynamics on platelet deposition, by using stenosis and aneurysm geometries. They found that platelet deposition was highest in areas of recirculation, and reached a minimum in regions of high shear. Biasetti et al. (2012) used an idealised 2D geometry of a fusiform aneurysm to investigate vortical structures within the flow. With the addition of transport equations to model species involved in the coagulation cascade, Biasetti et al. (2012) were able to observe the convection of thrombin in the domain due to the vortical structures, which led to the accumulation of thrombin in the distal portion of the aneurysm.

Menichini & Xu (2016) proposed, and further modified (Menichini et al. 2016), a hemodynamic based model to predict thrombus formation. Four species are modelled through convection-diffusion-reaction equations: resting and activated platelets, coagulant and bound platelets. Coagulant represents all species involved in the coagulation process and bound platelets are representative of thrombus. The activation of platelets is controlled through reaction equations that represent the activation of resting platelets due to exposure to 1) already activated platelets and 2) thrombus. Thrombus as a species is not modelled and instead reaction 2 is scaled by a relative residence time (RRT), with the assumption that thrombus concentration is high in regions of high RRT. The formation of coagulant, and in turn bound platelets, is controlled by time-averaged variables. Both species are predicted to form in regions of high RRT, and low time-averaged wall shear rate (TAWSR) and time-averaged wall shear stress (TAWSS). The model has been compared to a kinetics based model (Ngoepe & Ventikos 2016). The results show similar predictions by both models, but the hemodynamic model was able to make such predictions in a significantly reduced computational time. The model has also been shown to predict thrombus formation in patient specific geometries that is in good agreement with actual patient outcomes (Menichini et al. 2016, 2018) as seen in Figure 2.7. This model is utilised in this PhD project and the model is discussed in detail in section 3.2.

Menichini & Xu (2016) altered the growth kinetics to heavily accelerate the thrombus growth process. This was done due to a sensitivity test indicating that thrombus formation was independent of kinetic constants in this model. However this resulted in there being no connection

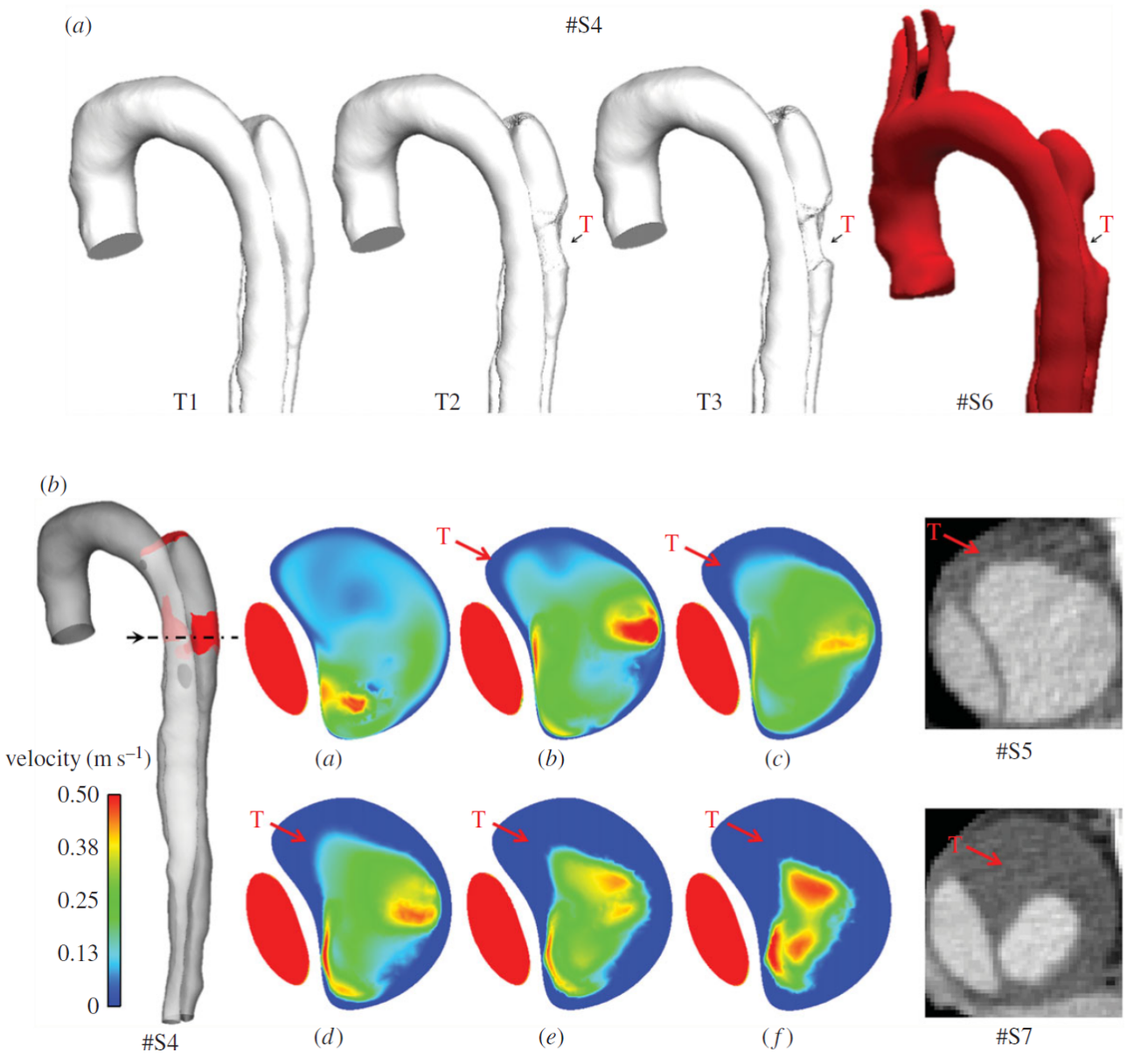

Figure 2.7: a) T1-T3 predicted thrombus growth alongside observed thrombus growth on follow up CT scan (S6). b) In plane velocity reducing to zero during the simulation in regions where thrombus growth was observed on follow up CT scans (S5 and S7), presented by Menichini et al. (2016).

between the simulation time taken for thrombus formation and actual real life time. Additionally, all areas of the wall were assumed to be thrombogenic, with the assumption that the required conditions (high RTT, low TAWSR) would not be met in the true lumen. Patients with Type B aortic dissection can display extremely complex geometries however, which may result in these conditions being met and thrombus being predicted to form in regions where the required biological factors would not actually be present.

2.5 Evaluation of Aortic Hemodynamics

Understanding aortic hemodynamics within a dissection is essential to fully study the disease and be able to predict how it may progress. In recent decades computational fluid dynamics (CFD) software and methodologies have been developed for application in the biomedical research field to simulate complex hemodynamics, and more recently 4D-flow MRI scans have allowed for *in vivo* hemodynamics to be assessed. Both methods allow for engineering tools and understanding to be applied to a critical medical problem with the potential of developing and advancing diagnostic and treatment strategies.

2.5.1 Computational Fluid Dynamics

CFD simulations of TBAD began with idealised studies which utilised 'phantom' geometries typically built based on general geometric features of a TBAD taken from literature (Tang et al. 2012, Fan et al. 2010, Soudah et al. 2015, Ben Ahmed et al. 2016). Simplistic idealised geometries are also useful in experimental set ups as they can be easily modified to investigate various parameters and the methodology is easily reproducible. Several experimental idealised studies of TBAD have been presented (Tsai et al. 2008, Chung et al. 2000*a*,*b*, Rudenick et al. 2013, Birjiniuk et al. 2017, 2019) and some studies have combined the computational and experimental methods to validate the methodologies and extract the maximum amount of data from the studies (Soudah et al. 2015, Zadrazil et al. 2020). While these idealised geometries are useful in studying one specific aspect of the disease by controlling all other features they are clearly limited and unphysiological due to the constructed geometry.

A significant advancement in the field of TBAD CFD simulations was the use of CT segmented patient-specific geometries. CT scans generally have a high spatial resolution and therefore complex geometries that often present in a TBAD (high tortuosity, small tears, small vessel sizes) can be clearly segmented and studied in simulation. The first studies which utilised patient-specific geometries provided a hugely valuable insight into aortic hemodynamics, and identified key flow features including flow distribution between the TL and FL dependant on

tear size which will impact pressure distributions and cross-lumen pressure gradients which may lead to aortic dilation, high wall shear stress around tears which may lead to further propagation of the dissection, and regions of low wall shear stress being favourable for thrombus formation (Chen et al. 2013a, 2013b, Cheng et al. 2010, 2013, 2014a, 2014b, Karmonik et al. 2008, 2011a, 2011b, 2012, 2013, Tse et al. 2011). Figure 2.8 shows velocity streamlines throughout the cardiac cycle derived by CFD simulation presented by Cheng, Juli, Wood, Gibbs & Xu (2014). Since then, CFD analysis of TBAD has been a growing field with further studies investigating TBAD hemodynamics in different patients with varying geometry complexities both pre and post-TEVAR, and gaining a mechanistic understanding of certain morphological parameters that have been highlighted to be influential in disease progression (Bonfanti et al. 2019, Dillon-Murphy et al. 2016, Osswald et al. 2017, Qiao et al. 2019, Rinaudo et al. 2014, Shang et al. 2015, Wan Ab Naim et al. 2014, 2016, Zhang et al. 2014). Further discussion on these studies of morphological parameters is presented in Section 2.6.

The use of CT segmented patient-specific geometries greatly improved the physiological accuracy of CFD simulations, however throughout these studies simplifications in terms of geometry were still made regarding aortic side branches. Methodologies have varied throughout the literature regarding which aortic side branches to include, with some studies not including any, some including only the aortic arch branches and a few including all major branches. The omission of side branches may have been due to image quality or the lack of information for outlet boundary conditions that would need to be applied at each branch. Jiang et al. (2019) conducted a study assessing the influence of aortic side branches on hemodynamics in a post-TEVAR model using three models (one including all branches, one including only the aortic arch branches, and one including only the abdominal branches), and the results showed that omitting branches can significantly impact flow, velocity and wall shear stress results. Jiang et al. (2019) reduced the inlet flowrate to account for omitted branches, however this adjustment was not always made in studies that omitted branches. Therefore, the effect of omitting branches and not accounting for such omissions in the inlet flowrate is unclear. Furthermore, Jiang et al. (2019) did not include a model with no aortic branches, a common geometry observed in the literature.

A critical component of building a CFD model is the inlet velocity profile (IVP). Various inlet

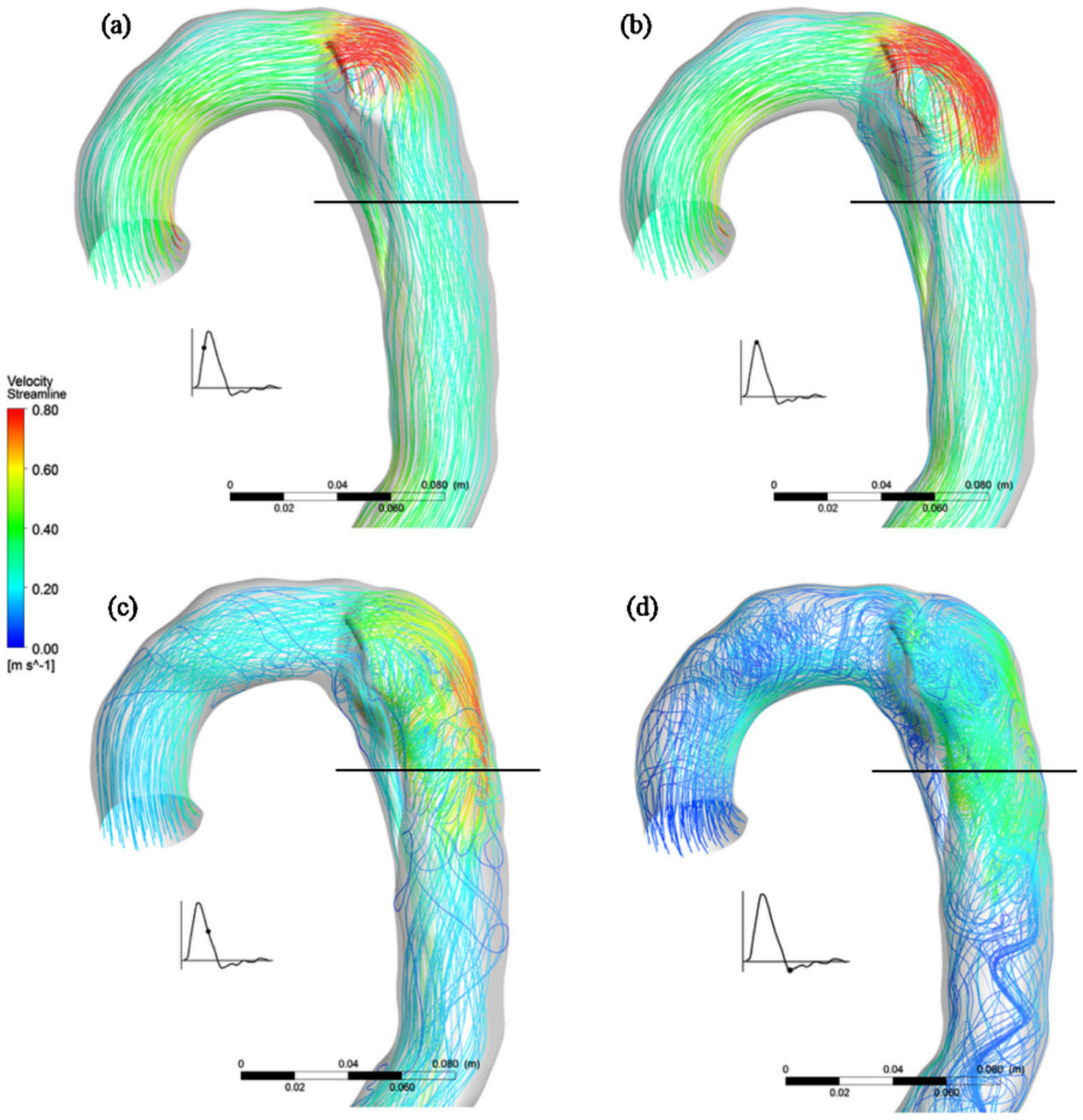

Figure 2.8: Velocity streamlines modelled by CFD simulation presented by Cheng et al. (2014).

velocity profiles can be applied, including idealised or patient-specific derived flat, parabolic, Womersely, 2D and 3D - the vast majority of TBAD CFD studies to date have used an idealised or patient-specific derived flat IVP. Several studies have analysed the influence of different types of velocity profiles on flow throughout various regions of the cardiovascular system, including in the carotid bifurcation (Campbell et al. 2012, Moyle et al. 2006, Wake et al. 2009) and coronary arteries (Myers et al. 2001). Studies by Chandra et al. (2013), Morbiducci et al. (2013), Pirola et al. (2018) and Youssefi et al. (2018) have assessed the impact of inlet boundary condition

on aortic hemodynamics. These studies show that the use of a spatially varying 2D velocity profile, and separately the inclusion of all three velocity components in a 3D velocity profile, greatly impacts the hemodynamics and related parameters in the ascending aorta and aortic arch. The effect of the inlet profile on descending aorta hemodynamics was found to be less significant.

Youssefi et al. (2018) compared a 2D, parabolic and flat IVP, and showed simple parameters such as velocity patterns, peak through plane velocity and radial velocity were similar between the three velocity profiles in the descending aorta. Derived parameters such as helicity, flow asymmetry (a measure of the skewness of the profile) and flow dispersion (a measure of the sharpness of the flow profile) showed mixed results of being consistent or varying between profiles for two different patients (one healthy patient and one patient with a bicuspid valve and dilated ascending aorta). Morbiducci et al. (2013) showed little difference in TAWSS values between a 3D, 2D, flat and fully developed flat IVP in the descending aorta of a healthy patient, however the developed flat IVP did induce altered OSI patterns. Additionally, helical properties of the flow were not captured in the systolic phase by the developed and plug flow profiles. However, in contrast, Pirola et al. (2018) found little difference in helical patterns throughout the cardiac cycle, TAWSS and oscillatory shear index (OSI) in the descending aorta between a 3D, 2D and flat IVP in patients with various aortic valve diseases. Chandra et al. (2013) studied an abdominal aortic aneurysm, implementing a 3D, 2D, Womersley and flat IVP, to assess the effect of inlet profile on hemodynamics and wall mechanics in a fluid-structure interaction (FSI) simulation. Their results showed that the 2D profile produced results very close to those of the 3D profile in terms of velocity patterns, and wall stresses and strains, all of which were underestimated with the flat and Womersley profile.

All of the aorta-based studies were conducted in non-dissected aortas. In these cases, the descending aorta is of a near ideal cylindrical shape, owing itself to the flow developing, potentially leading to differences in inlet profiles being lost. In dissection cases the geometry is complex, can be tortuous and have multiple channels present, all of which can create disturbed flow patterns. Additionally, many type B dissections present with the primary entry tear just distal to the left subclavian artery (LSA) on the aortic arch. All of these factors may result in the

inlet profile having a greater impact on descending aorta hemodynamics.

The availability of complete sets of patient data of high enough quality to extract both the inlet velocity profile and geometry can be difficult to access. This may be due to a lack of high-quality imaging machines in hospitals, or due to certain scans not being taken either because of the patient's condition or because of time pressures to administer treatment. It is often the case that only a CT scan used for diagnosis purposes is available, from which the geometry can be extracted. In this scenario, a generic inlet profile is usually taken from literature and applied to the geometry. With this, not only are the patient-specific velocity details lost, but also other features of the cardiac cycle change, including the flow waveform and the stroke volume. The stroke volume is the total volume of blood ejected by the heart with each beat, which has a typical value of 94 $\pm$ 15 mL (Maceira et al. 2006). Currently, there is no work indicating the effect of such non-patient-specific inlet profiles on aortic hemodynamics in TBAD simulations, despite so much of the literature utilising non-patient specific inlet boundary conditions.

All CFD studies assume a rigid wall and intimal flap which of course is not physiologically accurate as the aorta is a compliant vessel. However, modelling both fluid and wall mechanics through an FSI simulation is challenging. Only a small number of patient-specific FSI simulations of TBAD can be found in the literature, and most of these studies had very limited wall displacement ($<$ 1-2mm) Alimohammadi et al. (2015), Qiao et al. (2015). Most recent 2-way coupled FSI studies were able to accommodate realistic flap motion of up to 6.2mm in a single TBAD case Bäumler et al. (2020) and greater than 4mm in idealised models Chong et al. (2020), while an experimental study Birjiniuk et al. (2017) reported a maximum flap motion of up to 14.3mm. These studies do show the impact of assuming a rigid wall as decreased cross-lumen pressure differences and pulse pressures have been found when wall motion is account for Bäumler et al. (2020), Chong et al. (2020). Furthermore, work by Alimohammadi et al. (2015) showed that while global flow patterns and wall shear stress was not significantly impacted by the rigid assumption, areas of particularly low wall shear stress and the estimation of derived parameters such as oscillatory shear index were affected more significantly. Bonfanti et al. (2017) aimed to overcome the computational cost of FSI by developing a moving wall boundary condition to be applied during a CFD simulation, and their results showed that pres-

sures were more accuratley captured than a rigid CFD model. However in this work the flap was assumed to be a rigid membrane.

All FSI models discussed here are limited by their non-patient specific material properties. Given that TBAD patients are most often treated medically with antihypertensive drugs (completely non-invasive) or with TEVAR (a minimally invasive procedure), there are very few opportunities to obtain dissection tissue samples for experimental purposes. For this reason, there is limited data on TBAD tissue mechanical properties in the literature. Furthermore, no FSI model has yet been presented with patient specific flap and wall thicknesses.

2.5.2 4D-flow MRI Analysis

In recent years, the use of 4D-flow MRI scans has allowed for aortic hemodynamics to be assessed from a single scan of a patient. A 4D-flow MRI scan captures velocities in each of the three Cartesian directions within a defined 3D volume at multiple time points over the cardiac cycle. By post-processing these scans velocities throughout the aorta can be evaluated without the need for CFD. Studies of TBAD using only 4D-flow MRI data have been presented. Clough et al. (2012), Sherrah et al. (2017), Jarvis et al. (2020), Allen et al. (2019) and François et al. (2013) presented studies which showed the capability of 4D-flow MRI to assess hemodynamic parameters such as stroke volume, velocity, flow rate and helical flow patterns throughout the aorta and through tears - the number of patients in each studied varied between 6 and 19. Figure 2.9 shows streamlines derived from 4D-flow MRI data throughout the cardiac cycle presented by François et al. (2013). Takei et al. (2019) presented a single case study utilising 4D-flow MRI data to assess FL flow before and after TEVAR. 4D-flow MRI based studies by Burris et al. (2019) and Burris et al. (2020) have shown that increased retrograde flow through the primary entry tear correlates to FL growth.

These studies clearly show the potential for assessing aortic hemodynamics using 4D-flow MRI data. Such analysis has the potential to be extremely valuable due to the short times required to process the data and the fact that the velocities are measured *in vivo* and therefore not subject to the same errors as CFD simulations which rely on set boundary conditions and are

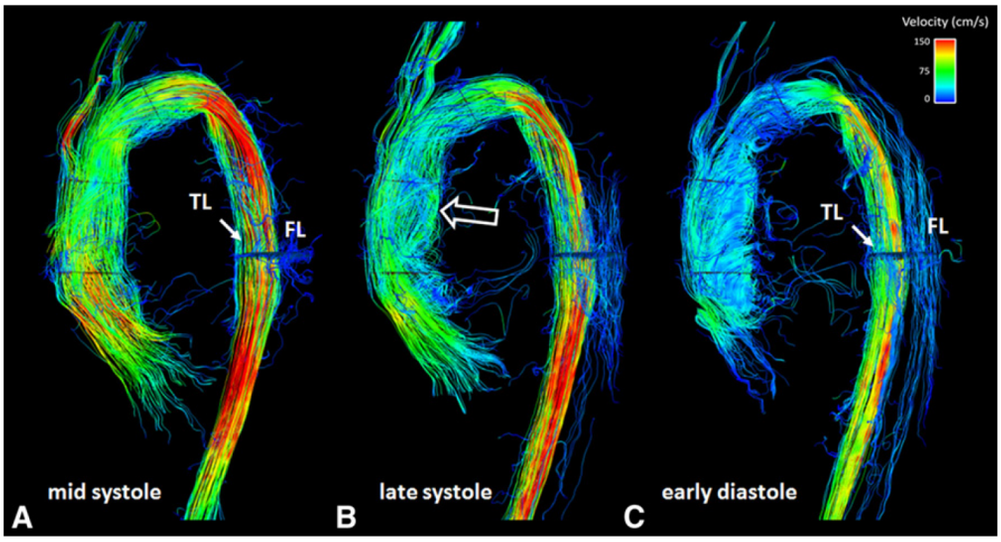

Figure 2.9: Velocity streamlines derived from 4D-flow MRI data throughout the cardiac cycle presented by François et al. (2013).

limited in terms of wall motion. However, there are limitations to 4D-flow MRI analysis which can result in errors in the data. The main limitation is the time taken for the scan to be performed. In order to keep the scan time to a minimum and to an acceptable length for a patient compromises in quality are made. The first is in the spatial resolution which is usually in the order of magnitude of millimetres (roughly 2.5 mm^3 (Zilber et al. 2021)). This means that for dissections that have small channels, as often is the case in TBAD when either the TL or FL is compressed, the voxel size is similar to the channel size and therefore the quality of the data in that region is very low. The relatively large voxel size also means that accurately capturing the near wall hemodynamics is very challenging, and parameters such as TAWSS cannot be accurately measured. Furthermore, the number of time points within the cardiac cycle scanned is limited again to reduce the total scan time. This means that interpolation is required to evaluate the entire cardiac cycle. Furthermore, to take a 4D-flow MRI scan a velocity encoding (VENC) parameter must be set which indicates the general magnitude of velocities that are captured.

Both CFD and 4D-flow MRI analysis have advantages and disadvantages, and these two methods to evaluate aortic hemodynamics can be combined to utilise the benefits of high quality results produced by CFD with patient-specific flow details that can be derived from 4D-flow MRI data. As previously mentioned studies CFD studies have begun to utilise 4D-flow MRI

derived flowrates, with the most comprehensive model to date being presented by Pirola et al. (2019) which utilised a through-plane inlet velocity profile derived from 4D-flow MRI. However the implementation of a fully patient-specific 4D-flow MRI based CFD workflow (3D inlet-velocity profile and patient specific outlet boundary conditions) has yet to be presented and fully evaluated.

2.6 Morphological Parameters That Influence the Progression of Type B Aortic Dissection

Once treatment has been administered there are various ways in which aortic dissection can progress. As discussed previously, the desired outcome of any treatment is complete false lumen thrombosis. However there are a variety of other possible outcomes - any level of thrombosis that is incomplete, false lumen expansion and possibly rupture, true lumen expansion and reduction with the possibility of the true lumen collapsing. Many morphological parameters have been identified to influence disease progression through anatomical studies, and various computational and experimental studies have been conducted to investigate such parameters. The following sections these morphological parameters and the current understanding of their influence on varying patient outcomes.

Tear Number, Size and Location

Evangelista et al. (2012) conducted an anatomical analysis of 184 Type A (n = 108) and B (n = 76) patients. They identified maximum entry tear diameter to be a strong indicator of patients that are at high risk of further complications, due to the increase in flow through the FL. Evangelista et al. (2012) acknowledge that, although maximum entry tear diameter was found to be statistically significant for predicting complications, it may not always correlate with tear size. Kitamura et al. (2015) also conducted an anatomical study of 224 Type B patients, and identified that the location of the primary tear on the outer curvature of the aortic arch correlated with further complications and the requirement for intervention. Qin et al. (2012) anatomically analysed the scans of 124 Type B patients treated with TEVAR

and identified the number of tears to correlate with the extent of FL thrombosis - increasing tear number reduced the chance of FL thrombosis. In terms of aortic growth there are mixed conclusions - through a study of 24 BMT patients Kotelis et al. (2016) found that an increase in the number of tears increased the risk of aortic growth, while Tolenaar et al. (2013a,b) found that a reduction in aortic growth with an increasing number of tears through studies of 60-62 BMT patients. Through a study of 14 TEVAR and 13 BMT patients Menichini (2018) found an increase in the number of tears to correlate with FL growth in both groups. Furthermore, an increase in the distance between the first post-stent re-entry tear and distal end of the stent graft was correlated to an increase in FL thrombosis.

Ben Ahmed et al. (2016) presented a computational study using various idealised geometries in which they investigated the influence of tear size and number, among other features. Firstly, a straight idealised geometry was used, with two tears (proximal and distal) of equal size, varying from 4mm to 10mm and then to 20mm. The percentage of flow reporting to the false lumen increased with tear size. The size of either the proximal or distal tear was then varied. A larger proximal tear (and smaller distal tear) increased FL pressures, and the reverse of a smaller proximal tear (larger distal tear) reduced FL pressures. Finally, each tear was occluded in turn, and the occlusion of the proximal tear resulted in reduced FL pressures. Thus, Ben Ahmed et al. (2016) concluded that large proximal tears, and the absence of distal tears, can be identifiers for unfavourable hemodynamic conditions that may put patients at risk of further complications. An obvious limitation of the study was the use of a straight rigid walled idealised geometry, and a patient specific geometry would be preferable when investigating such morphological parameters.

Rinaudo et al. (2014) conducted computational studies on 25 TBAD patients. The models created from the patients CT scans included the ascending and descending aorta, and the aortic arch branches - branches extending from the descending aorta were not included. Various morphological parameters were measured, and the height of the entry tear was found to correlate with the percentage of flow through the FL. The modelling of patient specific geometries certainly improves the accuracy of results, however an important limitation of the study are the boundary conditions imposed - a flat pulsatile inlet flow rate was applied to all models, and

the outlet boundary conditions were defined as percentages of inlet flow. More physiological boundary conditions would be beneficial to the study. Cheng et al. (2013) also studied the size and location of the primary tear in patient specific geometries. Four TBAD patients were modelled, and the tear size (represented by height and maximum width) and position (represented by the vertical distance between the tear and top of aortic arch) were measured. Cheng et al. (2013) found that a larger tear resulted in a larger percentage of inlet flow reporting to the false lumen. Similar results were found by Zadrazil et al. (2020) through a combined experimental and computational study of four different tear sizes and size ratios between multiple tears - increase in re-entry tear size increased FL flow, wall shear stress and the cross-lumen pressure difference. The results of Cheng et al. (2013) and Zadrazil et al. (2020) agree with Rinaudo et al. (2014), and similarly the models have limitations in the fact that the outlet boundary conditions are non-physiological.

Girish et al. (2016) conducted ex vivo experiments using 25 porcine aortas in which aortic dissections were artificially created to investigate the influence of the number of tears and location on FL thrombosis. The morphology of the aortas varied between the presence of a single proximal tear, a single distal tear, and a proximal and distal tear. A single proximal tear increased FL pressure, while a single distal tear reduced FL pressure. When both a proximal and distal tear were present the pressure in both lumen were approximately equal. These results are in line with the findings of Ben Ahmed et al. (2016). A key limitation of the experiment was that water was used as the fluid, thus the viscosity and flow properties would vary with the use of blood, potentially effecting pressure measurements. Additionally, the maximum number of tears present in the model was two, and it is known that a patient can present with many more tears along the aorta which can influence outcome as Qin et al. (2012) identified and is discussed above.

Aorta Length, Area and Volume

Kim et al. (2014) analysed 38 TEVAR patients and found that an increase in maximum false lumen diameter pre-TEVAR was a predictor for an increase, or no change, in false lumen volume post-TEVAR. Marui et al. (2007) performed a retrospective anatomical study of 141 BMT patients, and identified a number of factors that were predictors of late on set complications.

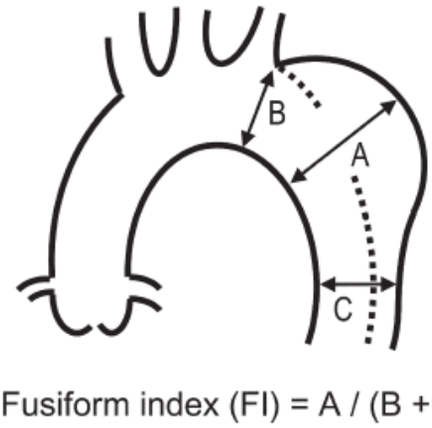

Figure 2.10: Diagram showing the locations used to calculate the fusiform dialation index (FI). A is the maximum diameter of the descendingaorta, B is the diameter of the distal aortic arch, and C is the diameter of the descending aorta at the level of the origin of the main pulmonary artery (Marui et al. 2007)

Two of these factors were the maximum aorta diameter and the fusiform dilation index (FI) at the time of diagnosis. The fusiform dilation index is defined as FI = A / (B + C), where A is the maximum diameter of the descending aorta, B is the diameter of the distal aortic arch, and C is the diameter of the descending aorta at the level of the origin of the main pulmonary artery - see figure 2.10.

As discussed previously, Qin et al. (2012) performed an anatomical analysis of 124 TEVAR patients. From this study, the maximum diameter of the false lumen in the aorta was identified also as a predictor of incomplete thrombosis. Sailer et al. (2017) found several parameters that were predictors of late onset complications for BMT patients, defined as fatal or non fatal aortic rupture, rapid aortic growth, aneurysm formation, organ or limb ischemia, or new uncontrollable hypertension or pain. Two of the identified parameters were maximum aorta diameter and the circumferential extent of the false lumen (CEFL) in angular degrees. Figure 2.11 demonstrates the measurement taken to determine the CEFL. The CEFL was chosen as a parameter to study due to the comparability of the parameter across patients. Particularly in the acute phase of aortic dissection the intimal flap can be very mobile, resulting in varying diameters/volumes of the FL throughout the cardiac cycle. However the CEFL stays constant throughout the cardiac cycle, as shown in figure 2.11D.

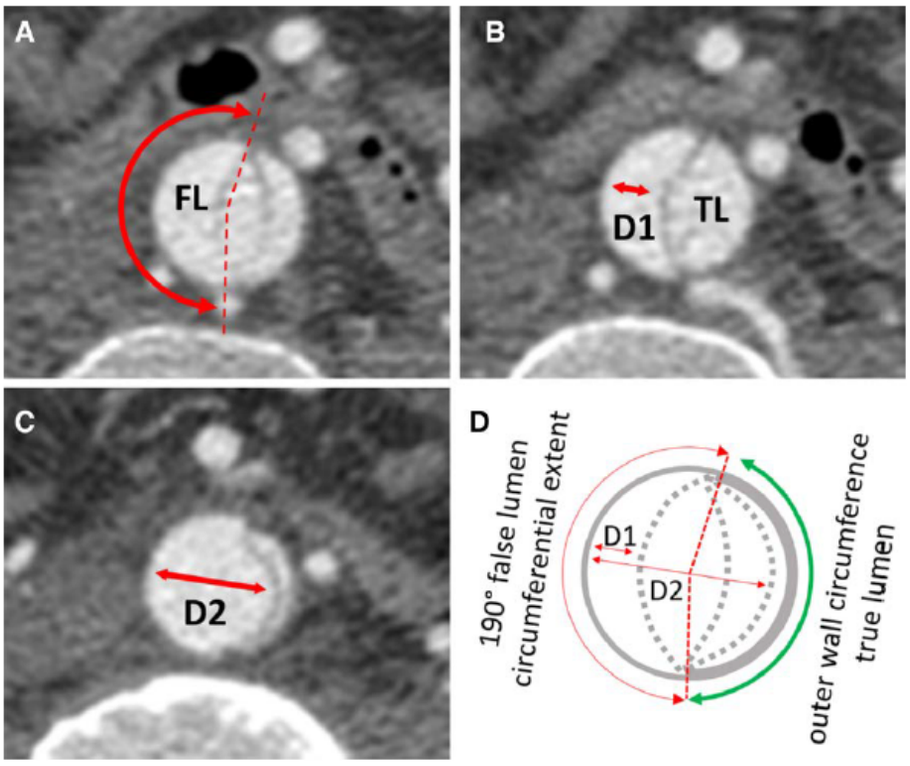

Figure 2.11: Diagram showing the measurement of the circumferential extend of the false lumen (CEFL). A-C shows the mobility of the intimal flap throughout the cardiac cycle. D demonstrates that the CEFL stays constant while the intimal flap moves, presented by Sailer et al. (2017).

False Lumen Perfusion of Side Branches

Another parameter identified through the anatomical study by Qin et al. (2012) to correlate with FL thrombosis was the number of large branches originating from the false lumen. It was found that an increase in FL side branches reduced the extent of FL thrombosis, and for all patients that had complete FL thrombosis zero FL side branches were identified. Tolenaar et al. (2014) and Menichini (2018) also conducted anatomical studies on 42 and 27 patients, respectively, and found that the involvement of FL side branches reduced FL thrombosis. However, in contrast to the study by Qin et al. (2012), Tolenaar et al. (2014) found that 5 of the 16 patients that achieved complete FL thrombosis did have some level of FL side branch involvement. Kamman et al. (2017) analysed the ADSORB data and found that for BMT patients, the number of side branches originating from the false lumen was a predictor of false lumen expansion.

Ge et al. (2017) identified the number of thoracic false lumen branches to be a predictor of

thoracic aorta growth. The correlation of thoracic false lumen branches differs to the findings of Qin et al. (2012) and Kamman et al. (2017), which identified large FL vessels specifically as a key parameter, as only intercostal arteries and other small vessels extend from the thoracic false lumen. This influence of intercostal arteries however was also identified in the anatomical analysis of 83 BMT patients by Sailer et al. (2017). As discussed, the parameters identified in this study by Sailer et al. (2017) were indicators of late onset complications, as opposed to aortic growth specifically. They also identified false lumen outflow to be a predictor. False lumen outflow was calculated as the sum of assumed outflows to branches identifed to be originating from the false lumen. For example, if the celiac trunk was identified as being perfused by the false lumen, 550 mL/min would be added to that patients false lumen outflow. This is a similar measurement as purely identifying the number of false lumen branches, with the added level of effectively weighting the branches depending on their size. However, this has limitations in the fact that the actual flow rate to these branches can vary drastically between patients.

Overall Risk Due to Identifiable Parameters

While numerous morphological parameters have been identified to influence the progression of Type B aortic dissection, only one study was found in the literature which presented an insight into the combined influence of such parameters. As discussed throughout this section, Sailer et al. (2017) identified the circumferential extent of false lumen, maximum aortic diameter, false lumen outflow and number of intercostal arteries as predictors of late onset complications. In addition to these parameters connective tissue disease was also found to be an indicator. Using these five parameters, Sailer et al. (2017) developed a risk-prediction model.

If the baseline survival function of a population is known then the absolute probability of a patient experiencing a complication within a given time period can be calculated. The so-called 'linear predictor' is calculated as: 0.841×(connective tissue disease - 0.169) + 0.021× (false lumen circumferential extent - 249) + 0.071×(maximum aortic diameter - 37) - 0.001×(false lumen outflow - 650)×0.094× (number of intercostals - 11.7). The absolute probability of a complication within a given time period is then: (1 - baseline survival for given time period)$^{\exp(\text{linear predictor})}$. If the baseline survival for a population is unknown then a relative risk based on a ranking of patients can be calculated as: 0.841×(connective tissue disease) +

0.021×(false lumen circumferential extent) + 0.071×(maximum aortic diameter) - 0.001×(false lumen outflow) - 0.094×(number of intercostals). Patients are ranked dependant on their score, with a score of up to 6.05 being ranked as low risk, between 6.06 and 7.0 as intermediate risk, and above 7.0 as high risk.

This model was based on a retrospective study and is yet to be validated external to the workings of Sailer et al. (2017), but the combination of these measurable influencing parameters into an overall 'risk of complications' factor is very attractive for a clinical setting. It is easily applicable and can allow doctors to be more patient specific in their treatment and follow up procedures.

2.7 Summary and Research Objectives

Type B aortic dissection is a critical disease that can lead to devastating and potentially fatal complications. Several studies have identified a range of morphological parameters that correlate to varying disease progressions. However, to date no single parameter has been identified to be independently predictive of an outcome on which clinical decisions can be made. Being the largest artery in the body, critical for transporting blood, it is understandable that anatomical analysis alone cannot fully represent the disease. Having a clear understanding of the hemodynamic state of each individual patient is essential, particularly with TBAD given the vast range of morphologies that can present. Methodologies for using CFD simulations to study TBAD have advanced significantly over the past decade, and with the most recent developments in the use of 4D-flow MRI, there is the potential for fully-patient specific simulations to be conducted.

Thus, the main objective of this PhD project is to fully develop and evaluate a 4D-flow MRI based CFD workflow for simulation of TBAD, and utilise this methodology to study critical morphological parameters highlighted in the literature to influence disease progression. Current literature does not provide a clear picture on the impact of non-patient specific simulation inputs, and therefore evaluation of key parameters such as geometry segmentation and inlet velocity profiles will be conducted, before the workflow as a whole is evaluated. Patient-specific modelling through CFD has the potential to provide valuable in-depth information that can be

used in the clinical setting to optimise treatment planning based on each individual case.

Chapter 3

Methodology

This chapter presents the fundamental governing equations required to computationally simulate flow and thrombus formation. Following this, the methodology used to build the computational models in order to numerically solve these equations is laid out. This includes details on geometry segmentation, mesh generation and boundary conditions. Additionally, the workflow for processing and analysing 4D-flow MRI data is described.

3.1 General Governing Flow Equations

To mathematically describe the behaviour and properties of a fluid, the principal of conservation of mass and momentum can be applied to a fluid volume. Blood consists of particles (red blood cells, white blood cells and platelets) suspended in a fluid (plasma). In large arteries, such as the aorta, it is common practice to describe blood as one continuum medium. By assuming a constant temperature and neglecting the effect of any heat transfer (as is done in this thesis), velocity and pressure, and any derivative parameters such as wall shear stress, can be determined at all points of space and time.

The general conservation of mass states that the rate of mass accumulation in volume V is equal to the net mass flow rate through the surface of V. The mass flow rate is equal to the

volumetric flow rate multiplied by the fluid density, with the volumetric flow rate equal to the fluid velocity normal to the surface multiplied by the area of the surface through which the fluid flows. From this, the conservation of mass for an arbitrary shaped control volume gives Equation 3.1.

$$\frac{d}{dt}\int_V \rho dV = -\int_S \rho \mathbf{u}.\widehat{\boldsymbol{n}} dS \tag{3.1}$$

Gauss' divergence theorem states

$$\int_S \boldsymbol{a}.\widehat{\boldsymbol{n}} dS = \int_V \boldsymbol{\nabla}.\boldsymbol{a} dV \tag{3.2}$$

where,

$$\boldsymbol{\nabla} = \frac{d}{dx}\widehat{\boldsymbol{i}} + \frac{d}{dy}\widehat{\boldsymbol{j}} + \frac{d}{dz}\widehat{\boldsymbol{k}}. \tag{3.3}$$

Applying Gauss' divergence theorem to Equation 3.1, where $\boldsymbol{a} = \rho\boldsymbol{u}$, gives the continuity equation:

$$\frac{d\rho}{dt} + \boldsymbol{\nabla}.(\rho\boldsymbol{u}) = 0 \tag{3.4}$$

For incompressible fluids, an assumption that is common to make when studying the flow of blood, the derivative of density with respect to both time and space will be zero, and thus the continuity equation reduces to Equation 3.5.

$$\boldsymbol{\nabla}.\boldsymbol{u} = 0 \tag{3.5}$$

The conservation of momentum can be applied to a control volume by considering the application of Newton's second law to a solid body. This law states that the net change in momentum of a body is equal to the sum of forces acting on the body. A key difference that must be considered is that in addition to the forces acting on the control volume that result in a change in momentum, the fluid itself can also transport momentum within the control volume. This leads to a general conservation of momentum for a control volume that states:

$$\begin{array}{ccccc} \text{rate of momentum} & & \text{net momentum} & & \\ \text{accumulation} & = & \text{flow rate through} & + & \begin{array}{c}\text{sum of forces}\\ \text{acting on V}\end{array} \\ \text{in volume V} & & \text{the surface of V} & & \end{array}$$

The net momentum flow rate through the surface of V can be derived in a similar manner as Equation 3.1, giving:

$$\frac{d}{dt}\int_V (\rho \boldsymbol{u}) dV = -\int_S (\rho \boldsymbol{u}) \mathbf{u}.\widehat{\boldsymbol{n}} dS \tag{3.6}$$

The sum of forces acting on the volume V can be split into two terms: body forces and surface forces. Body forces are those that act on the bulk of the fluid inside the control volume, such as gravity, electric forces, and magnetic forces. Thus, the contribution by body forces can be represented by the following term.

$$\int_V \rho \boldsymbol{F} dV \tag{3.7}$$

The surface forces are the forces exerted at the surface of the control volume by the surrounding fluid. There are two contributions to the overall surface forces: f_1 is the pressure force exerted by the surrounding fluid normal to the surface of the control volume; f_2 arises from friction due the action of viscosity, and the fluid resisting local deviations in velocity. Combining these contributions gives a term for the total surface forces.

$$\int_S \boldsymbol{f}_1 dS + \int_S \boldsymbol{f}_2 dS = -\int_S p\widehat{\boldsymbol{n}} dS + \int_S \boldsymbol{\tau} \cdot \boldsymbol{n} dS \tag{3.8}$$

$\boldsymbol{\tau}$ is the viscous stress tensor, and for Newtonian fluids it is assumed there is a linear relationship between stress and velocity gradients. By combining equations 3.6, 3.7 and 3.8, applying Gauss' divergence theorem and simplifying, the conservation of momentum reduces to:

$$\rho \frac{\partial \boldsymbol{u}}{\partial t} + \rho \boldsymbol{u} \cdot \boldsymbol{\nabla} \boldsymbol{u} = -\boldsymbol{\nabla} p + \mu \nabla^2 \boldsymbol{u} + \rho \boldsymbol{F} \tag{3.9}$$

For 3D flow Equation 3.9 represents 3 equations, one for each Cartesian direction. By combining these 3 equations with Equation 3.5 there are 4 equations with 4 unknowns. This group of

partial differential equations is known as the Navier-Stokes equations, and are the essential governing equations that describe a fluid flow across space and time.

For a non-Newtonian fluid with a varying viscosity the assumption of a linear relationship between stress and velocity gradients does not hold. Instead the stress tensor is a general function of space and time ($\boldsymbol{\tau} = f(x,t)$), and the momentum equation becomes:

$$\rho\frac{\partial \boldsymbol{u}}{\partial t} + \rho\boldsymbol{u}\cdot\boldsymbol{\nabla}\boldsymbol{u} = -\boldsymbol{\nabla}p + \nabla\cdot\boldsymbol{\tau} + \rho\boldsymbol{F} \tag{3.10}$$

3.2 Modelling Thrombosis

As discussed in section 2.4.1, Menichini & Xu (2016) proposed a novel hemodynamic model to predict the formation and growth of thrombus in dissected aortas, which was then further modified by Menichini et al. (2016). This model is utilised in studies presented in Chapters 4, 5 and 9, and the following section describes the fundamental equations that drive thrombus formation.

For simulations to complete in a reasonable computational time, several assumptions are made. Primarily, only a limited number of species are modelled, and the prediction of thrombus formation is based on time-averaged parameters. Potential regions of thrombus growth are, in one way, identified through a fictitious parameter called residence time (RT). This parameter is used to identify regions of flow stagnation and recirculation, which are key features identified in the literature, as discussed in section 2.4.1, that favour thrombus formation. RT is a tracer of the blood itself, and is modelled by the following standard transport equation:

$$\frac{\partial RT}{\partial t} + v\cdot\nabla RT = D_{\mathrm{RT}}\nabla^2 RT + 1 \tag{3.11}$$

where D_{RT} is the self-diffusivity of blood ($1.14\times10^{-11}\,m^2s^{-1}$). The source term of $+1$ gives a unit increase in RT with each unit increase of time. As RT will continuously rise as the simulation continues, and cardiac cycles pass, the increase in RT is normalized with respect to

cycle period and the resulting non-dimensional variable is referred to as relative residence time (RRT).

Many biological species are involved in thrombus formation. However, in this model platelets in three states (resting (RP), activated (AP) and bound (BP)) are modelled to simplistically represent the stages of thrombus formation. Resting and activated platelets are modelled by a standard convection-diffusion-reaction transport equation:

$$\frac{\partial c_{\mathrm{i}}}{\partial t} + v \cdot \nabla c_{\mathrm{i}} = D_{\mathrm{P}} \nabla^2 c_{\mathrm{i}} + S_{\mathrm{i}} \qquad i = AP, RP \tag{3.12}$$

where c_{i} is the concentration of species i and D_{P} is the diffusivity of the platelets ($1.6 \times 10^{-13}\, m^2 s^{-1}$). S_{i} represents the source term which is the sum of two contributing reactions. The first (r_1) is the reaction whereby already activated platelets induce the activation of RPs. The second reaction (r_2) is the activation of RPs due to exposure to thrombin. Thrombin is a species in the thrombosis process that is not modelled, and therefore the assumption is made that the concentration of thrombin would be high in areas of high RRT. Thus, with kinetic constants k_1 ($0.15\ s^{-1}$) and k_2 ($0.5\ s^{-1}$), the two reactions can be represented by the following equations:

$$r_1 = k_1[AP][RP] \qquad r_2 = k_2[RP]RRT \tag{3.13}$$

The concentrations [AP] and [RP] are normalised against their initial values, and thus represent a probability of encountering that relevant species, rather than an exact value of concentration. While thrombin exposure and the self propagation of activation drives the conversion of platelets from their resting to activated state, initial activation occurs due to exposure of subendothelium cells when a vessel wall is damaged. Furthermore, high shear rates have been linked to platelet activation and such shear rates can often be found in regions near tears in a dissection. As both subendothelium exposure and the initiation and presence of tears occurs in the patient before the time point at which computational modelling begins, a background activation level of 5% of the inlet RP concentration is assumed to account for any activation that would have already occurred.

As described in section 2.4, the coagulation cascade involves many steps to produce fibrin, which assists in the cross linking of platelets to form clots. In this model, the coagulation cascade as a whole is represented by the variable coagulant (C). Through a flux boundary condition discussed in section 3.6, C initially forms on the vessel wall in areas of low shear stress, following which it is transported into the blood stream, where the transport is convection dominated. However, when the coagulant enters regions of stagnation and high RRT (such as regions of thrombus formation), and when the coagulant diffuses to the thrombus surface, the transport is diffusion limited. The time taken for these two steps (convection in bulk followed by diffusion in thrombus regions) vastly vary. Thus, to model the transport simply the coagulant is modelled through a shear-dependant diffusive mechanism:

$$\frac{\partial C}{\partial t} = D_{c_{eff}} \nabla^2 C + k_c \, \phi_{Ccontrol}[AP] - k_{c2} \, \phi_C \, (1 - \phi_{\dot{\gamma}})[AP] \tag{3.14}$$

$$D_{c_{eff}} = \phi_{\dot{\gamma}} D_c \tag{3.15}$$

$$\phi_{Ccontrol} = \phi_{BP} \tag{3.16}$$

$$\phi_{\dot{\gamma}} = \frac{\overline{\dot{\gamma}_t}^2}{\overline{\dot{\gamma}}^2 + \overline{\dot{\gamma}_t}^2} \tag{3.17}$$

Equation 3.17 dictates the influence convection has on the overall concentration of C. Compared to the threshold value of $\overline{\dot{\gamma}_t}$ $50\,s^{-1}$, when shear rates are high $\phi_{\dot{\gamma}}$ tends to 0, and the coagulant is consumed (carried in the blood stream, unable to deposit on a surface). When shear rates are low $\phi_{\dot{\gamma}}$ tends to 1, leaving the transport of coagulant to be dominated by diffusion. BP represents thrombus, which is modelled as a static, non-diffusive, non-convective, variable, the production of which is also controlled by $\phi_{\dot{\gamma}}$.

$$\frac{\partial BP}{\partial t} = k_{BP} \, \phi_{BPcontrol} \, \phi_{\dot{\gamma}}[AP] \tag{3.18}$$

$$\phi_{BPcontrol} = \phi_C \phi_{RRT} \phi_{AP} \tag{3.19}$$

The kinetic constants k_{BP} (12 $nmolL^{-1}s^{-1}$), k_C (16 $nmolL^{-1}s^{-1}$) and k_{C2} (6 n$molL^{-1}s^{-1}$)

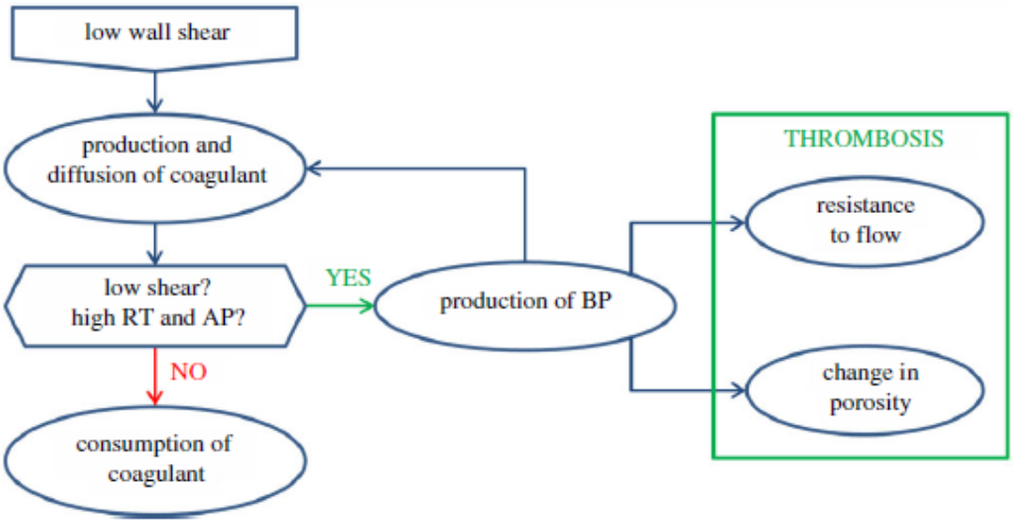

Figure 3.1: Feedback loop regulating thrombus formation (Menichini et al. 2016)

have been set to artificially accelerate thrombus formation based on previous sensitivity tests (Menichini & Xu 2016) to ensure simulations can complete in a feasible time frame.

The production of BP initiates a feedback loop to produce more coagulant. This feedback loop can be seen in Figure 3.1, and is driven by $\phi_{Ccontrol}$ and $\phi_{BPcontrol}$ which are coefficients that combine switching functions dependant on BP, C, RRT and AP concentrations. The switching function for each variable (ϕ_i) is calculated through the follow equation:

$$\phi = \Pi \frac{X_i^2}{X_i^2 + X_{i_t}{}^2} \tag{3.20}$$

From this equation it can be seen that ϕ_i can hold a value between 0 and 1. If the local concentration of any of the variables C, BP or RRT is significantly smaller than their threshold value ($RRT_t = 0.85$, $C_t = 10nmol/L$, $BP_t = 20nmol/L$, $AP_t = 15$) the reaction dependant on that variable will stop.

Finally, the momentum equation (Equation 3.10) is modified to include the influence of the presence of BP on the flow. The momentum equation is multiplied by clot porosity defined as:

$$\epsilon = max(1 - \frac{BP^2}{BP^2 + BP_t^2}, 0.75) \tag{3.21}$$

Thus, porosity varies from 0.75 (when complete thrombosis has occured) to 1 (where there is

no thrombus). The momentum equation also has an additional source (S_M) to represent the resistance to flow produced by the presence of thrombus. With both of these modifications the momentum equation becomes:

$$\rho\frac{\partial\epsilon\boldsymbol{u}}{\partial t} + \nabla\cdot(\rho\epsilon\boldsymbol{u}\times\boldsymbol{u} = -\nabla p + \nabla\cdot(\mu(\nabla\boldsymbol{u} + \nabla\boldsymbol{u}^T))) - \epsilon S_M \tag{3.22}$$

$$S_M = k_M\frac{BP^2}{BP^2 + BP_t^2}\boldsymbol{u} \tag{3.23}$$

where $k_M = 10^7\, kgm^3s^{-1}$.

In all thrombosis simulations blood was modelled as a non-Newtonian fluid, for which the Quemada model was adopted (Quemada 1978). Quemada reported the following expression to describe the viscosity of a suspension fluid:

$$\mu = \mu_{\mathrm{P}}(1 - \frac{k_0 + k_\infty\sqrt{\dot\gamma/\dot\gamma_{\mathrm{c}}}}{1 + k_\infty\sqrt{\dot\gamma/\dot\gamma_{\mathrm{c}}}}\frac{\phi}{2})^{-2} \tag{3.24}$$

where μ is the blood viscosity, μ_{P} is the viscosity of plasma, k_0 and k_∞ are intrinsic viscosities, $\dot\gamma$ and $\dot\gamma_{\mathrm{c}}$ are normal and critical shear rate respectively and ϕ is the volume fraction of particles (hematocrit level in this case). Table 3.1 gives the values of these parameters that were used.

Table 3.1: Values of parameters used in the Quemada model for blood viscosity.

Variable	**Value**	
μ_{P}	1.2x10^{-3} Pa.s	(Mimouni 2016)
k_0	4.33	(Mimouni 2016)
k_∞	2.07	(Mimouni 2016)
$\dot\gamma$	calculated in Ansys CFX during simulation	
$\dot\gamma_{\mathrm{c}}$	1.88 s^{-1}	(Mimouni 2016)
ϕ	0.45	

3.3 Numerical Methods

As described in section 3.1, the Navier-Stokes equations consist of partial differential equations. If it is justified to make assumptions and simplifications, such as steady state or unidirectional

flow, it is possible to solve the Navier-Stokes equations analytically and determine an exact solution. However, without any simplification of the equations, it is not possible to solve them analytically and instead numerical methods are used to obtain an approximate solution. Numerical methods involve the discretization of the geometry and time domain into small subdomains. The discretization of the geometry is known as meshing, and is discussed in detail in section 3.5, and time discretization involves splitting the time domain into small intervals known as time steps. The time step used in each study is defined for each simulation in all relevant chapters.

There are three main methods used to obtain solutions: the finite difference, finite volume and finite element methods. The finite difference method involves approximating the differential equations at each point in time and space. The finite volume method involves integrating the partial differential equations over each control volume in the domain (defined through the meshing procedure), which is transformed into an system of algebraic equations, through discretization of the integral equations. This system of algebraic equations can then be solved iteratively (Versteeg & Malalasekera 2007). The finite element method involves solving a minimization problem. An approximate solution is substituted into the partial differential equations, resulting in a residual. The objective is then to adjust the approximate solution to minimise this residual, therefore meaning each subsequent approximate solution is increasing in accuracy (Desai & Kundu 2001).

All simulations presented in this study were implemented in ANSYS CFX, which uses a unique hybrid finite-element/finite-volume method to obtain solutions (ANSYS 2006). In all numerical methods the aim is to produce an accurate solution. The accuracy of the solution depends of the quality of the mesh produced, and the size of the time step used. The accuracy and level of convergence of the solution can be inferred by the root-mean-square residual reported at each time step. A solution is said to be tightly converged at a RMS residual value of 1×10^{-6}, well converged at 1×10^{-5} and loosely converged at 1×10^{-4} (Kuron 2015). ANSYS CFX recommends that a RMS residual value of 5×10^{-4} and below is required for a solution to be considered reasonable converged (ANSYS 2014). In all flow simulations a RMS of 1×10^{-5} was set, and in thrombus simulations a RMS of 5×10^{-5} was set.

3.4 Geometry Reconstruction

The patient-specific geometries used throughout this thesis were created from CT scans in Mimics (Materialize HQ, Leuven). Several image segmentation steps were followed to isolate the aorta within the scans. Thresholding (selecting all pixels that fall between a lower and upper limit of pixel intensity) formed an initial 2D mask on all slices within a scan. Mask splitting and region growing were then used to isolate the aorta and eliminate any floating pixels. Finally manual segmentation was carried out in which each individual slide was checked and modified if necessary to ensure all appropriate pixels were selected. For a dissected aorta compared to a healthy aorta manual segmentation is extremely important as there can be complex and sometimes unclear sections of the geometry, particularly around tears, often due to motion artifacts since a CT scan is a static picture.

After 2D masks were finalised on each slice a 3D model was automatically generated in Mimics. An automated smoothing process of the entire model was completed, before final manual smoothing of sharp edges and corners was carried out through use of the contour smoothing tool or in Meshmixer (Autodesk, Inc, 2020). Figure 3.2 shows a work flow diagram of the steps included in creating a geometry for use in a simulation.

While the segmentation process utilises as many automated steps as possible there is still manual segmentation required, particularly when segmenting complex geometry regions such as tears and the intimal flap. To assess the error induced by the manual steps an inter- and intra-user sensitivity test was conducted. A single case was segmented three times by user A on three separate days, and was then segmented by two other users, B and C. The segmented lumen volumes for users A, B and C, as well as for the second and third segmentations for user A are reported in Table 3.2. The results showed that inter and intra-user errors of up to 7.2% and 2.6%, respectively, were observed. While a relatively small error, this should be considered when interpreting simulation results.

The geometry segmented from a CT scan can also be impacted by the phase in which the scan was taken. A CT scan can be taken with or without contrast. If contrast is administered the

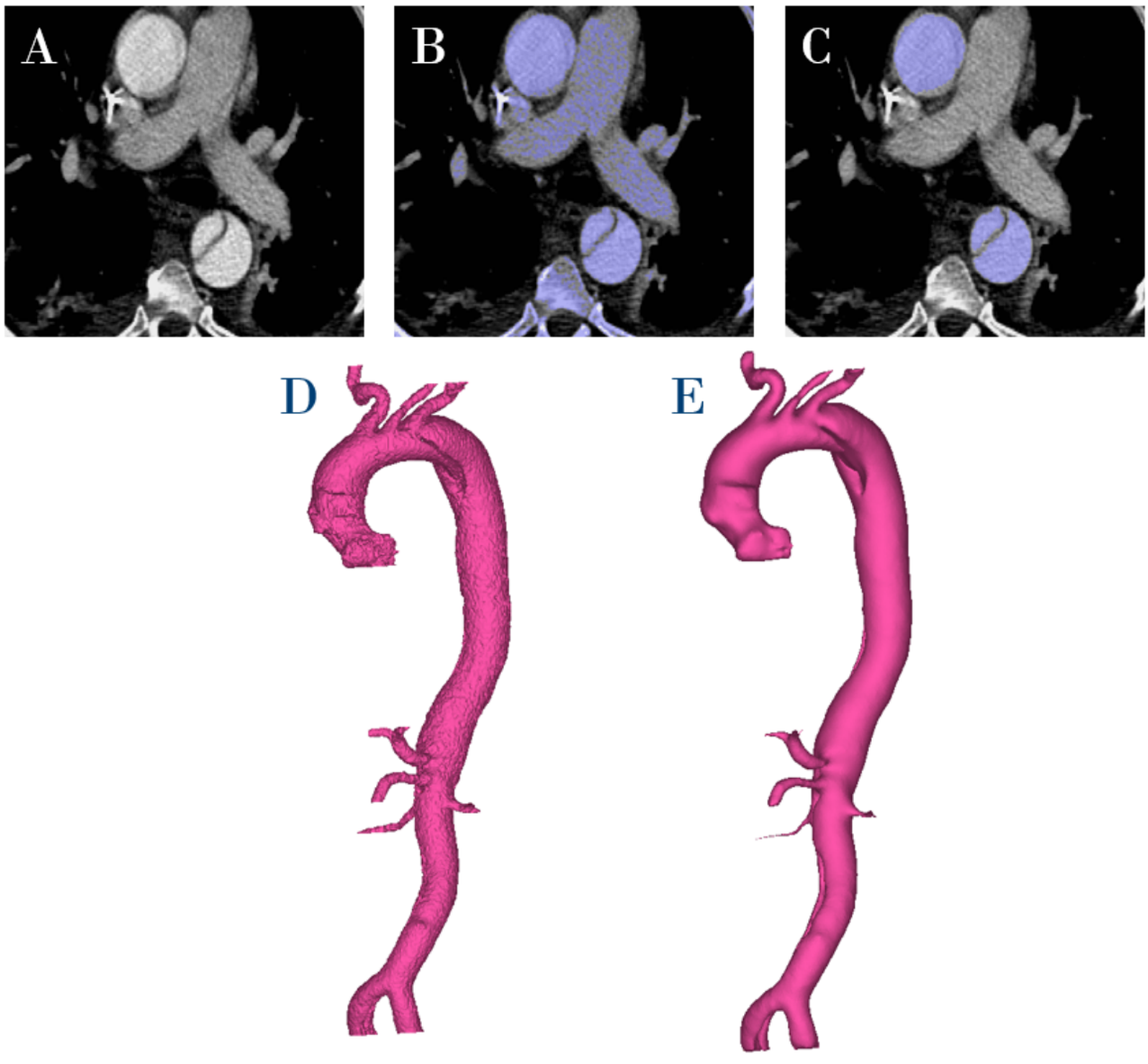

Figure 3.2: The steps of creating a 3D model from CT scans in Mimics. A: A CT scan is imported - here one axial slice is shown. B: Thresholding is carried out as the first step of creating a mask. C: The mask is refined through masking splitting, region growing and manual segmentation. D: A 3D model is created. E: Automatic and manual smoothing is carried out.

scan can be taken in the arterial or venous phase, which indicates whether the contrast was circulating in the arteries or veins at the time the image was captured. Data was not available to quantify the difference in lumen volume segmented from an arterial phase image compared to a venous phase image. Given the aorta is the largest artery and is easily identifiable on CT images it is expected that the error between arterial and venous segmentation would not significantly impact simulation results, however this is a point that should be noted when considering reconstruction from CT images.

Table 3.2: Total lumen volume segmented by user A on day 1, 2 and 3, and by users B and C.

	User A			**User B**	**User C**
	Day 1	**Day 2**	**Day 3**		
Lumen Volume $[cm^3]$	298.0	290.3	293.9	308.6	286.4

Finally, a sensitivity test was conducted to understand the impact of smoothing on the final geometry volume. The automated smoothing tool within Mimics allows for two parameters to be set: the smoothing factor (ranging from 0-1) and the number of iterations (ranging from 1-500). Additionally, the setting 'compensate shrinkage' can either be set to on or off - this is a setting designed to preserve the shape of the geometry during the smoothing process. When the smoothing factor and number of iterations were low (0.1 and 50, respectively) the difference in lumen volume between the smoothed and original geometries was 2.1% when compensate shrinkage was turned off. However, at the highest values of the smoothing factor and number of iterations the lumen volume reduced by 41.6% with compensate shrinkage turned off. Therefore, the compensate shrinkage setting was kept on in all smoothing steps.

To independently test the two adjustable parameters the number of iterations was first kept constant at 100 while the smoothing factor was increased from 0 to 1 in increments of 0.1, after which the smoothing factor was kept constant at 0.5 while the number of iterations was increased from 0 to 500 in increments of 50. At all increments of both settings the main lumen volume changed by less than 0.001%, indicating the bulk geometry was not significantly altered by the smoothing process and velocity and flow results from simulations will be minimally impacted. Wall shear stress results may still be impacted by the smoothness of geometry (and therefore mesh) therefore after globally smoothing the models, focus was placed on ensuring any abnormally sharp regions were corrected. The smoothing tool was found to impact small branches and tears and therefore geometries were manually altered if needed to ensure branches and tears were the correct size as measured directly from the CT scan.

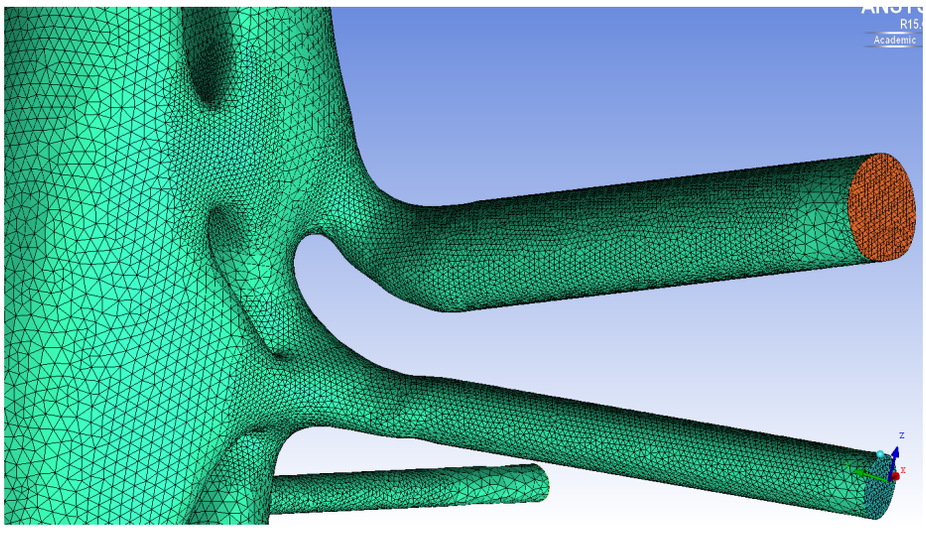

Figure 3.3: Computed mesh using densities in areas that require local refinement.

3.5 Meshing

As discussed in section 3.3, in order to analytically solve the Navier-Stokes equations the spatial domain must be discretized into many cells through the meshing process. Domains can be discretized into either structured or unstructured meshes. Structured meshes involve dividing the domain into cells that are generally uniform in size and shape. This type of mesh is best reserved for idealised geometries. However, in patient-specific models, and particularly in dissection models, there can be very complex areas of geometry. In these cases, despite being of slightly lower quality compared to structured meshes, unstructured meshes are more suitable as there is much more flexibility in terms of cell shape and size. For this reason, all patient-specific models presented in this thesis used an unstructured mesh.

Before meshing any geometry, any inlet and outlets surfaces were cut to create flat surfaces. For each model, a centreline was generated through the geometry in Mimics and planes normal to this centreline were inserted at the position where the inlet and outlets were to be cut. All outlets were extended 40-60 mm to avoid flow recirculation near the outlet, and also to minimise the effect the outlet boundary conditions may have on upstream flow. Furthermore, before meshing, densities were applied to the geometry, around areas that had sharp bends or corners, and areas that required a high level of detail (for example, tears and branches). The densities defined mesh sizing parameters that overrode any global parameters set, to give areas

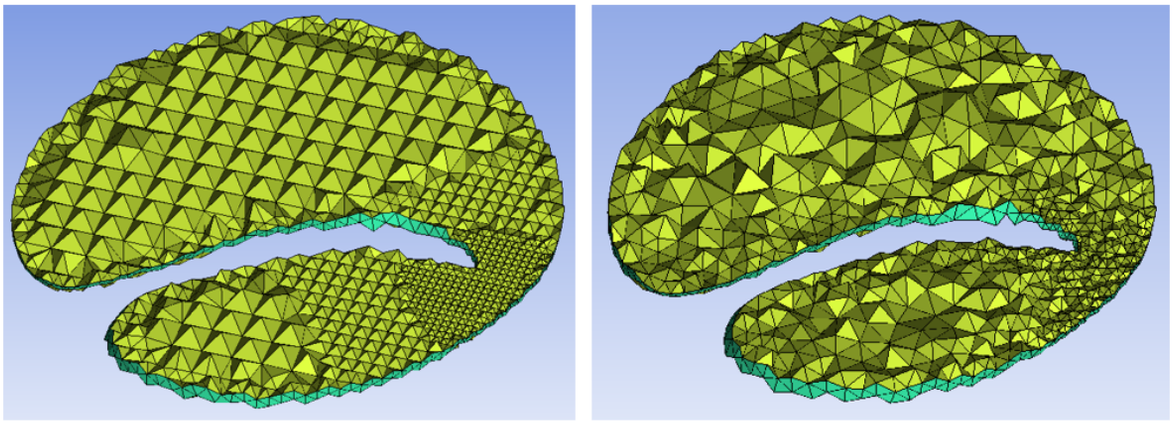

Figure 3.4: Axial cut-plane of the aorta which show volume meshes created using the Octree (left) and Delaunay (right) method.

of finer mesh. This can be seen is Figure 3.3.

Computational meshes were created in three steps, using ICEM (v15 or v19, Ansys Inc.). To begin, a robust Octree mesh was computed. The Octree mesh has a constant element size throughout the inner volume of the mesh, excluding areas near the boundary and densities. This can create quality issues in that element volume transitions can be quite rapid. To overcome this a Deluanay mesh was computed. This mesh has varying sized elements, allowing for much smoother transitions. Figure 3.4 shows the difference between the Octree and Deluanay volume meshes. The Deluanay method requires an existing mesh for the surface, and fills in the volume mesh. Therefore, the previously computed surface layer of the Octree mesh was used, resulting in an overall mesh that had a robust surface layer, to ensure all intricacies of the flow were captured on the surface, with a smooth transitioning inner volume mesh. Finally, 10 prism layers were created, extruding from the wall, to allow for high accuracy within the boundary layers. Smoothing of the mesh was then carried out to improve quality.

In order to find an appropriate balance between accuracy of results and computational time, mesh sensitivity tests were carried out in all cases - these tests ensured the CFD results were independent of the mesh, but the number of elements used in the mesh was minimised. To conduct the tests, three meshes were created for a each geometric model. The number of elements increased by a factor of approximately 1.5-2$\times$ between the three meshes, creating a fine, medium and coarse mesh. Qualitative visual comparison of wall shear stress contours was first

conducted to identify any significant regions of inconsistent results. Quantitative comparison of mean and maximum velocity and wall shear stress on selected planes was then carried out and the chosen mesh for each model had a % difference less than an acceptable threshold value, typically 5% in this thesis, for each hemodynamic parameter between the selected mesh and a more refined mesh. Additionally, in Chapter 4 where differences in precise quantitative hemodynamic results between various simulations were important, the grid convergence index (GCI) was also evaluated. GCI was calculated through the following equations (Roache 1994, Craven et al. 2009):

$$r \approx (\frac{N_3}{N_2})^{1/3} \approx (\frac{N_2}{N_1})^{1/3} \tag{3.25}$$

$$p = \frac{ln(\frac{|f_1 - f_2|}{|f_2 - f_3|})}{ln(r)} \tag{3.26}$$

$$E_3 = \frac{(\frac{f_2 - f_3|}{f_3})}{r^p - 1}, \qquad E_2 = \frac{(\frac{f_1 - f_2|}{f_2})}{r^p - 1} \tag{3.27}$$

$$GCI_{3,2} = F_S|E_3|, \qquad GCI_{2,1} = F_S|E_2| \tag{3.28}$$

Where $N_{1,2,3}$ is the number of elements in mesh M1 (coarse), M2 (medium) and M3 (fine), $f_{1,2,3}$ is the hemodynamic variable of interest, and F_S is the "factor of safety" equal to 1.25 (Craven et al. 2009). Final mesh element numbers are reported for individual models in each chapter, and further information on mesh sensitivity tests for individual models is reported in Appendix A.

3.6 Boundary Conditions

Setting appropriate boundary conditions is essential in CFD to ensure the simulation results are accurate and reliable. Additionally, when modelling arterial flow it is important to make sure they are physiological, and encompass the effect of the distal arterial tree that is not included in the geometry chosen for CFD simulation.

Inlet

All models in this thesis are of the entire aorta, beginning with the ascending aorta distal to the aortic valve. Therefore, any inlet boundary condition should ideally accurately mimic the ejection of blood flow from the left ventricle, through the aortic valve and into the ascending aorta. Various inlet velocity profiles have been utilised throughout the literature, initially starting with idealised conditions such as flat, parabolic or Womersley velocity profiles (Alimohammadi et al. 2014, Chen, Müller-Eschner, von Tengg-Kobligk, Barber, Böckler, Hose & Ventikos 2013, Cheng et al. 2010, Dillon-Murphy et al. 2016, Tse et al. 2011). In recent years, advancing technology in both imaging and data processing has allowed for patient-specific velocity data to be captured in the form of 2D-PC MRI and more recently 4D-flow MRI scans. From these, through plane (TP, two-dimensionally varying velocity profile normal to the inlet plane) and 3D (extractable from 4D-flow MRI scans only) inlet velocity profiles can be extracted. Chapter 4 presents a study assessing the influence of various inlet velocity profiles on hemodynamics and thrombus formation. Details on the type of inlet profile used in each study is discussed in each chapter.

Outlet

With multiple outlet branches in a TBAD model, outlet boundary conditions are pivotal in determining flow throughout the aorta. Previous work has identified the 3-element Windkessel model to be the preferred condition used for replicating physiological results (Pirola et al. 2017). The 3-element Windkessel model treats the aorta and circulatory system as comparable to an electric circuit, with resistances and compliances, as shown in Figure 3.5. The three components seen in the circuit represent the following within the aorta: R_1 is the proximal resistance, R_2 is the distal resistance (encapsulating the cumulative resistive effect of all distal vessels), R_T is

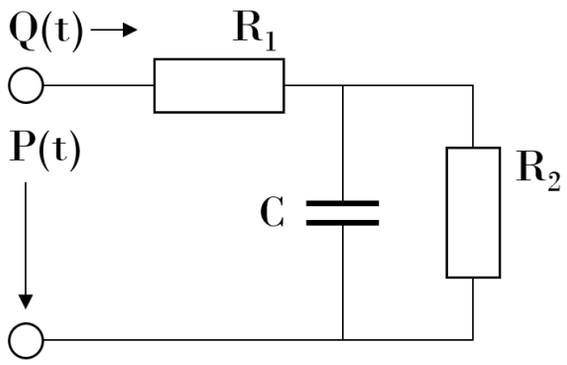

Figure 3.5: An electric circuit representing the aorta and circulatory system. R_1 and R_2 represent the proximal and distal resistances of the aorta and downstream branches respectively. C represents the compliance of the branches, Q(t) the blood flow and P(t) the pressure drop across the aorta.

the sum of R_1 and R_2, and C_T is the compliance of the vessel.

The model relates flow, Q, and pressure, P, through the following equation (Reymond et al. 2009):

$$\frac{\delta Q}{\delta t} = \frac{1}{R_1}\frac{\delta P}{\delta t} + \frac{P}{R_1 R_2 C_\mathrm{T}} - (1 + \frac{R_1}{R_2})\frac{Q}{R_1 C_\mathrm{T}} \tag{3.29}$$

The proximal resistance for a given branch i can be calculated using Equation 3.30:

$$R_{1i} = \frac{\rho c_i}{A_i} \tag{3.30}$$

where c and A are the wave speed and the area of the branch, respectively. Equation 3.31 can be adopted to determine the wave speed (Reymond et al. 2009), and is particularly well suited for branches with a diameter greater than 5mm.

$$c_i = \frac{a_2}{{d_i}^{\mathrm{b}_2}} \tag{3.31}$$

where d_i is the diameter of branch i and constants a_2 and b_2 are 13.3 and 0.3, respectively (Reymond et al. 2009).

The total resistance for branch i can be calculated as the ratio of mean pressure to mean flow rate through branch i:

$$R_{\mathrm{T}i} = \frac{\overline{P_i}}{\overline{Q_i}} \tag{3.32}$$

The distal resistance for branch i can then be calculated as:

$$R_{2i} = R_{\mathrm{T}i} - R_{1i} \tag{3.33}$$

Finally, the compliance of each outlet vessel is calculated through Equation 3.34:

$$C_i = \frac{\tau_t}{R_{\mathrm{T}i}} \tag{3.34}$$

To calculate R_{Ti}, and all subsequent parameters, average pressure and flow waveforms are required for each branch. Invasive Doppler wire (DW) readings can provide the required pressure waveforms, however these measurements can not justifiably be taken without another medical reason for intervention, and therefore usually do not exist for medically managed patients, and only rarely exist for TEVAR patients. Non-invasive imaging modalities such as echocardiography, phase-contrast MRI and 4D-flow MRI can provide flow and velocity measurements. In cases where no patient-specific data is available literature values for both average pressures and flow splits can be used. The data available and used to calculate Windkessel parameters in this thesis varied in each study and is discussed on a case-by-case basis in each chapter.

Wall

In all simulations in this thesis the wall was assumed to be rigid, with a no-slip boundary condition. This is a common assumption in TBAD computational studies, justified by data indicating the reduced mobility of the wall and flap, such as intimal flap calcification (De Jong et al. 2014) or the chronic state of the dissection (Peterss et al. 2016), or simply the increased computational complexity and cost of including wall and flap mechanics. However, it has been

shown that neglecting wall and flap motion can impact simulation results (Alimohammadi et al. 2015, Bäumler et al. 2020, Chong et al. 2020). Discussion on the likely impact of the rigid wall assumption on individual studies is presented in each chapter. General discussion on this limitation and the ongoing work being carried out to understand the extent of this assumption on hemodynamics and thrombus formation is presented in Chapter 10.

For the thrombosis model, all species were set to zero flux at the wall, except the coagulant which is controlled by the following variable flux condition:

$$D_{Ceff}\frac{\partial C}{\partial n}\bigg|_{wall} = \begin{cases} k_c & if\, TAWSS < 0.15\, Pa\, and\, BP \leq 200\, nM, \\ 0 & otherwise \end{cases} \tag{3.35}$$

The TAWSS threshold was set to 0.2 Pa in the original model development by Menichini et al. (2016). Following this, the threshold was further tuned to a value of 0.15 Pa to match observed thrombus in TBAD follow-up data. Therefore, the 0.15 Pa was implemented in this thesis.

3.7 Analysing Results

All simulation results were processed in EnSight (Ansys, Inc) and/or ParaView. Various parameters that were evaluated throughout the studies in this thesis are defined in the following section.

Wall shear stress (τ_w) is the tangential force acting on the inner wall due to the blood flow. As the flow is pulsatile, a commonly adopted parameter is the time averaged wall shear stress (TAWSS). TAWSS is calculated through the following equation:

$$TAWSS = \frac{1}{T}\int_0^{\mathrm{T}} |\tau_w| dt \tag{3.36}$$

Due to the periodic flow and changing pressure gradients there can be areas in the aorta in which the flow reverses direction. The degree to which this occurs can be represented by the oscillatory shear index (OSI) which shows the degree to which the wall shear stress deviates

from its average direction. OSI is calculated through the following equation:

$$OSI = \frac{1}{2}(1 - \frac{AWSS}{TAWSS}) \tag{3.37}$$

AWSS is the average wall shear stress and is calculated through the following equation:

$$AWSS = \frac{1}{T}|\int_0^{\mathrm{T}} \tau_w dt| \tag{3.38}$$

The pressure difference between the true and false lumen, ΔP, was was defined as follows.

$$\Delta P = P_{falselumen} - P_{truelumen} \tag{3.39}$$

3.8 Processing 4D-flow MRI Data

4D-flow MRI data is used throughout this thesis to provide *in vivo* data from which patient-specific boundary conditions can be derived and also for validation of CFD results. All 4D-flow MR images were processed following the workflow laid out in Figure 3.6, which presents the example of extracting the inlet flow waveform from a swine 4D-flow MRI scan studied in Chapter 8. This methodology utilises an in-house MATLAB code previously developed in our group (Pirola et al. 2018, 2019), and the key steps are as follows:

- Magnitude and three directional (foot-head (FH), anterior-posterior (AP), right-left (RL) DICOM images are reviewed to ensure the images are of high enough quality and any aliasing (where abnormally high velocities are not captured by the scan and instead pixels are set to have no value) is manually corrected.
- The DICOM images are read by an in-house MATLAB code which outputs velocity fields as .vtk files at all time intervals in the cardiac cycle that were selected at the time of scanning. This step can be performed for the whole 3D scan volume or for the aorta volume only segmented from the magnitude images.

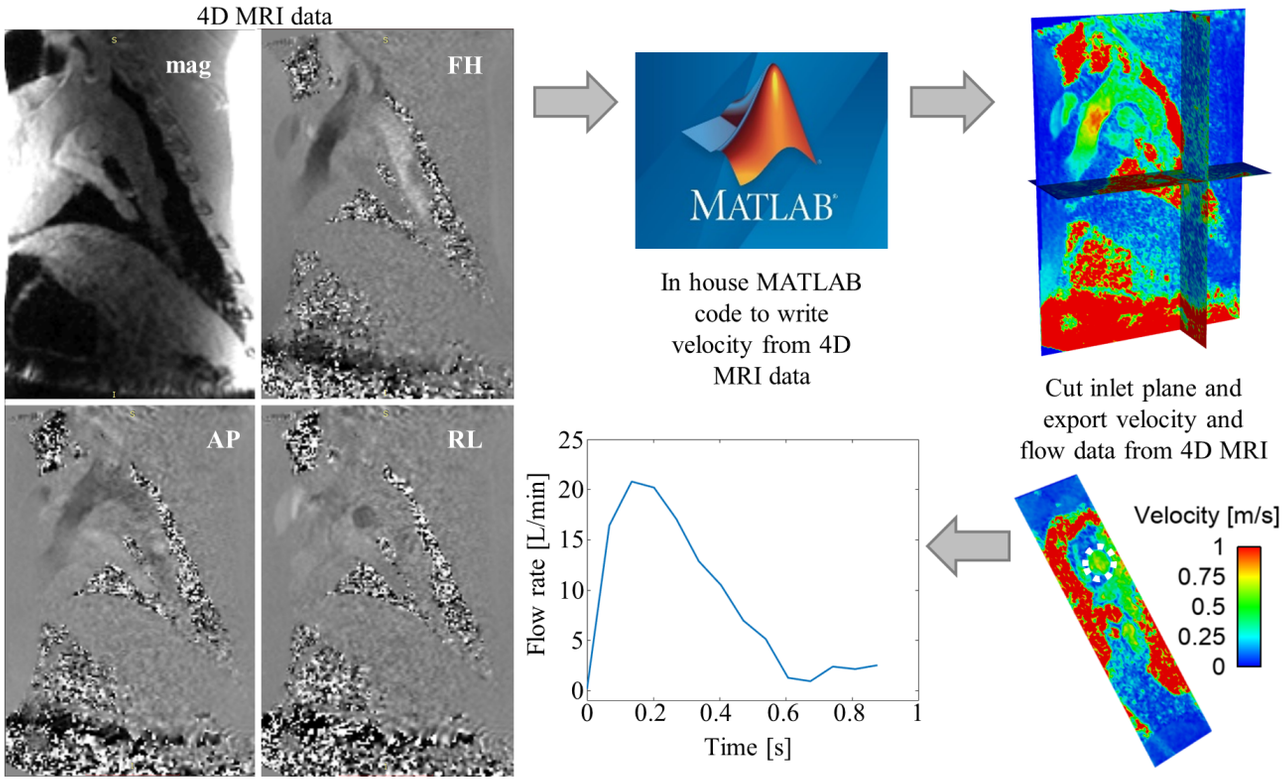

Figure 3.6: Workflow to process and analysis 4D flow MRI scans to extract flow data. Flowrate shown as an example is extracted from 4D-flow MRI scan of swine model presented in Chapter 8.

- The .vtk files are opened in EnSight and planes can be cut at any selected location within the volume.
- The flowrate through the selected planes is calculated using built-in functions in EnSight and exported for each time point in the cardiac cycle.
- Any other hemodynamic analysis including volume rendering of velocity fields, streamlines, and evaluating mean and maximum velocities in selected regions is also performed in EnSight.

Chapter 4

The Influence of Inlet Boundary Condition on Aortic Hemodynamics[†]

This chapter presents a study assessing the influence of various inlet velocity profiles (IVPs) on hemodynamics in CFD simulations of TBAD. As discussed in section 3.6, the choice of inlet boundary condition is a critical input in order to simulate physiological hemodynamics, and as seen in section 2.5 various studies have been conducted to investigate inlet boundary condition choice in the aorta and other cardiovascular regions. However, no study has yet been conducted to assess the influence of IVP on TBAD hemodynamics specifically. Therefore, this chapter focuses on determining the influence of various IVPs on TBAD hemodynamics under two scenarios. The first is where patient-specific flow data is available – in this case the use of 3D, 2D and flat IVPs is compared. The second scenario is where no patient-specific flow data is available – in this case generic flat profiles are studied and the effect of non-patient-specific stroke volume and waveform is assessed.

[†]This chapter is adapted from: *Armour CH, Guo B, Pirola S, Saitta S, Liu Y, Dong Z, Xu XY (2020) The influence of inlet velocity profile on predicted flow in type B aortic dissection. Biomechanics and Modeling in Mechanobiology 20:481-490*

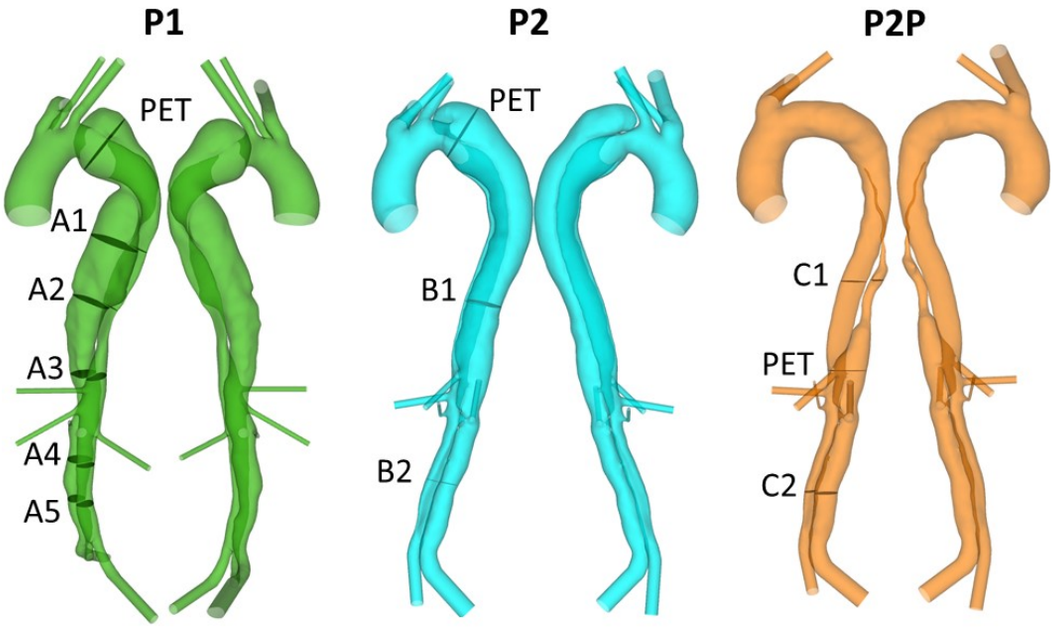

Figure 4.1: Geometries of P1, P2 and P2P used for simulation. The primary entry tear (PET) in each model is indicated, as well as planes on which pressure readings were taken (A1-5, B1-2 and C1-2) (Armour et al. 2020).

4.1 Methodology

Three sets of images acquired from two patients treated for acute TBAD at the Zhongshan Hospital in Shanghai, China, were used in this study. As shown in Figure 4.1, P1 and P2 represent pre-TEVAR models, extracted from diagnosis CT scans, both of which have dissections extending from the level of LSA down to the aortic bifurcation. P2P is a post-TEVAR model of P2, used to represent the type of TBAD geometry with a PET further down the descending aorta. All three geometries were segmented using the methodology laid out in section 3.4. On the diagnosis scan of P2 partial thrombosis of the proximal false lumen can be seen. Therefore, to evaluate the effect of IVP on thrombus formation in addition to hemodynamics the initial dissection geometry was recovered by including the thrombosed section in the false lumen.

3D IVPs were extracted from the 4D-flow MRI data of P1 and P2 using an in-house MATLAB processing tool, presented in previous studies (Pirola et al. 2018, 2019). Figure 4.2 shows the workflow for extracting the 3D IVP for P1 as an example. The first step involves spatially registering the CT segmented geometry to the 4D velocity data produced from processing the 4D-flow MRI as in section 3.8. While a perfect match between the two volumes is impossible due

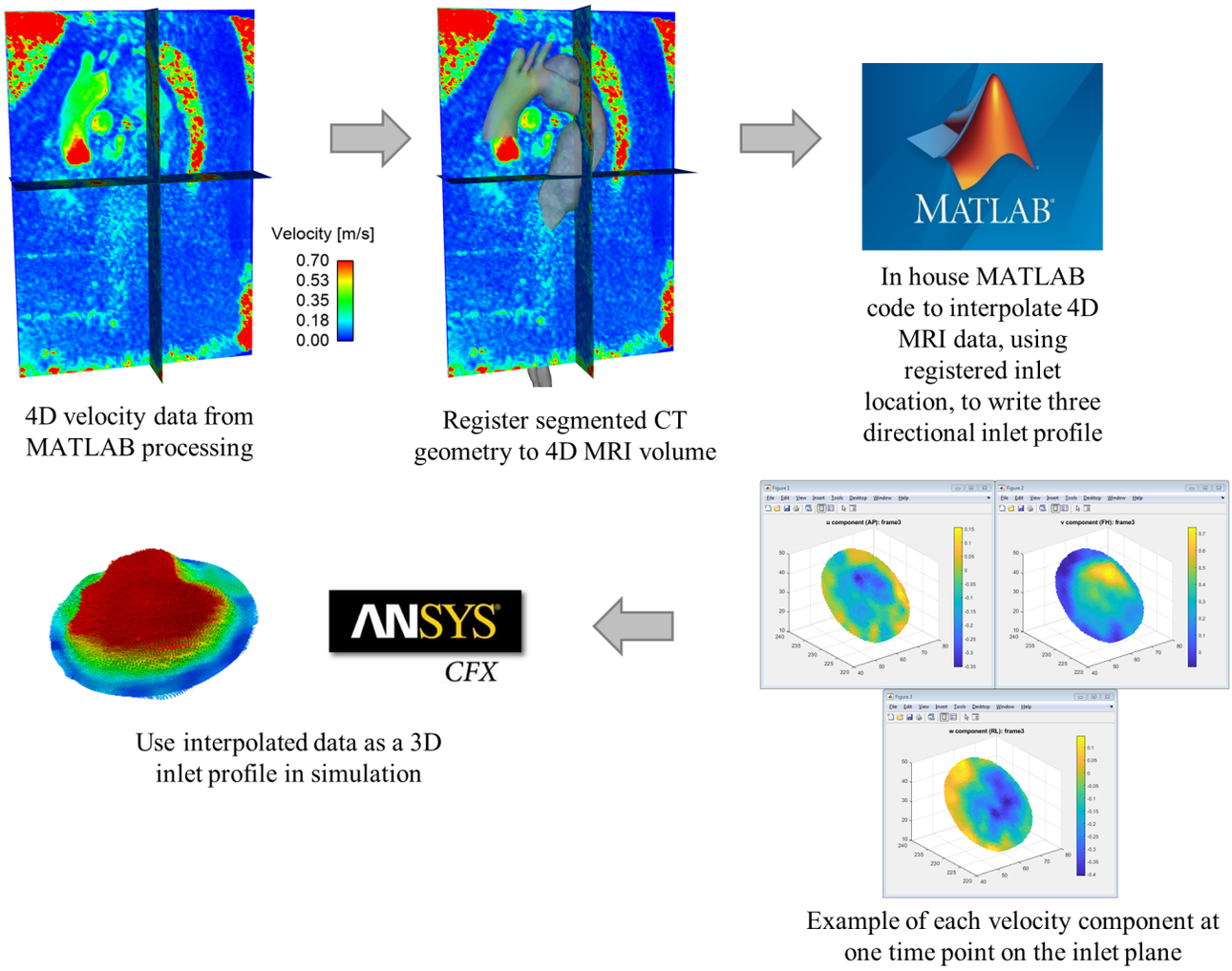

Figure 4.2: Workflow to extract 3D inlet velocity profile from 4D-flow MRI data.

the the 4D-flow MRI scan providing dynamic images at multiple time points over the cardiac cycle, the coronary arteries and braceocephalic artery are used as anatomical landmarks during the registration process on both the CT and 4D-flow MRI images to ensure the bodies are well matched, most importantly in the ascending aorta. The registered geometry is then cut and meshed following the methodology laid out in section 3.5. An stl file of the newly orientated inlet is then imported into a MATLAB script which interpolates the 4D-flow MRI velocity data at the inlet location and outputs a velocity file for each direction which can be read by ANSYS-CFX in simulation.

From the results obtained with the 3D IVP simulation, a through-plane (TP) and flat velocity profile were derived using Ansys EnSight (v10.2) and additional in-house MATLAB tools. As

post-TEVAR 4D-flow MRI was not available for P2P, the 3D, TP and flat IVPs extracted for P2 were used. Furthermore, to assess the effect of non-patient-specific stroke volume and flow waveform, two additional IVPs were tested on P2 – the flat profile for P2 with a 25% reduction in flow (Flat75%), and the flat profile for P1. Flat75% and FlatP1 had a stroke volume of 87 and 85 mL, respectively, compared to the patient-specific IVPs for P2 which had a stroke volume of 115 mL. Figure 4.3 shows the flow waveforms for all inlet boundary conditions tested as well as the 3D, TP and flat IVPs for P1 and P2.

All meshes constructed for this study were unstructured and consisted of a hexahedral core, with 10 prismatic layers. Mesh sensitivity tests conducted consisted of transient flow simulations with flat IVPs. Global time-averaged wall shear stress (TAWSS) patterns were first compared visually to check qualitative consistency. Mean and maximum velocity and TAWSS were then quantitatively compared at selected planes throughout the aorta, focusing on areas within the dissection and near tears. The mesh was refined until differences in these parameters between the chosen mesh and a finer mesh were less than 3.5%. The grid convergence index (CGI) was also calculated, and the chosen mesh had a CGI of $< 5.5\%$ for velocities and TAWSS at all selected planes, in line with previous studies (Craven et al. 2009, Tedaldi et al. 2018). Further details on the mesh sensitivity study can be found in Appendix A.1. The final meshes contained 6.2, 5.8 and 4.1 million elements for P1, P2 and P2P, respectively.

In all simulations 3EWK models were applied at the outlets. For P1 invasive DW pressure readings were available and branch flows were estimated from the 4D-flow MRI scan. With these inputs, 3EWK parameters were calculated following the methodology laid out in section 3.6. For P2 and P2P, the same methodology for calibrating the parameters was followed based on several assumptions. First, invasive pressure measurements from P1 were adopted as these were not available for P2 or P2P. Furthermore, the 4D-flow MRI scan for P2 was only of high enough quality to extract flowrates to the arch branches. Therefore, the proportion of flow to the abdominal branches was assumed to be the same as that for P1. The 3EWK parameters were adjusted for the Flat75% and FlatP1 IVPs simulated in P2 to account for the lower inlet flowrate. As no 4D-flow MRI scan for P2P was available, the branch flow split for P2 was assumed. Additionally, the flow through the LCCA in P2P was assumed to be the sum of the

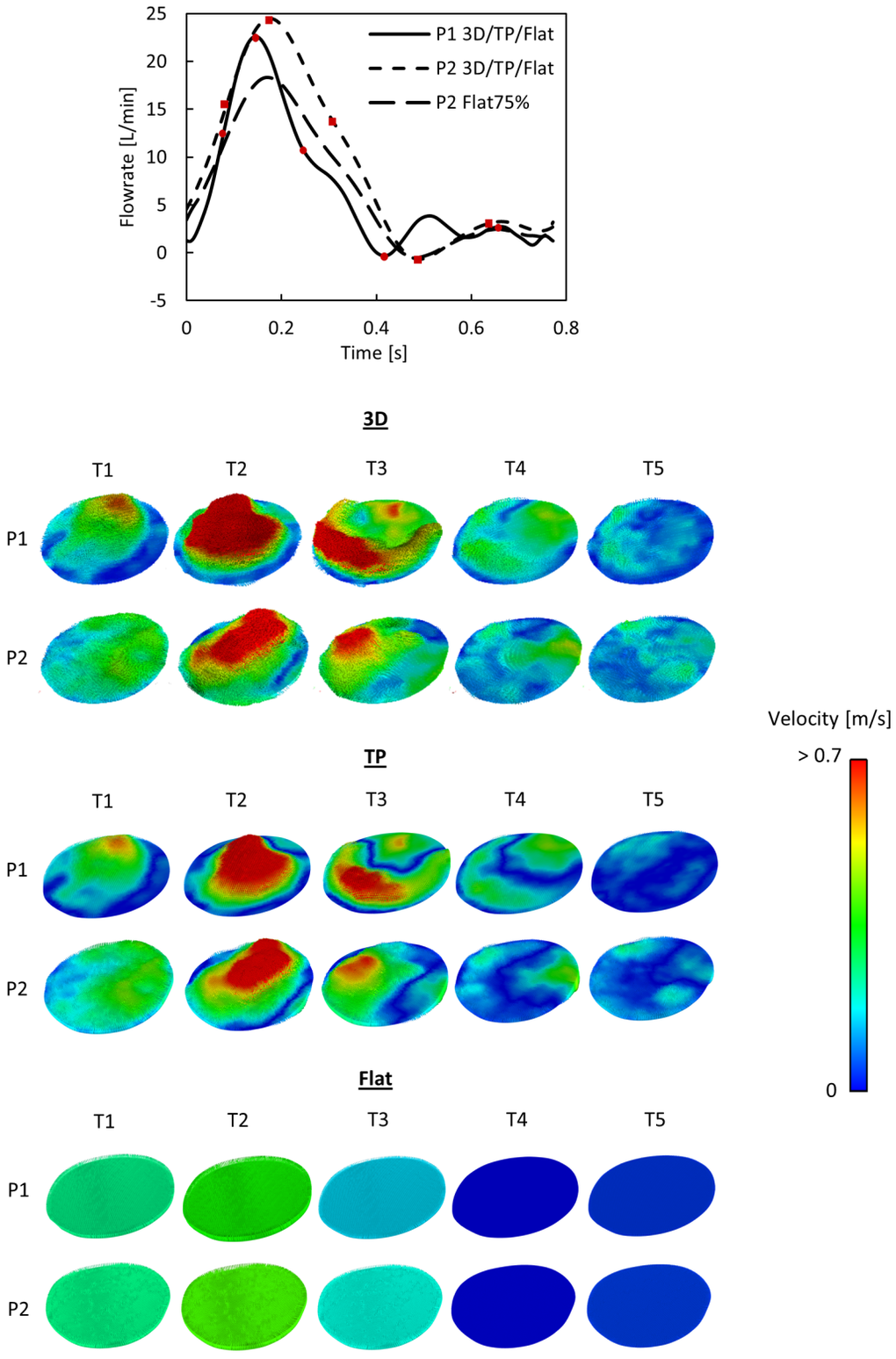

Figure 4.3: Top: Flowrate of inlet velocity profiles derived from 4D-flow MRI scans of P1 and P2, studied in each geometry. Bottom: 3D, TP and flat inlet velocity profiles for P1 and P2 at time points (T1 – T5) throughout the cardiac cycle. Time points are indicated by red circles and squares for P1 and P2, respectively, on flowrate curves (adapted from Armour et al. 2020).

Table 4.1: Top: P1 measured average pressures at each aortic side branch, used to calculate 3EWK parameters for P1, P2 and P2P. Bottom: Flow splits for each aortic side branch used to calculate 3EWK parameters for P1, P2 and P2P. Branches include brachiocephalic (BRAC), left common carotid (LCCA) and left subclavian (LSA) artery, celiac trunk (CEL), superior mesentric artery (SMA), right (RR) and left (LR) renal, and right (RI) and left (LI) iliac.

	BRAC	**LCCA**	**LSA**	**CEL**	**SMA**	**RR**	**LR**	**RI**	**LI**
					Average pressure [mmHg]				
P1	83	83	83	83	83	83	83	81	81
					Flow split [%]				
P1	11.6	3.1	6.4	20.0	8.5	11.4	19.4	9.8	9.8
P2	14.0	4.6	10.6	9.5	16.0	10.2	17.4	8.8	8.8
P2P	14.0	15.2	-	9.5	16.0	10.2	17.4	8.8	8.8

flow through the LCCA and LSA in P2 as the LSA was occluded during the TEVAR procedure and revascularisation was not performed. Table 4.1 shows the P1 measured average pressure values and 4D-flow MRI derived branch flow splits used to calculate the 3EWK parameters for each model.

The blood was assumed to be a Newtonian fluid with a viscosity of 0.004 Pa.s and a density of 1060 kg.m^3. The flow was assumed to be laminar based on calculations of the peak Reynolds number, Womersley number and critical Reynolds number for transition to turbulence reported by Kousera et al. (2012). A summary of these key flow parameters is given in Table 4.2. A time step of 0.001 s was used, all simulations were run for a minimum of four cardiac cycles to ensure periodic solutions, and the final cycle was used for analysis.

Table 4.2: Key flow parameters of the inlet flow waveform for patients P1, P2 and P2P. Re - Reynolds number; $\mathrm{Re_c}$ - critical Re, equal to 250α (Kousera et al. 2012); α - Womersley number.

	P1	**P2**	**P2P**
Cycle Period [s]	0.770	0.774	0.774
Peak Re	3560	3815	3999
$\mathrm{Re_c}$	5189	5280	5037
α	20.8	21.1	20.1

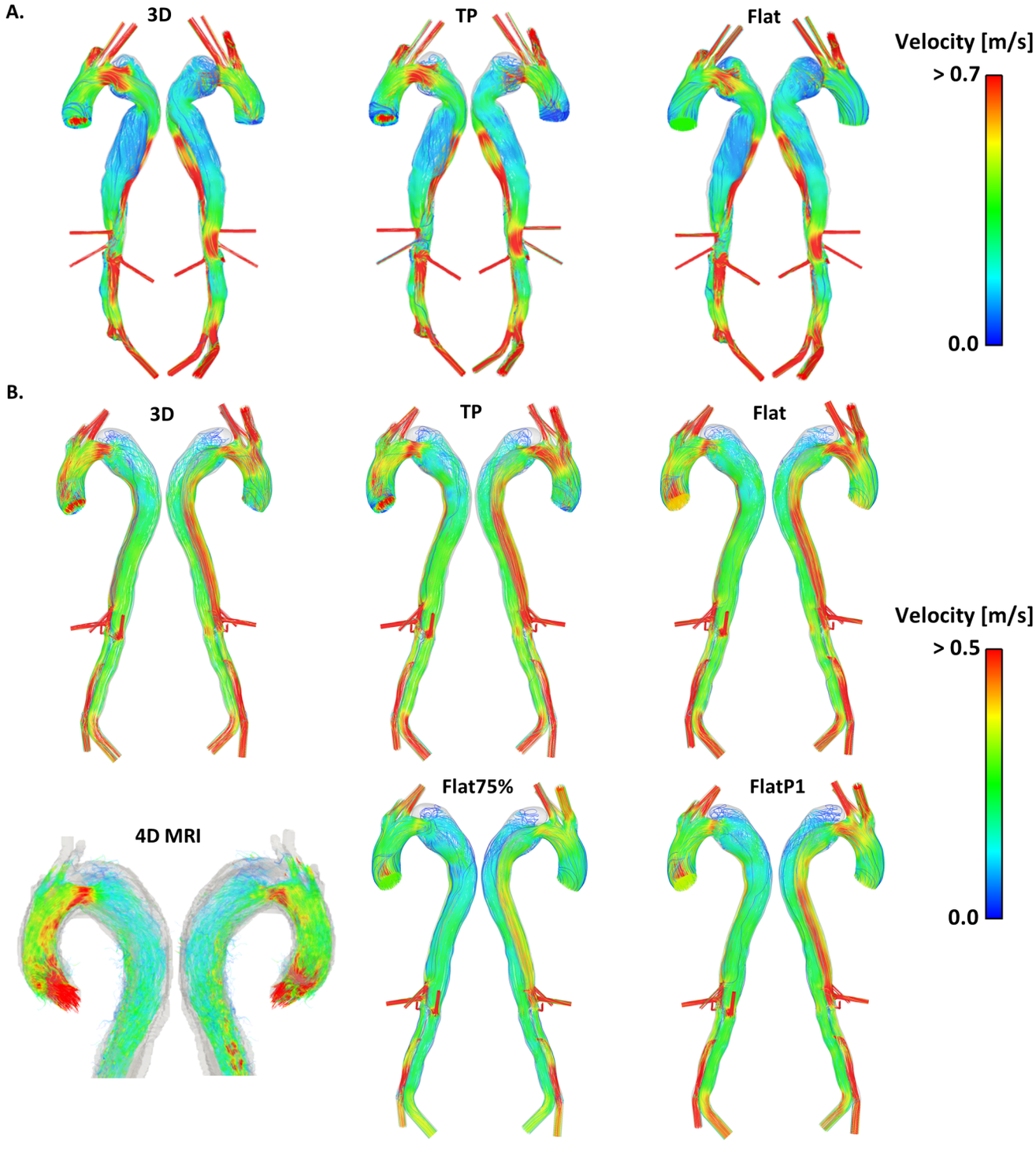

Figure 4.4: Peak systolic streamlines for A: P1 with a 3D, TP and Flat inlet velocity profile (IVP), B: P2 with a 3D, TP, Flat, Flat75% and FlatP1 IVP, with 4D-flow MRI derived streamlines for comparison (Armour et al. 2020).

4.2 Results

4.2.1 Flow patterns

Peak systolic velocity streamlines for each IVP studied can be seen in Figure 4.4 for P1 and P2, and Figure 4.5 for P2P. Additionally, Figure 4.4 also includes the peak systolic velocity streamlines derived from the 4D-flow MRI scan for P2. The equivalent 4D-flow MRI data for P1 was previously reported by Pirola et al. (2019). For validation of the computational methods used throughout this study, the streamlines obtained with 3D IVP for P1 and P2 were compared to their respective 4D-flow MRI streamlines. For both P1 and P2 the velocity streamlines show good agreement between the 3D IVP and 4D-flow MRI. High velocity jets through the PET are captured for both patients, with the peak velocity of the 3D IVP and 4D-flow MRI being 0.9 and 1.1 m/s (Pirola et al. 2019) for P1, respectively, and 0.6 and 0.7 m/s for P2, respectively. The velocity patterns are also well captured in the descending aorta, with lower FL velocities in P1 seen in both the 3D IVP and 4D-flow MRI images, while the higher TL velocities observed in the 4D-flow MRI streamlines for P2 are correctly modelled with the 3D IVP. Based on this validation, all other IVPs are compared to their respective 3D IVP results.

In all models the streamlines do not vary drastically between the 3D, TP and flat IVPs. However, looking in detail at certain areas differences can be observed. In the ascending aortas, higher velocity values as well as more helical flow are observed with the 3D and TP IVP compared to the flat IVP. Focusing on the PET on the aortic arch of P1 and P2, both patients see a reduced volume of high velocity through the suppressed TL with the flat IVP compared to the 3D IVP. Both patients also have an area of low velocity in the upper FL at the aortic arch. In this region, there are varied velocity patterns, however the low flow means visual comparison is difficult as there are fewer streamlines. The difference in flow patterns are clearer in the resulting TAWSS contours in this region, which are discussed in the following section. The maximum velocity varies by $< 3.5\%$ between the 3D, TP and flat IVPs for both patients. The mean velocity in the PET varies by $< 2\%$ for P2 between the three IVPs, and for P1 between

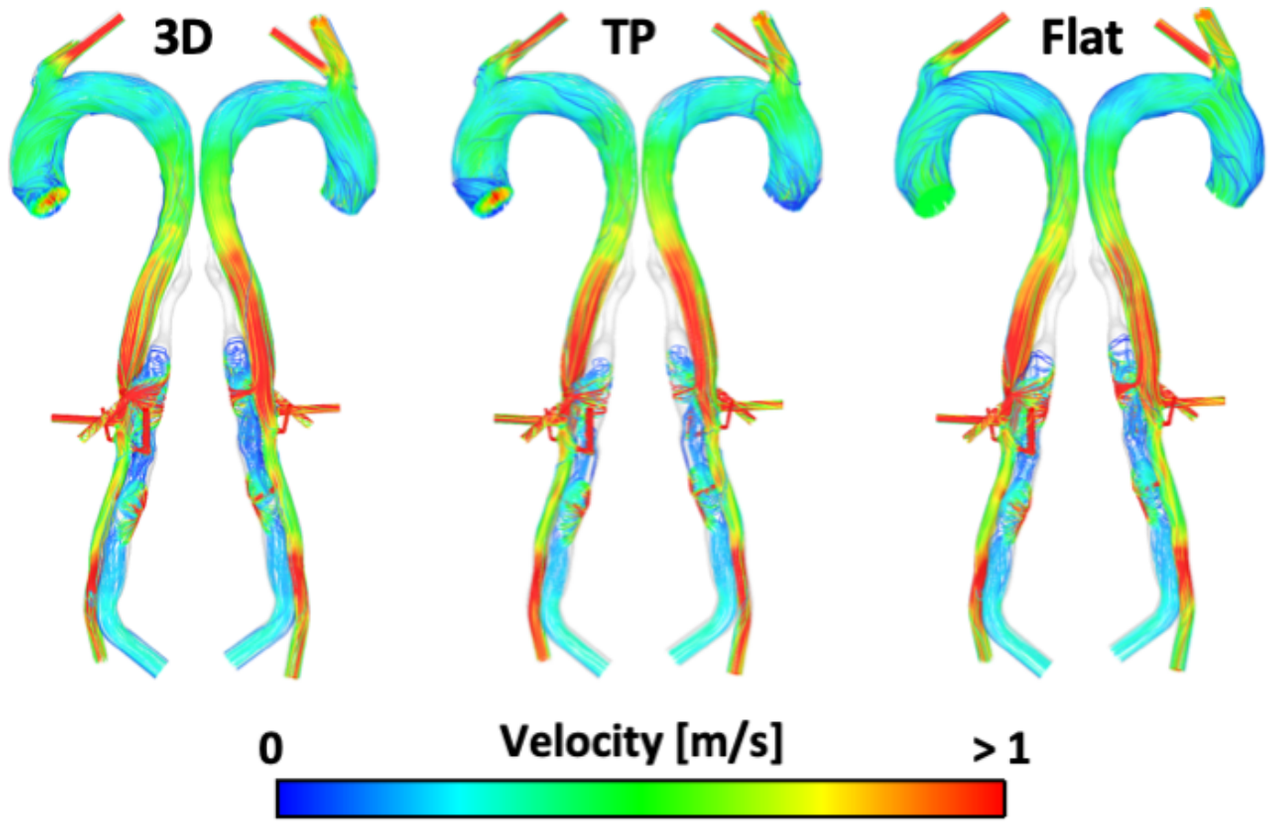

Figure 4.5: Peak systolic streamlines for P2P with a 3D, TP and Flat inlet velocity profile (Armour et al. 2020).

the 3D and 2D IVP. However, comparing the flat to 3D IVP in P2 results in an increase in mean velocity by 8.6%. With the Flat75% and FlatP1 inlet profiles for P2, the maximum velocity at the PET is reduced by 28% and 12%, respectively, compared to the 3D IVP. For P2P the peak velocity through the PET varies by $< 1\%$.

4.2.2 Wall shear stress

Figures 4.6, 4.7 and 4.8 show the TAWSS distributions for P1, P2 and P2P, respectively. Also shown is the absolute difference in TAWSS between each inlet profile and the gold standard 3D IVP results. As expected, large variations in TAWSS are seen throughout the ascending aorta and aortic arch. Throughout most of the descending aorta there is little difference in TAWSS. However, looking at key areas of interest, important differences can be observed. Comparing the patient-specific 3D, TP and flat IVPs, near the PET on the aortic arch of P1 and P2, there are variations for TAWSS below 1 Pa, and particularly < 0.2 Pa (a key threshold value when

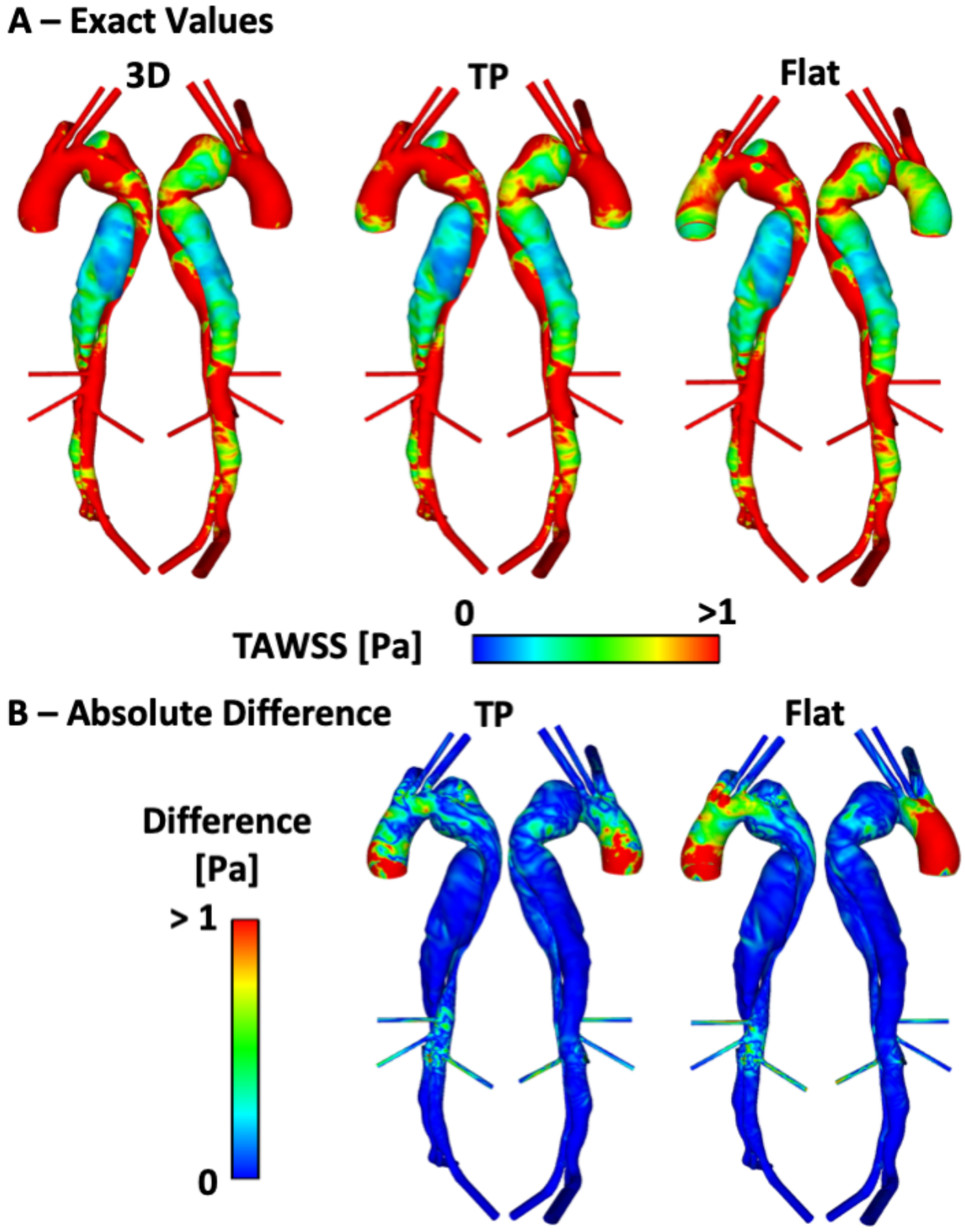

Figure 4.6: A: P1 TAWSS values with a 3D, TP and Flat inlet velocity profile (IVP). B: Absolute difference in TAWSS values between the 3D IVP and the two other IVPs (Armour et al. 2020).

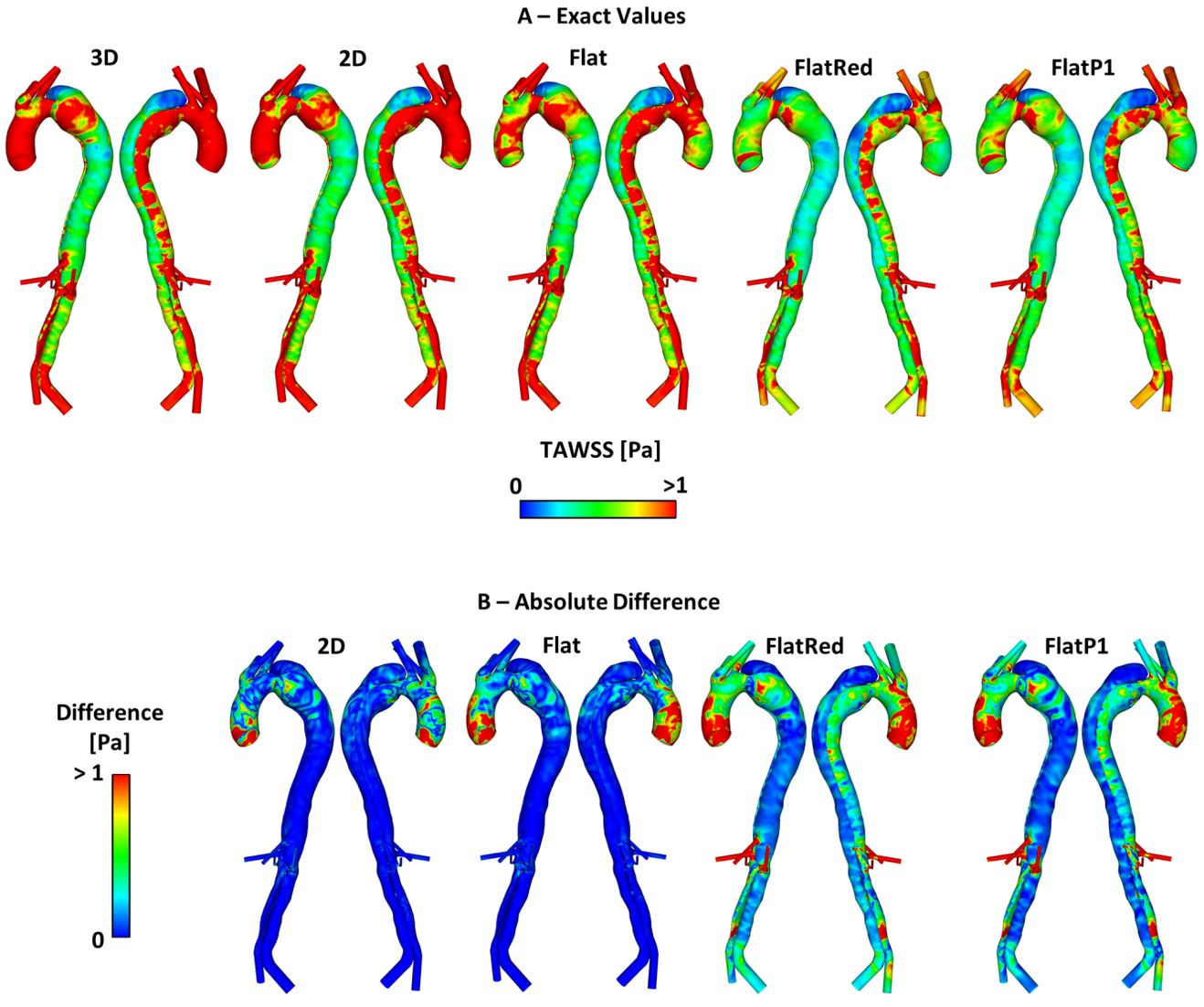

Figure 4.7: A: P2 TAWSS values with a 3D, TP, Flat, Flat75% and FlatP1 inlet velocity profile (IVP). B: Absolute difference in TAWSS values between the 3D IVP and the four other IVPs (adapted from Armour et al. 2020).

predicting thrombus formation (Menichini & Xu 2016, Menichini et al. 2016, 2018)). Within the PET for both P1 and P2, the mean and maximum TAWSS vary by up to 6% compared to the 3D IVP results, with the largest difference occurring when the flat profile is used. Another area in which differences are observed is near additional tears around the main abdominal branches in P1, P2P and to a lesser extent P2, with areas of TAWSS differing usually by $<$ 1 Pa. Considering the non-patient-specific Flat75% and FlatP1 IVPs in P2 it can be seen from the TAWSS and absolute difference TAWSS maps that both predicted substantially lower TAWSS in many regions. The difference in maximum and mean TAWSS compared to the 3D

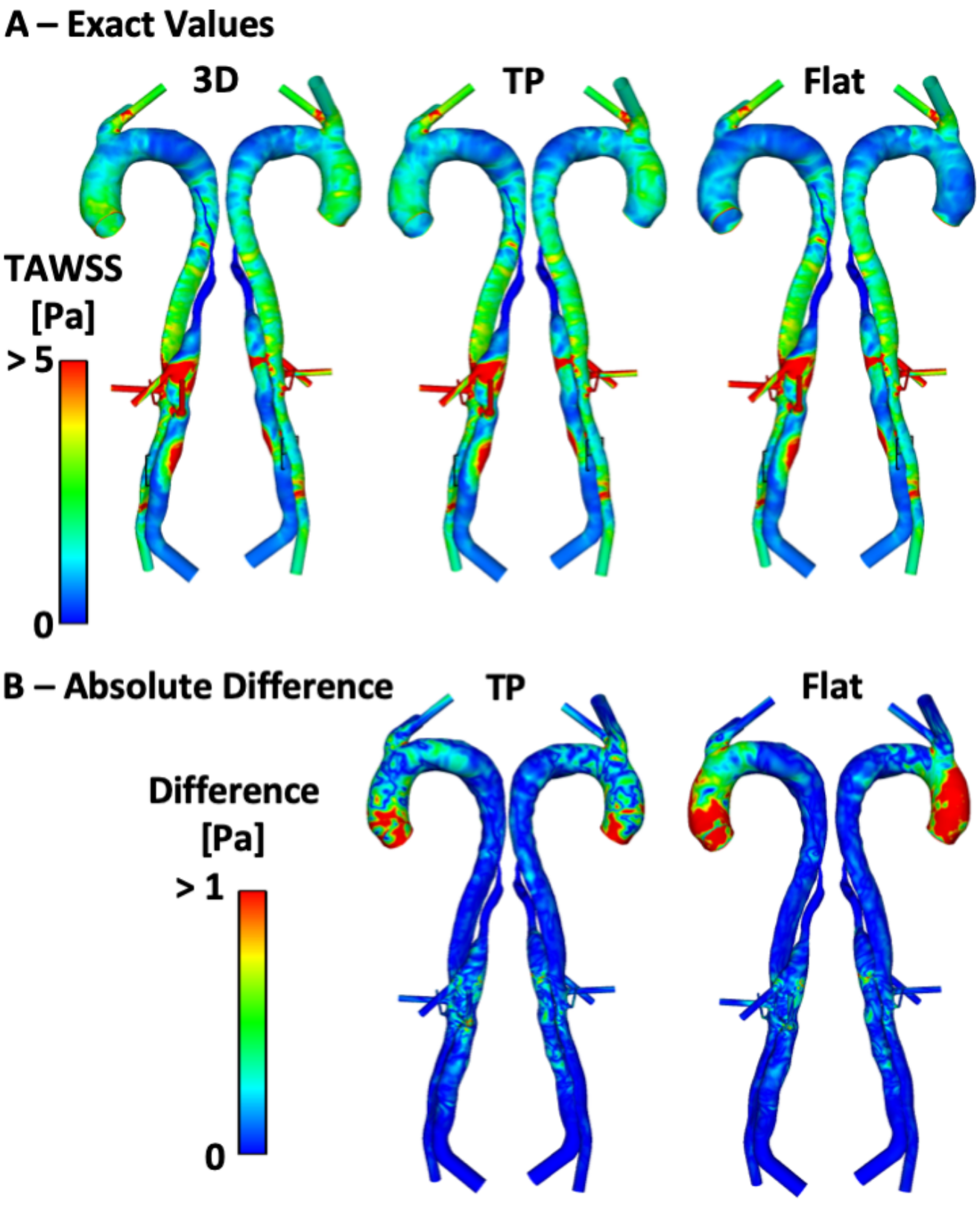

Figure 4.8: A: P2P TAWSS values with a 3D, TP and Flat inlet velocity profile (IVP). B: Absolute difference in TAWSS values between the 3D IVP and the two other IVPs (Armour et al. 2020).

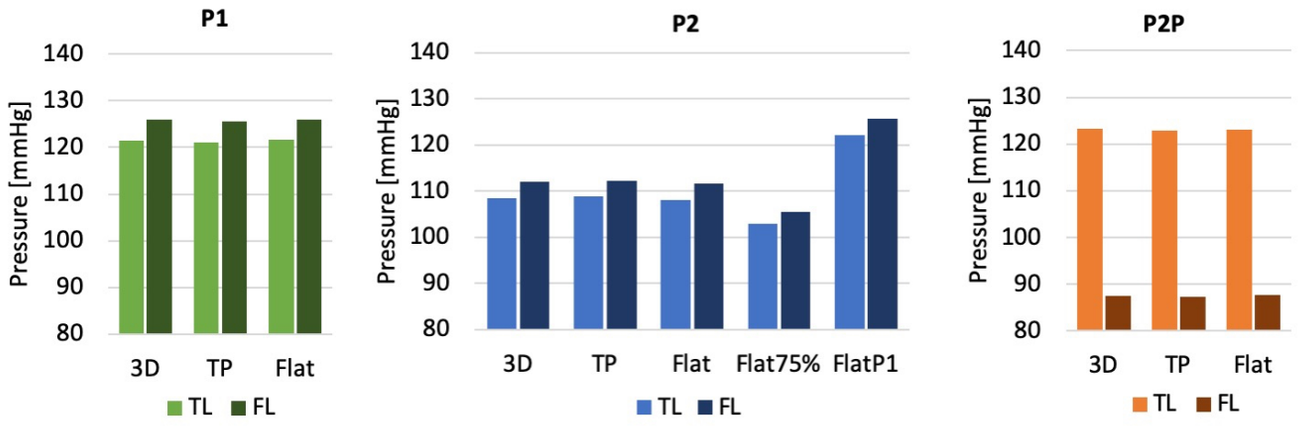

Figure 4.9: Average pressure within the true (TL) and false lumen (FL) at peak systole for P1, P2 and P2P, for all inlet velocity profiles applied (Armour et al. 2020).

IVP in the PET ranges from -27 to -35%. The absolute difference TAWSS contours show the extent to which the predicted values change throughout the entire descending aorta, with larger differences in the TL. Within the descending aorta, the mean and maximum TAWSS values vary by up to 27% compared to the 3D IVP for the non-patient-specific profiles.

4.2.3 Pressure

Figure 4.9 shows the spatially averaged pressure throughout the TL and FL at peak systole for P1, P2 and P2P with all IVPs, while Table 4.3 gives the pressure difference between the FL and TL for each case – pressure was calculated on planes shown in Figure 4.1 and averaged within each lumen. It can be seen for all models there is little variation between the patient-specific 3D, TP and flat IVPs absolute pressure within each lumen, with a maximum error of 1% across all three models. In terms of pressure difference between the lumen, using a TP IVP produced errors of up to 0.5% compared to the 3D IVP, while using a flat IVP produced errors of up to 6%, across all three models. In P2, results obtained with the Flat75% and FlatP1 IVPs are markedly different from those with the 3D IVPs, with errors of up to 6% and 13%, respectively, for absolute pressures with the lumen, and errors of up to 25% and 6%, respectively, for pressure difference between the lumen.

Table 4.3: Cross-lumen pressure difference (ΔP) for each patient with simulated inlet profiles. FL: false lumen, TL: true lumen. (Armour et al. 2020)

	3D	**TP**	**Flat**	**Flat75%**	**FlatP1**
P1	4.5	4.6	4.3	-	-
P2	3.4	3.5	3.5	2.6	3.6
P2P	-35.7	-35.6	-35.4	-	-

4.3 Discussion

Considerable efforts have been made to improve the clinical relevance and potential utility of CFD simulations, and the inlet boundary condition is a key parameter of such simulations when assessing the physiological accuracy of the results. Studies have shown that hemodynamics in the ascending aorta and aortic arch differ greatly between results obtained with 3D, TP and flat IVPs (Morbiducci et al. 2013, Pirola et al. 2018, Youssefi et al. 2018). They also suggest that within the descending aorta the flow is developed and any differences due to the inlet profile are likely to have dissipated, resulting in similar predictions regardless of the shape of IVP. These studies however were conducted in either healthy or aneurysmal aortas. The influence of inlet condition on type B dissection simulations specifically has not be reported prior to this study.

For many patients, only a CT scan used for diagnosis purposes is available, from which any temporal flow data is not available. In this case, it has been common in past studies to adopt a generic inlet profile (Alimohammadi et al. 2014, Chen et al. 2013, Cheng et al. 2010, Dillon-Murphy et al. 2016, Tse et al. 2011) and the effect of this procedure is unreported. Therefore, the impact of working with a non-patient-specific inlet profile was also investigated in this study. This was done through simulating a second flat profile in P2, which was calculated by a 25% reduction in flow throughout the cardiac cycle, and also by simulating the flat profile of P1 within P2. These two additional simulations allowed for the effect of reduced stroke volume and a varied flow waveform to be analysed separately.

Across all hemodynamic parameters (velocity, flow patterns and TAWSS), significant differences were observed in the ascending aorta of all geometric models when comparing the results obtained with different IVPs, reiterating previous findings that 3D IVPs are indispensable to

faithful reproduction of flow characteristics in the ascending aorta (Morbiducci et al. 2013, Pirola et al. 2018, Youssefi et al. 2018). Our results also showed that there were differences induced by the varied IVPs in the descending aorta, and these were confined to regions near the entry and re-entry tears. Closer inspection of the region around the PET in P1 and P2 revealed that while there was little notable difference in flow patterns, the absolute difference TAWSS contours (Figures 4.6b and 4.7b) revealed discrepancies in the proximal FL around the PET. Values of TAWSS and instantaneous wall shear stress are crucial in the prediction of thrombosis (Menichini & Xu 2016, Menichini et al. 2016, 2018), atherosclerosis (Alimohammadi et al. 2017) and retrograde dissection (Osswald et al. 2017). Therefore, it is necessary to determine to what extent such variations might affect the predicted thrombus formation. To this end, additional thrombus predicting simulations were performed, using the model presented in section 3.2. The results are shown in Figure 4.10, and it can be seen that the main area of thrombosis in the proximal FL, identified in the follow-up CT scan also shown in Figure 4.10, was well captured by all IVPs. The model also predicted additional thrombus formation in the thoracic FL, which is not evident in the CT scan. This may be attributed to possible differences between the reconstructed dissection geometry and its true original state, as reconstructing the pre-thrombus FL by simply removing the thrombus could have missed any changes in tear size and FL dimension.

Other idealised IVPs have been commonly used, such as parabolic and Womersley velocity profiles. Their influences on flow patterns and hemodynamic parameter have been studied in the aorta (non-TBAD) by various researchers (Youssefi et al. 2018, Morbiducci et al. 2013, Chandra et al. 2013). To avoid duplication of effort, parabolic and Womersley profiles were not included in this study. Nevertheless, the results obtained with these IVPs would be expected to be closer to those with the TP IVP than Flat IVP when the same flow waveform is used.

Simulations with the Flat75% and FlatP1 IVPs demonstrated the effect of using a non-patient-specific flow condition. The peak systolic flowrates for the 3D, FlatP1 and Flat75% IVP were 24.5, 22.6 and 18.4 L min^{-1}, respectively, and the peak velocity through the PET reflected these differences, with a smaller error being induced by the FlatP1 IVP than the Flat75% IVP. As the magnitude of wall shear stress is directly influenced by the flow rate, it is not surprising

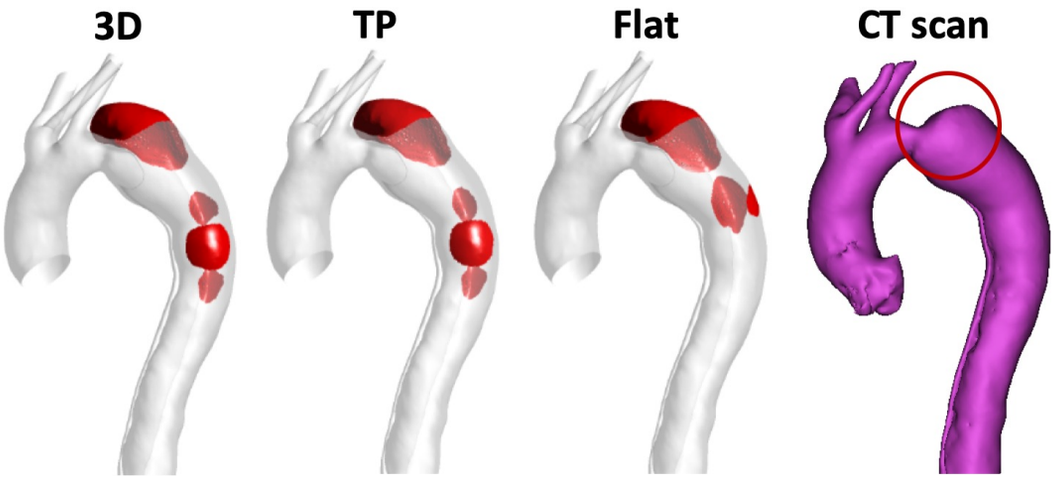

Figure 4.10: Predicted thrombus formation (shown in red) in P2 with a 3D, TP and Flat inlet velocity profile, alongside partially thrombosed (highlighted in red circle) geometry of P2 segmented from CT scan (Armour et al. 2020).

that TAWSS values are sensitive to the choice of flow waveform, especially the corresponding stroke volume. Using the two non-patient-specific flow waveforms caused errors of up to - 35% in TAWSS in the PET and lower TAWSS throughout the descending aorta - in particular, there were larger areas below 0.15 Pa in the FL. Based on the threshold values in our thrombus prediction model, it is likely that thrombus would form throughout the FL in places it would not with the other IVPs. Therefore, using a non-patient-specific stroke volume would likely either over-predict or under-predict thrombus formation.

Comparisons with *in vivo* MRI flow data showed that all patient-specific IVPs (3D, TP and Flat) were able to reproduce flow through the PET both qualitatively and quantitatively. Closer examinations revealed that while all IVPs were adequate for reproducing the general flow pattern and shape of the high velocity jet through the PET, a smaller volume of high velocities was obtained with the flat IVP. Quantitative comparisons of peak systolic velocities through the PET demonstrated high level of agreement - 0.9 m/s with all IVPs for P1, compared to 1.1 m/s from 4D flow MRI (Pirola et al. 2019); and 0.6 m/s with all IVPs for P2, compared to 0.7 m/s from 4D flow MRI. Finally, it is worth noting that the thoracic FL is characterised by slow flow, making it difficult to conduct quantitative comparisons due to large uncertainties in the 4D-flow MRI data.

Pirola et al. (2019) also reported invasive DW pressure measurements for P1, which showed

the TL to have a higher average pressure compared to the FL, with the difference being 2.3 mmHg. This is contradictory to the simulations in this study which predicted a higher pressure in the FL, with an average cross-lumen pressure of 4.6 mmHg for the 3D IVP. This discrepancy was also found by Pirola et al. (2019) in their CFD simulation of P1 and is likely attributed to the rigid-wall assumption which ignored the effect of flap motion. Considering the cross-lumen pressure difference predicted by the other patient-specific IVPs, for both P1 and P2, the TP IVP induced a negligible error, while the Flat IVP produced errors of up to 6%. In P2, both non-patient-specific IVPs predicted a higher-pressure FL with errors up to 25% using Flat75%, suggesting that the peak flow rate has a stronger influence on the predicted luminal pressure difference than the shape of flow waveform. Regarding the average pressure values within each lumen, comparisons for P2 (Figure 4.9) clearly demonstrated the importance of the shape of flow waveform, in addition to stroke volume. The implication of these findings is that patient-specific flow waveforms should be used for reliable predictions of pressure and luminal pressure difference in TBAD.

This study involved several limitations. First and foremost, the aortic wall and intimal flap were assumed to be rigid. As discussed in section 3.6, the rigid wall assumption can influence computational results. In this study, the mobility of the flap is particularly important for the models of P1 and P2 which simulated the early pre-TEVAR stage of the disease. FSI studies by Alimohammadi et al. (2015), Bäumler et al. (2020) and Qiao, Zeng, Ding, Fan, Luo & Zhu (2019) suggested that while FL flow was not qualitatively affected by the rigid wall assumption, substantial differences were noted in regions of low TAWSS between the rigid and FSI models, which may influence predicted thrombus results. Furthermore, the dynamic mobility of the intimal flap could have a strong influence on the predicted pressure values (Bäumler et al. 2020). The mechanical behaviour of stent-graft in post-TEVAR models has also been studied recently (Qiao et al. 2019, 2020), which could be incorporated into the post-TEVAR model (P2P). Additionally, blood was assumed to be a Newtonian fluid in this study. However, its quantitative effect on flow patterns and hemodynamic parameters in TBAD has been investigated (Cheng et al. 2010), and the consistency across all simulations in this study negates any influence of viscosity when comparing IVPs. Finally, as shown in Section 3.4, errors

of up to 7.2% in lumen volume were observed in an inter-user study of geometry segmentation. This error in lumen volume is relatively low but could have a small influence on simulation results. However, as the focus of this study was on changing the IVP while keeping all other model parameters constant, the results can be reliably interpreted to understand the influence of IVP choice on simulated aortic hemodynamics.

4.4 Summary

Work presented in this chapter demonstrates the importance of the choice of IVP in type B aortic dissection simulations. The results show that, qualitatively, there was little difference in TAWSS, velocity and flow patterns throughout the aorta when comparing patient-specific 3D, TP and flat IVPs. However, TAWSS values especially in the range between 0 and 1 Pa differed, with the flat IVP showing larger deviations from the results obtained with 3D IVPs. It was found that all essential hemodynamic parameters in type B aortic dissections could be predicted with good accuracy using TP IVPs. Hence, when patient-specific velocity data is available, a TP IVP should be used instead of a flat IVP.

Access to patient-specific flow data can be challenging and this study presented the first analysis of the impact of using non-patient-specific flow waveforms. Such waveforms produced significantly different results. The maximum velocity through the PET was strongly dependant on the peak systolic flow rate, while the simulated stroke volume had a direct influence on TAWSS. Predicted TL and FL pressures and luminal pressure difference were highly sensitive to the chosen peak systolic flow rate and the shape of flow waveform. Therefore, CFD results obtained with a generic flow waveform must be treated with caution when quantitative values of TAWSS and pressure are of interest. In the absence of 4D-flow MRI data, efforts should be made to obtain patient-specific stroke volume and adjust a generic flow waveform accordingly, even for qualitative analysis of hemodynamics in aortic dissections.

The results of this chapter can aid in future computational studies of TBAD, by providing an understanding of the implications of chosen inlet IVPs.

Chapter 5

The Effect of Side Branches on Aortic Hemodynamics and Thrombus Formation

This chapter presents work that examines the effect of side branches on aortic hemodynamics and thrombus formation. As discussed throughout Chapter 2, CFD studies of TBAD in the literature have varied in their inclusion of major aortic side branches, with some including only the supra-aortic branches, and others not including any branches at all. For studies which have excluded certain side branches there has also been mixed methodologies for adjusting the inlet flow rate accordingly. Thus, the first focus of this chapter is assessing the impact of neglecting major branches on the physiological accuracy of simulation results, and the effect of adjusting the inlet flow rate to account for excluded branches. Following this, the second focus is on FL perfused minor side branches, which are usually excluded in TBAD simulations, and their impact on hemodynamics and thrombus formation.

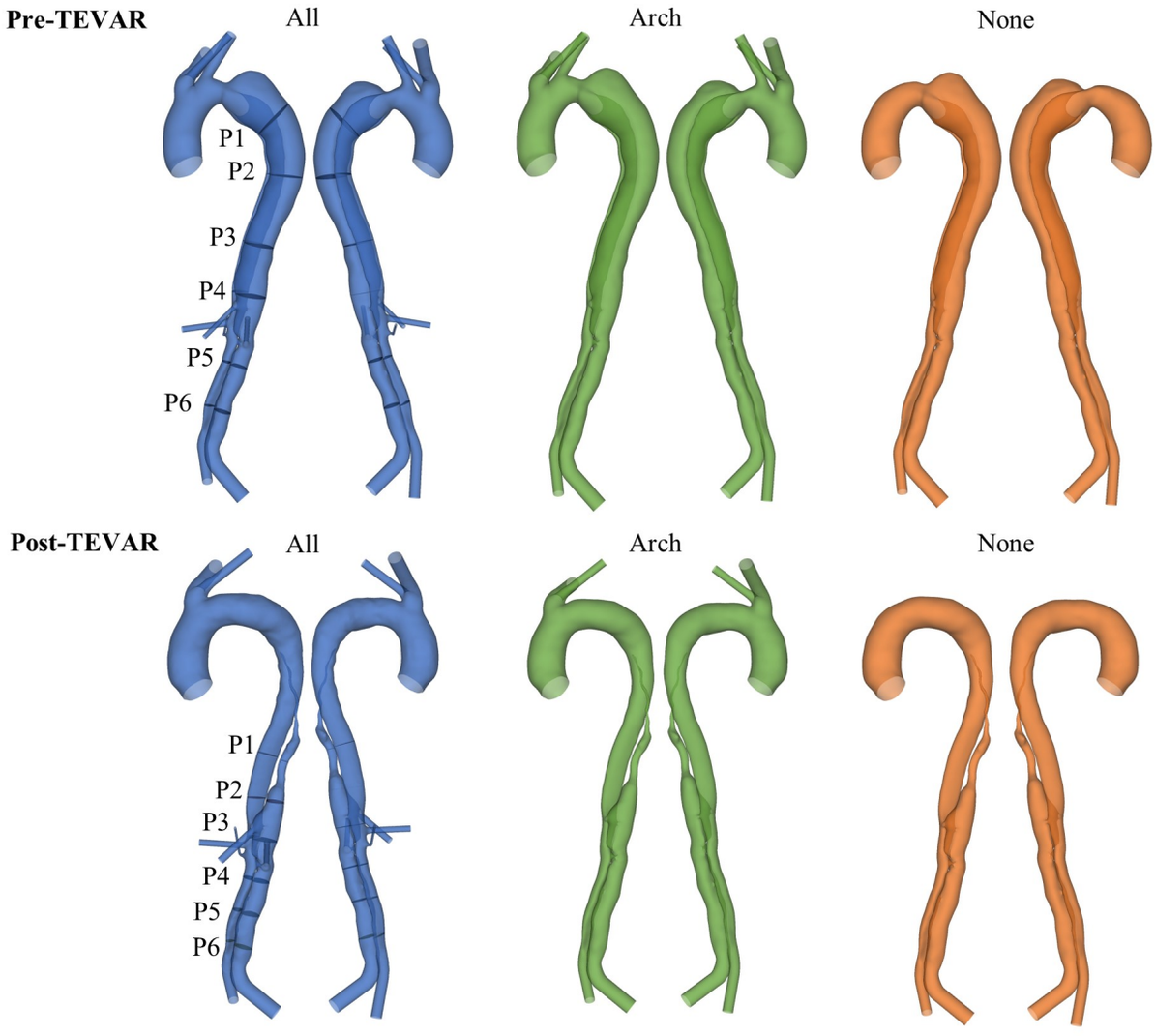

Figure 5.1: Pre and post-TEVAR geometries used for simulation. 'All' - including all major side branches; 'Arch' - including only supra-aortic branches; 'None' - including no side branches. Planes P1-P6 used to analyse pressure are shown for example in 'All' models.

5.1 Methodology

To investigate the impact of the exclusion of major aortic branches on hemodynamic results a patient treated with TEVAR at Zhongshan Hospital, Shanghai was selected for analysis. Both the pre and post-TEVAR models were segmented from CT scans to include all major aortic side branches following the practices laid out in Section 3.4. Two further geometric models were created for each of the pre and post-TEVAR models - first, in the 'Arch' models the abdominal aorta branches (CEL, SMA, RR and LR) were removed leaving just the aortic arch branches (BRAC, LCCA and LSA (the LSA was already occluded due to the stent graft in the

post-TEVAR model)) and LI and RI; second, in the 'None' models all abdominal and aortic arch branches were removed leaving just the LI and RI. These six models can be seen in Figure 5.1.

Using the methodology discussed in Section 4.1, a flat profile was extracted from a diagnostic 4D-flow MRI for this patient. As discussed previously, studies in the literature have varied in their methodology as to whether the inlet flowrate was reduced in a model in which aortic side branches were excluded. Therefore, in each model in which side branches were excluded, both the original flat profile ('Full') and an adjusted flat profile ('Adj') were simulated. The profile was adjusted for the 'Arch' and 'None' models by deducting the volume of blood reporting to the excluded branches - the volumes were measured from the simulation of the model that contained all aortic branches (reported in Table 5.1). Thus, the 'Full' simulations had a stroke volume of 114 cm^3, 'Arch-Adj' had a stroke volume of 67 cm^3, and 'None-Adj' had a stroke volume of 30 cm^3. Reducing the stroke volume of a through-plane or 3D inlet velocity profile derived from the 4D-flow MRI is challenging due to the implementation method in Ansys CFX, hence the choice of a flat inlet velocity profile in this study. While the results of Chapter 4 showed a through-plane or 3D inlet velocity profile produce more accurate results the aim of this study is to compare the 'All', 'Arch' and 'None' models and therefore the consistency of inlet velocity profile across the models will not affect the conclusions drawn from the results.

In all simulations 3EWK models were applied at the outlets. Model parameters were tuned using flow splits derived from the diagnostic 4D-flow MRI and invasive DW readings following the methodology in Section 3.6. The 3EWK models parameters were kept consistent across models when aortic branches were removed.

After investigating the impact of the exclusion of major aortic branches on hemodyanmic results, two further patients from the ADSORB trial (Brunkwall et al. 2014), one pre-TEVAR (PI) and one post-TEVAR (PII), were selected to examine the role of FL perfused minor branches on hemodynamics and thrombus formation. From CT scans both patient-specific models were segmented to include all major side branches (the LSA was again occluded due to the stent graft in PII). An additional model for each patient was then created which included additional

Table 5.1: A: Pre-TEVAR and B: Post-TEVAR percentage of inlet flow and total volume (cm^3) reporting to each side branch for all models. *LSA was occluded by the stent graft in post-TEVAR models.

A: Pre-TEVAR									
	BRAC	**LCCA**	**LSA**	**CEL**	**SMA**	**RR**	**LR**	**RI**	**LI**
	% of inlet flow reporting to branch:								
All	0.16	0.05	0.11	0.15	0.11	0.06	0.10	0.13	0.14
Arch-Full	0.27	0.08	0.20	-	-	-	-	0.22	0.23
Arch-Adj	0.27	0.08	0.20	-	-	-	-	0.22	0.23
None-Full	-	-	-	-	-	-	-	0.48	0.52
None-Adj	-	-	-	-	-	-	-	0.49	0.51
	Total volume (cm^3) reporting to branch:								
All	17.9	5.5	13.1	17.2	12.3	6.3	11.8	14.6	15.7
Arch-Full	30.6	9.5	22.6	-	-	-	-	25.2	26.4
Arch-Adj	17.8	5.5	13.2	-	-	-	-	14.8	15.4
None-Full	-	-	-	-	-	-	-	55.2	59.1
None-Adj	-	-	-	-	-	-	-	14.8	15.3
B: Post-TEVAR									
	BRAC	**LCCA**	**LSA***	**CEL**	**SMA**	**RR**	**LR**	**RI**	**LI**
	% of inlet flow reporting to branch:								
All	0.17	0.17	-	0.14	0.11	0.07	0.09	0.14	0.12
Arch-Full	0.27	0.28	-	-	-	-	-	0.23	0.22
Arch-Adj	0.27	0.29	-	-	-	-	-	0.22	0.22
None-Full	-	-	-	-	-	-	-	0.51	0.49
None-Adj	-	-	-	-	-	-	-	0.50	0.50
	Total volume (cm^3) reporting to branch:								
All	19.1	18.9	-	16.1	12.5	8.0	10.8	15.7	13.2
Arch-Full	30.9	32.4	-	-	-	-	-	25.8	25.3
Arch-Adj	17.8	19.1	-	-	-	-	-	15.1	15.0
None-Full	-	-	-	-	-	-	-	58.5	55.8
None-Adj	-	-	-	-	-	-	-	14.4	14.4

false lumen fed branches. 11 FL fed intercostal arteries (ICA) were identified in PI (creating model PI+ICA), and the inferior mesenteric artery (IMA) in the abdominal aorta was identified to branch from the FL in PII (creating model PII+IMA). All four models are shown in Figure 5.2. As both the IMA and ICA are small branches, segmenting them straight from the CT images can be challenging due to the relatively low pixel quality. Therefore, after accurately locating the branches from the CT scans their radius was manually set to match literature data – about 1.6mm for the IMA; about 2mm for each ICA (Du et al. 2015).

As no patient-specific flow information was available for PI and PII, inlet and outlet boundary conditions were developed based on data from the literature. In these simulations, a flat inlet

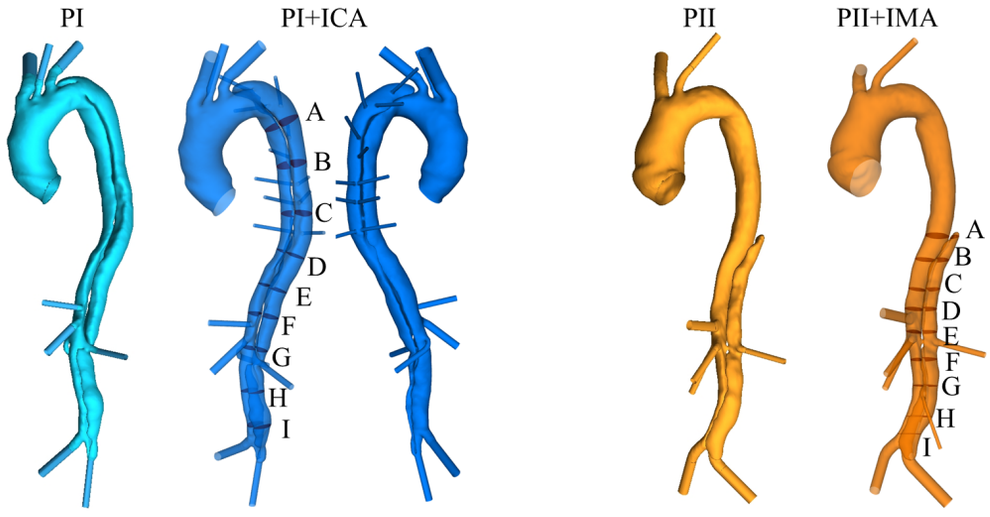

Figure 5.2: Geometric models used for simulations: (left) PI geometry without and with 11 FL fed intercostal arteries (ICA); (right) PII geometry without and with the false lumen (FL) fed inferior mesenteric artery (IMA). Planes A-I used for analysis shown in each patient.

velocity profile, of period 1.3 s, was applied (Dillon-Murphy et al. 2016). 3EWK were tuned for all outlets, expect the intercostal arteries. Total resistance (R_T) and compliance (C) for each branch were taken from a previous study (Dillon-Murphy et al. 2016), and the individual proximal R1 and distal R2 resistances were calculated through the methodology presented in Section 3.6. For the intercostal arteries in model PI+ICA, a fixed flowrate boundary condition was applied, with 5% of the inlet flow being directed to the 11 intercostals in total (Lewis & McKenna 2010).

All patients and the modified models were meshed following the methodology of Section 3.5, and further details on mesh sensitivity tests can be found in Appendix A.2. Flow was assumed to be laminar in all models, and a uniform time step of 0.005 s was used. Simulations were run until a periodic solution was reached and the final cycle was used for analysis. Pressures were evaluated on planes throughout the dissection (1-6 in P1, and A-H in PI and PII) and the location of these planes can be seen in Figures 5.1 and 5.2 for all patients. After hemodynamic simulations were run in all patients, the thrombus model presented in Section 3.2 was implemented in PII and PII+IMA. A time step of 0.005 s was used, and simulations were run until negligible further thrombus growth was predicted - this occurred after 16 cycles in both PII and PII+IMA.

5.2 Results

5.2.1 Major aortic branches

Flow patterns. The percentage of inlet flow and total blood volume reporting to each outlet was evaluated and is summarised in Table 5.1 for all pre and post-TEVAR models. Looking at the 'Arch' and 'None' models, it can be seen that, as would be expected, the percentage of inlet flow reporting to each branch increases when other branches are removed. However, the volume of blood reporting to each branch is corrected when the inlet flow rate is suitably adjusted. In the 'Arch-Adj' and 'None-Adj' models, the volume of blood reporting to each branch varies by less than 1.8 cm^3 compared to the corresponding value in the 'All' models.

As can be seen in Figure 5.1, the patient presented with a large primary entry tear (PET) on the aortic arch. This resulted in the majority of descending aorta flow (62.4%) reporting to the FL in the 'All' pre-TEVAR model. As can be seen from the data in Table 5.2, the exclusion of various branches reduced this percentage, but all reductions were relatively small. The changing stroke volumes in the 'Adj' models as well as the changing TL/FL flow split impacted the mean and maximum velocity within the PET - these values are also reported in Table 5.2.

The exclusion of branches and adjusted stroke volume also clearly impacted global velocity patterns which can be seen at peak systole in Figure 5.3A and B for the pre and post-TEVAR models, respectively. Pre-TEVAR, compared to the baseline 'All' model, the 'Arch-Full' model saw similar ascending aorta velocities, however thoracic TL and abdominal TL and FL velocities

Table 5.2: Proportion of descending aorta (DA) flow reporting to the TL and FL, and mean and maxmimum velocity through the primary entry tear (PET) in all pre-TEVAR models.

	DA flow split		**PET velocity**	
	TL (%)	**FL (%)**	**Mean**	**Max**
All	37.6	62.4	0.58	0.19
Arch-Full	39.4	60.6	0.53	0.15
Arch-Adj	39.6	60.4	0.30	0.08
None-Full	37.9	62.1	1.04	0.37
None-Adj	39.1	60.9	0.28	0.08

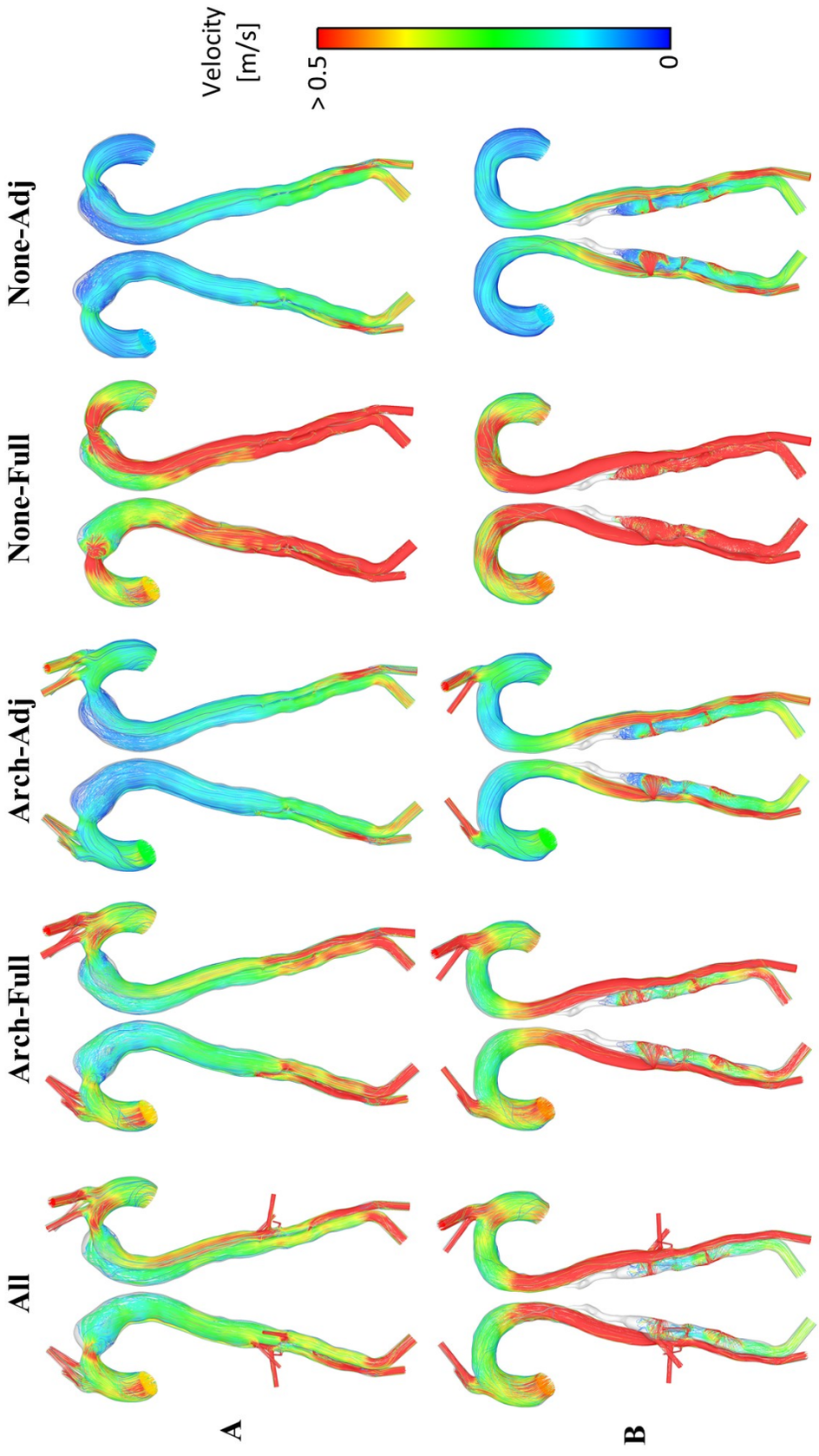

Figure 5.3: Peak systolic velocity streamlines. A: Pre-TEVAR models. B: Post-TEVAR models.

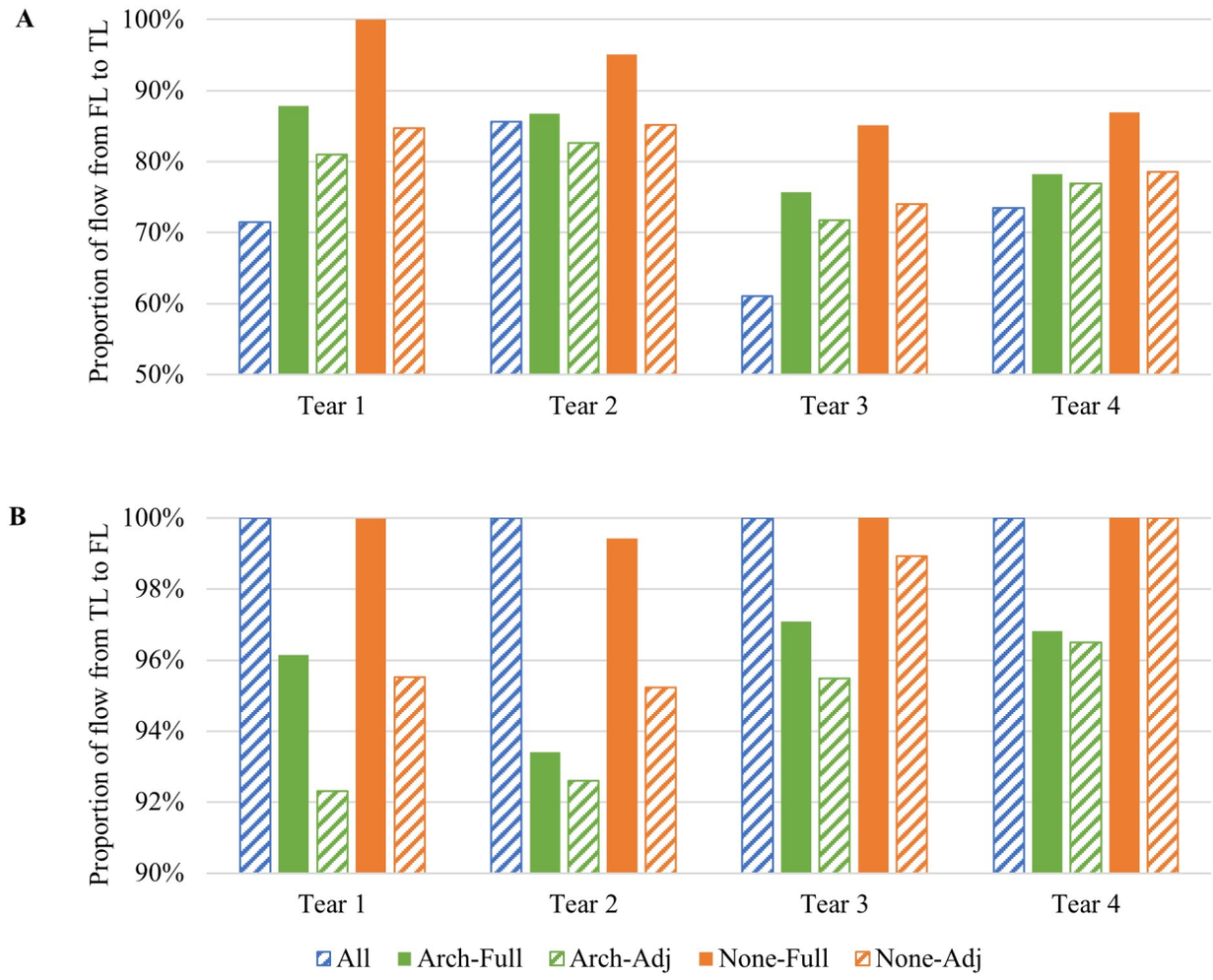

Figure 5.4: Proportion of flow report from the A: FL to TL in pre-TEVAR models and B: TL to FL in the post-TEVAR models through four re-entry tears.

increased. The 'None-Full' model saw similar proximal ascending aorta hemodynamics, however velocities were increased throughout the whole aorta from the aortic arch to the bifurcation. The adjusted stroke volume 'Arch' and 'None' models saw lower velocities throughout the models, as would be expected. Similar trends were observed in the post-TEVAR models. Compared to the 'All' model, the 'Arch-Full' model had comparable thoracic velocities and increased abdominal FL velocities. In line with the pre-TEVAR results the 'None-Full' model saw significantly increased velocities throughout the aortic arch, thoracic and abdominal aorta. The adjusted stroke volume models in the post-TEVAR case saw similar velocity patterns in the FL, however, TL velocities were reduced compared to the 'All' model.

The direction of flow through the tears was evaluated and the results are presented for the pre and post-TEVAR models in Figure 5.4A and B, respectively. The patient presented with four

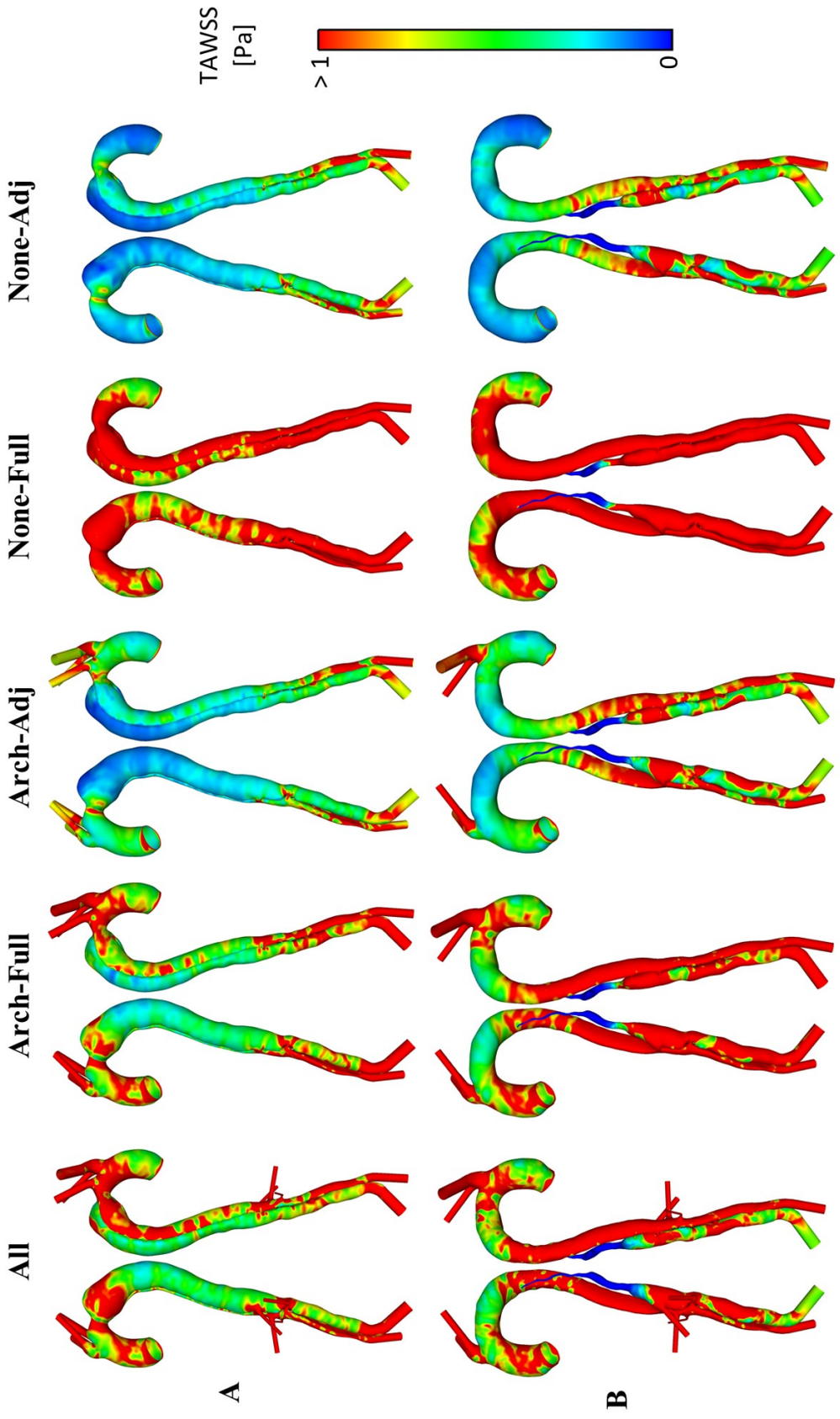

Figure 5.5: Time averaged wall shear stress (TAWSS). A: Pre-TEVAR models. B: Post-TEVAR models

Table 5.3: Time averaged wall shear stress (TAWSS) in the thoracic (Thor) and abdominal (Abd) aorta for all pre and post-TEVAR models.

	Pre-TEVAR		**Post-TEVAR**	
	Thor [Pa]	**Abd [Pa]**	**Thor [Pa]**	**Abd [Pa]**
All	0.7	1.2	1.3	2.5
Arch-Full	0.5	1.7	1.2	2.6
Arch-Adj	0.2	0.9	0.6	1.2
None-Full	1.3	4.7	3.5	7.6
None-Adj	0.2	0.9	0.5	1.1

re-entry tears which remained patent post-TEVAR. In the pre-TEVAR model the direction of flow was predominantly from the FL to the TL in all tears. At tears 1, 3 and 4 the percentage of flow from the FL to the TL increased compared to the 'All' model for all other simulations. Most significantly, at tear 1 71% of the flow was from the FL to the TL, and this was increased to 100% in the 'None-Full' model. At these three tears the error induced by the exclusion of branches was lessened by using the adjusted stroke volume. At tear 3 the 'Arch' and None Full models both increased the percentage of flow from FL to TL, while the 'Adj' models slightly reduced the percentage.

Post-TEVAR the direction of flow was 100% from the TL to the FL through all tears in the 'All' model. While the error was less significant compared to the pre-TEVAR models, the exclusion of branches did again impact the flow through the tears, with the largest difference being at tear 1 in the 'Arch-Adj' model where the TL to FL flow through the tear was reduced to 92%. Post-TEVAR, the adjusted stroke volume models increased the error induced by the exclusion of branches, an opposite trend compared to the pre-TEVAR models. Furthermore, the 'None' models induced smaller errors than the 'Arch' models.

Wall shear stress. TAWSS patterns, seen in Figure 5.5A and B for the pre and post-TEVAR models, respectively, varied between models in line with the changing velocity results - increased abdominal TAWSS in 'Arch-Full' models; increased TAWSS throughout the whole descending aorta in 'None-Full' models; reduced TAWSS throughout the aorta in 'None-Adj'. Quantitative analysis also highlighted the changing TAWSS patterns. Average TAWSS in the thoracic and abdominal aorta in all pre and post-TEVAR models is reported in Table 5.3, and it can be seen that TAWSS can be significantly over-predicted when the stroke volume is not adjusted,

Table 5.4: Cardiac cycle mean and peak systolic pressures throughout the TL and FL in all pre-TEVAR models, on planes P1-P6, the location of which are shown in Figure 5.1.

	Cardiac cycle mean pressures [mmHg]					
	P1	**P2**	**P3**	**P4**	**P5**	**P6**
			TL			
All	95.2	95.7	94.8	94.7	94.7	94.4
Arch-Full	166.3	166.1	166.0	165.9	165.6	165.0
Arch-Adj	97.1	97.0	96.9	96.9	96.7	96.5
None-Full	370.0	369.6	369.2	369.0	367.6	365.6
None-Adj	97.0	97.0	96.9	96.9	96.7	96.5
			FL			
All	95.5	95.5	95.5	95.4	95.4	95.4
Arch-Full	166.4	166.4	166.4	166.4	166.2	166.1
Arch-Adj	97.1	97.1	97.1	97.1	97.0	97.0
None-Full	370.7	370.7	370.6	370.5	369.7	369.5
None-Adj	97.1	97.1	97.0	97.0	97.0	96.9
	Peak systolic pressures [mmHg]					
	P1	**P2**	**P3**	**P4**	**P5**	**P6**
			TL			
All	117.3	117.8	116.1	115.8	115.8	115.2
Arch-Full	190.7	190.4	190.2	190.2	189.3	188.2
Arch-Adj	110.9	110.8	110.7	110.8	110.5	110.1
None-Full	428.6	427.5	426.6	426.5	423.0	418.5
None-Adj	110.2	110.1	110.0	110.0	109.7	109.3
			FL			
All	118.1	118.2	118.3	118.4	118.9	119.5
Arch-Full	191.2	191.3	191.5	191.7	191.9	192.5
Arch-Adj	111.1	111.1	111.3	111.4	111.7	112.1
None-Full	430.7	430.7	430.7	431.1	429.7	430.7
None-Adj	110.3	110.4	110.5	110.7	110.8	111.2

with increases of up to 280% ('None-Full' abdominal region) compared to the base 'All' case. Adjusting the stroke volume however did not simply lead to accurate TAWSS predictions, with under-predictions of up to 68% ('None-Adj').

Pressure. Predicted pressures were evaluated on planes P1-P6 (shown in Figure 5.1) in all models. Tables 5.4 and 5.5 report the cardiac cycle mean and peak systolic pressures for the pre and post-TEVAR models, respectively, on all planes. With the exception of plane P2, the FL had a higher pressure than the TL in the pre-TEVAR 'All' model, while the TL had a higher pressure at all points in the post-TEVAR all branches model. By comparing the other models to the 'All' model, these results show the highly significant impact of not adjusting the stroke

Table 5.5: Cardiac cycle mean and peak systolic pressures throughout the TL and FL in all post-TEVAR models, on planes P1-P6, the location of which are shown in Figure 5.1.

Cardiac cycle mean pressures [mmHg]						
	P1	**P2**	**P3**	**P4**	**P5**	**P6**
			TL			
All	96.4	95.8	96.0	96.5	96.5	95.9
Arch-Full	168.2	167.9	168.0	167.8	167.6	166.6
Arch-Adj	98.2	98.0	98.0	98.0	97.9	97.5
None-Full	385.7	384.2	384.5	384.0	383.2	378.2
None-Adj	94.1	94.0	94.0	94.0	93.9	93.6
			FL			
All	83.3	83.2	83.2	83.1	83.0	83.0
Arch-Full	160.2	160.0	160.0	159.9	159.7	159.7
Arch-Adj	94.9	94.8	94.8	94.8	94.7	94.7
None-Full	355.2	354.7	354.5	354.3	353.5	353.3
None-Adj	91.4	91.4	91.3	91.3	91.3	91.2
Peak systolic pressures [mmHg]						
	P1	**P2**	**P3**	**P4**	**P5**	**P6**
			TL			
All	128.9	127.1	127.9	130.0	130.1	128.0
Arch-Full	204.2	203.1	203.6	203.5	203.4	200.1
Arch-Adj	117.7	117.2	117.5	117.6	117.6	116.5
None-Full	488.7	483.3	485.0	483.3	481.6	461.9
None-Adj	110.8	110.4	110.7	110.7	110.7	109.7
			FL			
All	95.3	95.3	95.2	95.2	95.0	95.2
Arch-Full	180.3	179.6	179.7	179.9	179.6	179.8
Arch-Adj	107.6	107.5	107.5	107.6	107.5	107.8
None-Full	390.7	388.9	388.9	388.8	387.2	387.3
None-Adj	101.8	101.7	101.7	101.7	101.7	101.9

volume when side branches are excluded. Across both cardiac cycle mean and peak systole results, utilising the full inlet profile while the abdominal branches were excluded ('Arch-Full') increased pressures between 56% and 93%. Absolute pressures in the 'Arch-Full' models reached a maximum peak systolic value of 204 mmHg - this would be classed as an extreme hypertensive case. Implementing the full inlet profile when all branches were excluded ('None-Full') resulted in absolute pressure increases between 260% and 327%, simulating absolute pressures of up to 489 mmHg which is not physiologically possible. By adjusting the stroke volume according to the side branches that were removed predicted pressures were within a reasonable error. The 'Arch-Adj' models produced errors ranging from 1.4% to 14.1%, while the 'None-Adj' models produced errors ranging from 1.4% to 15.0%.

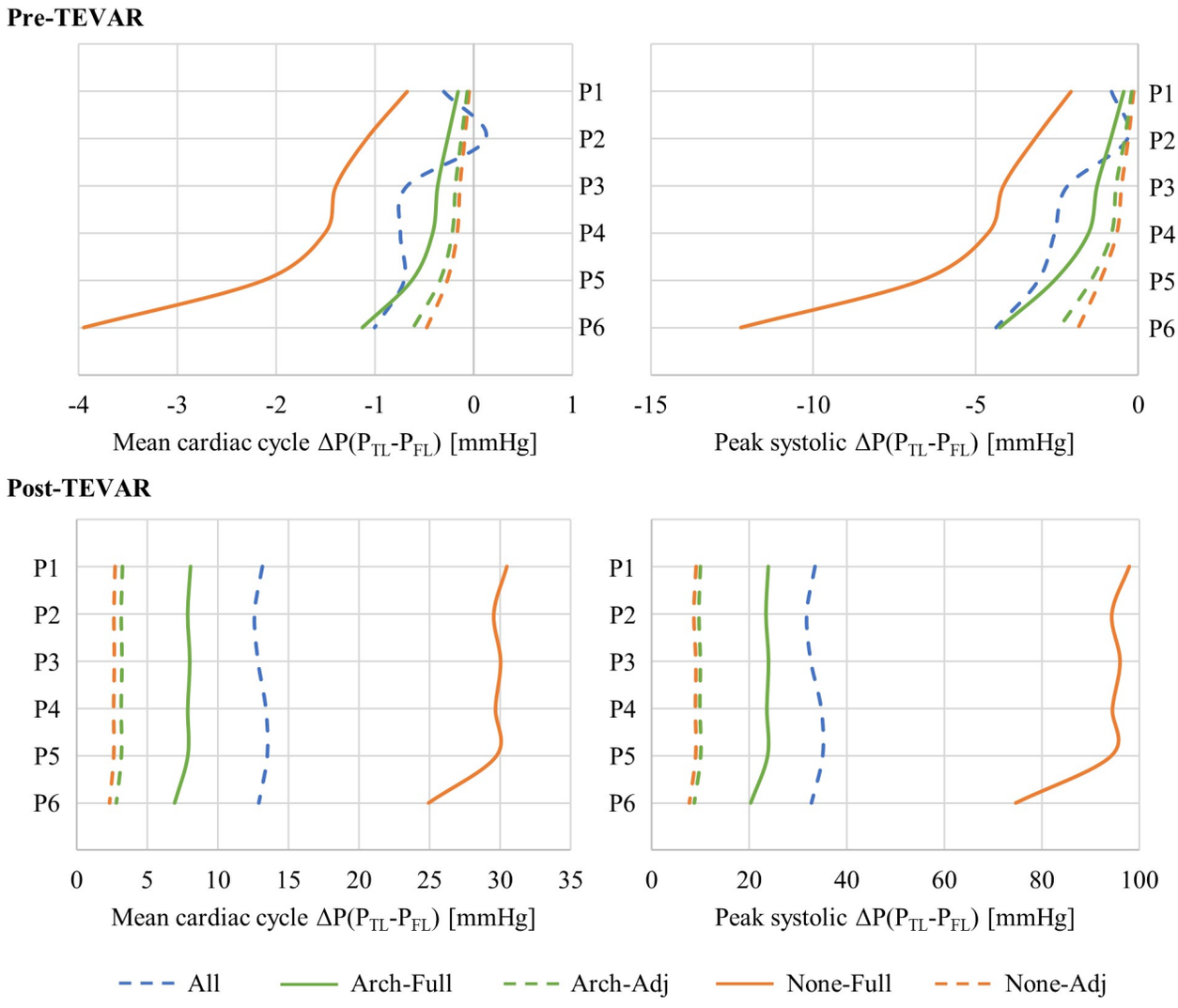

Figure 5.6: Mean cardiac cycle and peak systolic pressure difference ($\Delta P(P_{TL} - P_{FL})$) on planes P1-P6, the location of which are shown in Figure 5.1, for all pre and post-TEVAR models.

The varying branch exclusion and inlet stroke volume combinations had a different impact on cross-lumen pressure difference. The mean cardiac cycle and peak systolic cross-lumen pressure difference for all pre and post-TEVAR models are shown in Figure 5.6. In both pre and post-TEVAR models it can be seen that the trends are the same for mean cardiac cycle and peak systolic cross-lumen pressure differences, but peak systole saw higher magnitudes of pressure difference. It can be seen from these figures that the 'None-Full' models always over predicted the cross-lumen pressure difference, and to a large extent at peak systole in the post-TEVAR model. All adjusted stroke volume models produced similar cross-lumen pressure differences which were under predictions compared to the 'All' model. The 'Arch-Full' models were most accurate in predicting the cross-lumen pressure difference, with the error being larger in the

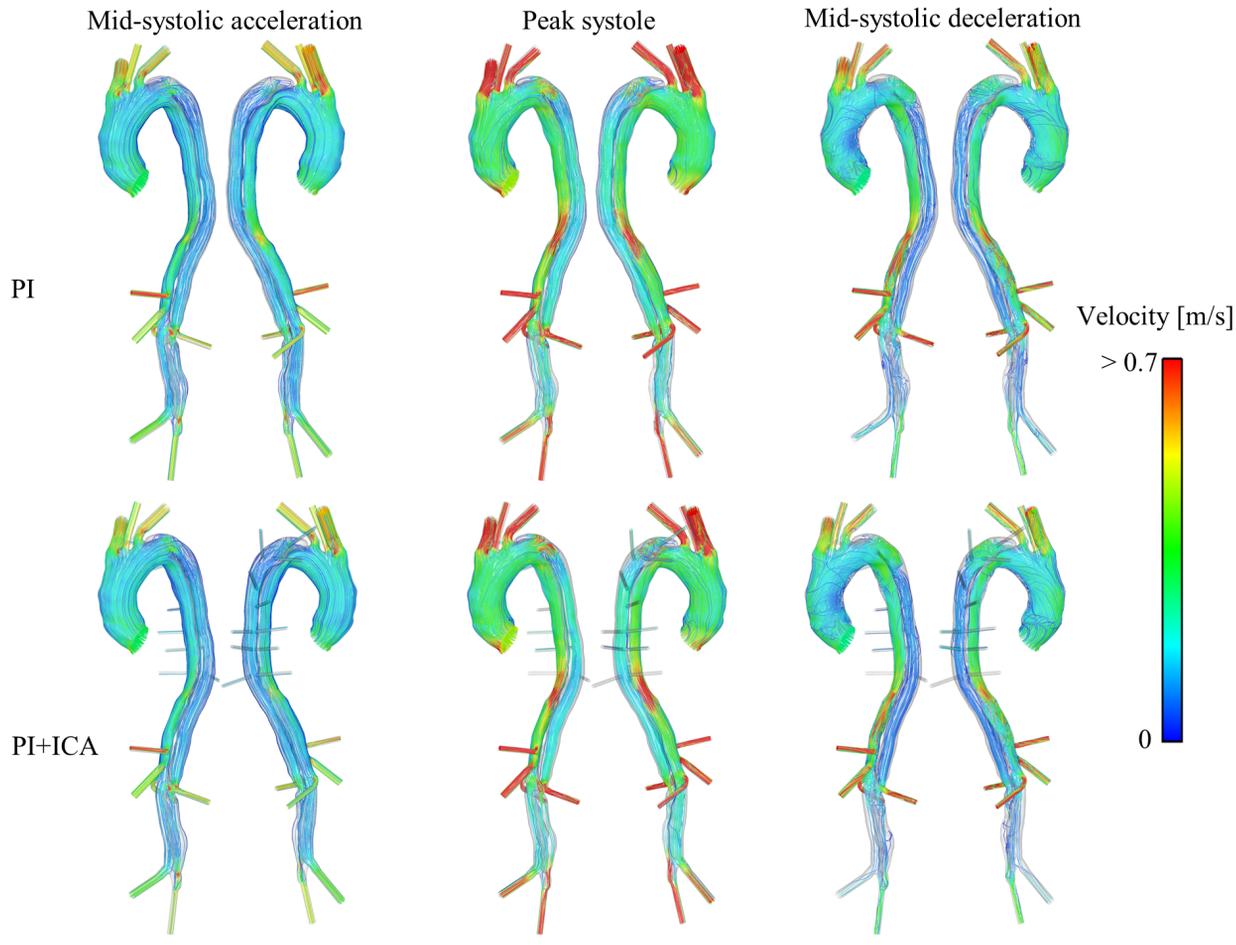

Figure 5.7: Velocity streamlines throughout the systolic phase for PI and PI+IMA.

post-TEVAR model which had a larger baseline cross-lumen pressure difference.

5.2.2 FL perfused minor aortic branches

Flow patterns. Figure 5.7 shows the velocity streamlines for PI and PI+ICA at the selected systolic time points. Comparing PI and PI+ICA, there was hardly any difference globally, although quantitative variations were noted. Including the ICA caused a 13.4% increase in peak systole maximum velocity in the jet through the primary entry tear distal to the LSA (about 0.73 m s^{-1} in PI; about 0.82 m s^{-1} in PI+ICA), and a smaller yet noticeable decrease in velocity in the TL approximately two-thirds down the thoracic aorta. These local changes are due to the inclusion of the ICA drawing more blood into the FL – the percentage of descending aorta flow entering the FL increased from 30 to 32% when the ICA were included.

Figure 5.8 shows the velocity streamlines at mid-systolic acceleration, peak systole, and mid-

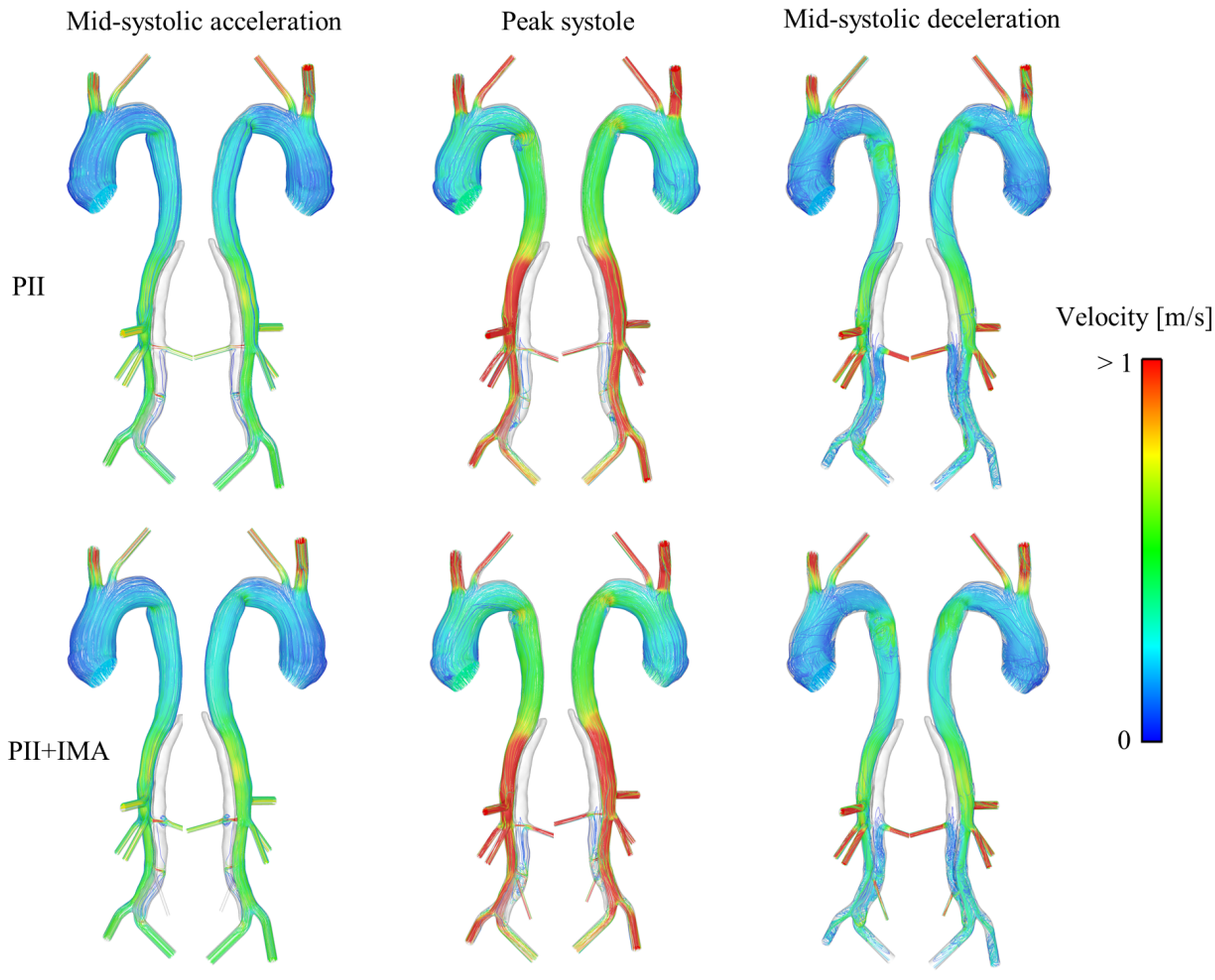

Figure 5.8: Velocity streamlines throughout the systolic phase for PII and PII+IMA.

systolic deceleration for PII and PII+IMA. Comparing the models, there was little difference in the thoracic aorta at any time point. However, in the abdominal aorta, the inclusion of the IMA altered the local flow in the FL, particularly at peak systole. About 2.2% of the total inlet flow reported to the IMA, which caused a small increase (3.9%) in the percentage of abdominal flow (below the renal arteries) recorded in the FL. As the same inlet flowrate was adopted in all simulations, the IMA flow came from redistribution of flow through other branches. This resulted in small changes in flow through the BRAC (0.8%), LCCA (0.5%) and CEL (0.5%).

Wall shear stress. Figure 5.9 shows the TAWSS maps for PI, PI+ICA, PII and PII+IMA. As with the velocity results, for both patients the inclusion of the additional FL branches did not induce any qualitative changes in TAWSS patterns. Considering PI and PI+ICA, the presence of the ICA did induce local increases of TAWSS around the branch ostia, but the volume-averaged TAWSS in the segment of thoracic FL containing the ICA only increased by

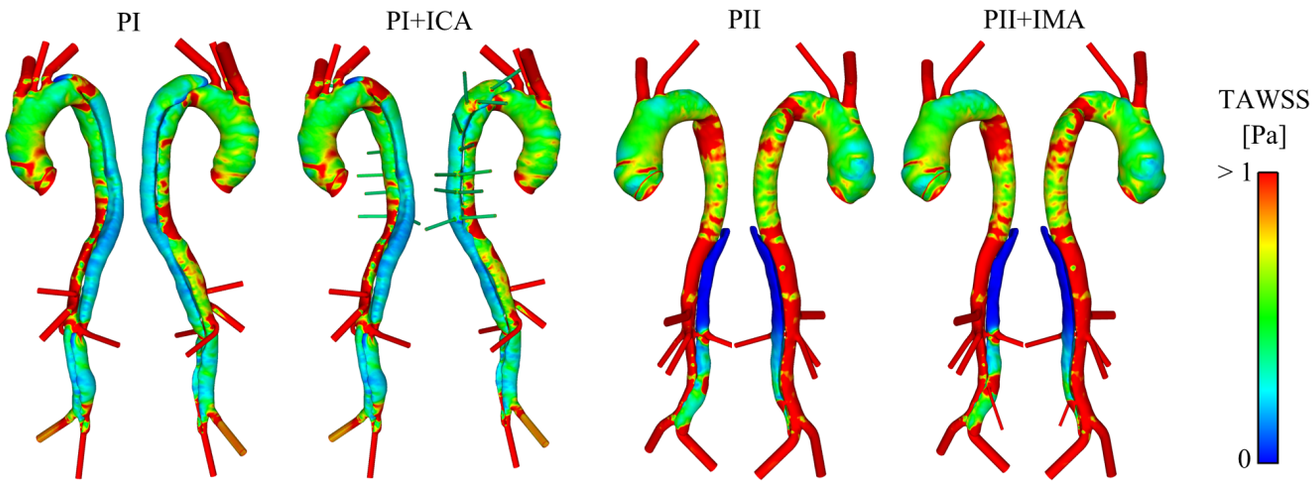

Figure 5.9: Time-averaged wall shear stress (TAWSS) for models PI, PI+ICA, PII and PII+IMA.

7.8%, from about 0.5 to about 0.53 Pa. For PII/PII+IMA, the most notable difference can be observed in the abdominal aorta where including the IMA substantially increased the local TAWSS in the abdominal FL. As a result, the volume-averaged TAWSS in the abdominal FL increased by 25.1%, from about 0.68 to about 0.85 Pa.

Pressure. The pressure difference between the TL and FL was evaluated on planes in each model (A-I, shown in Figure 5.2) and the peak systolic results are presented in Figure 5.10. For PI where the FL pressure was higher than the TL except in the upper thoracic aorta (planes A and B), the inclusion of the ICA decreased the cross-lumen pressure difference. For PII where the TL pressure was higher than the FL throughout the aorta, the inclusion of the IMA resulted in a reduction in FL pressure, hence an increase in TL-FL pressure difference. Generally, for both patients, the change in pressure difference was small, with a maximum shift in pressure difference observed across all simulations being just over 1 mmHg on plane A in PII/PII+IMA. Furthermore, cross-lumen difference in mean pressure over the entire cardiac cycle varied by $<$0.13 mmHg for all models at all locations.

Thrombus formation. Predicted thrombus formation, alongside actual observed thrombus formation from the 1-year follow-up CT scan can be seen in Figure 5.11 for PII and PII+IMA. PII correctly predicted complete thrombosis in the thoracic FL above the CEL. However, there was overprediction of thrombus growth in the abdominal aorta, as seen in the follow-up scan

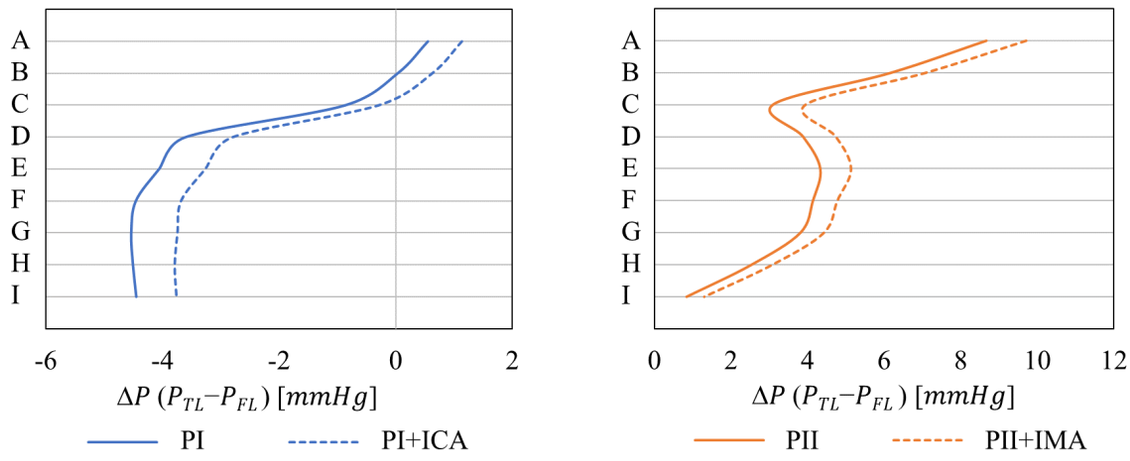

Figure 5.10: Peak systolic cross-lumen pressure difference ($\Delta P(P_{TL} - P_{FL})$) on planes A-I, the location of which is shown in Figure 5.2, for PI and PII.

there was virtually no thrombus formation in the abdominal FL. With the inclusion of the IMA, PII+IMA saw a reduction of this overprediction in the abdominal FL, with 15.3% less abdominal thrombus formation compared to PII, while still correctly predicting the thoracic FLT. The total thrombus volume formed in PII and PII+IMA was approximately 32 and 25 cm^3, respectively, while the thrombus volume observed on the final follow-up CT scan was approximately 14 cm^3.

5.3 Discussion

Over time, simulations of TBAD have progressed from idealised models to CT segmented patient-specific geometries. However in patient-specific simulations aortic side branches have often been excluded. This has been justified due to either absent patient data to tune outlet boundary conditions or the fact that TBAD only affects the descending aorta and thus the dissection is the area of interest. This meant that previous studies often excluded all side branches (Cheng et al. 2010, 2013, 2014, Menichini et al. 2016, 2018) or abdominal branches were excluded leaving only the aortic arch branches (Alimohammadi et al. 2015, Cheng et al. 2014, Qiao et al. 2019, Rinaudo et al. 2014, Shang et al. 2015, Wan Ab Naim et al. 2014, 2016). Depending on the branches excluded, using a full stroke volume will result in unphysiological volumes of blood passing through different parts of the aorta. Among the previously mentioned

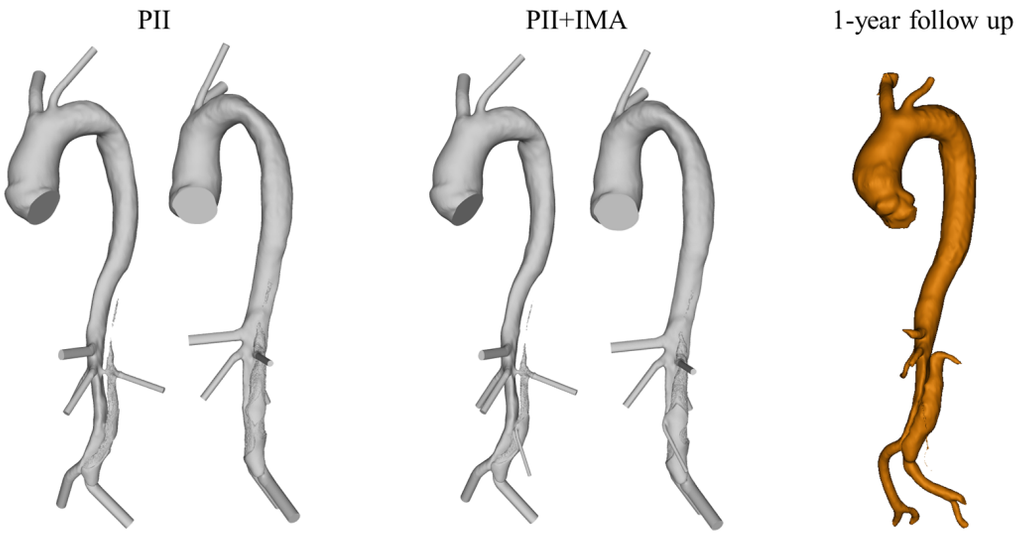

Figure 5.11: Predicted thrombus formation after 16 cycles for PII and PII+IMA alongside actual observed thrombus formation from 1-year follow up CT scan

studies only two (Cheng et al. 2014, Menichini et al. 2018) reduced the inlet flow rate or stroke volume to account for the flow through some excluded branches.

Jiang et al. (2019) presented a study of two post-TEVAR patients in which they examined the effect of removing only the abdominal branches in one case (similar to 'Arch' models in the current study), and removing only the aortic arch branches in another case. This chapter aimed to provide further understanding into the influence of excluding side branches on aortic hemodynamics by simulating both pre and post-TEVAR models. The case of removing only the arch branches was not investigated here as it was found that the practice of removing all branches was more common, thus the 'None' models were created. Furthermore, Jiang et al. (2019) adjusted the inlet stroke volume depending on the branches removed, as was done in the 'Adj' models in this chapter. Since the inlet stroke volume is not always adjusted in work reported in the literature, simulations were also performed for cases with excluded branches but full stroke volumes.

All results were compared to the corresponding baseline 'All' model for both pre and post-TEVAR to assess the impact of branch removal and stroke volume adjustment. The removal of the abdominal branches with a full stroke volume produced global velocity patterns (Figure 5.3) most inline with the 'All' case, and similar trends were seen in TAWSS patterns. Adjusting the stroke volume resulted in the correct volume of blood reporting to each branch, however it meant

unrealistically low blood volumes in the thoracic aorta, resulting in underestimated velocity and TAWSS, and lower average abdominal TAWSS due to the varied flow distribution. The exclusion of all branches ('None' models) either significantly over or under predicted velocity and TAWSS depending on if the inlet stroke volume was adjusted or not.

The impact on flow distribution, particularly flow through re-entry tears was significant. As seen in Figure 5.4, while the dominant direction of flow was not switched in any of the modified models, it did significantly differ between cases. In the post-TEVAR 'All' model the flow was 100% from the TL to the FL, which is logical as the stent-graft occludes the large PET meaning the vast majority of the flow is in the TL, and re-entry tears allow for small amounts of flow to enter the FL. With the abdominal branches excluded, the low pressure outlets that will pull flow into the FL are removed, resulting in some back-flow to the TL occurring. Similarly in the pre-TEVAR models the majority of the flow was from FL to TL in the 'All' case, and with the abdominal branches removed this increased, with more flow going into the TL due to the lack of FL outlet. Of course there are low pressure outlets with TL perfused side branches so the trend may be reversed in other patients that have different configuration of TL or FL perfused branches, but generally the removal of these branches will alter the distal pressure fields that drive flow throughout the models.

Early simulations of TBAD often applied zero pressure outlet boundary conditions, meaning any pressure results could only be evaluated relative to the rest of the domain. With 3EWK becoming the norm for physiological outlet boundary conditions, as is implemented in this study, simulated pressures can represent absolute pressures within the aorta. In terms of pressure, the effect of not adjusting the inlet stroke volume when branches were removed was highly significant. Using an unadjusted stroke volume, absolute pressures drastically increased, by up to 93% when abdominal branches were removed ('Arch' models) and up to 327% when all branches were removed ('None' models). The 'None' models pressure values were simply unphysiological, and if the inlet flow rate is not adjusted then the 3EWK should be re-tuned to account for the increased blood volume reporting to the remaining outlet branches. The 'Arch' models pressure values were high and would be classed as extremely hypertensive, however in some cases they may still seem physiological which could lead to incorrect conclusions on the

pressure values within a patient. By simply adjusting the inlet stroke volume absolute pressures were predicted within 15% for both the 'Arch' and 'None' models compared to the 'All' models.

Cross-lumen pressure differences were also affected by removing branches. Both pre and post-TEVAR, the 'None-Full' models significantly over estimated the cross-lumen pressure differences, again to unphysiological values in some cases. Interestingly, the 'Arch-Full' models, while generally underestimating the pressure differences, produced results closest to the 'All' models. As previously discussed, side branches, particularly the abdominal branches given they are within the dissection region, will provide low pressure outlets which will pull flow towards them thus impacting the pressure distribution throughout the aorta, and these results show how their exclusion can alter cross-lumen pressure differences. This is important as these pressure differences have been implicated in FL expansion, so accurately predicting them is crucial.

While the literature varies in the exclusion of major side branches, with an increasing number of studies including all major side branches, minor side branches are usually excluded. Many of these minor side branches are often perfused by the FL. Given FL thrombosis is the desired outcome of any treatment, this chapter also aimed to understand the influence of FL perfused minor branches on hemodynamics and FL thrombosis. Thus, two further cases were studied: a pre-TEVAR case was modelled without (PI) and with (PI+ICA) 11 FL perfused ICA, and a post-TEVAR case was modelled without (PII) and with (PII+IMA) the FL perfused IMA.

The presence of FL perfused minor branches was shown to locally alter flow patterns, with increased flow and velocities throughout the thoracic region in PI+ICA compared to PI, and increased flow and flow disturbance around the IMA in PII+IMA compared to PII. This increase in flow and velocities translated to an increase in TAWSS in the local branch areas. Including the ICA in PI+ICA caused a relatively small increase in TAWSS of about 2%. This is likely due to the fact that while the intercostals took 5% of inlet flow compared to the IMA's 2.2%, the 5% was split between 11 branches, meaning each branch received less than 0.5% of inlet flow, resulting in the increase in TAWSS being confined to the branch entry points. The inclusion of the IMA in PII+IMA resulted in a nearly 10% increase in average TAWSS in the abdominal aorta, and the area of high TAWSS in this region can be seen to have expanded (Figure 5.9).

Due to the local increase in TAWSS, PII+IMA predicted less thrombus growth in the abdominal FL compared to PII (Figure 5.11). The result of PII+IMA matched more closely to the follow-up CT scan; the latter showed virtually no thrombus formation in the abdominal aorta. There were still, however, small areas of thrombus formation in PII+IMA that deviated from the follow-up scan. Chapter 4 showed that the use of a non-patient-specific stroke volume (as in these models) could significantly alter TAWSS results, with a 25% reduction in stroke volume leading to a 35% reduction in TAWSS. While the applied stroke volume of 93 mL falls in the typical range of 94.15 mL (Maceira et al. 2006), it was not patient-specific, which might account for the slight difference between the predicted thrombus formation in PII+IMA and the *in vivo* results.

The over-prediction of thrombus was also clear when considering the total thrombus volumes, with PII and PII+IMA predicting 2.3× and 1.8× as much thrombus as observed on the final follow-up scan. Comparison of these values is however not entirely beneficial or accurate, as other morphological developments can have occurred between the baseline geometry and the final follow-up scan which cannot be accounted for in the CFD simulation. For example, in this patient, it was seen that the TL expanded, causing the thoracic FL to significantly reduce in size, hence the FL volume was reduced, but due to compression rather than thrombus formation. This cannot be simulated in the CFD model and instead thrombus formation was predicted in this region. Considering only the abdominal aorta where there was no observable significant morphological change between the TL and FL, PII predicted 1.8× the thrombus volume compared to the follow-up CT scan, while PII+IMA predicted a thrombus volume within 1% of the CT measured volume. This shows that when the lumen volumes are constant, and all branches are included in the geometry, the thrombus model is capable of accurately predicting thrombus volumes. However, while a promising result, comparison of quantitative values should be done cautiously as the thrombus volume measured on the CT scan may not be accurate. Identifying thrombus on a CT scan can be challenging as there is no blood flow in the region meaning the pixel intensity is low and comparable to the fluid and tissue surrounding the aorta - this makes accurate segmentation of thrombus difficult. Additionally, the volume of thrombus observed is known to vary between scan modalities, and therefore a quantitative

value measured from a single CT scan is likely not completely accurate.

The results of Chapter 4 showed that the use of non-patient-specific flow waveform and stroke volume can affect TL and FL pressures and their difference. There is therefore uncertainty in the absolute values of these parameters in PI and PII. However, this should not affect our comparison between two models (PI vs PI+ICA or PII vs PII+IMA) which used a consistent inlet velocity profile. The inclusion of the additional minor FL branches in PI+ICA and PII+IMA had a similar effect on reducing FL pressure. Again, this is logical considering the fact that these low-pressure exit points can help to alleviate FL pressure. Regarding cross-lumen pressure difference, it was increased in PII+IMA vs PII, but decreased in PI+ICA vs PI. This is because in the case of PII, the TL pressure was higher than FL pressure, hence a reduction in FL pressure would widen the TL and FL pressure difference, whereas the opposite was true for PI. Nevertheless, the predicted cross-lumen pressure differences were small in both patients, and the effect of including ICA in PI and IMA in PII and on pressure difference was insignificant.

While these results provide important insight into the consequences of methodological decisions, they also provide a mechanistic understanding from a clinical aspect of the role of FL perfused side branches, which have been identified as a predictor of various disease progressions. Anatomical studies have identified FL perfused branches to reduce thrombus formation in TEVAR patients (Qin et al. 2012, Tolenaar et al. 2014, Ge et al. 2017, Liu et al. 2018). The thrombosis simulation results suggest that FL perfused side branches do inhibit thrombus formation, due to the increased flow thereby reducing stasis and the likelihood for activated platelets to aggregate and adhere to the wall.

FL branches have also been identified to be predictive of aortic growth in medically managed patients (Kamman et al. 2017). False lumen expansion could not be modelled in this study, but the 1-year followup CT scan of PII revealed little change in abdominal FL volume from its baseline scan – Table 5.6 reports FL volume percentage changes for both PI and PII. PI did show FL expansion in the thoracic region at the 1-year follow-up CT scan, while complete thrombosis was achieved in the abdominal FL. The increased velocity in the jet through the

Table 5.6: Percentage change in FL volume by region between the baseline and 1-year follow-up CT scan for PI and PII. Thoracic: above celiac trunk; abdominal: below celiac trunk.

	Thoracic FL	**Abdominal FL**
PI	17.6%	-100%
PII	-100%	4.9%

entry tear due to the presence of the ICA led to an 11.6% increase in maximum TAWSS on the FL wall hit by the jet. This would likely cause further degradation of the already weakened FL wall and could contribute to FL expansion, potentially explaining the results of Kamman et al. (2017). The higher-pressure FL in PI may also promote FL expansion, however a larger cohort study would be required to assess the relative importance of the impact of FL perfused branches on TAWSS and cross-lumen pressure difference.

Sailer et al. (2017) specifically identified FL perfused ICA to be a predictor of late-onset complications. This cannot be explained by comparing the results obtained with and without the inclusion of ICA as late-onset complications cover a variety of potential outcomes, such as rapid aortic growth, aortic rupture, limb or organ ischemia, and new refractory hypertension or pain. However, the results do show that the inclusion of ICA can significantly alter velocity magnitudes in critical areas such as the entry tear, and the presence of ICA should not be simply ignored, as has been done commonly.

The models included in this chapter have several limitations. The inlet and outlet boundary conditions for PI and PII were taken from the literature, when ideally these would be tuned with patient-specific data. As discussed, the non-patient-specific stroke volume likely had an impact on TAWSS and therefore thrombus results, and a more accurate prediction can be made with a patient-specific tuned boundary condition. Additionally, all models were assumed to have a rigid wall. This assumption means the aortic wall motion and more importantly the intimal flap motion were neglected. The intimal flap is known to be flexible in early dissection stages, with increasing stiffness as the dissection ages (Peterss et al. 2016). Chong et al. (2020) showed that flap motion increased FL flow and diastolic wall shear stress values, in turn significantly reducing the total area of low TAWSS – a parameter shown to be crucial for thrombus formation predictions. Patient-specific studies (Alimohammadi et al. 2015, Bäumler et al. 2020, Qiao et al.

Figure 5.12: A small intercostal artery branching from the false lumen near the aortic arch is identified in the red circle.

2015) have also highlighted the effect of wall motion on regions of low TAWSS. Furthermore, in relation to the post-TEVAR models the compliance of the stent-graft (the focus of recent studies by Qiao et al. (2019, 2020) will be significantly different to the aortic wall.

As shown discussed in Section 3.4 the inter- and intra-user error in geometry segmentation can impact the lumen volume by up to 7.6%. However, given this study considers a geometry and then removes various combinations of branches, the baseline core lumen volume is constant. Therefore, any conclusions drawn from the results can be attributed to the removal of the branches rather than an error in the initial segmentation process. A separate but related limitation is the resolution of the CT scan. While CT scans are known to be high quality images for geometry segmentation the resolution is still on a comparable scale to small tears and branches (e.g. ICA with a diameter of 1-2 mm or small tears with a diameter of a few millimetres). Branches or tears which are smaller than the image resolution will not be seen and will therefore be missed in the segmentation process. Other small branches and tears that can be identified could potentially have a large error in the segmented size - for example, Figure 5.12 shows an intercostal artery branching from FL near the aortic arch that can be identified but the size of which is on a similar scale to the image resolution. This potential error was accounted for in this study by manually setting the size of the ICAs and IMA to match literature values.

5.4 Summary

This chapter demonstrates the implication of excluding major and minor aortic side branches in both pre and post-TEVAR TBAD models. Considering major side branches, flow results differed when various branches were excluded, more so when all branches were excluded rather than just the abdominal branches. This is important to highlight as although the focus of TBAD studies is on dissection hemodynamics, the inclusion of aortic arch branches which are not within the dissection can increase the physiological accuracy of results. The results also show that if the prediction of pressure is desired and branches are excluded, the inlet flow rate or stroke volume should be adjusted accordingly or the 3EWK parameters should be re-tuned for increased flowrates if they are in use as boundary conditions. However, overall, it is concluded that results vary too significantly when any aortic side branches are excluded, even when the inlet stroke volume is adjusted, and the work throughout this thesis therefore includes all major side branches. Considering minor side branches, while the results show their inclusion does impact hemodynamics and thrombus formation, the impact is much smaller than that of excluding major branches. Thus, minor side branches are not included in any further study in this thesis.

Chapter 6

Evaluation and Verification of Patient-Specific Modelling of Type B Aortic Dissection

In the preceding chapters of this thesis various simulation inputs have been addressed in depth, with Chapter 3 presenting general CFD methodology, Chapter 4 evaluating the importance of patient-specific inlet velocity profile, and Chapter 5 examining the role of aortic side branches and their influence on aortic hemodynamics and thrombus formation. This chapter builds on the results of the previous chapters, implementing the recommended patient-specific boundary condition based on *in vivo* data acquired from five TBAD patients. By using patient-specific CT segmented geometry containing all major side branches, 3D inlet velocity profile derived from 4D-flow MRI data, and 3EWK outlet models tuned using 4D-flow MRI derived flows and invasive pressure measurements, fully patient-specific simulations have been carried out. The 4D-flow MRI data and Doppler-wire (DW) pressure readings for each patient are also used for qualitative and quantitative comparisons to evaluate and validate the patient-specific simulation workflow.

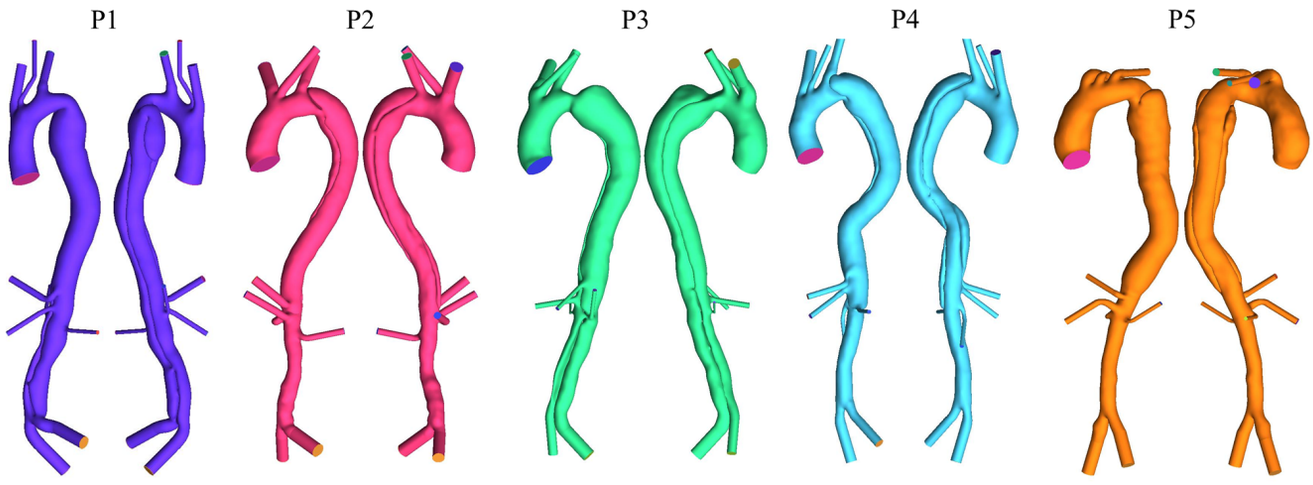

Figure 6.1: Patient-specific geometric models reconstructed from CT scans.

6.1 Methodology

Five TBAD patients (P1-P5) from Zhongshan Hospital, Shanghai, were included in the study presented in this chapter. For all patients a diagnostic CT and 4D-flow MRI scan were available. Geometries were segmented from the CT scans following the methodology of Section 3.4 and the reconstructed models are shown in Figure 6.1. Computational mesh was generated following the methodology of Section 3.5 and mesh sensitivity tests were conducted to ensure mesh independent solutions. Further details on the mesh sensitivity tests can be found in Appendix A.3. The final meshes selected contained 4.0 million, 4.3 million, 5.6 million, 4.8 million and 5.0 million for P1, P2, P3, P4 and P5, respectively.

For each patient a 3D inlet velocity profile was extracted from the 4D-flow MRI data, as described in Section 4.1. Additionally, from the 4D-flow MRI scan flow splits to the branches were determined by placing planes at various locations along the aorta and measuring the change in flowrate before and after such planes. Depending on image quality planes were placed between each aortic branch to determine flowrates to the BRAC, LCCA and LSA individually, or planes were placed before and after the aortic branches with flow being distributed between the three branches based on the area of each branch. Flow through the abdominal branches was determined by measuring the change in flowrate at planes before and after the branches and was then distributed based on area. Each patient was treated with TEVAR and during the procedure invasive DW pressure measurements were taken just before the stent-graft was

Table 6.1: Key flow parameters of the inlet flow waveform for patients P1-P5. Re - Reynolds number; Re_c - critical Re, equal to 250α (Kousera et al. 2012); α - Womersley number.

	P1	**P2**	**P3**	**P4**	**P5**
Cycle Period [s]	0.658	1.048	0.774	0.942	0.858
Peak Re	3595	3507	3821	4081	4734
Re_c	4643	4656	5280	4330	4469
α	18.6	18.6	21.1	17.3	17.9
Stroke Volume $[mL]$	74	116	117	117	113

deployed, providing the cardiac cycle pressure curves at different locations. These DW readings along with the 4D-flow derived flow splits were used following the methodology of Section 3.6 to calibrate 3EWK parameters for all branches in each patient model.

In all simulations the blood was modelled as non-Newtonian using the Quemada model, which is reported in Section 3.2 alongside the relevant model constants. The flow was assumed to be laminar based on calculations of the peak Reynolds number (Re), Womersley number and critical Re for transition to turbulence reported by Kousera et al. (2012). A summary of these key flow parameters is given in Table 6.1. The peak Re for P5 was slightly above the critical Re however as the values were close the flow was modelled as laminar for computational efficiency. A time step of 0.001 s was used throughout and all simulations were run until a periodic solution was achieved. The final cycle was used for analysis. Analysis included qualitative and quantitative assessment of velocity, kinetic energy (KE), flow patterns and pressure throughout the dissection. KE, calculated through Equation 6.1, was evaluated in 5 regions of the aorta: ascending aorta (AAo); aortic arch (AA); proximal descending aorta (Prox-DAo); Mid-DAo; Distal DAo (Dis-DAo). A description and definition of these regions can be seen in Figure 6.2. For the Proximal-DAo, Mid-DAo and Distal-DAo where the dissection was present kinetic energies were calculated in the TL and FL separately. In all regions the volume average KE was evaluated. Additionally, the false lumen ejection fraction (FLEF), Equation 6.2, defined by Burris et al. (2020), was measured at the primary entry tear (PET) in all patients.

4D-flow MRI scans were processed following the methodology of Section 3.8 from which velocities were qualitatively and quantitatively assessed in the same way as the CFD results. For a detailed comparison of the measured and predicted flow fields the Pearson's correlation coeffi-

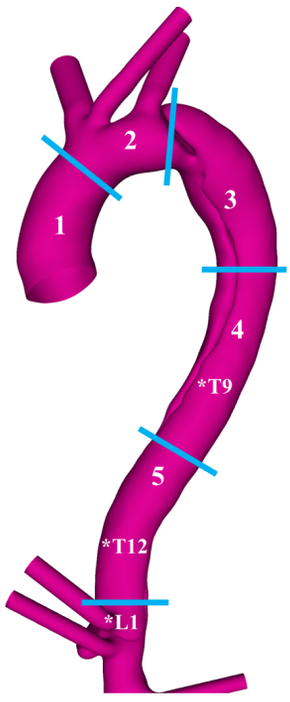

	Location	Description
1	Ascending aorta (AAo)	Inlet to the braceocephalic artery
2	Aortic arch (AA)	Braceocephalic artery to left subclavian artery
3	Proximal descending aorta (Prox-DAo)	Left subclavian artery to vertical Dao
4	Mid descending aorta (Mid-DAo)	Distal Prox-DAo to half the distance to celiac trunk
5	Distal descending aorta (DAo)	Distal Mid-DAo to celiac trunk
*T9, *T12, *L1 indicate the locations of the lumbar spinal points		

Figure 6.2: Definition of regions of the aorta (1-5) used for analysis of kinetic energy. Locations of lumbar spinal points T9, T12, L1, used for analysis of pressure, are also indicated.

cient (R) was evaluated to measure the linearity between the CFD and 4D-flow MRI velocities in the five regions of the aorta shown in Figure 6.2. This is a statistical method that has been employed in previous biomedical studies to assess agreement between 4D-flow MRI and CFD or experimental velocities (Manchester et al. 2021, Miyazaki et al. 2017, Puiseux et al. 2019). From the 4D-flow MRI scans, the FLEF was also measured at the PET and kinetic energies were derived and compared with those obtained from the CFD simulations. Due to the low spatial resolution within the dissection the kinetic energies were evaluated for whole regions rather than in the TL and FL individually.

$$KE = \frac{1}{2}\rho v^2 \tag{6.1}$$

where ρ is blood density and v^2 is velocity magnitude.

$$FLEF(\%) = \frac{Retrograde flow_{Diastolic}}{Antegrade flow_{Systolic}} \tag{6.2}$$

Table 6.2: Geometric features of patients P1-P5. [a]Ascending aorta (AAo) diameter calculated based on inlet area. [b]Maximum descending aorta (DAo) diameter measured on the axial slices of the CT scans. [c]Primary entry tear (PET) measured as the maximum axial diameter of the tear. [d]Start and end point of dissection; LSA - distal to the left subclavian artery; BIF - aortic bifurcation; SMA - superior mesentric artery; CEL - celiac trunk; LR - left renal artery. [e]Length of dissection measured along the centreline of each 3D model. [f]Tortuosity calculated as the length of dissection along the centreline divided by the straight verticle distance between the start and end of dissection.

	P1	**P2**	**P3**	**P4**	**P5**
AAo diameter[a] [cm]	2.9	3.7	3.6	3.3	3.2
Max DAo diameter[b] [cm]	4.4	3.8	5.2	4.9	3.9
Number of tears	5	5	5	5	5
PET size[c] [cm]	3.2	2.0	2.3	1.6	0.9
Dissection location[d]	LSA-BIF	LSA-SMA	LSA-BIF	LSA-CEL	LSA-LR
Length of dissection[e] [cm]	34.0	28.7	41.6	23.2	40.4
Tortuosity[f]	1.05	1.14	1.13	1.29	1.04

6.2 Results

6.2.1 Geometric features

Table 6.2 reports various geometric features for each patient. Both the AAo diameter and maximum DAo diameter varied among the patients (2.9 - 3.7 cm in the AAo and 3.8 - 5.2 cm in the DAo). All patients had 5 tears in total, with varying sizes of PET (0.9 - 3.2 cm). The dissection began at the LSA in all patients, and extended the full length of the aorta to the bifurcation in P1 and P3, while the TL and FL combined above the CEL in P5, above

Table 6.3: Diameter of each aortic side branch for all patients. Standard branch diameters reported by Du et al. (2015) and Uberoi et al. (2011) are also given. Branches include brachiocephalic (BRAC), left common carotid (LCCA) and left subclavian (LSA) artery, celiac trunk (CEL), superior mesentric artery (SMA), right (RR) and left (LR) renal, and right (RI) and left (LI) iliac.

	Branch diameter [mm]								
	BRAC	**LCCA**	**LSA**	**CEL**	**SMA**	**RR**	**LR**	**RI**	**LI**
Standard	12.4	7.4	8.5	7.8	8.7	5.2	5.2	12.0	12.0
P1	10.2	5.0	9.0	7.3	5.4	4.4	4.2	13.5	13.4
P2	15.3	10.0	12.3	10.4	9.3	8.5	8.2	13.6	16.5
P3	14.9	8.5	11.5	5.7	7.3	3.2	4.8	11.8	15.1
P4	12.5	7.0	10.4	6.7	6.0	4.8	4.6	12.7	10.7
P5	13.4	7.3	9.5	6.1	8.1	4.2	4.7	15.2	15.1

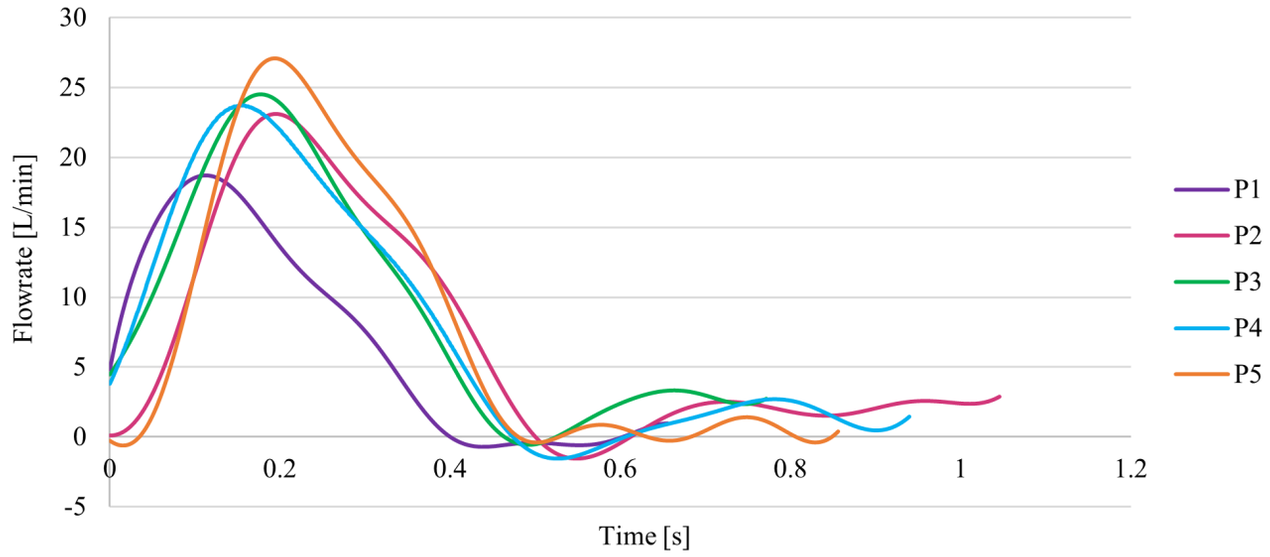

Figure 6.3: Inlet flow waveforms for patients P1-P5 derived from 4D-flow MRI scans and imposed in CFD simulations.

the SMA in P2 and at the LR in P4. There was also varying levels of tortuosity between the patients, with a near 1 value in P1 and P5 (not tortuous), and the highest value of 1.29 in P4. Table 6.3 reports the diameters for all side branches for each patient. Also reported in Table 6.3 are standard healthy diameters for each branch which have previously been reported by Du et al. (2015) and Uberoi et al. (2011). It can be seen that the measured diameters do vary between patients and from the standard value for some branches, for example large diameters were seen in all branches in P2, while individual branches in P1 (LCCA) and P3 (RR) were small compared to other patients and standard values.

6.2.2 Inlet flow waveforms and measured pressure

The inlet flow waveforms extracted from the 4D-flow MRI data had varying characteristics for each patient. Table 6.1 reports key parameters and Figure 6.3 shows each of the waveforms. Among the patients the cardiac cycle period varied between 0.658 and 1.048 seconds, the peak systole flow varied between 18.7 and 27.1 L/min, and all waveforms contained a period of retrograde flow. Patients P2-P5 had a stroke volume between 113 and 117 mL while P1 had a substantially lower stroke volume of 74 mL. The systolic, diastolic and average pressure measured from the DW waveforms recorded at the PET and spinal lumbar locations T9, T12

Table 6.4: 3-element Windkessel parameters for all branches in patients P1-P5. Branches include brachiocephalic (BRAC), left common carotid (LCCA) and left subclavian (LSA) artery, celiac trunk (CEL), superior mesentric artery (SMA), right (RR) and left (LR) renal, and right (RI) and left (LI) iliac. Reported parameters are proximal resistance (R1), distal resistance (R2) and compliance (C).

	BRAC	**LCCA**	**LSA**	**CEL**	**SMA**	**RR**	**LR**	**RI**	**LI**
P1									
R1 $[\times 10^8 Pa.s.m^{-3}]$	0.9	4.4	1.2	1.8	3.7	6.0	6.7	0.5	0.5
R2 $[\times 10^8 Pa.s.m^{-3}]$	6.9	28.0	8.9	4.0	7.5	10.0	12.0	9.5	9.7
C $[\times 10^{-9} m^3.Pa^{-1}]$	2.3	0.6	1.8	3.1	1.6	1.1	1.0	1.8	1.8
P2									
R1 $[\times 10^8 Pa.s.m^{-3}]$	0.3	0.9	0.6	0.8	1.1	1.3	1.4	0.4	0.3
R2 $[\times 10^8 Pa.s.m^{-3}]$	10.8	24.8	16.6	6.5	7.8	9.3	10.0	16.6	11.4
C $[\times 10^{-9} m^3.Pa^{-1}]$	1.6	0.7	1.0	2.4	2.0	1.7	1.6	1.0	1.5
P3									
R1 $[\times 10^8 Pa.s.m^{-3}]$	0.4	1.3	0.6	3.3	1.8	12.2	4.9	0.6	0.3
R2 $[\times 10^8 Pa.s.m^{-3}]$	6.9	20.6	8.9	4.6	2.9	12.3	6.2	10.9	6.8
C $[\times 10^{-9} m^3.Pa^{-1}]$	2.5	0.8	1.9	2.3	3.8	0.7	1.6	1.6	2.5
P4									
R1 $[\times 10^8 Pa.s.m^{-3}]$	0.5	2.1	0.8	2.3	2.9	4.9	5.4	0.5	0.8
R2 $[\times 10^8 Pa.s.m^{-3}]$	4.4	13.8	6.4	2.0	2.4	3.2	3.7	5.2	7.3
C $[\times 10^{-9} m^3.Pa^{-1}]$	3.6	1.1	2.5	4.2	3.3	2.2	2.0	3.1	2.2
P5									
R1 $[\times 10^8 Pa.s.m^{-3}]$	0.5	1.9	1.0	2.8	1.5	6.6	5.0	0.3	0.3
R2 $[\times 10^8 Pa.s.m^{-3}]$	7.9	15.5	4.6	3.6	2.2	6.9	5.6	5.1	5.2
C $[\times 10^{-9} m^3.Pa^{-1}]$	2.2	1.0	3.2	2.8	5.0	1.3	1.7	3.3	3.3

and L1 (the locations of which are shown in Figure 6.2) are reported for each patient later in Table 6.8. P1, P2 and P3 had systolic pressures greater than 125 mmHg throughout the aorta, while P4 and P5 presented with lower pressures (systolic values ranging from 74 to 90 mmHg).

6.2.3 3-element Windkessel parameters

Table 6.4 reports the 3EWK parameters for all branch outlets, calculated based on branch area, average flowrates measured from 4D-flow MRI data and average pressures measured from DW readings. Again, there are substantial variations among the parameters, due to the variability in area, average flowrate and average pressure inputs.

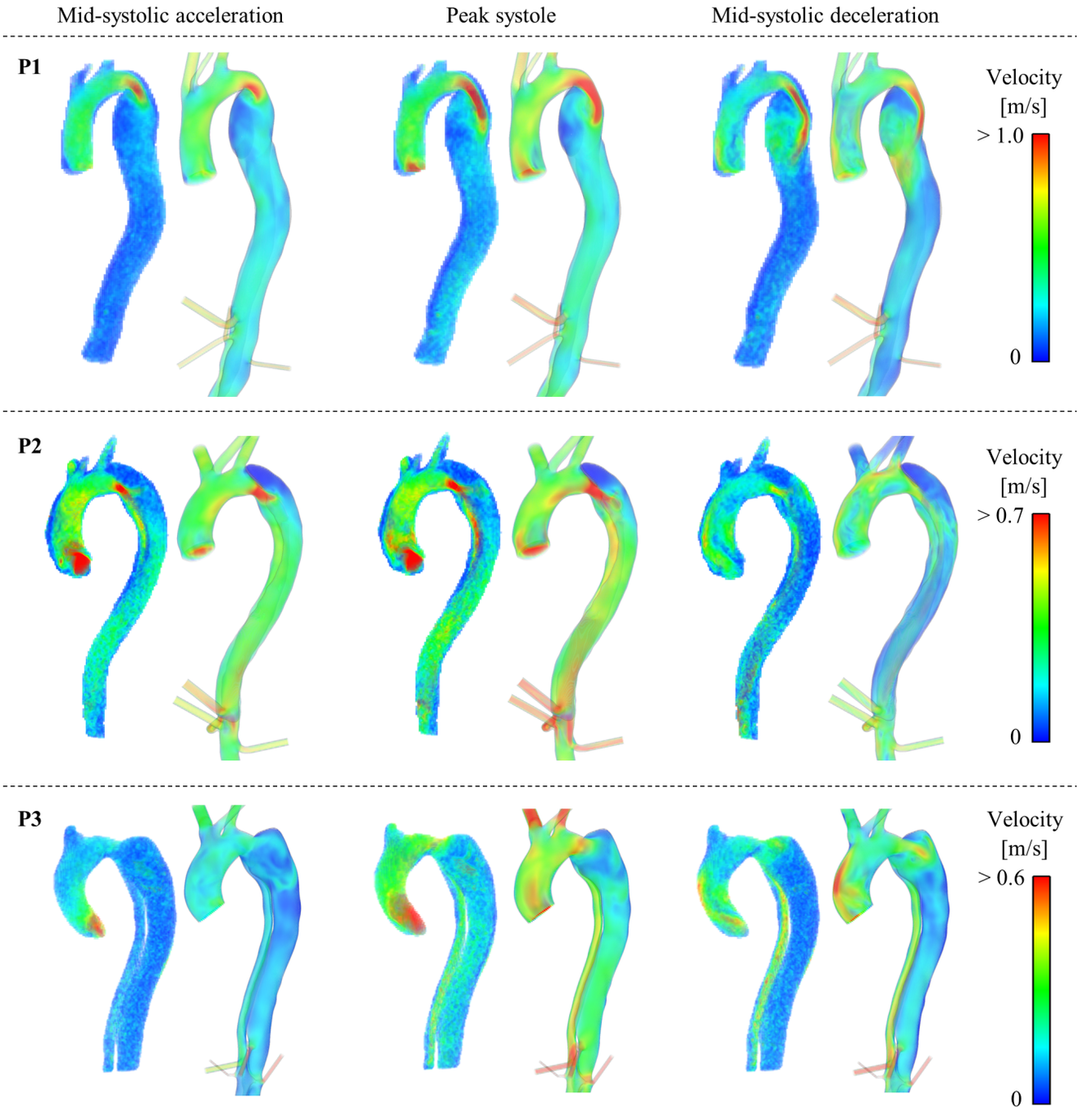

Figure 6.4: Mid-systolic, peak systole and mid-systolic deceleration velocity fields for P1, P2 and P3. For each patient at each time point the 4D-flow MRI derived velocity field is shown on the left alongside the CFD predicted velocity field on the right.

6.2.4 Flow patterns

Figures 6.4 and 6.5 show instantaneous velocity fields throughout the systolic phase from both the 4D-flow MRI data and the CFD simulations for all patients. In all cases it can be seen that there is good qualitative agreement between the simulated velocities and the *in-vivo* data. The high velocity jet through the PET in each patient was well captured both in terms of magnitude

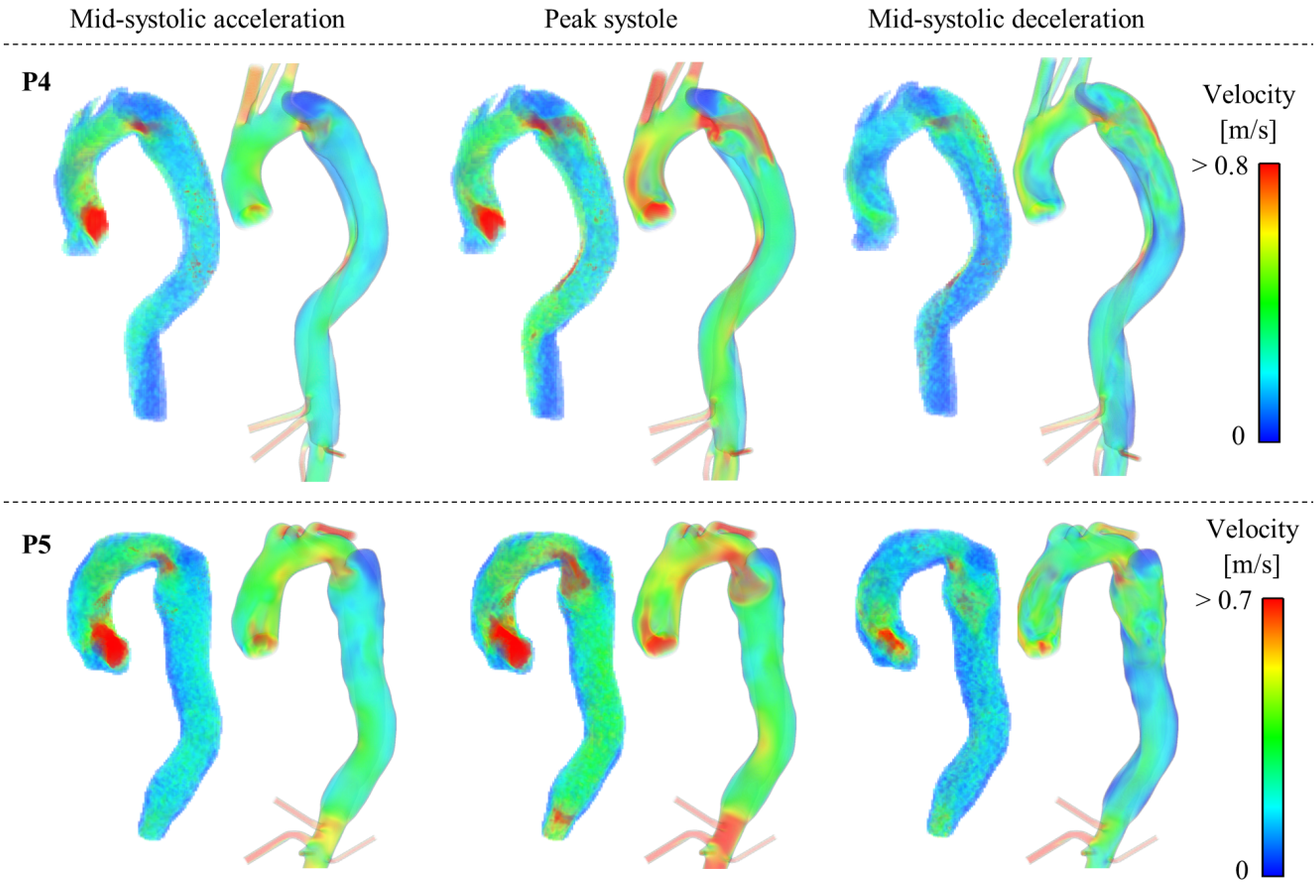

Figure 6.5: Mid-systolic, peak systole and mid-systolic deceleration velocity fields for P4 and P5. For each patient at each time point the 4D-flow MRI derived velocity field is shown on the left alongside the CFD predicted velocity field on the right.

and shape throughout the cardiac cycle. Generally, velocity magnitudes in the distal aorta were also well captured, with for example high TL velocities in the mid thoracic dissection of P4 both visible in the 4D-flow MRI data and CFD results.

Table 6.5 reports both the Pearson correlation coefficient (R) and the mean absolute error (MAE) between the CFD and 4D-flow MRI data in regions throughout the aorta, broken down into the three velocity components u_x, u_y and u_z. In line with the qualitative analysis, there is good agreement between the data across all patients, with weaker agreement at certain points - high positive and moderate positive correlations are defined as an R value greater than 0.7 and 0.5, respectively (Mukaka 2012). In the AAo, AA and Prox-DAo (regions where there are generally higher velocities and the MRI images are of better quality) 80% of the reported R values across each velocity component for all patients had an R greater than 0.5. Agreement was weaker in the Mid-DAo and Dis-DAo, where only 37% of R values were greater than 0.5.

Table 6.5: Pearson correlation coefficient (R) and mean absolute error for each velocity component u_x, u_y and u_z in the 5 regions of the aorta shown in Figure 6.2 for all patients.

		AAo	AA	Prox-DAo	Mid-DAo	Dis-DAo
		Pearson Correlation Coefficient (R)				
P1	$\mathbf{u_x}$	0.66	0.77	0.76	0.65	0.37
	$\mathbf{u_y}$	0.71	0.53	0.44	0.41	0.54
	$\mathbf{u_z}$	0.72	0.71	0.44	0.30	0.18
P2	$\mathbf{u_x}$	0.81	0.68	0.67	0.72	0.32
	$\mathbf{u_y}$	0.66	0.63	0.66	0.64	0.42
	$\mathbf{u_z}$	0.76	0.63	0.60	0.25	0.19
P3	$\mathbf{u_x}$	0.69	0.78	0.64	0.38	0.28
	$\mathbf{u_y}$	0.62	0.62	0.60	0.56	0.53
	$\mathbf{u_z}$	0.38	0.41	0.25	0.06	0.12
P4	$\mathbf{u_x}$	0.70	0.55	0.73	0.55	0.73
	$\mathbf{u_y}$	0.61	0.47	0.23	0.27	0.23
	$\mathbf{u_z}$	0.77	0.67	0.15	0.18	0.15
P5	$\mathbf{u_x}$	0.56	0.75	0.70	0.17	0.63
	$\mathbf{u_y}$	0.40	0.53	0.78	0.68	0.66
	$\mathbf{u_z}$	0.58	0.72	0.53	0.22	0.25
		Mean Absolute Error [m/s]				
P1	$\mathbf{u_x}$	0.10	0.10	0.14	0.05	0.05
	$\mathbf{u_y}$	0.17	0.16	0.22	0.11	0.12
	$\mathbf{u_z}$	0.09	0.08	0.16	0.07	0.06
P2	$\mathbf{u_x}$	0.11	0.12	0.13	0.07	0.12
	$\mathbf{u_y}$	0.16	0.10	0.13	0.16	0.25
	$\mathbf{u_z}$	0.11	0.07	0.10	0.07	0.09
P3	$\mathbf{u_x}$	0.08	0.06	0.07	0.06	0.06
	$\mathbf{u_y}$	0.11	0.10	0.07	0.09	0.13
	$\mathbf{u_z}$	0.08	0.07	0.06	0.06	0.06
P4	$\mathbf{u_x}$	0.14	0.11	0.09	0.09	0.09
	$\mathbf{u_y}$	0.21	0.18	0.18	0.16	0.16
	$\mathbf{u_z}$	0.14	0.08	0.11	0.10	0.10
P5	$\mathbf{u_x}$	0.13	0.15	0.10	0.06	0.10
	$\mathbf{u_y}$	0.21	0.11	0.11	0.09	0.11
	$\mathbf{u_z}$	0.15	0.09	0.10	0.06	0.07

While reporting R values indicates the existence of linearity between the variables it does not indicate whether the data follows the trendline of $x = y$, which in this study is desirable. By considering the corresponding MAE for each R value reported, the general over/under estimation of velocities by the CFD compared to the 4D-flow MRI data can be assessed. The maximum MAE for P1-P5 was 0.22, 0.25, 0.13, 0.21 and 0.21 m/s, respectively, while the average MAE across all regions in all patients was 0.11 m/s. Neither the R value nor the MAE

Table 6.6: Maximum peak systolic primary entry tear (PET) velocity and false lumen ejection fraction (FLEF, defined in Equation 6.2 measured from 4D-flow MRI scan and predicted from CFD simulation for each patient.

	P1	**P2**	**P3**	**P4**	**P5**
	Maximum PET Velocity [m/s]				
4D-flow MRI	1.8	1.2	0.9	1.7	1.2
CFD	1.6	0.9	0.6	1.6	1.2
	FLEF (%)				
4D-flow MRI	10.7	0.8	0.0	0.0	3.6
CFD	11.1	14.6	0.0	0.0	6.4

alone can fully describe the agreement between the data sets, thus for further detail scatter plots for each reported R value can be found in Appendix B.

Table 6.6 reports the maximum peak systolic velocity and FLEF measured from the 4D-flow MRI data and CFD results at the PET for quantitative comparison and evaluation. In all patients the maximum velocity was well predicted by the CFD simulations, with a maximum error of 0.31 m/s in P2. All CFD maximum velocities were lower than their relative 4D-flow MRI measured velocities. In P1 and P5 varying levels of FLEF were measured in the 4D-flow MRI and the CFD correctly predicted these patterns, particularly well in P1. In P3 and P4 there was no reverse flow at the PET, equating to a FLEF of zero, and this was again correctly predicted in the CFD simulation. In P2 a very low FLEF of 0.8% was measured from the 4D-flow MRI data while the CFD predicted a FLEF of 14.6%. Reasons for this discrepancy are explained in Section 6.3.

Table 6.7 reports the volume average peak systolic kinetic energy in the five regions throughout the aorta for both the CFD and 4D-flow MRI results. From the CFD results it can be seen that P1, P2, P3 and P5 all saw higher kinetic energies in the TL than the FL, while the trend was reversed for P3 who had higher kinetic energies in the FL compared to the TL. In all regions across all patients (with the exception of the AAo in P2 and P3) the kinetic energy values predicted by CFD were higher than the corresponding 4D-flow MRI derived values, with the greatest difference observed in the AAo of P4.

Table 6.7: Volume averaged peak systolic kinetic energy in 5 regions the location of which are shown in Figure 6.2 (AAo - ascending aorta; AA - aortic arch; Prox-DAo - proximal descending aorta; Mid-DAo - mid descending aorta; Dis-DAo - distal descending aorta) for patients P1-P5.

		Volume Averaged Kinetic Energy [Pa]							
				Prox-DAo		**Mid-DAo**		**Dis-DAo**	
		AAo	**AA**	**TL**	**FL**	**TL**	**FL**	**TL**	**FL**
P1	CFD-separate	187	151	189	23	66	38	128	55
	CFD-combined			148		43		68	
	4D-flow MRI	111	63	94		25		30	
P2	CFD-separate	125	99	184	29	138	76	238	71
	CFD-combined			93		106		146	
	4D-flow MRI	163	54	53		65		122	
P3	CFD-separate	80	73	21	46	24	86	34	100
	CFD-combined			24		35		48	
	4D-flow MRI	104	46	22		22		21	
P4	CFD-separate	219	152	119	117	185	46	147	68
	CFD-combined			118		69		89	
	4D-flow MRI	101	73	65		57		56	
P5	CFD-separate	121	147	86	74	101	42	154	63
	CFD-combined			78		53		86	
	4D-flow MRI	111	52	63		43		52	

6.2.5 Pressure

Table 6.8 reports the systolic, diastolic and average pressure at various locations throughout the aorta (in the ascending aorta, and in the TL and FL at the PET and throughout the dissection at the lumbar spinal locations T9, T12 and L1, the location of which are indicated in Figure 6.2) for both invasive DW values and CFD predicted values for all patients. Average pressures were generally well captured for all patients, with differences of less than 15% between DW and CFD values. P2 and P3 had the strongest agreement between DW and CFD within the dissection, with a maximum error of 7 mmHg at systolic TL-L1 for P2 and 9mmHg at systolic TL-PET for P3, while diastolic values were better matched throughout the dissection. However, there were significant errors in absolute systolic and diastolic values across the remaining patients. P1, P4 and P5 saw maximum errors of 36, 20 and 24 mmHg. P1 had larger systolic errors while P4 and P5 had larger diastolic errors.

Furthermore, significant TL/FL cross-lumen pressure differences measured by the DW were not predicted by the CFD simulations, the largest being in P1 where a cross-lumen pressure

Table 6.8: Doppler-wire (DW) measured and CFD predicted systolic, diastolic and average pressures throughout the aorta. Ascending aorta (AA); true (TL) and false (FL) lumen; primary entry tear (PET); spine vertebrae locations (T9/T12/L1). DW pressure curves were not available for P3 AA, P4 TL-PET and P4 FL-L1 to determine average pressures; the dissection in P5 did not extend to L1.

Pressure [mmHg]											
				TL				**FL**			
			AA	**PET**	**T9**	**T12**	**L1**	**PET**	**T9**	**T12**	**L1**
P1	**systole**	DW	126	125	130	131	126	126	152	154	155
		CFD	122	120	118	118	118	118	118	118	119
	diastole	DW	91	86	87	81	85	87	83	82	83
		CFD	74	73	73	73	73	73	73	73	73
	average	DW	108	105	106	108	106	106	110	109	113
		CFD	99	98	98	98	98	98	98	98	98
P2	**systole**	DW	134	135	137	137	139	125	129	130	134
		CFD	131	131	132	132	132	131	132	133	133
	diastole	DW	89	87	89	86	87	86	89	88	91
		CFD	84	85	86	86	87	85	86	86	87
	average	DW	110	107	109	106	108	104	107	107	112
		CFD	108	108	108	107	107	108	108	108	108
P3	**systole**	DW	125	130	133	135	134	135	141	137	137
		CFD	140	139	139	138	138	140	141	141	141
	diastole	DW	92	94	95	97	94	96	98	92	92
		CFD	94	93	93	93	93	93	93	93	93
	average	DW	-	111	113	115	113	114	117	113	113
		CFD	117	116	116	116	115	117	117	116	116
P4	**systole**	DW	74	85	85	84	85	85	92	93	93
		CFD	99	98	90	90	89	91	91	91	91
	diastole	DW	49	61	61	57	58	56	59	56	56
		CFD	41	41	41	41	41	41	41	41	41
	average	DW	61	-	75	70	71	69	75	73	-
		CFD	66	66	64	64	64	64	64	64	64
P5	**systole**	DW	90	109	109	106	-	93	91	95	-
		CFD	98	98	95	94	-	93	94	94	-
	diastole	DW	61	69	70	71	-	62	60	61	-
		CFD	46	47	47	47	-	47	47	47	-
	average	DW	75	79	79	81	-	76	74	72	-
		CFD	71	72	71	70	-	71	71	71	-

difference of 29 mmHg was measured with the DW while the CFD predicted no cross-lumen pressure difference at this time and spatial point. The largest cross-lumen pressure difference predicted by CFD was 8 mmHg, at the PET of P4. Of course, individual time points are likely to have larger variations and it can be seen that using average values the largest cross-lumen

pressure difference recorded with the DW was 9 mmHg in P5 at T12, while nearly all other locations across all patients had an average cross-lumen pressure difference less than 5 mmHg.

In total, pressure was evaluated at 43 spatial points among the five patients. At 35 of the points the pulse pressure (defined as the systolic pressure minus the diastolic pressure) was higher with the CFD values compared to the DW pressure readings. The points where this was not the case were in the FL of P1 where systolic pressures were significantly underestimated by CFD, and the TL of P2 where PP values were close but slightly higher with the DW readings.

6.3 Discussion

Computational fluid dynamics simulations of type B aortic dissection have been adopted by various research groups to gain an understanding of the complex hemodynamics of the disease, and to provide a mechanistic understanding for various disease progressions. Many different studies of varying complexity were discussed in Chapter 2. Chapters 3, 4 and 5 presented current best methodological practices and examined the impact of patient-specific inputs in terms of geometry and inlet boundary condition on the accuracy of simulation results. This chapter aimed to build on the conclusions of the previous chapters, to simulate 5 TBAD geometries, utilising the maximum amount of *in vivo* anatomical (CT scans) and flow data (4D-flow MRI scans and invasive DW pressure readings) that can be obtained.

As seen by the geometric data reported in Table 6.2 all five TBAD patients presented with dissections that varied in terms of tortuosity, TL/FL configuration, and dissection length. The patients also showed variations in the size of aortic branches (reported in Table 6.3). Notable differences included large branch diameters in P2, likely due to a generally larger aorta given the consistent higher than standard value across all branches. Individual branches that were abnormally small compared to the other patients and standard values included the LCCA in P1 and the RR in P3, possibly due to malperfusion.

The patients also presented with varying measured hemodynamics in terms of inlet flow waveforms and pressure values. P2-P5 all had a stroke volume within the normal range of 94±15 mL

(Maceira et al. 2006), while P1 at 74 mL was slighly below the lower limit of the normal range. The systolic phase accounted for between 48% and 61% of the cardiac cycle for all patients, with similar waveforms that differed in their peak value and period.

3EWK parameters were calculated (Table 6.4) for each branch in all patients using the average flowrate to each branch determined from the 4D-flow MRI data and the average pressure determined from the DW pressure measurements taken during the TEVAR procedure. The branch diameter was also taken into account both as a required value to calculate R1 but also due to the fact that the abdominal flow measured from the 4D-flow MRI scan was split between the branches based on their area. Given the individual data that was input to determine the 3EWK parameters the resulting values for each patient also significantly varied.

Since 4D-flow MRI is not usually required for clinical diagnosis of aortic dissection, it is common that patient-specific flow data are not available, and boundary conditions are therefore often taken from literature in such cases. The data presented in this study (branch diameters and 3EWK parameters) provides multiple new sets of parameters which can be used in future studies. If researchers only have a CT scan, geometric features from that CT scan can be compared to the five patients presented here and corresponding simulation parameters can then be selected that best match the available information.

The five patients in this study were simulated and the CFD results were compared to processed 4D-flow MRI data in order to validate the workflow. CFD predicted velocity fields showed good agreement to the *in vivo* flow data for all patients (Figures 6.4 and 6.5), in particular the shape and size of the high velocity jet through the PET in each patient was well captured by the CFD model. Global quantitative analysis demonstrated the agreement between the CFD and 4D-flow MRI velocity data through the Pearson correlation coefficients. Generally, stronger correlations were seen in the AAO, AA and Prox-DAo compared to the Mid-DAo and Dis-DAo across the patients. Due to the small channels and lower velocities in the Mid-DAo and Dis-DAo the 4D-flow MRI was of poorer quality in these regions, meaning measured velocities likely have a higher error and the registration process required to spatially match the CT and 4D-flow MRI geometries for comparison is more challenging. However, the dominant direction of flow (u_x or

u_y depending on the geometry orientation) mostly still saw reasonable correlations greater than 0.5, while the non dominant components (mainly u_z) had the lowest R values. Generally the R values found in this study are inline with values reported in previous studies: R = 0.64-0.92 in a healthy patient (Miyazaki et al. 2017); R=0.63 in an idealised aortic aneurysm geometry (Puiseux et al. 2019); and R=0.74-0.87 in an ascending aorta aneurysm patient (Manchester et al. 2021).

Local quantitative analysis (Table 6.6) showed that the velocity magnitude in the PET was well matched between the CFD and 4D-flow MRI results, with the largest error of 0.3 m/s in P2 and P3. The PET velocity was underestimated in all patients compared to the 4D-flow MRI derived value, and this was the case in previous studies including Chapter 4 of this thesis and also in the work of Pirola et al. (2019). Interestingly, the 4D-flow MRI data reported a higher maximum velocity in the PET region, while generally throughout the aorta on average the CFD predicted higher velocities, particularly in the AAo and AA. This was emphasised in the KE results where the vast majority of regions saw higher KE with the CFD compared to the 4D-flow MRI. Considering the KE CFD results on their own, all patients except P3 (which generally had lower KE values throughout the aorta compared to the other patients) saw higher TL KE than FL KE. This is logical as P1, P2, P4 and P5 had a compressed TL increasing the velocity of the flow passing through it while P3 had a compressed FL resulting in higher velocities there. This is inline with the work of Jarvis et al. (2020) which found on average KE was approximately 8 times higher in the TL compared to the FL in a study of 6 TBAD patients.

There may be two sources of error causing the discrepancies in velocity results between the CFD and 4D-flow MRI data which relate to the relatively low image quality of the 4D-flow MRI scan. The first being that the size of the smaller branches (including the LCCA) is on a comparable scale to the voxel size of the scan ($1.875 \times 1.875 \times 2.5\ mm^3$ for all patients) which may cause inaccuracy in measured flows, thus the measured flow to the arch branches may be higher than reality, resulting in slightly less flow entering the descending aorta and through the tear. The second is the potential error in the extracted inlet velocity profile. Both abnormally high and low velocities may not be fully captured as the scan parameters (such as the velocity

encoding (VENC) which dictates the range of velocities that are accurately captured) are set to minimise scan time in the clinical setting for the benefit of the patient. The use of dual VENC which repeats the scan to record a lower and higher velocity range can help to overcome this potential error source (Nett et al. 2012, Ha et al. 2016, Concannon et al. 2020), however this is challenging in the clinical setting as it significantly extends the scan time. Furthermore, the lower image quality means that there is some variation in the flowrate extracted depending on the location at which the plane is placed. To evaluate the likely extent of this error, 3 planes were placed near the aortic root in P1, 5 mm apart, with plane 1 closest to the aorta valve, plane 2 distal to plane 1 and still within the velocity jet, and plane 3 most distal to the valve and just slightly distal to the tip of the high velocity jet. The peak and average flowrates and stroke volume derived from plane 2 differed by a small 1.5%, -3.2% and -2.7%, respectively, compared to plane 1, while the peak and average flowrates and stroke volume derived from plane 3 differed by -11.2%, -10.3% and -8.9%, respectively, compared to plane 1. This error was minimised across all simulations by ensuring the plane placed to extract all inlet velocity profiles was set well within the high velocity jet, however there likely will have been some degree of error in the final inlet velocity profiles. Both of these sources of error may have resulted in a slightly lower than true stroke volume being applied in the CFD simulation. The results of Chapter 4 showed the significant impact a reduced stroke volume can have on hemodynamic results, with at 25% reduction in stroke volume resulting in up to 28% and 35% reduction in velocity and wall shear stress, respectively. However, the results of this chapter suggest that any stroke volume error was likely small as there was no significantly impact velocity fields. As seen by the quantitative and qualitative analysis, local regions of altered velocity patterns were still well captured by the CFD, such as the area of high velocity in the mid-thoracic TL of P4 at mid-systolic deceleration and the increased velocity around the abdominal branches of P5 at peak systole. Bozzi et al. (2017) showed that a deviation of $\pm 18\%$ in the mean inlet velocity impacted pressure and wall shear stress results significantly, which may explain the more significant deviation in predicted pressures compared to the DW measured values.

As well as velocities, flow patterns (Table 6.6) were well captured by the CFD simulations compared to the *in vivo* data. The lack of any flow reversal (represented by FLEF) at the PET

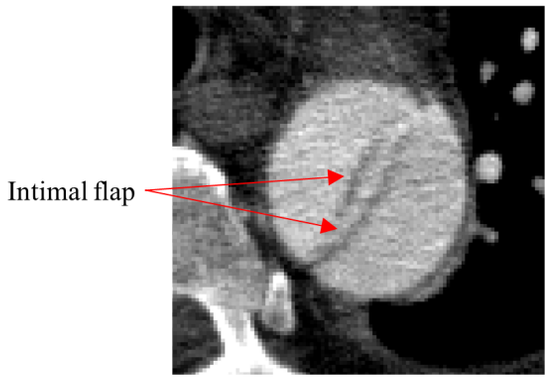

Figure 6.6: Motion artefact visible due to flap motion on the axial view of the descending aorta on the CT scan for P2. Red arrows indicate the intimal flap (darker line in the middle of the aorta).

in P3 and P4 was correctly predicted by the CFD, and the varying levels of FLEF in P1 and P5 were also inline with 4D-flow MRI results. The FLEF results for P2 were not consistent, with a significant over-prediction by the CFD simulation. On the CT scan for P2 there is clear motion artefact around the PET which is shown in Figure 6.6 - this is commonly observed on dissection CT images given the scan captures a static image but the aorta and intimal flap are mobile. This means that during segmentation there was likely some degree of error relating to the exact shape and size of the PET, and any deviation from the true geometry will impact flow through the tear, thus this is likely the source of the FLEF error in this case.

CFD predicted pressures were compared to the *in vivo* DW measurements to evaluate agreement (Table 6.8). Average pressures predicted by the CFD were in reasonable agreement with the DW values, meaning the general pressure environment and extent of pressure elevation was captured. However, there were significant errors both in terms of absolute systolic and diastolic values and cross-lumen pressure differences. There are several factors that may contribute to these errors, the first being variation in the time at which scans and pressure measurements were taken. The DW measurements were taken during the TEVAR procedure, before the stent-graft was deployed, which would have been on a different day to when the diagnostic CT and 4D-flow MRI scans were taken. It is known that dissections can progress rapidly in the acute phase, including stiffening of the intimal flap (Peterss et al. 2016). Any progression of the disease between the diagnostic scan and TEVAR procedure may have resulted in varied pressure and flow fields within the aorta. Chapter 4 showed the significant impact peak systolic

inlet flowrate and general flow waveform can have on predicted pressures, and therefore change due to disease progression may result in different flow splits and therefore cross-lumen pressure differences.

Another factor that may contribute to the error in systolic and diastolic values is the way in which the pressure data is used to tune the 3-EWK parameters. It can be seen from the methodology laid out in Section 3.6 that to calculate the 3-EWK parameters average flow and average pressure at each branch is required. To do this, the average pressure measured from the DW pressure curve is calculated and utilised. The pressure at each branch is initialised with the corresponding measured diastolic value, however at no point in the methodology is the maximum systolic pressure taken into account. This may explain why the CFD simulations predict the average pressures in the aorta, but often miss the extreme maximum value in the cardiac cycle.

Moreover, while invasive DW pressure measurements are considered the gold-standard there is likely still some degree of error in these readings themselves. Discussions with our collaborators who conducted the surgeries in which the pressure readings were taken highlighted potential error sources. In dissections the TL and FL can at times be very narrow, and with the highly mobile intimal flap early on in the disease it is possible that flap motion may cause the DW tip to come into contact with the tissue thus influencing the pressure reading. Furthermore, the geometry of dissections means there are often areas of high velocity and complex flow patters, particularly around tears - a clear example of which can be seen in the PET in all patients in Figures 6.4 and 6.5. This makes it challenging to achieve a steady reading on the DW. In this case the reading may be taken multiple times and averaged to minimise the error however to reduce the surgery time this is not always possible.

Finally, the rigid wall assumption in these simulations likely impacted the pressure results. Recent work using an idealised geometry by Chong et al. (2020) showed that rigid wall simulations can overestimate systolic pressures and underestimate diastolic pressures and therefore overestimate pulse pressure. It was seen that in most cases the pulse pressure was overestimated by the CFD simulations in this study, and wall and flap motion may rectify this to bring the

pulse pressures more inline with the DW readings. A patient-specific study by Bäumler et al. (2020) showed that rigid simulations can overestimate cross-lumen pressure differences. Given the rigid simulations in this study generally underestimated cross-lumen pressure differences compared to DW readings it is unclear if wall motion would account for this error given the conclusion of Bäumler et al. (2020) would suggest inclusion of wall motion would further decrease this pressure difference. A recent study (Zimmermann et al. 2021) combined experimental and computational methods in which a patient-specific TBAD model was 3D printed and embedded in a physiological flow circuit. Pressure measurements were then taken within the experimental aorta and a 4D-flow MRI scan of the set up was also taken. A fluid-structure interactions (FSI) CFD simulation of the patient-specific model was then carried out and the results showed accurate prediction of the cross-lumen pressure difference at multiple locations in the dissection. The catheter pressure readings and 4D-flow MRI scan are expected to be of better quality than the *in vivo* data of the current study, given the controlled experimental condition, but the well matched CFD pressure results indicate the importance of flap and wall motion. For clarity and further understanding, a fully coupled fluid-structure-interaction simulation of the patients in this study would allow for the impact of the rigid assumption to be properly evaluated.

As discussed in previous chapters and in detail in Section 3.4, the models presented in this study will have some level of error in segmented volume (up to 7.2%) due to the inter and intra-user variability when performing the segmentation. The results in this chapter showed good agreement between the CFD simulations and *in vivo* 4D-flow MRI data, suggesting that there is no significant impact due to segmentation error. However, further development of more automated segmentation methods using machine learning technologies would reduce the manual input in the segmentation process and improve geometry accuracy.

6.4 Summary

This chapter presents CFD simulation of five TBAD patients, following a workflow that incorporated the maximum amount of anatomical and flow data that can be acquired *in vivo*:

patient-specific geometries from CT scans, inlet velocity profiles and outlet flowrates derived from 4D-flow MRI scans, and invasive DW pressure readings. The patients presented with varying dissection geometries and differing aortic branch sizes, resulting in a range of 3-EWK parameters which have been presented here. This data can be utilised in future studies where researchers do not have patient-specific flow data to tune Windkessel parameters, but want to implement values which represent the studied geometry. The CFD results were evaluated and compared with the processed 4D-flow MRI scans, and strong agreement in flow patterns and velocity magnitudes throughout the cardiac cycle was seen in all patients. CFD predicted pressures were compared against DW measurements, and average pressures were predicted within an acceptable margin of error for all patients, however there were significant errors in the CFD predicted instantaneous systolic and diastolic pressures, and cross-lumen pressure differences were generally underestimated by the CFD, all of which can be investigated further with FSI studies.

Chapter 7

Evaluation of Thrombosis Model for Clinical Application

As discussed throughout Chapter 2, the ultimate desired outcome of any treatment method of TBAD is complete thrombosis of the FL. Being able to predict thrombus formation in a patient is therefore highly desirable and many models have been developed towards this end. Early kinetic models were valuable in modelling the complex thrombosis process, however they were not applied to patient-specific geometries due to their complexity and the extremely high computational time that would be required. The development of Menichini & Xu's (2016) model, which was presented in detail in Section 3.2 was a significant advancement in the field by overcoming the barrier of application to patient-specific geometries, with good agreement achieved between predicted and actual thrombosis patterns shown on follow-up scans (Menichini et al. 2016, 2018). While the thrombus model simplifies the overall process by tracking the transport and interactions of four species (resting (RP), activated (AP) and bound platelets (BP), and coagulant (C)) and a non-reactive tracer representing the residence time (RT) it still takes several days, sometimes weeks, to complete a simulation depending on the geometry. In this chapter the key variables within the model are assessed and the model equations are further reduced in order to improve its computational efficiency. An idealised model is initially used for computational efficiency, with the resulting simplified model then tested in a patient-specific

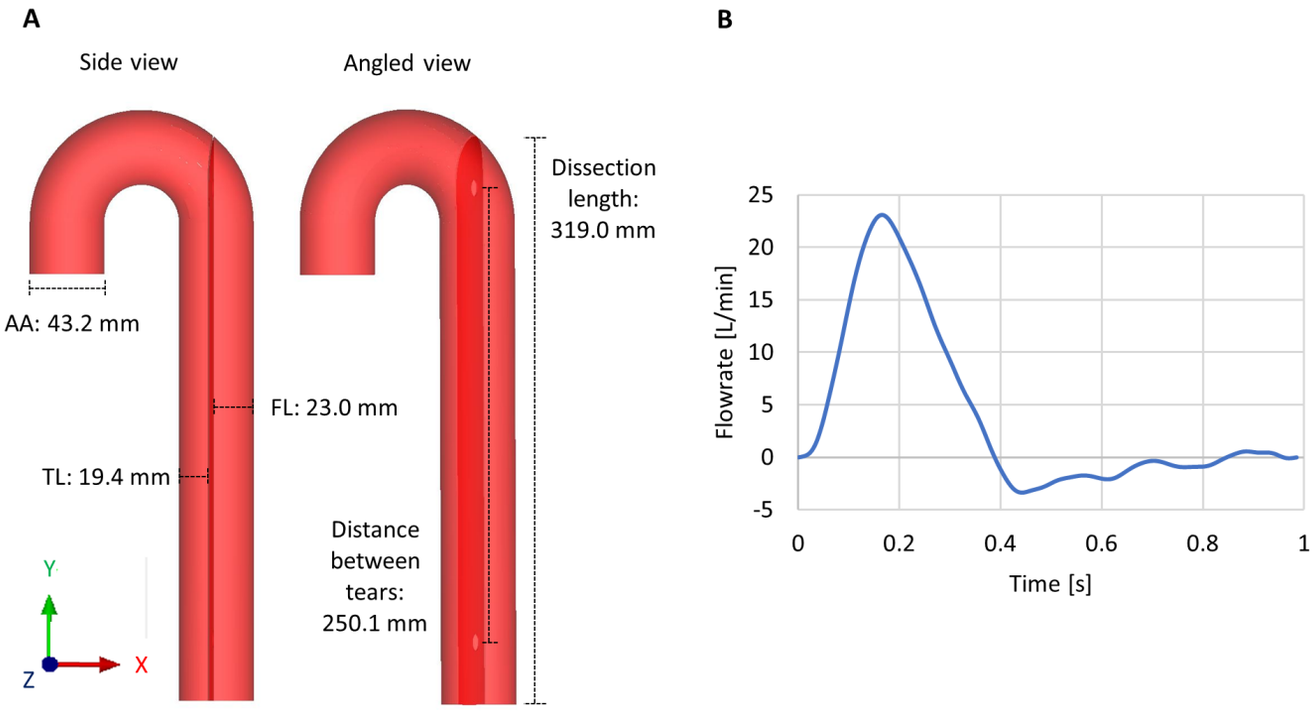

Figure 7.1: A: Idealised geometric model. Diameters of the ascending aorta (AA), true (TL) and false lumen (FL), dissection length and distance between tears are indicated. B: Inlet flowrate used in simulation of the idealised geometry (Chong et al. 2020).

geometry.

7.1 Methodology

A 3D phantom geometry previously presented in the work of Chong et al. (2020) was used for initial evaluation of the model. The idealised geometry consisted of a 180 degree arch from the ascending to descending aorta, with the TL and FL separated by a crescent shaped intimal flap of thickness 0.8 mm. Figure 7.1A shows the geometry with relevant dimensions noted. The geometry was meshed following the methodology presented in Section 3.5, with mesh sensitivity tests conducted to ensure a mesh independent solution, further details of which can be found in Appendix A.4. A final mesh of 2.4 million elements was chosen. Following the preliminary analysis on the idealised geometry, the geometry (and mesh) of PII studied in Chapter 5 was used for patient-specific evaluation of the simplified thrombosis model.

For the idealised geometry an inlet flowrate (shown in Figure 7.1B) taken from Chong et al.

(2020) was applied in the form of a flat velocity profile which had a period of 0.985 s and a peak systolic flowrate of 23.1 L/min. The bottom of the FL was treated as a wall, with the bottom of the TL being the only outlet in the domain. A 3-element Windkessel model was applied at this outlet with parameters ($R1 = 6.6242 \times 10^6$ Pa s m^{-3}; $R2 = 1.8233 \times 10^8$ Pa s m^{-3}; $C = 9.4731 \times 10^{-9}$ m^3 Pa^{-1}) taken from Chong et al. (2020). For the patient-specific model, the same flat inlet velocity profile and outlet 3EWK models and parameters used in Chapter 5 taken from Dillon-Murphy et al. (2016) were applied. In all simulations the flow was assumed to be laminar and the blood was modelled as non-Newtonian through the Quemada model presented in Section 3.2.

Initial evaluation of the model parameters was conducted using the idealised geometry. BP is clearly necessary to represent the thrombus and therefore must be kept in all simulations. Coagulant is an important species that can both build up and be consumed and is driven by shear rate which is the basis of the model, and strongly influences where BP forms. Therefore the focus of the study was assessing the need to model AP, RP and RT. As AP and RP are modelled through similar equations and are dependant on each other through reactions 1 and 2, simulations were run by removing both of them at the same time, rather than individually. For each simulation, thrombus growth time, final thrombus volume and growth patterns were compared. The original model was first run until no significant change in thrombus volume was observed, which in this case was 20 cycles. Each subsequent simulation was then run for 20 cycles also to compare results. Once tests were complete with the idealised geometry, the original and simplified models were run using the patient-specific geometry. Again, the original model was run first until thrombus growth had plateaued, which occurred after 16 cycles. The simplified model was then also run for 16 cycles to compare to the original model, and also to evaluate if the effect of model reduction is dependant on model geometry. All simulations in this study used a time step of 0.005 s.

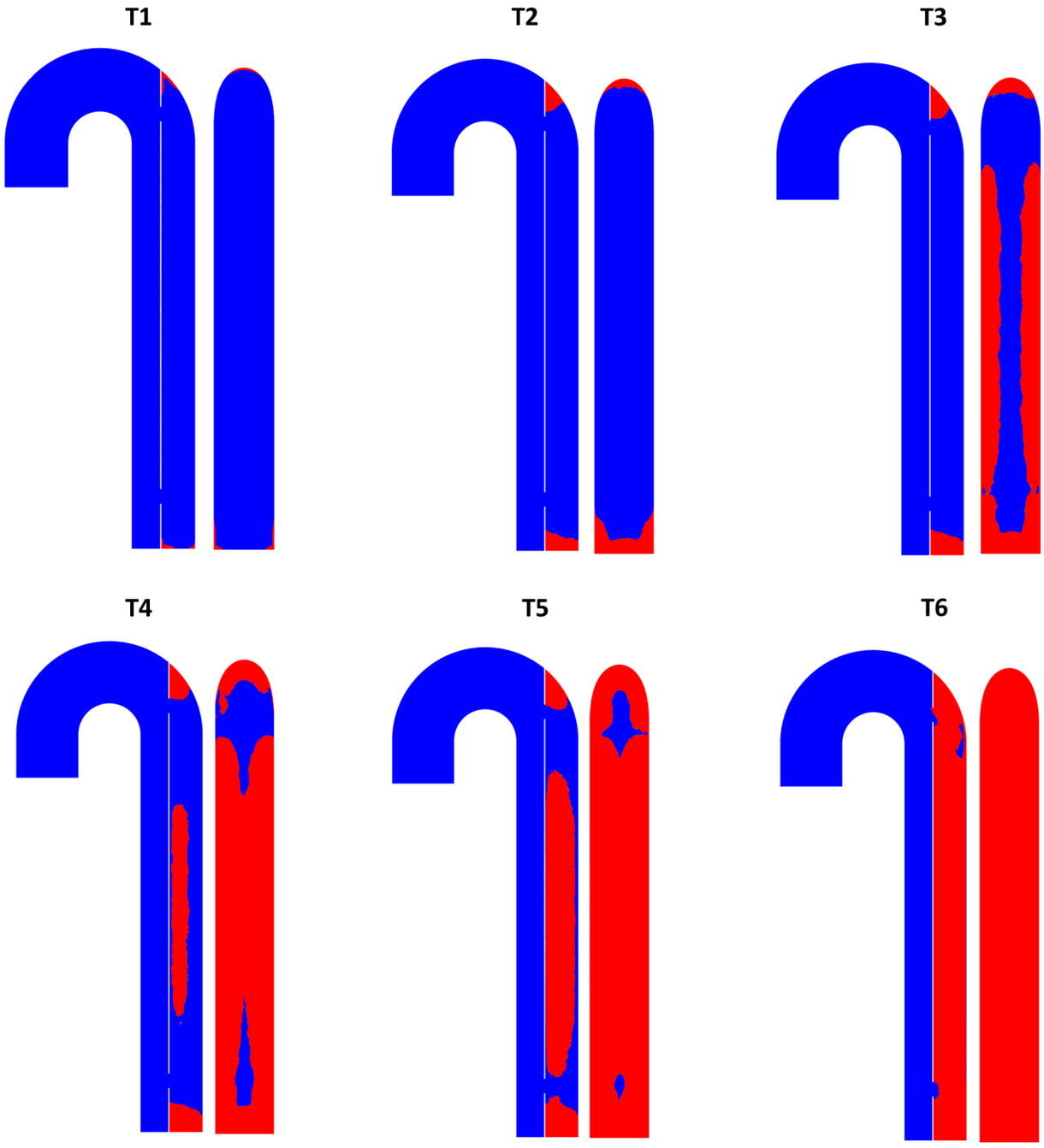

Figure 7.2: Thrombus (shown in red) growth patterns with the original model after T1: 6, T2: 10, T3: 13, T4: 14, T5: 16 and T6: 20 cycles. For each time point the central aorta x-y plane is shown on the left and the central FL y-z plane is shown on the right.

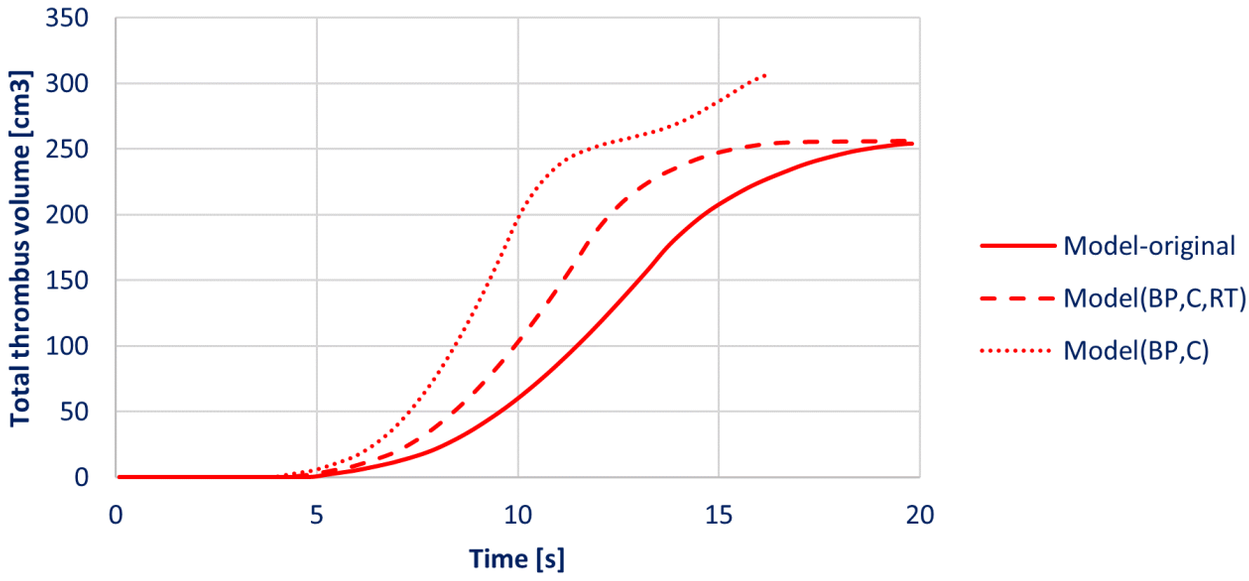

Figure 7.3: Total thrombus volume as a function of time for the original model (Model-original), model without activated and resting platelets (Model(BP,C,RT)), and model without activated and resting platelets and residence time (Model(BP,C)) in the idealised geometry.

7.2 Results

7.2.1 Idealised geometry

The original thrombus model (Model-original) was run and thrombus growth was observed to stabilise after 20 cycles. Growth patterns throughout the simulation (after T1: 6, T2: 10, T3: 13, T4: 14, T5: 16 and T6: 20 cycles) on the central aorta x-y plane and the central FL y-z plane can be seen in Figure 7.2. Thrombus growth began in the upper and lower sections of the FL. Growth then began on the anterior and posterior sides of the FL wall, gradually filling inwards. The centre on the FL between the two tears showed complete thrombosis first and the remaining regions near the tears then slowly thrombosed before complete thrombosis of the FL was achieved. Figure 7.3 shows total thrombus volume as a function of time for the original model (along side other tested models). It can be seen that initial growth was slow, growth then accelerated between cycles 5 and 11 before slowing down and reaching a plateau at 20 cycles.

AP and RP were then removed from the model. Thrombus growth began to develop as observed with the original model, however at a significantly slower pace. Figure 7.4A shows thrombus

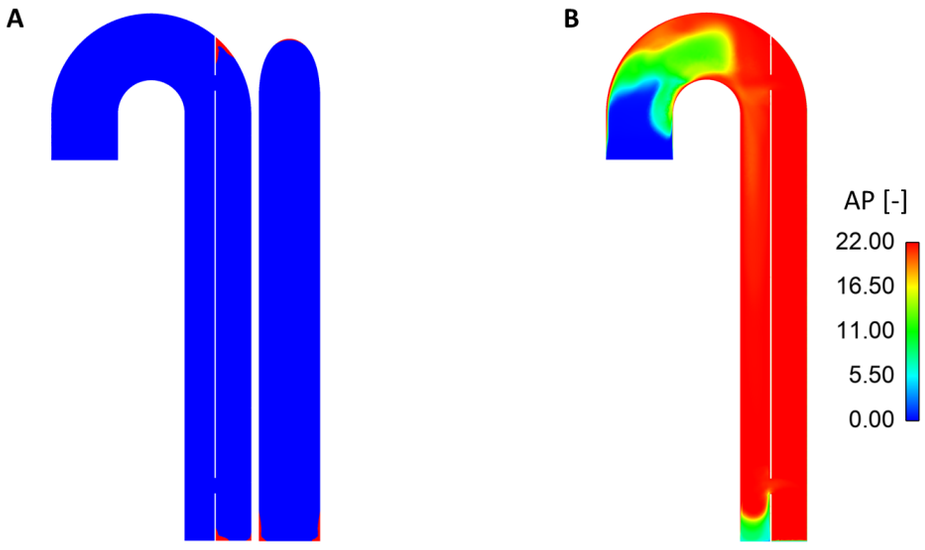

Figure 7.4: A: Thrombus growth (shown in red) after 20 cycles without activated and resting platelets modelled and no adjustment to kinetic constants k_{BP}, k_C and k_{C2}. The central aorta x-y plane is shown on the left and the central FL y-z plane is shown on the right. B: Average AP distribution over cycle 3 in the original model. AP is modelled relative to the inlet concentration hence it is dimensionless.

growth beginning in the upper and lower FL regions in the model without AP and RP, but that is after 20 cycles while this same point was reach after 6 cycles with the original model. Equations 3.18 and 3.14 show that BP and C are dependant on AP concentration, therefore to increase the growth rate when AP was removed, the kinetic constants k_{BP}, k_C and k_{C2} were increased, creating Model(BP,C,RT). Figure 7.4B shows average AP distribution after cycle 3 in the original model - cycle 3 is the first cycle where the thrombus model is in full operation following 2 initialisation cycles. It can be seen that AP concentration is high in the FL, with an average value of 20.7. Therefore, k_{BP}, k_C and k_{C2} were increased by a multiple of 21 and the simulation was re-run. Figure 7.5 shows thrombus growth patterns throughout the simulation for this accelerated Model(BP,C,RT), and growth patterns match very well with the original model. The only noticeable difference between these two models, which is clear from the graph in Figure 7.3, is the number of cycles taken for thrombus growth to plateau (roughly 17 vs the original 20).

Given these results showed that AP and RP only influenced the rate of thrombus growth rather than its total volume or growth pattern, AP and RP were kept out of the model and in addition RT was also removed, creating Model(BP,C) - k_{BP}, k_C and k_{C2} were also kept increased by

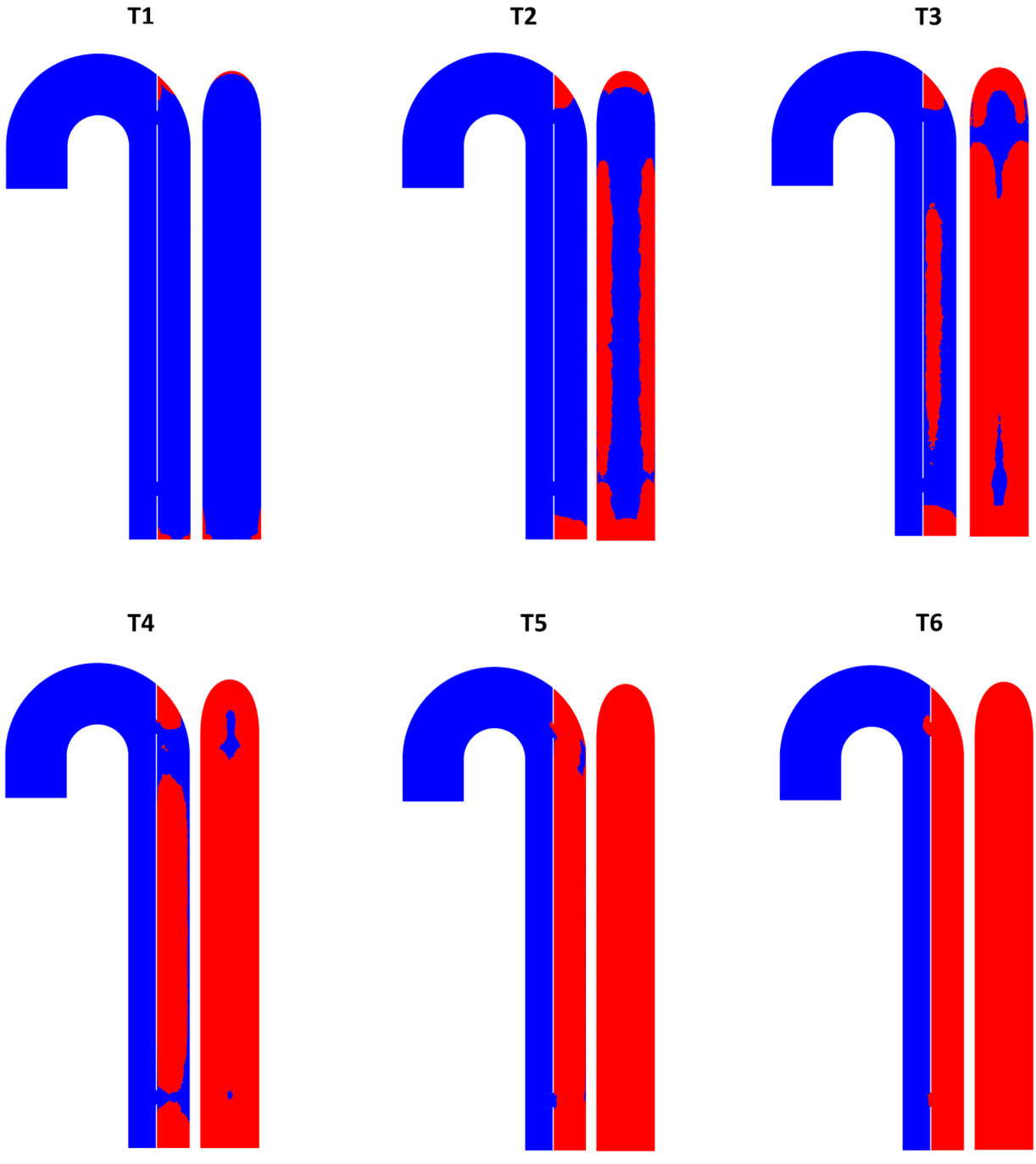

Figure 7.5: Thrombus (shown in red) growth patterns without activated and resting platelets modelled (Model(BP,C,RT)) after T1: 6, T2: 10, T3: 13, T4: 14, T5: 16 and T6: 20 cycles. For each time point the central aorta x-y plane is shown on the left and the central FL y-z plane is shown on the right.

a factor of 21 in this model. Figure 7.6 shows growth patterns for this model throughout the simulation, and total thrombus volume over time is also shown in Figure 7.3. It can be seen that thrombus growth within the FL follows the same patterns as the original model and Model(BP,C,RT) to begin with but at a faster rate, with near complete thrombosis of the FL

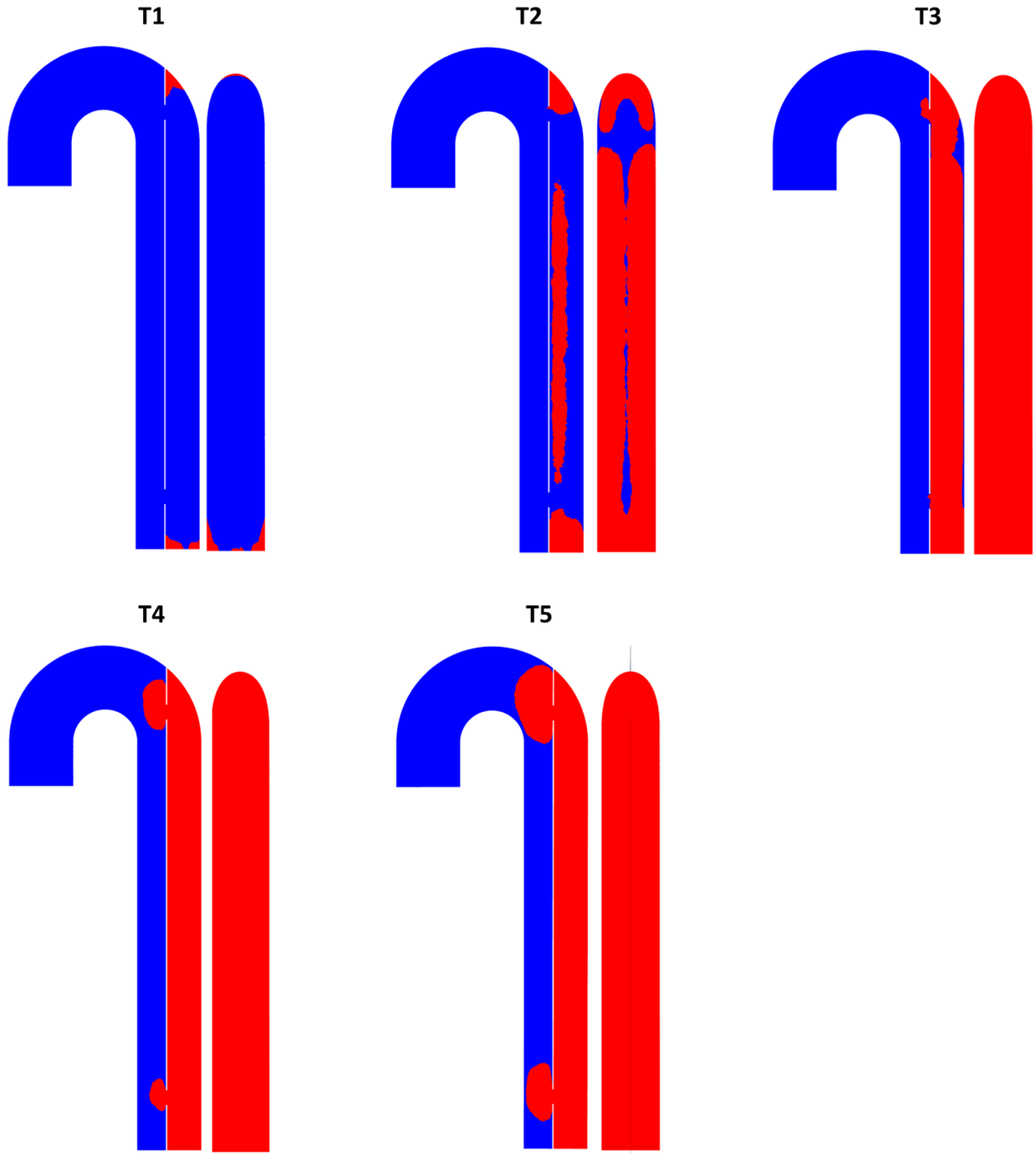

Figure 7.6: Thrombus (shown in red) growth patterns without activated and resting platelets and residence time modelled (Model(BP,C)) after T1: 6, T2: 10, T3: 13, T4: 14 and T5: 16 cycles. For each time point the central aorta x-y plane is shown on the left and the central FL y-z plane is shown on the right.

achieved after 13 cycles. However, thrombus then continued to grow into the TL. The distal end of the aortic arch was occluded with thrombus by the end of cycle 16, at which point the simulation stopped due to uncontrollable pressures given blood could not flow out of the domain.

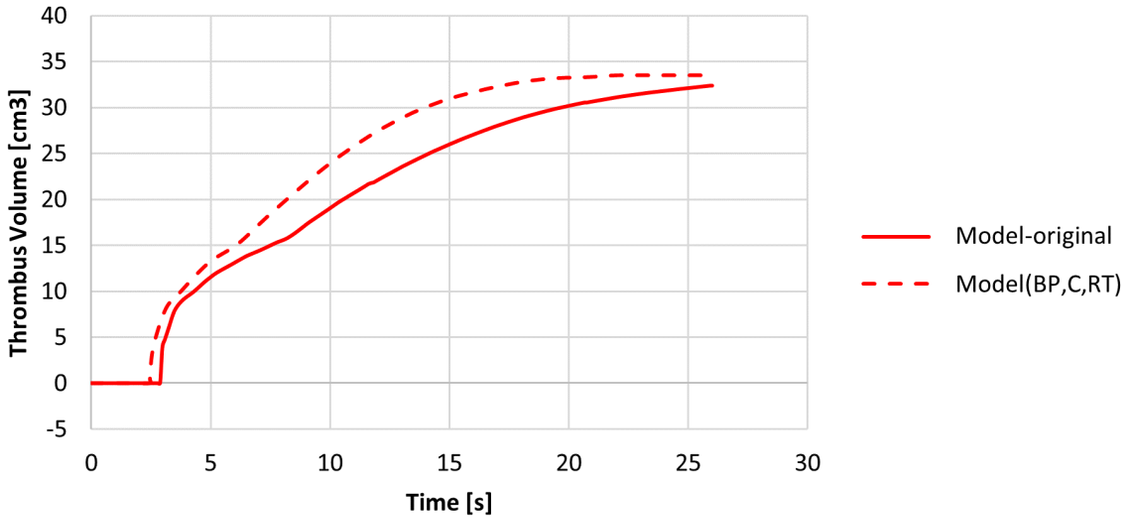

Figure 7.7: Total thrombus volume as a function of time for the original model (Model-original) and model without activated and resting platelets (Model(BP,C,RT)) in the patient-specific geometry.

7.2.2 Patient-specific geometry

The idealised geometry tests demonstrated that Model(BP,C,RT) in which AP and RP were removed was able to predict complete FL thrombosis in line with the original model results, although the rate of thrombus growth was strongly influenced by the value of k_{BP}, k_C and k_{C2}. Removal of RT did not affect FL thrombus growth patterns however it did result in non-physiological thrombosis of the TL. Therefore, RT was kept in the model, k_{BP}, k_C and k_{C2} were kept multiplied by a factor of 21, and Model(BP,C,RT) was run in the patient-specific geometry of PII.

Use of the simplified Model(BP,C,RT) in the patient-specific geometry showed similar results as in the idealised geometry. Figure 7.7 shows that the thrombus volume reached a plateau value after approximately 13 cycles with Model(BP,C,RT) compared to the 16 cycles with the original model. The growth patterns throughout the FL can be seen in Figure 7.8 which shows the evolution of the FL surface in PII for both models. From this it can be seen that thrombus growth patterns and overall thrombus volume were not impacted, but thrombus growth rate was accelerated in Model(BP,C,RT).

Each simulation was partitioned and run in parallel mode using 16 cores, and Table 7.1 re-

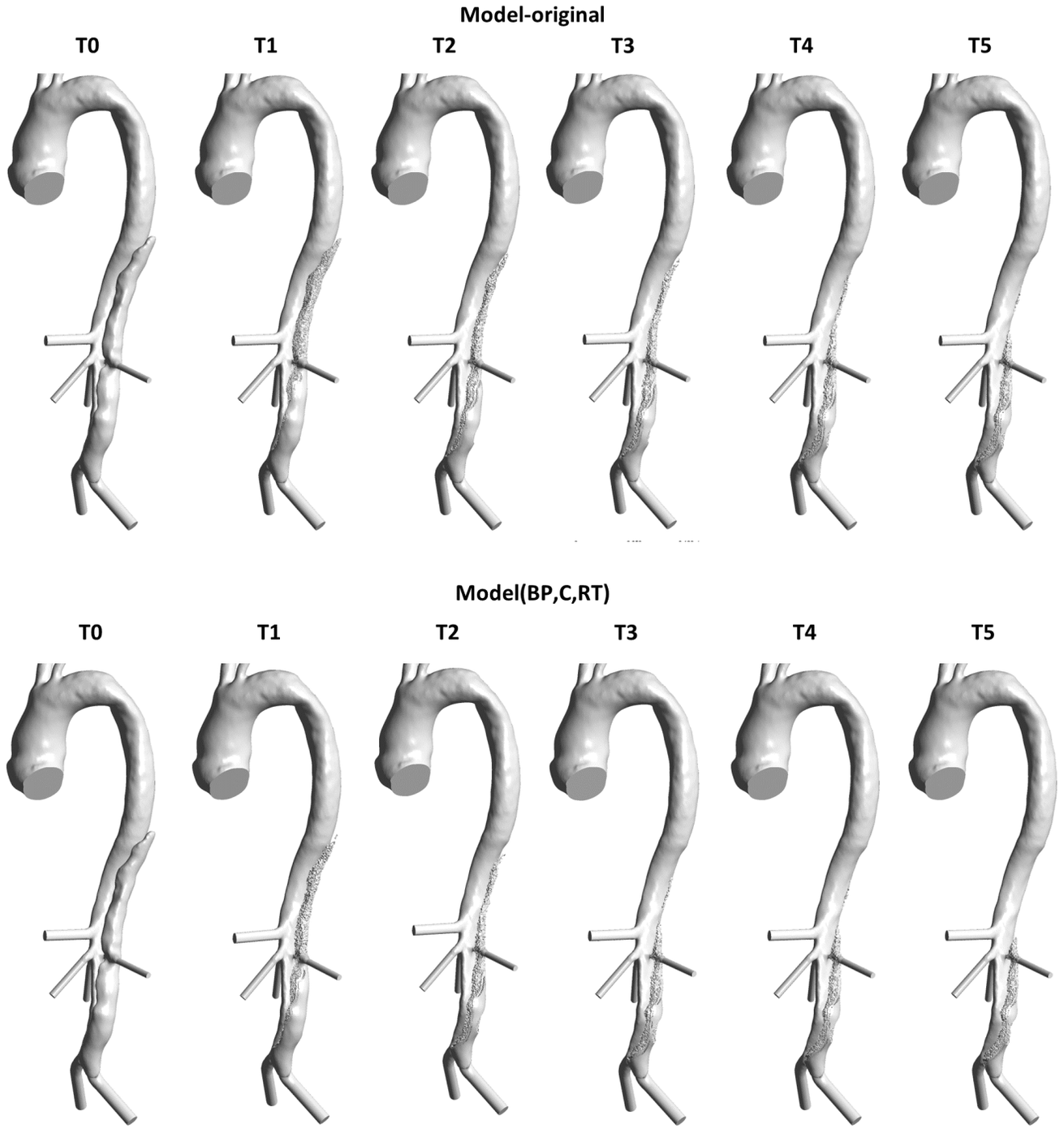

Figure 7.8: Evolution of PII false lumen surface after T1: 6, T2: 10, T3: 13, T4: 14 and T5: 16 cycles for the original model and Model(BP,C,RT).

ports the time taken for each model to reach a plateau in total thrombus volume. For the patient-specific geometry, there was no significant change in thrombus after 79 and 165 hours of simulation time for Model(BP,C,RT) and the original model, respectively, a 52% reduction in computational time.

Table 7.1: Number of hours taken for idealised and patient-specific simulations to reach a plateau in thrombus volume. All simulations were run in parallel with the idealised geometry using 12 cores and the patient-specific geometry using 16 cores.

Idealised geometry	
Model-original	168
Model(BP,C,RT)	105
Patient-specific geometry	
Model-original	165
Model(BP,C,RT)	79

7.3 Discussion

Being the desirable outcome of treatment of TBAD, understanding and predicting the thrombosis process is critical when evaluating the outcome of TEVAR. The process is complex, starting with platelet recruitment, activation and aggregation due to exposure to subendothelium cells in a damaged wall, followed by the coagulation cascade in which the thrombus forms. Throughout both stages a multitude of biochemical species are involved in a series of intertwined biochemical reactions. Kinetic based models have been developed to simulate various different steps of this process, and to varying levels of complexity depending on the number of species included (Wootton et al. 2001, Sorensen et al. 1999*b*, Anand et al. 2006, Goodman et al. 2005, Leiderman & Fogelson 2011). These have provided insight into how platelets are recruited and the cascade that follows ultimately leading to the thrombus formation using small scale idealised geometries.

The desire to be able to predict if a dissected aorta will or will not thrombose presents different challenges. Detailed understanding of the thrombosis process at the cellular level is probably not necessary, and the kinetic models which provide such details cannot realistically be applied on a large scale to patient-specific geometries due to the shear number of species and equations required. Instead simplifications must be made, as Menichini & Xu (2016) did with their hemodynamics-based model, which represented the thrombus process through resting, activated and bound platelets and coagulant, and thrombus formation was driven by shear rates and residence times. The model was able to accurately predict thrombus patterns in patient-specific geometries (Menichini et al. 2016, 2018). However, running the model in parallel with 16 cores

as has been done in work to date, simulations take approximately 1-2 weeks to complete, depending on the geometry and amount of thrombus forming. This simulation time is still too long, so the motivation of this study was to simplify the model to explore the possibility of further reducing the model equations through evaluation of the modelled parameters first using idealised geometries and second using a patient-specific case.

The idealised geometry tests showed that equations describing the transport of AP and RP can be removed without affecting the predicted thrombus pattern. The only impact of their removal is on the rate of thrombus formation. If the values for k_{BP}, k_C and k_{C2} were kept the same as in the original model the thrombus formation rate was much slower. Given the source terms of BP and C (Equations 3.18 and 3.14) are dependant on AP concentration, the removal of AP and RP effectively means the C and BP source terms are multiplied by 1 rather than a value greater than 1, hence the the significantly reduced thrombus growth shown in Figure 7.4A after 20 cycles. From the idealised geometry tests the average AP concentration in the FL was approximately 21 hence k_{BP}, k_C and k_{C2} were multiplied by a factor of 21 in this study. This increase in these kinetic constants contributed to an increase in the rate of thrombus growth, with total thrombus volume reaching a plateau value after approximately 16 cycles with Model(BP,C,RT) as opposed to 20 with the original model. The increase is growth rate may also partially be due to the fact that BP is dependant on the switching function of AP (Equation 3.20). This switching function tends to 1 when AP concentrations are high, but of course never reaches 1. Therefore, when AP is modelled the switching function of AP will always be equal to a number less than 1, therefore slowing growth compared to the model without AP. Similar results were observed in the patient-specific model, with the thrombus volume reaching a plateau after approximately 13 cycles with Model(BP,C,RT) compared to 16 cycles with the original model.

The increase in k_{BP}, k_C and k_{C2} resulted in a reduction in the number of cycles required to reach total thrombus volume and therefore less computational time being required. However, part of this reduction in simulation time can be attributed to the fact that removing AP and RP means two fewer species modelled through convection-diffusion-reactions are required to be numerically solved in the domain. The model was run in the patient-specific geometry with AP

and RP removed but with no change to the value of k_{BP}, k_C and k_{C2}. The simulation took 95 hours to complete 16 cycles. Compared to the 165 hours for the original model this represented a reduction in computational time of 42%. After these 16 cycles, the same extent of thrombosis as the original model had not yet been achieved (as demonstrated in Figure 7.4 with the idealised geometry) and additional cycles would be required to reach the final thrombus volume. However, this test demonstrates the reduction in computational time due to removal of AP and RP and their respective equations. The further 10% reduction in time with Model(BP,C,RT) which took 76 hours to achieve the final thrombus volume can therefore be attributed to the increased k_{BP}, k_C and k_{C2} values. This is a good improvement in computational time and a step toward the model being more clinically applicable.

Excluding RT in addition to AP and RP (Model(BP,C)) showed varied impact on results in different regions of the dissection. In the FL, thrombus grew in the same patterns as the original model with the expected complete thrombosis achieved, but at a quicker rate. Again, the increased k_{BP}, k_C and k_{C2} values would have contributed to the increased thrombus growth rate with Model(BP,C). Additionally, as with AP, BP growth is dependant on the switching function of RT, and therefore the removal of RT again removes a factor which has a value less than 1, thus further increasing the rate of thrombus growth. Removing RT however created problems once the thrombus growth reached the TL - thrombus continued to grow into the TL ultimately blocking the whole channel which is unphysiological. The reason for this can be explained through examination of the shear rates and relative RT (RRT) values throughout the domain.

RRT can vary between 0 and 1 and is calculated by dividing RT by the maximum value of RT in the domain. Figure 7.9 shows cycle-averaged shear rates and RRT at the various time points throughout the simulation using the original model. At the beginning of the simulation high shear rate is observed through tears which inhibits thrombus growth as the shear rate threshold set for the model is 50 s^{-1}. As thrombus grows throughout the FL the shear rate through the tears gradually reduces as less flow enters the FL. By the end of the simulation shear rates around the tear and within the TL are lower than the threshold value of 50 s^{-1}, yet thrombus does not continue to grow in this region. This is because RRT is significantly

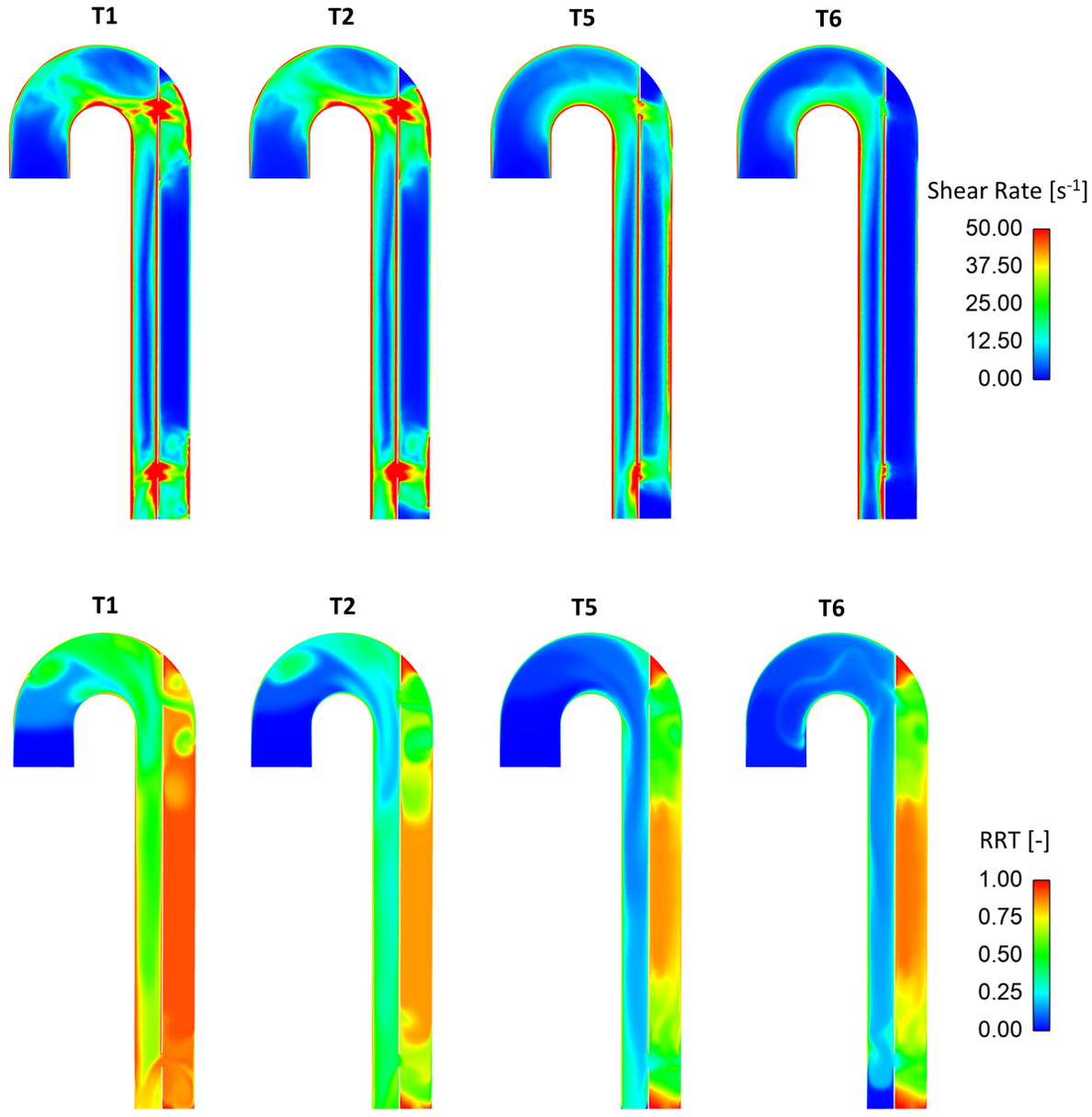

Figure 7.9: Central aorta x-y plane showing top: cycle average shear rate and bottom relative residence time (RRT) after T1: 6, T2: 10, T5: 16 and T6: 20 cycles.

lower than the threshold value of 0.85 in the TL area as can be seen in Figure 7.9. Thus, the switching function of RT in this region is tending towards 0 and thrombus growth stops. However, when RT is removed from the model the condition of low shear rate is met and there is no other controlling factor to stop the thrombus growth. Hence, the thrombus continues to grow into the TL as was observed.

The removal of RT along side AP and RP (Model(BP,C)) further reduced computational time, with complete thrombosis of the FL reached after approximately 12 cycles compared to the

original 20 cycles. It is possible to set regions of the domain as non-thrombogenic and turn off the thrombus model. With the idealised model this can easily be done - the TL can be set as non-thrombogenic and the FL thrombosis growth can be studied while taking advantage of the reduced computational time. However, this is more challenging to do in patient-specific geometries - the TL may not be as easily selected manually. Other regions in which thrombus would not physiologically occur but may meet the criteria of low wall shear and low RT, such as low flowrate side branches, would also need to be identified. However, these regions may not be identifiable until the thrombus is growing. This was the case when Model(BP,C) was tested in the PII. While initial hemodynamic analysis showed high shear rates at all side branches, thrombus growth caused the flow field to change and shear rates were reduced in the region of the FL perfused left renal artery. This resulted in unphysiological thrombosis of the left renal which occluded the branch. This method also may result in incorrect thrombus formation in patient-specific regions of the FL where shear rates are low but RT is also low. Thus, for patient-specific geometries RT should be kept in the model.

The results of this study show that AP and RP can be removed from the thrombus model with no impact on predicted thrombus growth pattern and final thrombus volume. With a carefully chosen values for k_{BP}, k_C and k_{C2}, the computational time can be substantially reduced. In this study, when AP and RP were removed the values of k_{BP}, k_C and k_{C2} were increased by a factor of 21 due to the original model hemodynamic results showing an average AP concentration in the FL of approximately 21. Additional study of the values of k_{BP}, k_C and k_{C2} would be beneficial to explore the effect of further increases of this value on thrombosis pattern and computational time.

Platelets are a critical component in the thrombosis process and therefore this model excluding the transport of AP and RP is evidently an over simplification. However, as previously stated, compromises between model complexities and model capabilities are required depending on the desired outcome of the model. In a clinical setting the activation, recruitment and reaction of platelets is not important. For treatment decision making doctors simply need to know whether and where thrombus is going to form, which this model is able to predict.

For the patient-specific case used in this study computational time to reach a stable thrombus volume was reduced from approximately 165 hours with the original model to 79 hours with Model(BP,C,RT). While simulation time will vary between patients dependant on aortic volumes and thrombus growth, and further study using a larger cohort is recommended to evaluate the simplified model in a range of complex geometries, the reduction in computational time achieved in this study most definitely makes the model more clinically applicable. Any further reduction in time is favourable for clinical applicability, and this may be possible through further evaluation of the kinetic parameters of BP and C.

7.4 Summary

The hemodynamic-based thrombus model developed by Menichini & Xu (2016) and presented in detail in Section 3.2 was evaluated in this Chapter with the aim of simplifying the model to improve computational efficiency. The results based on tests in both an idealised and patient-specific geometry showed that activated and resting platelets can be removed from the model with no impact on predicted thrombus formation, provided the kinetic constant for the thrombus growth is increased to account for the lack of high AP concentration which strongly influences thrombus growth rates. This leaves the thrombus prediction dependant on coagulant concentrations, and shear rate and residence time distributions. In the patient-specific geometry, computational time was reduced with the simplified model by 52% due to both the exclusion of two species that required modelling through convection-diffusion-reaction equations and the increased thrombus growth kinetic constant. This work advances the model in terms of applicability in the clinical setting.

Chapter 8

Application 1: The Influence of Re-entry Tears on Hemodynamics and Progression of Aortic Dissection

A key morphological parameter that has been highlighted in the literature (discussed in Section 2.6) to influence the progression of TBAD is the presence of re-entry tears. However, there are mixed conclusions regarding the impact of such tears, with conflicting results as to whether having more tears would increase (Kotelis et al. 2016) or decreases (Tolenaar et al. 2013a, 2013b) the risk of aortic growth. Some experimental, computational and animal studies have begun to explore this parameter, however previous studies were limited either due to non-physiological systems or model input data, or short time scales. Considering the current literature and the lack of well-controlled *in-vivo* longitudinal animal models, this chapter presents a study which aims to gain a comprehensive understanding of the role of re-entry tears on aortic hemodynamics in TBAD through a longitudinal study of a controlled swine model, by utilising and combining extensive medical imaging with image-based computational modelling.

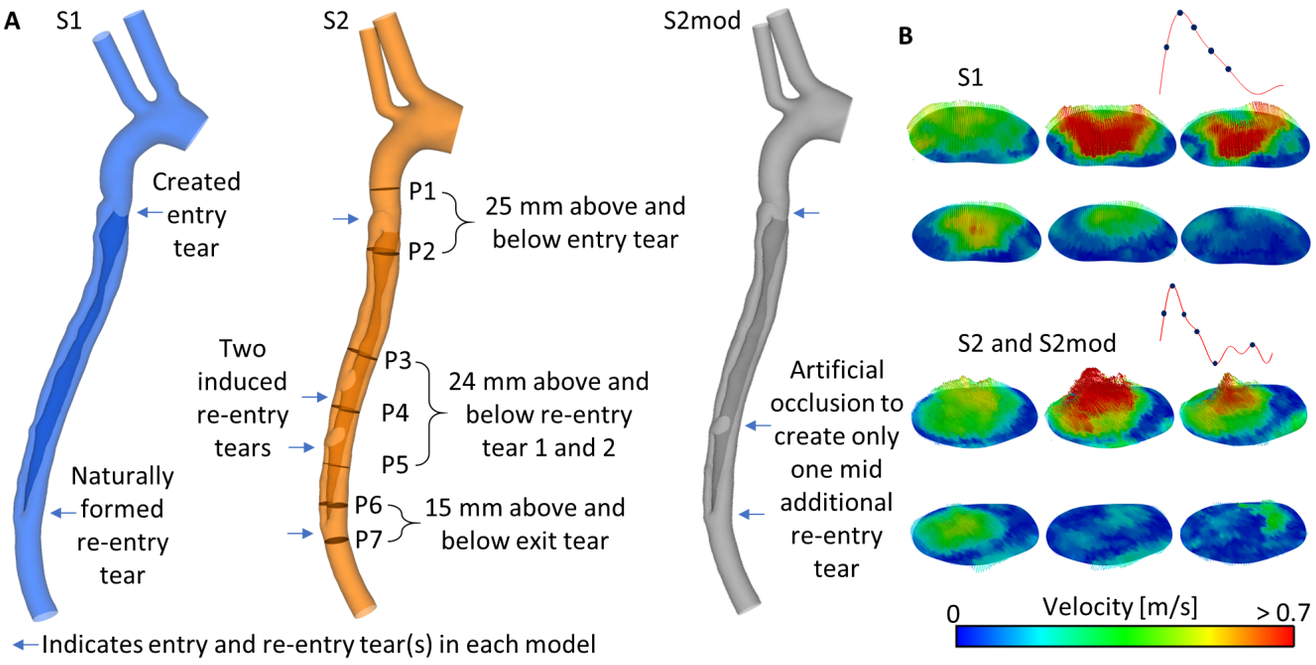

Figure 8.1: A – Geometry of S1, S2 and S2mod used for CFD. Analysis planes (P1-7) are indicated on S1. B – 3D inlet velocity profile for S1, S2 and S2mod, extracted from the 4D-flow MRI data of S1 and S2.

8.1 Methodology

One of the TBAD swine models developed and described by Guo et al. (2019) was selected for further analysis and used in the present study. Only a single swine (male, 68.5 kg, 4 months old) was included in this study and no other animals underwent the protocol described in the following section. The study was approved by the Institutional Animal Care and Use Committee of Fudan University, China (approval reference number Y2014-138). All procedures conformed to ARRIVE guidelines and the guidelines from Directive 2010/63/EU of the European Parliament on the protection of animals used for scientific purposes. In the original study (Guo et al. 2019), following the creation of the TBAD one re-entry tear naturally formed 25 cm below the primary entry tear. 20 months after the initial TBAD re-intervention was carried out and two additional re-entry tears were created in the middle section of the dissected aorta, resulting in a total of four tears. The distance from the left subclavian artery to the primary entry tear, additional re-entry tear 1, additional re-entry tear 2 and naturally formed re-entry tear was 7 cm, 21 cm, 26 cm and 32 cm, respectively. The location of each of these tears in indicated in Figure 8.1A.

Table 8.1: Information on model development: date and state of model at each scan point.

Scan	State of model
Scan 0 (S0)	1 month after the creation of TBAD
Scan 1 (S1)	9 months after the creation of TBAD
	Additional re-entry tears created
Scan 2 (S2)	1 month after re-intervention
Scan 3 (S3)	5 months after re-intervention
Scan 4 (S4)	9 months after re-intervention

After the creation of the TBAD and the additional re-entry tears, follow up scans, including CT and 4D-flow MRI, were taken at several time points as described in Table 8.1. 4D-flow MRI was performed using a 3T clinical MRI scanner (Magnetom Verio, Siemens Medical Solutions, Erlangen, Germany) with the following parameter setting: flip angle, 7 degrees; velocity encoding, 150 cms^{-1}; spatial resolution, (1.875-2.5) x (1.875-2.5) x 2.5 mm^3; temporal resolution, 39.2 milliseconds; and 14-25 frames/cardiac cycle. CT scans were performed with the Aquilion (Toshiba, Canon Medical Systems, Zoetermeer, The Netherlands) scanner, with a spatial resolution of 0.8 x (0.892-0.961) x (0.892-0.961) mm^3 and a kVp of 120.

All CT scans were processed and segmented following the geometry segmentation methodology presented in Section 3.4. Within Mimics, key morphological parameters were measured for further analysis; these included tear dimensions, distances between tears along the centreline of the geometry, and lumen volumes. Lumen volumes were calculated using Equation 8.1, where $S_{i,TL/FL}$ is the area of the TL or FL on slice i, h is the slice thickness and N is the total number of slices.

$$Vol_{FL} = \sum_{i=1}^{N} \frac{(S_{i,FL} + S_{i+1,FL}) \times h}{2} \tag{8.1}$$

To investigate the influence of re-entry tears in detail, two scans were chosen for further CFD analysis – S1 (9 months post dissection creation) and S2 (1 month post re-intervention and creation of two additional re-entry tears). Furthermore, an additional geometry, S2mod, was created in which the first re-entry tear in S2 was artificially occluded, thereby creating a model with only one additional tear. The final geometries of S1, S2 and S2mod can be seen in Figure

8.1A. The models were meshed following the methodology of Section 3.5, and mesh sensitivity tests were conducted to ensure that differences in mean and maximum velocity and wall shear stress on multiple planes throughout the dissection between the chosen mesh and a finer mesh were less than 5%. Further details on the mesh sensitivity test results can be found in Appendix A.5. The final meshes contained 3.9, 5.6 and 5.6 million elements for models S1, S2 and S2mod, respectively.

4D-flow MRI data acquired at each follow-up were processed using the methodology described in Section 4.1 to derive inlet velocity profiles, containing all three velocity components. Figure 8.1B shows the flow waveforms for S1 and S2 and the corresponding 3D inlet velocity profiles. Additionally, from the 4D MRI data, the flow distribution to the arch branches and the descending aorta was estimated. This was done by calculating the difference in flow through planes placed immediately before and after the arch branches, and splitting the flow between the two branches based on their cross-sectional areas.

Based on the experimental study by Rosentrater & Flores (1997), the swine blood was assumed to have a constant density of 1022 kgm^{-3} and was modelled as a non-Newtonian fluid dictated by Equation 8.2, where η is the viscosity, $\dot{\gamma}$ is the shear rate, $K = 0.08Pa.s^{\mathrm{n}}$ and n=0.55.

$$\eta = K \times \dot{\gamma}^{n-1} \tag{8.2}$$

The flow was assumed to be laminar based on the calculated peak Reynolds number (1400 for S1, 2400 for S2/S2mod – 2400) and critical Reynolds number (5000 for S1, 3400 for S2/S2mod) for transition to turbulence (Kousera et al. 2012). 3EWK models were applied at the three outlets of all models, with parameters tuned following the methodology of Section 3.6, based on flow split determined from the MRI data and invasive doppler-wire (DW) pressure readings taken during S3. The wall was assumed to be rigid, a time-step of 0.001 s was used, and all simulations were run for seven cardiac cycles to ensure a periodic solution. The final cycle was used for analysis. Based on the morphological measurements, 7 planes were selected for detailed analysis. These planes are defined in Figure 8.1A (in model S2) along with distances relative to nearby tears – all planes were perpendicular to the aorta wall and were fitted along

Table 8.2: Top – True (TL) and false (FL) volume percentage changes between follow up scans. Middle – maximum axial diameter of entry and naturally formed distal re-entry tear on scans S0-S3. Bottom - maximum sagittal diameter of created re-entry tear 1 and re-entry 2 two on scans S2 and S3.

Scan	**TL volume change (%)**	**FL volume change (%)**
S0 → S1	12.4	3.6
S1 → S2	14.1	19.7
S2 → S3	2.5	0.6
S3 → S4	-11.8	-6.2
S0 → S4	3.1	13.0
Scan	**Entry tear max axial axial diameter (mm)**	**Distal re-tear max axial diameter (mm)**
S0	19.3	8.8
S1	21.0	9.5
S2	21.8	12.1
S3	21.5	11.6
S4	21.8	9.9
Scan	**Re-entry tear 1 max sagittal diameter (mm)**	**Re-entry tear 2 max sagittal diameter (mm)**
S2	12.4	8.6
S3	13.6	8.8
S4	13.3	8.7

the centreline of each model. Flow distribution, reverse flow index (RFI), velocity, TAWSS and pressure were evaluated for all models. RFI was calculated through Equation 8.3 (Birjiniuk et al. 2017).

$$RFI = 100\% \times \frac{|\int_0^{\mathrm{T}} Q_{reverse}\, dt|}{|\int_0^{\mathrm{T}} Q_{reverse}\, dt| + |\int_0^{\mathrm{T}} Q_{forward}\, dt|} \tag{8.3}$$

where $Q_{forward}$ is flow down the aorta towards the bifurcation, $Q_{reverse}$ is flow up the aorta towards the aortic arch, and T is the cardiac cycle period.

8.2 Results

8.2.1 Morphological Changes

Table 8.2 shows the percentage change in TL and FL volumes between each scan. Between S0 and S1, during which the dissection would have been in the early stages with a compliant intimal

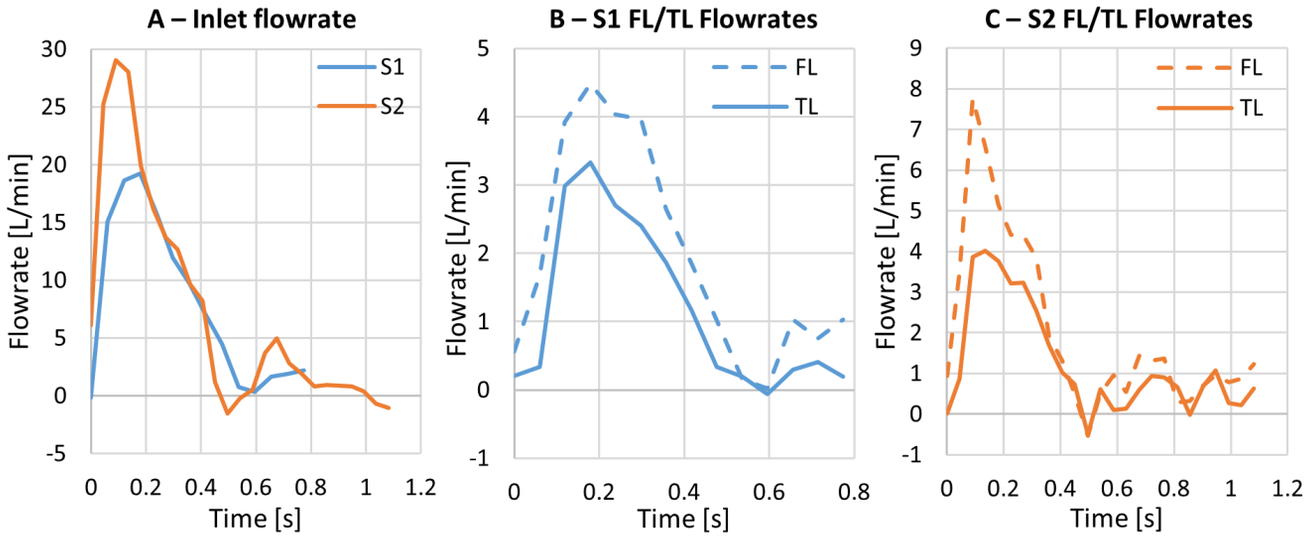

Figure 8.2: A - Inlet flowrate extracted from 4D MRI scan of S1 and S2. B - True (TL) and false (FL) lumen flowrates extracted from 4D MRI data of S1. C – TL and FL lumen flowrates extracted from 4D MRI data of S2. TL and FL flowrates in B and C were evaluated on plane 2, the location of which is shown in Figure 8.1.

flap, the TL showed obvious expansion while the FL volume change was minimal. Between S1 and S2 both the TL and FL expanded substantially. Between S2 and S3 there was very little change, followed by a reduction in volume between S3 and S4. Thus, after the creation of the additional tears (S2 onwards) there was slowing of the FL expansion and eventual FL reduction. All expansion and reduction in the TL and FL was uniform throughout the dissection – there were no local aneurysmal areas. Table 8.2 also reports the measured dimensions of the entry, created re-entry tears and naturally formed distal re-entry tear across the scans. It can be seen that the entry tear did not significantly change in size, while the naturally formed distal re-entry tear slowly expanded between S0 to S2 before reducing in size from S2 to S4. Both created re-entry tears initially grew from their original size of 5 mm and then remained a constant size between S2 and S4.

Table 8.3: Percentage of inlet flow reporting to each outlet, measured from 4D MRI data.

	S1 (%)	**S2** (%)
Arch branch 1	37.2	32.2
Arch branch 2	28.0	19.2
Descending aorta	34.9	48.6

8.2.2 MRI-based Flow Analysis

Figure 8.2 shows the volumetric flowrates derived from the 4D MRI data acquired at S1 and S2. The inlet flowrate is shown, as well as the TL and FL flowrates, measured on plane 2 (the location of which is shown in Figure 8.1). From this data it can be seen that the cardiac cycle at S1 was shorter than that at S2 (0.78 s and 1.08 s, respectively), while S2 had a higher peak inlet flowrate, and S1 a shorter diastolic phase. In both models the flow in the FL was measured to be higher than the flow in the TL. The flow distribution to the arch branches and the descending aorta is reported in Table 8.3, which shows that a higher percentage of inlet flow continued to the descending aorta in S2 than in S1, and more flow went through arch branch 1 than 2.

8.2.3 Computational Flow Analysis

Validation. First, computational results were compared with the corresponding 4D-flow MRI measurements. Figure 8.3 shows the 4D-flow MRI derived velocity fields at peak systole (Figure 8.3A) and the respective velocity streamlines for simulations S1 and S2 (Figure 8.3B). In both cases, velocity patterns matched well, with high velocity jets being captured through the entry tear and fairly regular flow elsewhere. Quantitative comparison was made following the methodology of Puiseux et al. (2019), in which a linear correlation between the MRI-measured and CFD-predicted peak systolic velocity magnitudes on a given plane was calculated. Figure 8.3C shows the selected planes around the entry tear in S1 and the correlation values. In general, better correlations were obtained above and across the entry tear than immediately below the tear.

Flow distribution. Flow in the TL and FL was evaluated by calculating the percentage of descending aorta flow passing through each lumen at the analysis planes defined in Figure 8.1A. As shown in Figure 8.4A, the presence of additional tears changed the FL/TL distribution. Near plane 2 (25 mm below the entry tear), TL flow was higher than FL flow in S1 but the trend was reversed in S2 and S2mod. In S2 and S2mod, moving down the aorta the flow redistributed

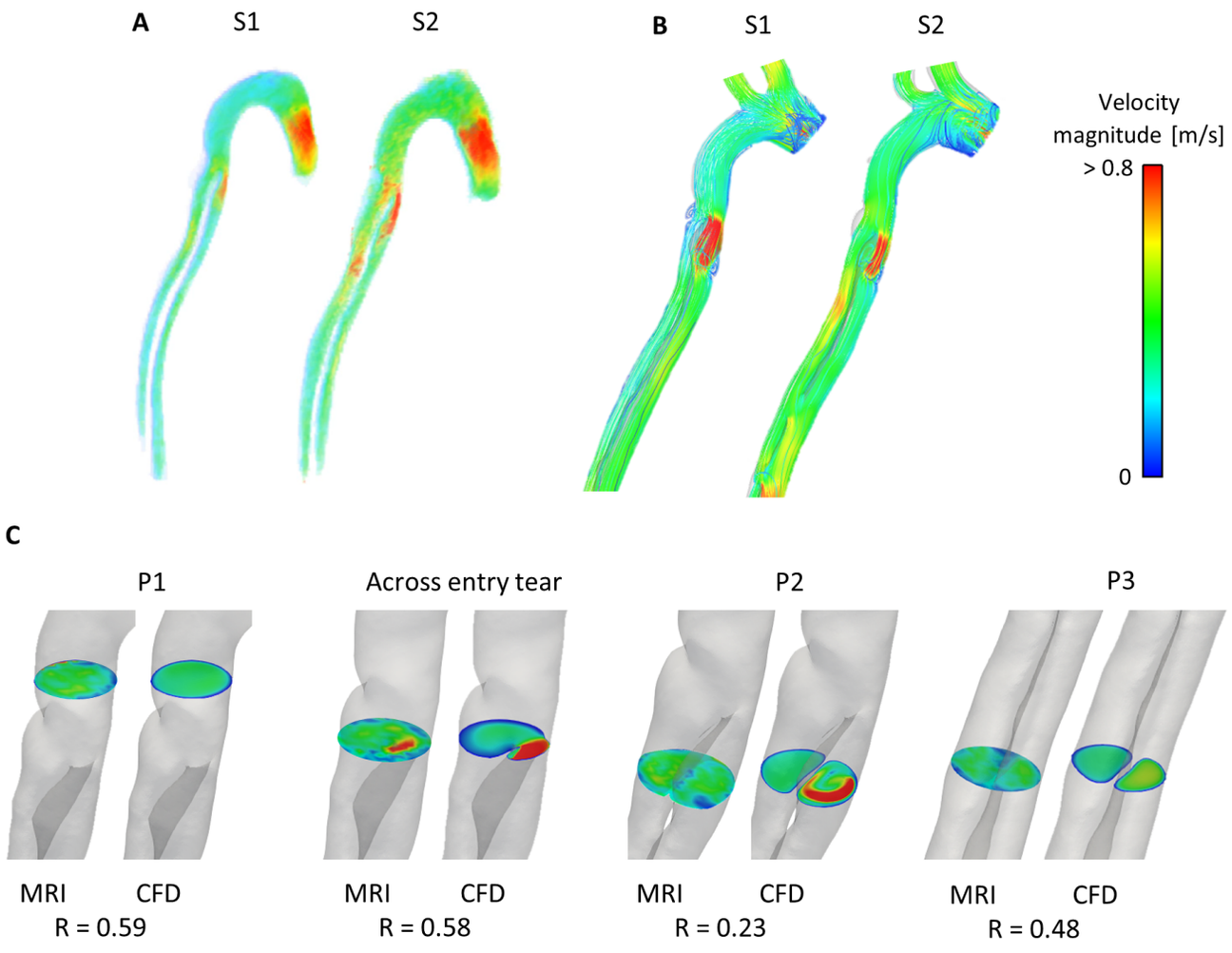

Figure 8.3: A - Peak systolic velocity magnitude derived from 4D MRI data of S1 and S2. B - Peak systolic velocity from CFD simulations of S1 and S2. C - MRI and CFD data on planes P1, P2 and P3 (the location of which is shown in Figure 8.1A) and across the entry tear for S1. R - linear correlation value between MRI and CFD.

from the FL to the TL through the additional tears. At the distal end of the dissection (plane 6) there was higher TL flow in all models. The presence of only one additional tear compared to two (S2mod vs S2) resulted in approximately 10% less flow entering the FL and redistributing to the TL, however the overall trend throughout the aorta did not change.

Figure 8.4B shows the comparison of RFI evaluated for all models on the analysis planes. As defined by equation 3, RFI measures the amount of flow travelling up the aorta. In general, S1 saw lower RFI values throughout the aorta, with a maximum value of 2.2% (equal on all planes in the FL), lower than that of S2 and S2mod at 9.9 and 4.9% (both in the upper TL), respectively. For S1, the RFI was higher in the FL than the TL at a consistent value throughout the dissection. This was not the case with S2 and S2mod – both saw higher RFI in the TL on

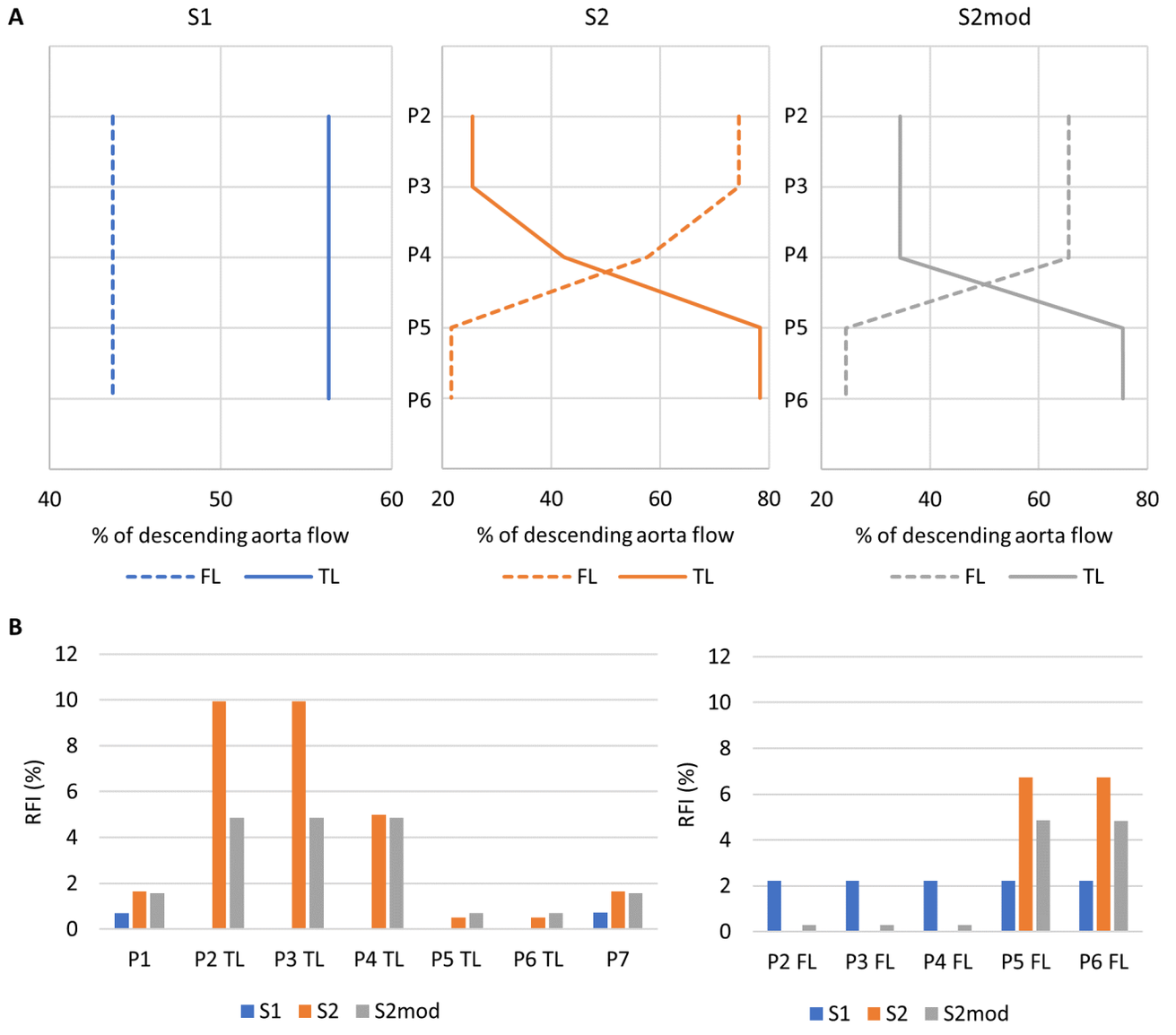

Figure 8.4: A - Distribution of descending aorta flow between the TL and FL, measured on each plane within the dissection (P2-P6) shown in Figure 8.1A for models S1, S2 and S2mod. B - Reverse flow index, calculated on each plane (P1-P7) shown in Figure 8.1A, for models S1, S2 and S2mod.

planes 2 to 4, and the trend switched on planes 5 and 6 in which the FL saw higher RFI values. Comparing S2 and S2mod, it can be seen that the number of additional tears greatly impacted the RFI. TL RFI was lower throughout the aorta in S2mod, with the largest difference of 113% on planes 2 and 3. Similar differences were seen in the FL on planes 5 and 6. Both S2 and S2mod had near zero values of RFI in the FL on planes 2-4.

RFI was also calculated on planes within each tear for all models, to evaluate the extent to which the direction of flow exchange between the TL and FL altered throughout the cardiac cycle. For the entry tear $Q_{forward}$ (Equation 8.3) was defined as flow from the TL to the FL,

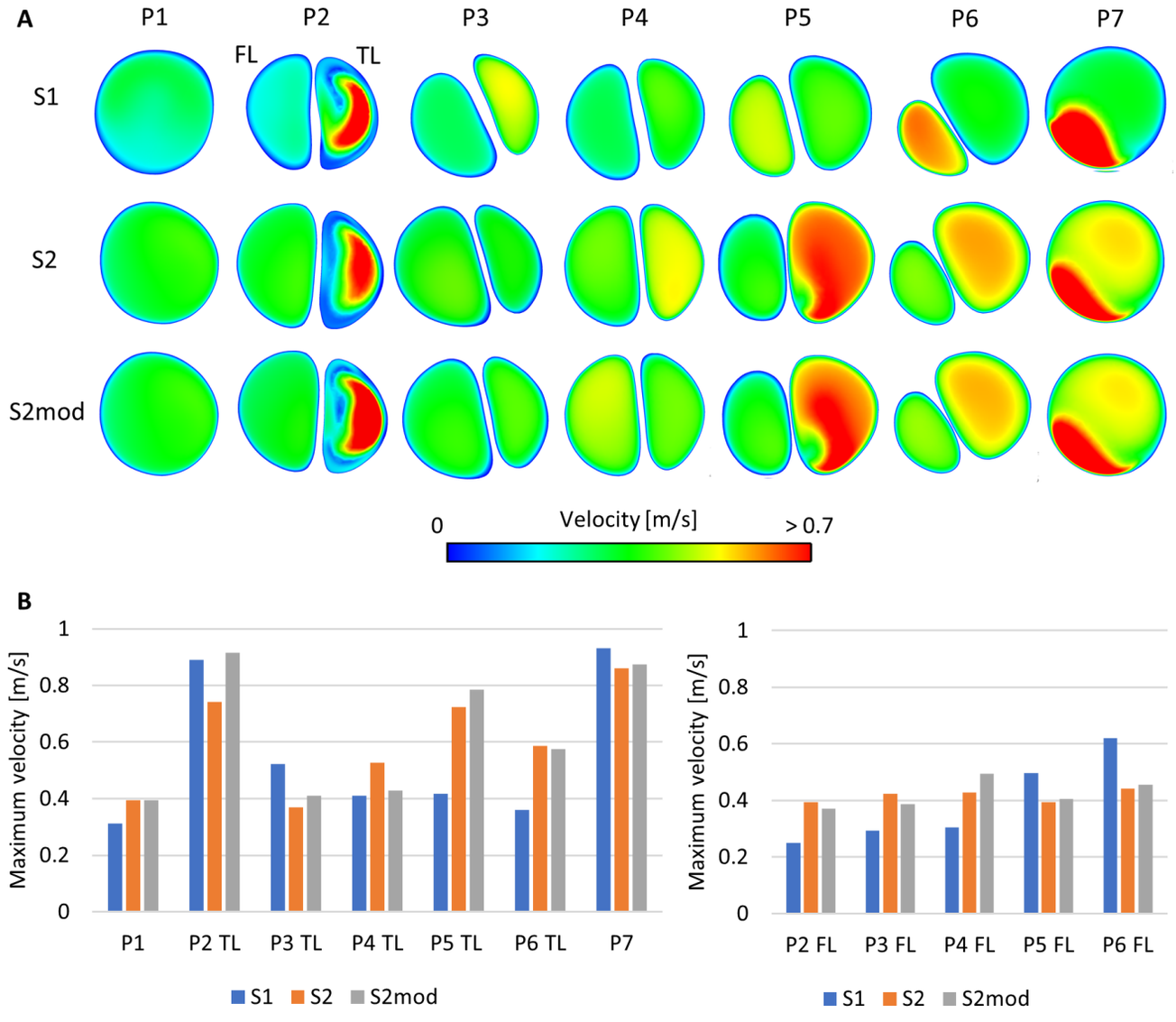

Figure 8.5: A – Peak systolic velocity contours on each plane shown in Figure 8.1A, for models S1, S2 and S2mod. B – maximum velocity on each plane shown in Figure 8.1A at peak systole, for models S1, S2 and S2mod. Values in the true (TL) and false (FL) lumen are reported on separate graphs.

while for all three re-entry tears $Q_{forward}$ was defined as flow from the FL to the TL. For S1, there was 2% RFI at both the entry and exit tear, indicating a small amount of reverse flow into the TL at the entry tear, and into the FL at the exit tear. The RFI was reduced to 0% at the entry tear for S2 and S2mod, however the exit tear RFI increased to 5% for S2mod, and to 8% for S2, with the reverse flow occurring at the beginning and end of the diastolic phase. For both S2 and S2mod the RFI through the middle re-entry tears was 0%, indicating flow was continuously from the FL to the TL throughout the cardiac cycle.

Velocity patterns. As well as peak systolic velocity streamlines shown in Figure 8.3, velocity

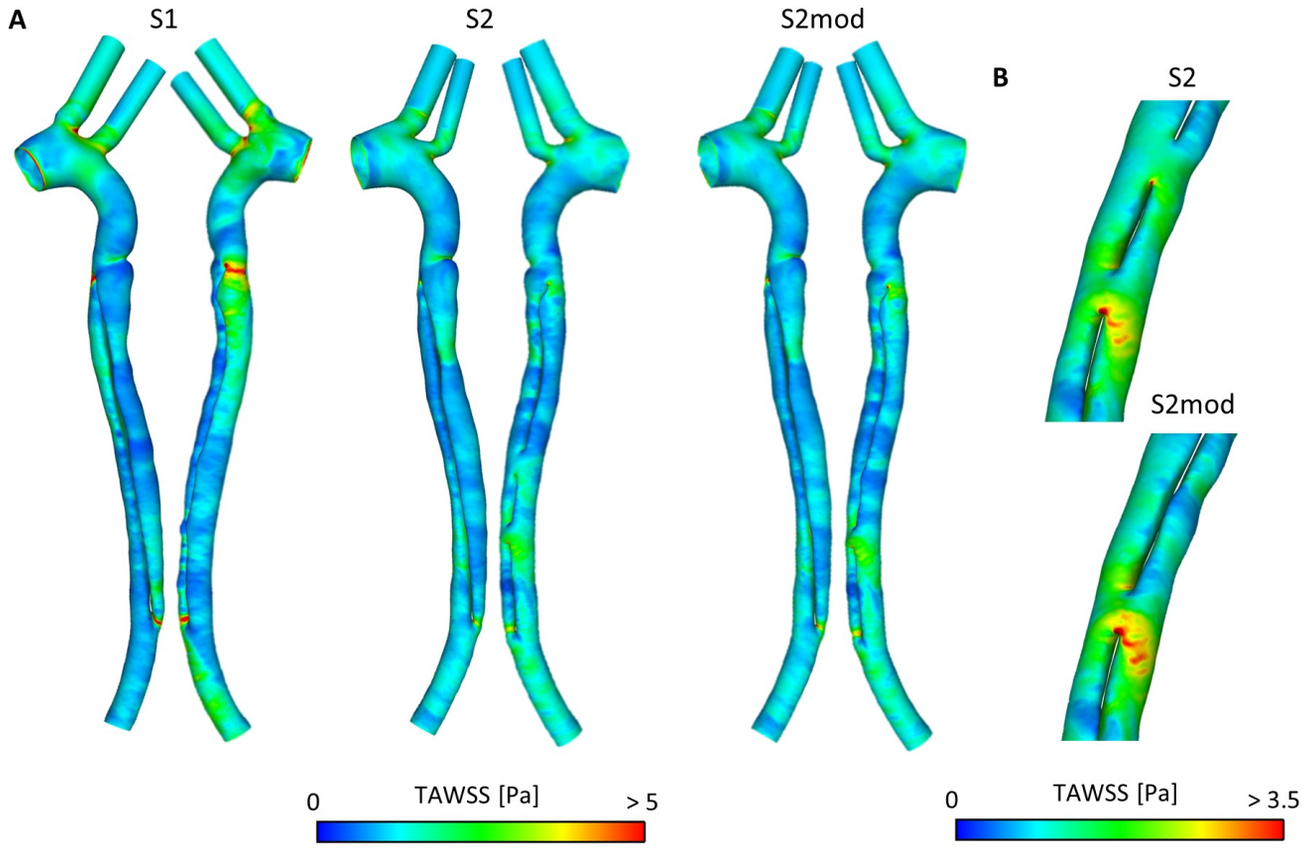

Figure 8.6: A – Time averaged wall shear stress (TAWSS) for models S1, S2 and S2mod. B – TAWSS around re-entry tears in models S2 and S2mod.

contours were visualised on each plane and these are shown in Figure 8.5A at peak systole when the largest differences among the three models were noted. Additionally, the maximum velocities on each of the selected planes are shown in Figure 8.5B. From Figure 8.5A, some key differences between the models can be seen. Varying velocity patterns were observed on plane 2 between S1 and S2/S2mod, while S2 and S2mod saw similar patterns but to a different maximum value. On planes 3 and 4, S2 and S2mod differed on which lumen had higher maximum velocity, likely due to flow redistribution occurring in S2 but not in S2mod. Towards the distal end of the dissection the effects of flow redistribution were clear, with higher velocities seen on plane 6 in the TL of S2/S2mod compared to S1, while S1 saw much higher FL velocities. Redistribution effects were also clear on plane 7, where two distinctive areas of high velocity were observed in S2/S2mod, while in S1 only the high velocity jet from the FL can be seen.

Wall shear stress. Figure 8.6 shows the TAWSS distribution for S1, S2 and S2mod. Similar levels of TAWSS can be seen across the models. As with the velocity results, the TAWSS

distributions varied as would be expected with the changes in flow distribution between the models. At the entry tear, S1 saw the highest TL TAWSS values, with a larger area of elevated TAWSS in the TL, followed by S2mod and then S2 (in line with the percentage of flow entering the TL in each model - Figure 8.4A). S2 and S2mod saw similar patterns throughout, with variations in S2mod of reduced FL TAWSS around the artificially occluded tear and increased TAWSS through the second re-entry tear. Furthermore, S1 saw the highest TAWSS values at the exit tear, compared to S2 and S2mod.

Pressure. Absolute FL pressures as well as the pressure difference between the TL and FL for each model throughout the systolic phase is shown in Figure 8.7. During mid-systolic acceleration and peak systole, S2 and S2mod saw nearly equal pressures, while S1 saw higher FL pressures at all points, by up to 6.9 mmHg. At mid-systolic deceleration the trend reversed and S1 saw lower pressures than S2 and S2mod, by up to 3.4 mmHg. The average FL pressure throughout the cardiac cycle was 54.8 mmHg, 50.8 mmHg and 50.8 mmHg for S1, S2 and S2mod, respectively. In terms of pressure difference between the TL and FL, it can be seen that apart from two locations in S2 (where the difference was close to 0) the FL had a higher pressure than the TL in all cases. In the proximal dissection (plane 2), the lowest pressure difference was observed in S2. During most of the systolic phase S1 had the largest pressure difference, followed by S2mod and then S2. This trend did not hold in the distal dissection (below plane 4) at mid-systolic deceleration, when pressure differences were below 1 mmHg.

8.3 Discussion

The number of re-entry tears has been highlighted as a potentially key parameter in dictating the progression of TBAD both pre (Kotelis et al. 2016, Tolenaar et al. 2013a, 2013b), and post TEVAR (Qin et al. 2012, Chen et al. 2017). Several experimental (Birjiniuk et al. 2019, Tsai et al. 2008, Girish et al. 2016, Rudenick et al. 2013) and computational al (Ben Ahmed et al. 2016, Zadrazil et al. 2020, Karmonik et al. 2011, Wan Ab Naim et al. 2014) studies have been conducted to determine how such tears influence aortic hemodynamics and

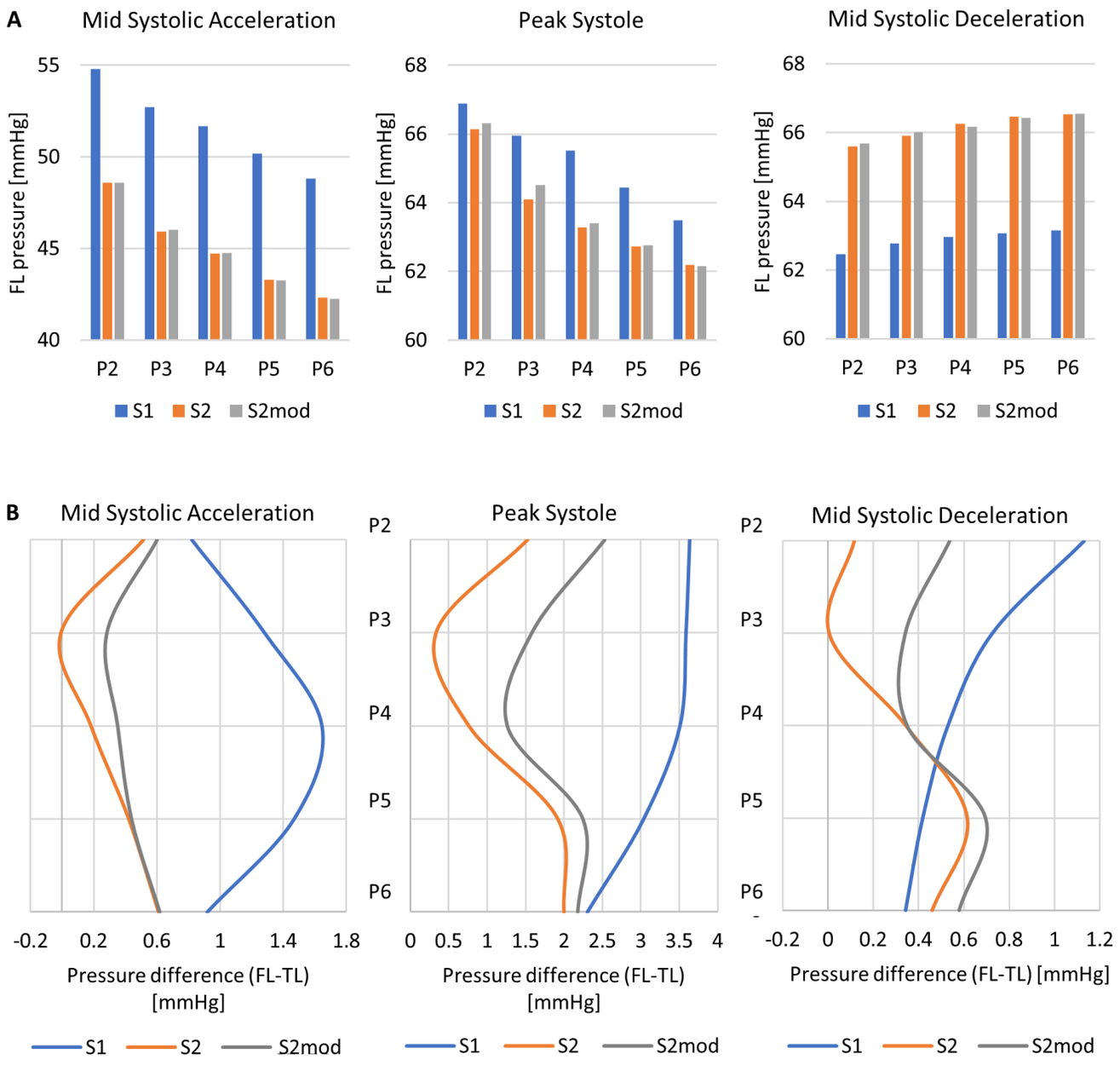

Figure 8.7: FL pressure on each plane (P2-P6) within the dissection shown in Figure 8.1A, at mid-systolic acceleration, peak systole and mid-systolic deceleration for models S1, S2 and S2mod. B – Pressure distribution throughout the aorta, on planes P2-P6, at mid-systolic acceleration, peak systole and mid-systolic deceleration for models S1, S2 and S2mod.

drive the progression. However, previous work was limited, either through idealised geometries, or generic or un-physiological boundary conditions, both of which are essential to accurately predict blood flow behaviours within the aorta.

Advancing on this work, the present study was able to combine the use of realistic geometries, extracted from CT scans, with physiological inlet velocity profiles, extracted from 4D MRI data, and accurately tuned outlet boundary conditions, based on invasive DW pressure readings.

With this combination of data, highly detailed and comprehensive computational models of TBAD, at various stages of the disease, were built. From these models, the influence of re-entry tears on aortic hemodynamics was assessed, and the results showed the strong influence of such tears on, primarily, flow redistribution and cross-lumen pressure difference.

From the results, it was seen that an increase in the number of tears allowed for flow redistribution from the FL to the TL. This is consistent with the findings of Wan Ab Naim et al. (2014), which showed that re-entry tears provide extra paths for blood flow between the lumen. Wan Ab Naim et al. (2014) reported that through the re-entry tear blood flowed from the FL to the TL during systole, and back to the FL during diastole. This pattern was only observed at the distal exit tear in this study, as the flow through the middle re-entry tears was from the FL to the TL throughout the entire cardiac cycle. The results of this study also showed that an increase in the number of additional re-entry tears increased the extent of the flow reversal at the exit tear. Therefore, despite the benefit of overall flow redistribution from the FL to the TL due to additional re-entry tears there may be a small local detrimental effect of increased backflow into the FL during diastole.

Such flow redistribution led to altered velocity patterns in the form of changes in velocity magnitudes and RFI. Birjiniuk et al. (2019) conducted an experimental study and found that the presence of additional re-entry tears significantly reduced RFI in the proximal upper FL. This is confirmed in this study, where it can be seen that the RFI decreased from 2.2% to nearly 0% with the introduction of one or two additional tears. Also in line with this study, Birjiniuk et al. (2019) found TL RFI to increase with the number of tears, as flow redirects from the FL to the TL. However, they found mixed results in the distal dissection, while this study showed a clear increase in FL RFI moving closer to the exit tear. Flow reversal would lead to oscillatory shear which in turn can cause elastin degradation (Chen et al. 2017) in the dissected media layer of the aorta wall, potentially leading to FL expansion. In a recent study by Burris et al. (2020), false lumen ejection fraction (FLEF), equivalent to the RFI calculated in this study, was derived from 4D-flow MRI data, and their results suggested that increased entry tear FLEF could be a predictor of aortic growth. This is in line with the current findings that the entry tear RFI was higher in S1, following which there was FL growth, whereas RFI

was zero in S2, after which there was FL reduction.

Pressure within the lumen is also an important factor when considering FL expansion. All models saw slightly higher pressure in the FL than TL, with the largest cross lumen pressure difference of 3 mmHg in S1. Furthermore, absolute FL pressures were found to be highest in S1, and reduced on average by 4 mmHg in S2 and S2mod. This is likely the reason why there was slow, uniform aortic growth between the first three scans. With an increase in the number of tears, the absolute FL pressure, and the pressure difference between the TL and FL reduced, with S2 having the smallest cross lumen pressure difference among the three models. This also agrees with the *in vivo* observations which saw a reduction in FL growth after the creation of the re-entry tears and eventually a reduction in FL volume. In addition to FL growth there was also expansion of the distal re-entry tear between S0 and S2. As well as a higher-pressure FL, high TAWSS in S1 (Figure 8.6) may have contributed to this, by wearing down the already damaged vessel wall at the tear point.

The finding that additional re-entry tears could reduce FL pressure and cross-lumen pressure difference is in line with previous experimental and computational studies (Tsai et al. 2008, Girish et al. 2016, Karmonik et al. 2011, Wan Ab Naim et al. 2014). Additionally, the results are consistent with the findings of the anatomical study of medically managed patients by Tolenaar et al. (2013a, 2013b) which suggested an increase in the number of tears decreased the risk of aortic growth. However, Kotelis et al. (2016) concluded from an anatomical study also of medically managed patients that an increase in the number of re-entry tears led to an increase in aortic growth. While it is not clear what caused discrepancies in the conclusions of these anatomical studies, detailed computational analysis including this work can highlight the underlying hemodynamic mechanisms that drive aortic growth.

An attempt was made to compare the predicted pressures in S1 and S2 with the invasive measurement made at S3, but the results were not encouraging. Simulations predicted a higher pressure in the FL, whereas the DW measurement recorded a higher pressure in the TL. This may be due to the fact that the measurement was made 16 and 4 months after S1 and S2, respectively, and at this point the cardiovascular condition might have changed. Furthermore,

the heart may be under different stress in the MRI/CT scan compared to during the surgical intervention when the measurements were taken. On the other hand, treating the aortic wall as rigid in the computational model might also introduce errors. Chong et al. (2020) showed that a rigid model can overpredict pulse pressure, causing varied discrepancies in cross-lumen pressure difference throughout the cardiac cycle, and Bäumler et al. (2020) showed that a mobile flap can reduce the mean cross lumen pressure difference by a factor of 0.63.

Currently, reinterventions to carry out fenestration procedures in type B aortic dissection are generally reserved to treating ischemia Hartnell & Gates (2005), Williams et al. (1993), Wuest et al. (2011). However, this study shows that in the case where FL pressure is higher than TL and hemodynamic conditions are not suitable for thrombus formation, the creation of additional tears may be beneficial to avoid aortic rupture, reduce FL expansion and stabilise the condition. Even after TEVAR there can be cases where patients experience FL expansion, for example in the unstented abdominal aorta, or due to stent-graft induced new entry tears (SINE) (Huang et al. 2018, Menichini et al. 2018). In these cases, it is not always possible to cover all re-entry tears to reduce FL flow, due to the potential ischemic complications that can occur when major or minor aortic branches are covered. In such a scenario fenestration may be beneficial to stabilise local expansion.

In this model the entry tear created 2 channels that were almost perpendicular to the proximal aorta, with the FL opening being larger than the TL. This allowed for the flow to split fairly evenly between the two lumen (in S1, 44% of descending aorta flow to the FL, 56% to the TL). As discussed throughout, this resulted in hemodynamic conditions which led to a higher pressure in the FL than the TL, and FL expansion. The creation of additional re-entry tears reduced this pressure difference, as well as absolute pressures, resulting in the slowing of FL expansion and eventual decrease in FL volume. However, the findings of Qin et al. (2012) and Chen et al. (2017) that an increase in the number of tears reduced the chance of thrombosis post-TEVAR suggest that additional re-entry tears are not beneficial in all circumstances. If a patient is experiencing FL thrombosis, it is likely that the conditions required to cause FL expansion may not arise, and fenestration intervention would be detrimental in this case. The absence of FL thrombus in this swine model meant that its influence on aortic flow and

pressure distributions could not be assessed. Given the single animal model cannot account for all possible disease scenarios it is emphasised that the conclusions of this study on the potential benefit of fenestration are drawn strictly on a case of a patent FL with a higher pressurised FL.

Considering these results, knowledge of TL and FL pressures appears to be crucial in evaluating whether intervention to create additional fenestrations would stabilise aortic growth or not. For all patients with aortic expansion, either pre-TEVAR or post-TEVAR due to SINE or abdominal growth, determining this cross-lumen pressure difference can be challenging. Obtaining Doppler-wire pressure measurements is an invasive procedure which cannot justifiably be carried out in the absence of another reason for invasive intervention. Therefore, non-invasive methods of determining pressure within the dissection are required. Image-based CFD simulations (as in this study) can provide detailed pressure gradients throughout the aorta, but as shown in Chapter 4 and in previous studies (Kousera et al. 2012, Pirola et al. 2017) the predicted pressure values are sensitive to the inlet and outlet boundary conditions. It is also possible to calculate pressure based on 4D-flow MRI data without having to carry out full CFD simulations, as demonstrated in a recent study of aortic coarctations (Saitta et al. 2019). This method can potentially be extended to other aortic diseases such as TBAD.

To validate the CFD simulation results, initial comparison to the 4D-flow MRI data was conducted. A good agreement of the global flow patterns was achieved, with local areas of high and low velocities captured well. Quantitative comparison revealed a correlation coefficient of approximately 0.6 in the non-dissected thoracic aorta and within the entry tear. The correlation coefficients reduced within the dissection, likely in some part due to the TL and FL diameters being small relative to the MR voxel size at these points. The lowest correlation at the upper dissection can be attributed to the longer extension of the high-velocity FL jet observed in the CFD model compared to the 4D-flow MRI. The quantitative comparison methodology was based on the work of Puiseux et al. (2019), who correlated CFD and 4D-flow MRI results of a well-controlled idealised experimental set up. Even with the extremely high-quality data the strongest correlation that was achieved between the raw MRI data and CFD was 0.67 (Puiseux et al. 2019). Therefore, the level of agreement achieved in this study was deemed acceptable.

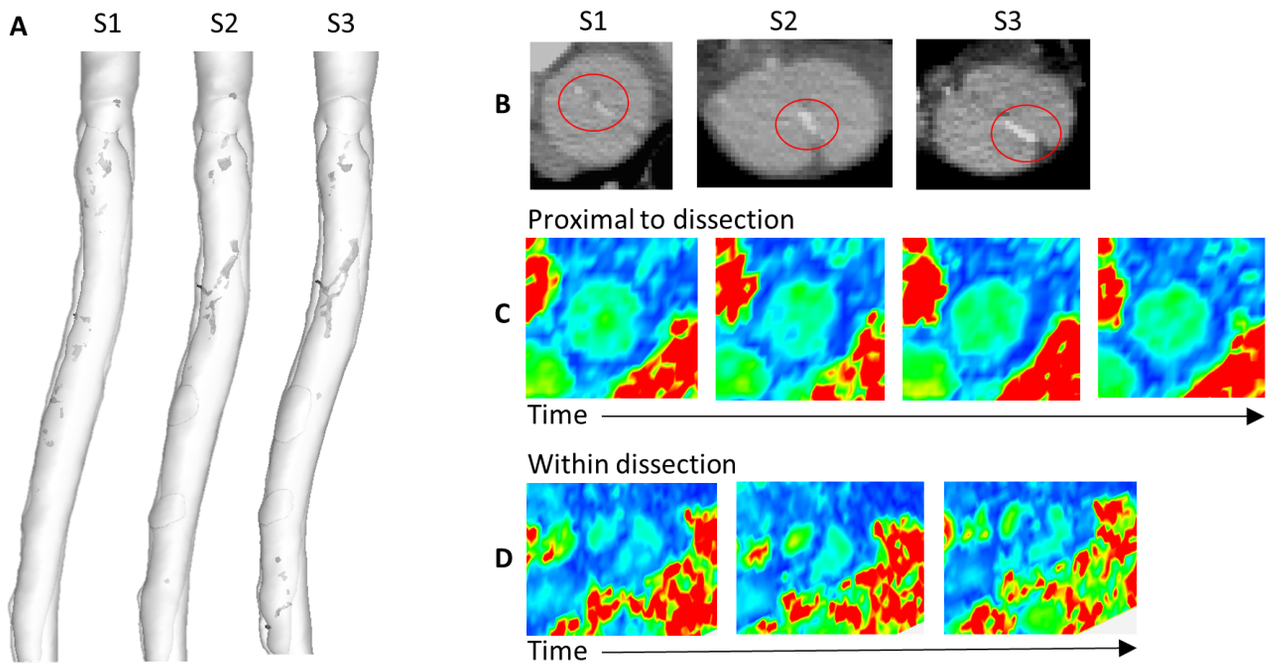

Figure 8.8: A - calcification (shown in black) throughout the dissection in scans S1, S2 and S3. B – areas of calcification (high intensity white pixels) within the intimal flap identified in scans S1, S2 and S3. C – velocities extracted from 4D MRI data in the upper thoracic aorta, proximal to the dissection at different time points throughout the systolic phase. D – velocities extracted from 4D MRI data within the dissection at different time points throughout the systolic phase.

There are limitations within this study. Since pressure measurement was only made at one follow-up time point (S3), the 3EWK models for all simulations (S1, S2 and S2mod) were tuned using the same pressure readings. This means that the pressure values calculated through CFD are likely not the true values, however given the consistency of methodology between the models, the pressure results can be compared across models. The key limitation of the model is the assumption of a rigid wall. The earliest scan simulated was S1, which was 9 months after the creation of TBAD. This is within the chronic phase of the disease, where it has been reported that flap mobility is greatly reduced (Peterss et al. 2016). Additionally, calcification was identified within the dissection and was seen to increase at each scan – this can be seen in Figure 8.8A and B. This is a common occurrence in dissected aorta and is known to increase flap stiffness (De Jong et al. 2014). With the evidence of a stiffer intimal flap, the effect of a rigid wall assumption on simulation results may not be as significant as previous studies have reported (Bäumler et al. 2020, Chong et al. 2020). Additionally, the lack of material properties for this model also meant performing an FSI simulation was challenging. While there was extensive temporal data in the form of 4D-flow MRI scans, the quality was not sufficient to be able to

extract any information regarding flap movement or general aorta compliance. Figure 8.8C and D show cross sectional planes of the dissection from the 4D-flow MRI scan at multiple time points throughout the systolic phase - it can be seen that poor image quality meant extracting flap and wall motion was not possible. Nevertheless, the implementation of a fluid-structure interaction model would improve the accuracy of predicted pressure. Since flap mobility varies significantly from the acute, subacute and chronic phase, it is also important to assess the potential impact of fenestration using multiple models at various stages of dissection. Finally, the error in lumen volume due to inter and intra-user variability in the segmentation process (as discussed in Section 3.4 and throughout each chapter) may impact results. While any impact is likely to be small given the lumen volume varied by at most 7.2% between users, this geometry specifically may be more exposed to inter-user differences due to the large amount of calcification in the flap which meant detailed manual segmentation was required to separate the TL and FL.

8.4 Summary

This chapter presents a longitudinal study of a controlled swine model, by means of combined 4D-flow MRI and computational modelling, assessing the influence of re-entry tears on aortic hemodynamics to understand their role in aortic growth. The results show that the introduction of additional re-entry tears, in certain situations, can be beneficial in reducing cross-lumen pressure differences, thus slowing and potentially reversing FL expansion. This study presents the potential role of fenestration, currently used to treat ischemic complications, to control rapid and/or continuous FL expansion in TBAD. Further study of a larger cohort of cases would be beneficial to develop clinically useful hemodynamic indicators of the need for fenestration.

Chapter 9

Application 2: Location of Reentry Tears Affects False Lumen Thrombosis Following TEVAR[†]

As discussed in Section 2.3.2, there is evidence suggesting that TEVAR is an effective treatment method for uncomplicated TBAD, yet it is still an invasive procedure that carries risks, which include standard surgical procedural risks and late-onset risks induced by the stent-graft, such as new reentry tears, endoleaks, retrograde dissection, and stent-graft migration, all of which may require further intervention (Liu et al. 2016, Sze et al. 2009). With the potential for such complications, it is desirable to understand and be able to predict the progression of the disease after TEVAR. This would allow, firstly, patients to be selected for TEVAR only if there is a high chance of FL thrombosis, and secondly, clinicians to tailor the TEVAR treatment to each patient individually.

A number of studies discussed in Section 2.6 have been conducted that provide insight into the thrombosis process post-TEVAR, including computational studies (Nauta et al. 2017, Wan Ab Naim et al. 2018, Menichini et al. 2018, van Bogerijen et al. 2014) which assessed aortic

[†]This chapter is adapted from: *Armour CH, Menichini C, Milinis K, Gibbs RGJ, Xu YX (2020) Location of Reentry Tears Affects False Lumen Thrombosis in Aortic Dissection Following TEVAR. Journal of Endovascular Therapy 27(3):396-404*

hemodynamics after TEVAR and several anatomical studies (Tolenaar et al. 2014, Qin et al. 2012, Ge et al. 2017, Kamman et al. 2017) which have identified morphological parameters of the aorta that influence the progression of the disease. For example, the presence of additional reentry tears was found to reduce the chances of FL thrombosis. Moreover, geometrical features of the stent-graft itself (such as the total length or diameter of the device) were analysed but did not show statistically significant correlations with FL thrombosis.

Stent-grafts are manufactured in set sizes, and given the limited sizing options it is possible that not all patients are receiving a best fit (in terms of both diameter and length). Additionally, as the primary entry tear is usually the largest, a stent-graft may be chosen with the primary objective of covering this tear, without consideration of further distal tears. Moreover, little work has been done to assess the influence of distal tears and their locations on TEVAR outcome. Therefore, the objective of this study was to investigate how the distance between the distal end of the stent-graft and first post-stent reentry tear may influence FL thrombosis after TEVAR using computational modelling of flow and thrombus formation in patient-specific geometries.

9.1 Methodology

Three patients (P1, P2, and P3) treated with TEVAR using a Gore TAG device (Gore Medical, Flagstaff, AZ, USA) in the acute phase for uncomplicated type B aortic dissection as part of the ADSORB trial (Brunkwall et al. 2014) were included in this study. Formal ethical approval was not required for this retrospective study, as prior agreement was made to undertake computational modelling using anonymised images and data. CT scans were acquired within the first month post-TEVAR and annually for up to 3 years. CT scans were performed using the Brilliance 40 (Philips Healthcare, Best, the Netherlands), Lightspeed VCT (GE Healthcare, Waukesha, WI, USA), or Volume Zoom (Siemens Healthineers, Erlangen, Germany) scanner, with a voxel size range of (0.47-0.77) $\times$ (0.47-0.77) $\times$ (0.8-1.5) mm^3 and a kVp of 120. Geometries were reconstructed from CT scans following the methodology presented in Section 3.4.

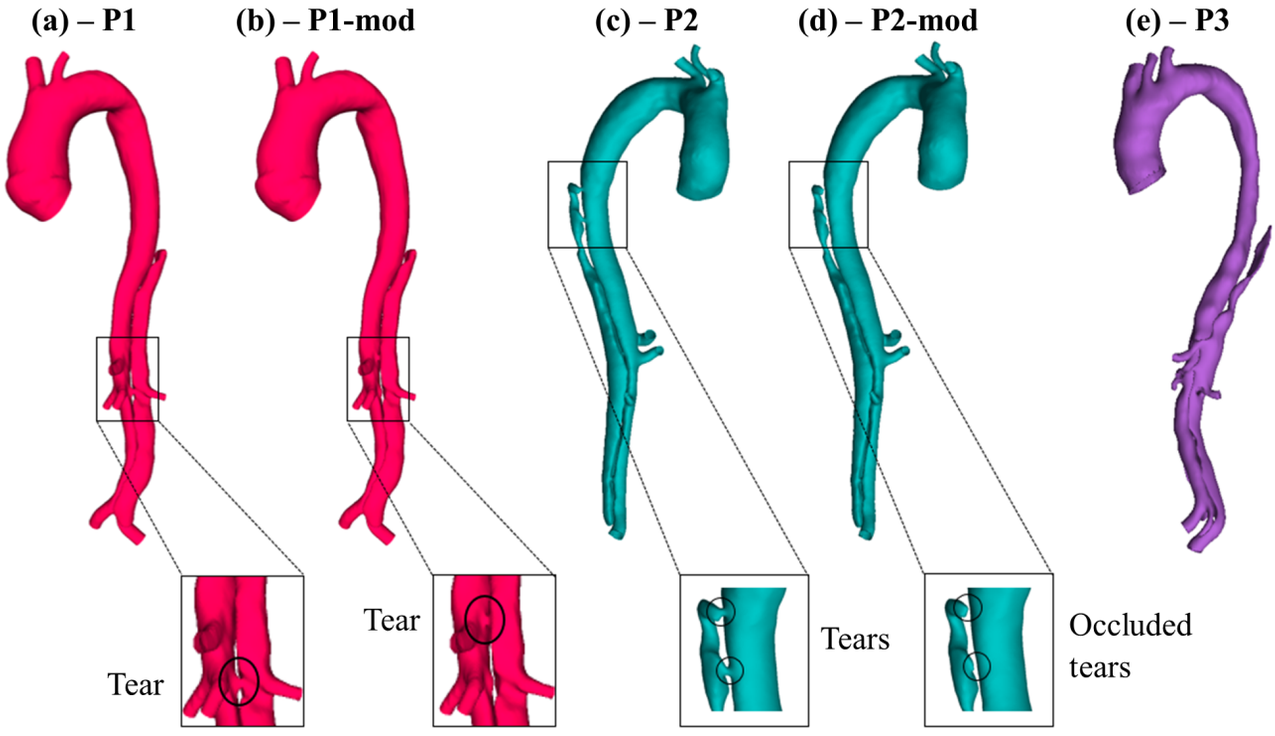

Figure 9.1: (a) P1, first post-procedure geometry; (b) P1-mod, modified geometry of P1 with the first post-stent reentry tear artificially moved proximally by 30 mm; (c) P2, first post-procedure geometry; (d) P2-mod, modified geometry of P2 with 2 proximal entry tears artificially occluded; and (e) P3, first post-procedure geometry (Armour et al. 2020).

For each reconstructed model, the false lumen volume was calculated using Equation 9.1.

$$Vol_{FL} = \sum_{i=1}^{N} \frac{(S_{i,FL} + S_{i+1,FL}) \times h}{2} \tag{9.1}$$

where $S_{i,FL}$ is the cross-sectional area of the FL for each axial slice i, N is the total number of axial slices, and h is the slice thickness. The FL was only present in the descending aorta, distal to the LSA, for all patients. Percentage changes in FL volume between the first and 1-year follow-up scans were calculated, as not all patients had follow-ups beyond 1 year.

In each reconstructed model, the distance between the distal end of the stent-graft and first post-stent reentry tear (SG-FRT) was measured along the centerline, which was fit using an automatic function in Mimics. To investigate the role of the SG-FRT distance, additional models were created. In the first post-TEVAR scan of P1, the FRT (originally located at the level of the left renal artery branching off the FL) was artificially moved upward by 30 mm toward the stent. In the first post-TEVAR scan of P2, two post-stent tears close to the

distal end of the stent-graft were occluded to simulate the extension of the stent-graft by 30 mm. Figure 9.1 shows P1 and P2 and their respective modified models (P1-mod and P2-mod) alongside P3. Each model included all major side branches with the exception of the LSA in P1 which was occluded by the stent-graft.

The 5 geometrical models were imported into ICEM and the fluid domain was meshed following the methodology laid out in Section 3.5, to create meshes consisting of 5 to 10 million elements each. Mesh sensitivity tests were carried out for all models and further details can be found in Appendix A.6. In order to focus on the influence of the SG-FRT distance on FL thrombosis, the same pulsatile inlet flow waveform taken from literature (Dillon-Murphy et al. 2016) was applied in all models. 3-element Windkessel models were applied at each outlet with the resistance and compliance parameters taken from the literature (Dillon-Murphy et al. 2016) as no patient flow data was available. A fixed time step of 0.005 seconds was used throughout the study, and each model was simulated for 4 cardiac cycles to ensure a periodic solution. Results from the last cardiac cycle were used to initialise the thrombosis model.

To simulate thrombus formation and growth over time, the shear-driven thrombosis model presented in Section 3.2 was implemented. A time step of 0.005 seconds was used and simulations were run until there were no further changes in predicted thrombus patterns. The number of cardiac cycles required varied between models: 20 cycles for P1 and P1-mod, 22 for P2 and P2-mod, and 20 for P3. For P2, two intercostal arteries were present in line with the two upper thoracic tears, meaning that flow from the true lumen would be diverted to these arteries as well as through the two tears. As the intercostal arteries were too small to segment from the CT scan, they were excluded from the computational model, resulting in artificially increased flow through the tears and thus higher time-averaged wall shear stress (TAWSS). As seen in Section 3.6 where the thrombus model boundary conditions are presented, TAWSS is a key parameter on which the coagulant flux boundary condition in the thrombosis model is dependent; therefore, a modified coagulant flux boundary condition from a previous study (Menichini et al. 2016) was applied in this region for P2. This condition gives a constant coagulant production balanced by coagulant consumption dependant on time-averaged shear rates.

Table 9.1: Anatomical measurements for each model.

	P1	**P1-mod**	**P2**	**P2-mod**	**P3**
Thoracic false lumen volume[a] %	-99.9	-	-83.2	-	-87.6
Abdominal false lumen volume[a] %	-15.6	-	-63.4	-	-32.7
SG-FRT distance, mm	111	81	0	141	155

Abbreviation: SG-FRT, distal end of the stent-graft to first reentry tear.
[a]False lumen volume percentage changes were taken between the first post-procedure scan and the 1-year follow-up. Volume changes are not reported for P1-mod and P2-mod as these are artificially modified models.

Predicted thrombus patterns were compared with the actual thrombus formation observed from follow-up scans. Additionally, comparisons were made between the original and modified models to assess the influence of SG-FRT distance on FL thrombosis.

9.2 Results

9.2.1 Anatomical Characteristics

Percentage changes in the FL volume between the first post-TEVAR and 1-year follow-up scans are reported in Table 9.1. All 3 patients had partial FL thrombosis, with P1 showing complete thrombosis in the thoracic FL but partial thrombosis in the abdominal FL. Both P2 and P3 had near complete thrombosis in the thoracic FL, with varying degrees of thrombosis in the abdominal FL. The SG-FRT distance, also reported in Table 9.1, varied across patients with P3 having the largest SG-FRT distance, followed by P1. P2 had a SG-FRT distance of 0 mm due to the presence of two tears just below the distal end of the stent-graft. The modified models had a reduced SG-FRT distance in P1-mod compared to P1 and increased SG-FRT distance in P2-mod compared to P2.

9.2.2 Flow Patterns and Related Parameters

Figures 9.2 and 9.3 show instantaneous velocity streamlines, and TAWSS and normalised pressure distributions, respectively, before initiating the thrombosis simulation. In P1 and P3 very

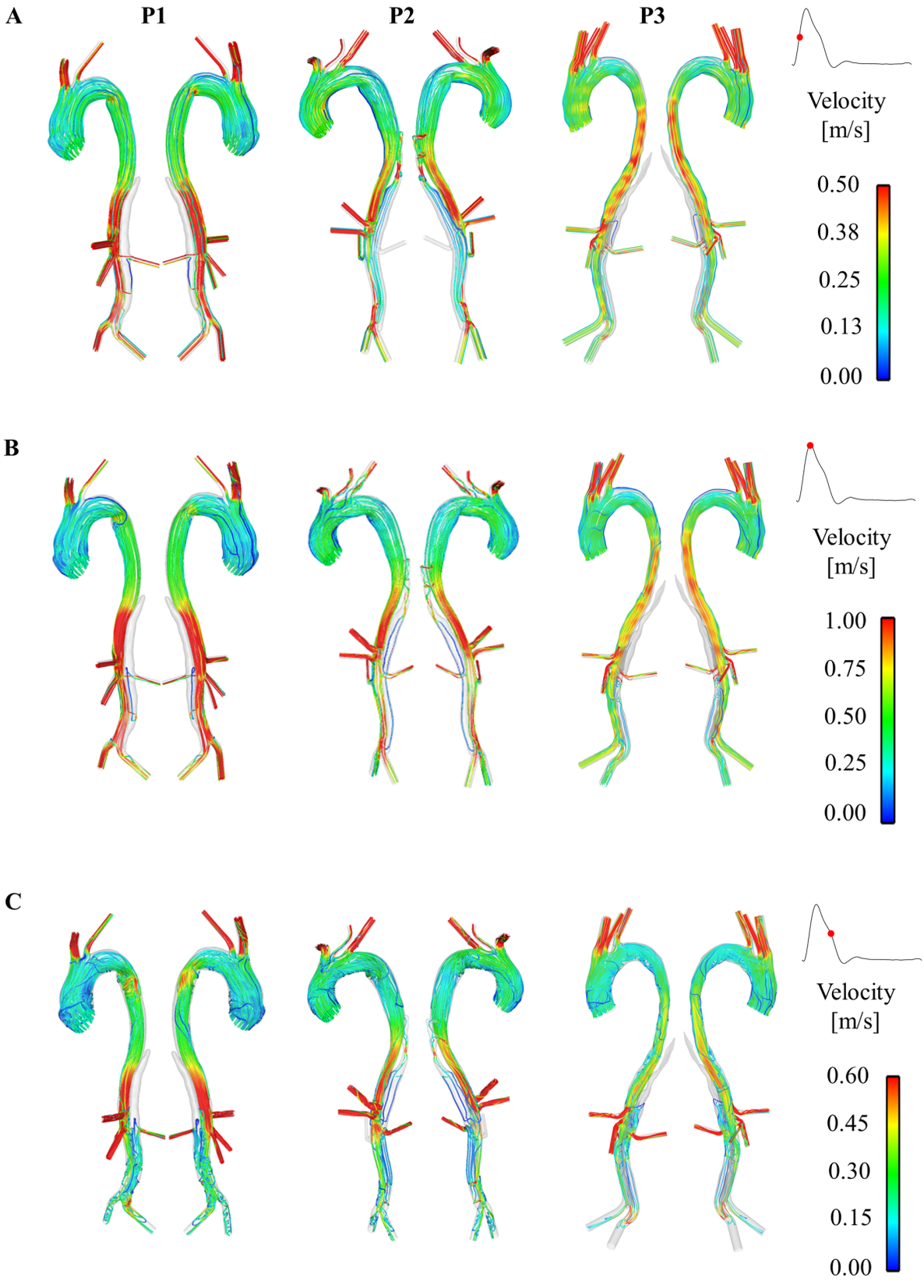

Figure 9.2: Instantaneous velocity streamlines at (A) mid-systolic acceleration, (B) peak systole, and (C) mid-systolic deceleration in P1, P2, and P3 (Armour et al. 2020).

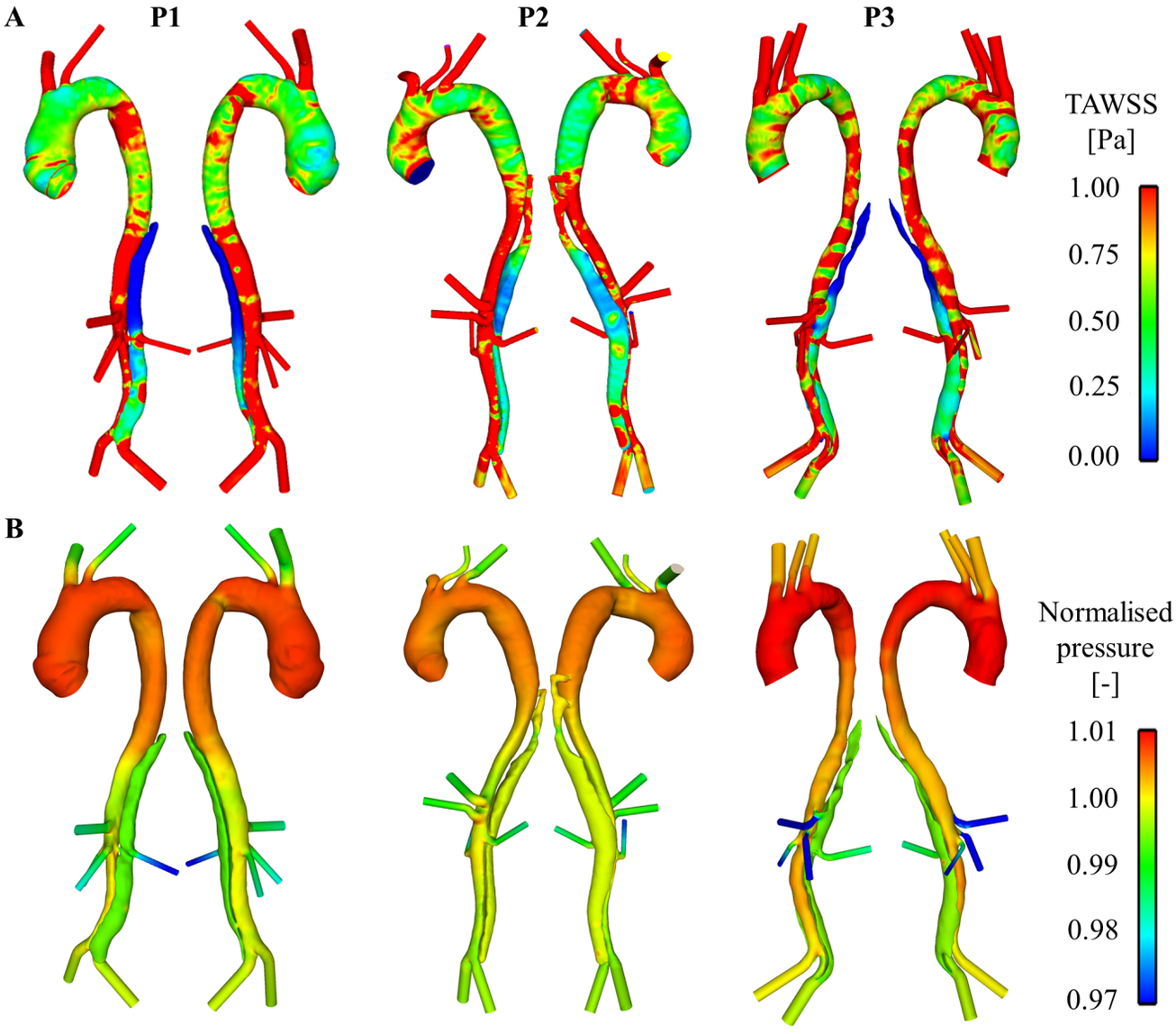

Figure 9.3: A: Time-averaged wall shear stress (TAWSS) distribution and B: Temporal average wall pressure normalised by the spatial average in patients P1, P2, and P3. Adapted from (Armour et al. 2020).

little flow was observed in the thoracic FL throughout the cardiac cycle. These 2 patients presented large SG-FRT distances, allowing flow to enter the distal FL, and there was no pressure gradient to drive the flow into the upper thoracic FL. For both patients this resulted in the thoracic FL having a lower pressure than the TL on average throughout the cardiac cycle. A higher pressurised TL was also observed in the abdominal aorta of both patients. Furthermore, the lack of thoracic FL flow resulted in very low TAWSS in this region for both patients, as seen in Figure 9.3A. P2, however, had higher flow and TAWSS in the thoracic FL due to proximal entry tears. The TL was of higher pressure than the FL in the region of the two proximal tears,

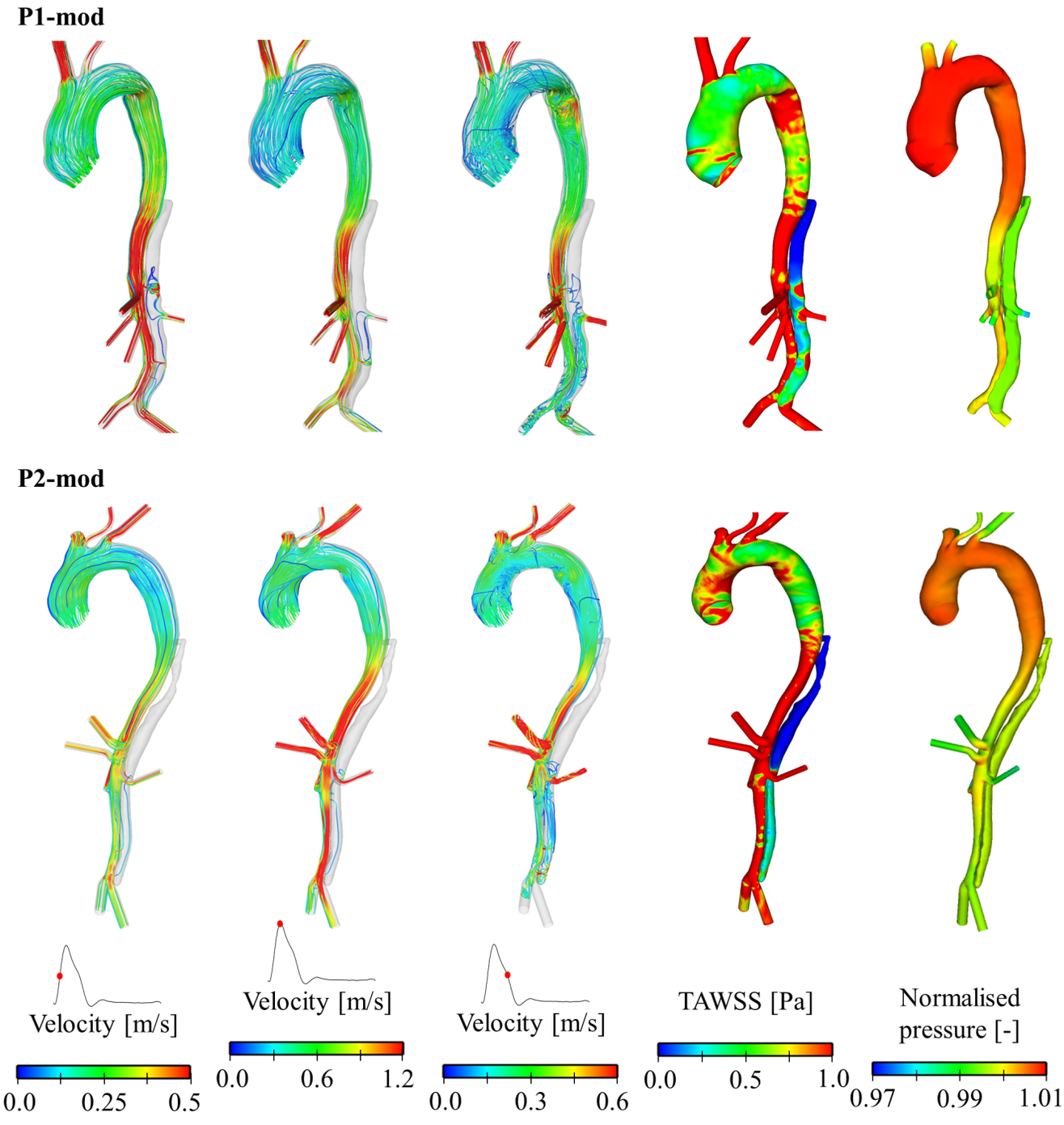

Figure 9.4: Instantaneous velocity streamlines at mid-systolic acceleration, peak systole and mid-systolic deceleration, time-averaged wall shear stress (TAWSS), and temporal average wall pressure normalised by the spatial average for P1-mod and P2-mod. Adapted from (Armour et al. 2020).

however quickly the pressure difference between the lumen reduced and throughout most of the dissection there were equal pressures between the TL and FL. In the most distal abdominal region of the dissection the FL was at a slightly higher pressure than the TL. In all patients, high TAWSS was observed in areas proximal to tears and branches. Disturbed flow with flow

recirculation between the tears was observed in the distal FL during the deceleration phase in all 3 patients, who notably all had tears near the bifurcation, creating an outflow channel for the FL.

Figure 9.4 shows instantaneous velocity streamlines, TAWSS, and normalised pressure distributions for P1-mod and P2-mod. The change of tear location in P1-mod did not significantly alter the volume of flow through the tear, with the percentage of inlet flow through the tear at peak systole being 1.30% in P1 and 1.27% in P1-mod. However, Figure 9.4 shows clearly that the change of tear location in P1-mod had repercussions on FL flow patterns and TAWSS, in particular in the region surrounding the tear. In the original model, the tear was in line with the renal arteries, so that the flow entering the FL either went straight into the left renal artery or to the abdominal FL. Therefore, almost no FL flow was observed above the renal arteries. Moving the tear upward resulted in an appreciable amount of flow in the region above the renal arteries, which circulated throughout the cardiac cycle. This resulted in an area of significantly higher TAWSS on the outer aortic wall opposite the relocated tear.

For P2-mod, covering the 2 proximal entry tears drastically altered the FL hemodynamics. Flow in the FL was reduced to near zero - flow through a mid-thoracic FL plane reduced from a peak systolic value of 1.03 L/min in P2 to 7.4×10^{-6} L/min in P2-mod. This resulted in very low TAWSS in this region in P2-mod. The occlusion of the thoracic entry tears also slightly reduced flow in the abdominal FL of P2-mod - in the mid abdominal aorta flow reduced from a peak systolic value of 1.39 L/min in P2 to 1.14 L/min in P2-mod, causing the average TAWSS in the abdominal FL to decrease slightly (0.52 Pa in P2-mod compared to 0.55 Pa in P2). This reduction in FL flow also caused the FL to be at a lower pressure than the TL throughout the thoracic region (unlike the original P2 case where pressures were mostly even between the lumen). The total % of inlet flow reporting to the FL-perfused left renal artery was calculated, and very little change was observed between the original and modified geometries (9.77% in P2; 9.66% in P2-mod).

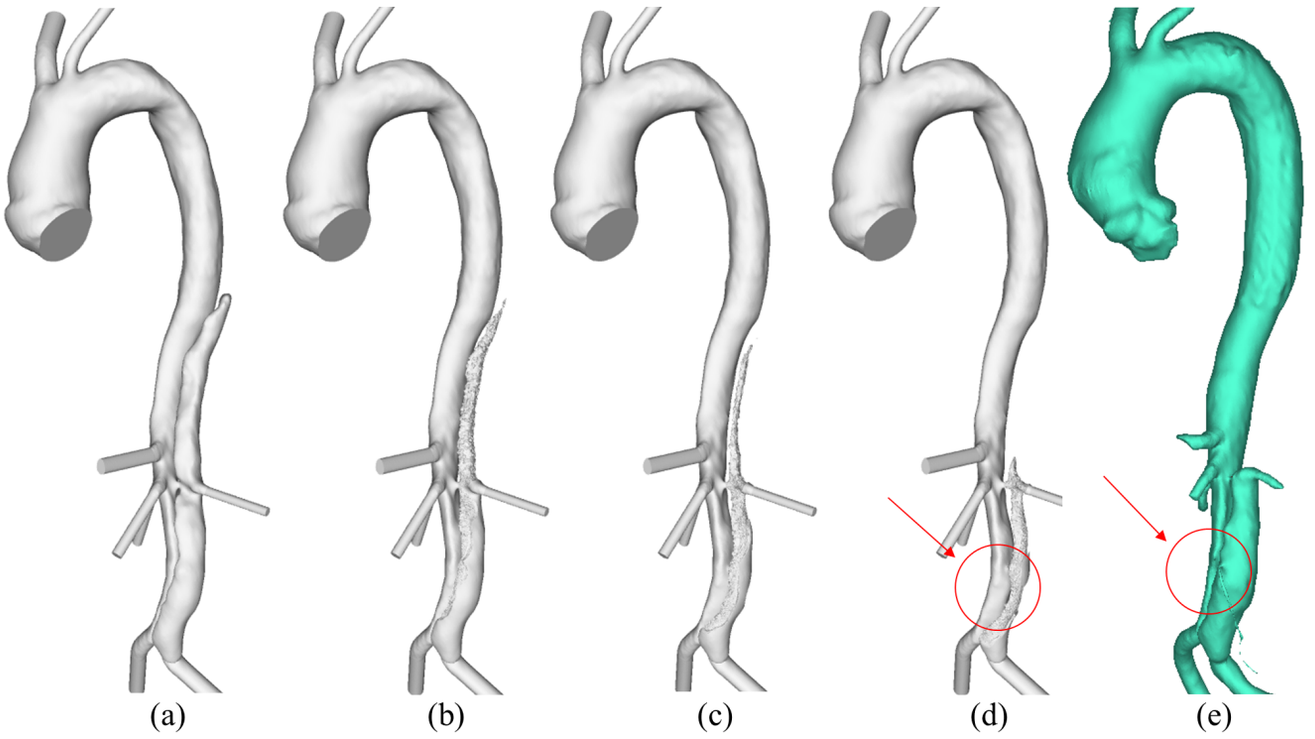

Figure 9.5: Evolution of false lumen (FL) surface in P1 following thrombus growth. (a) Reconstructed lumen surface based on the first post-procedure scan for P1 and predicted FL surface following thrombus growth at (b) 8, (c) 15, and (d) 26 seconds in comparison with (e) the reconstructed lumen surface based on follow-up scans acquired at 3 years post-procedure. Over-prediction of thrombus growth due to the exclusion of minor branches is highlighted in the red circles (Armour et al. 2020).

9.2.3 Thrombus Formation in the False Lumen

The predicted thrombus growth patterns for the original models are shown in Figures 9.5A-D, 9.6A-D, and 9.7A-D, along with the real geometries reconstructed from the corresponding follow-up CT scans shown in Figures 9.5E, 9.6E and F, and 9.7E. For all 3 patients, partial thrombosis was predicted in the FL where thrombus formation started from the top region and gradually expanded toward the first uncovered tear. A second region of partial thrombosis was also observed in-between the first and distal tears. For all patients, thrombus growth slowed down after about 20 seconds, until stopping at 26 to 28 seconds.

Comparisons with follow-up scans revealed a good overall agreement between the predicted thrombus growth and actual clinical observations. The model was able to capture the location of thrombus growth and correctly predicted incomplete thrombosis within a simulated time frame of 30 seconds. Some disagreements can be observed in P1 and P2. In P1 (comparing

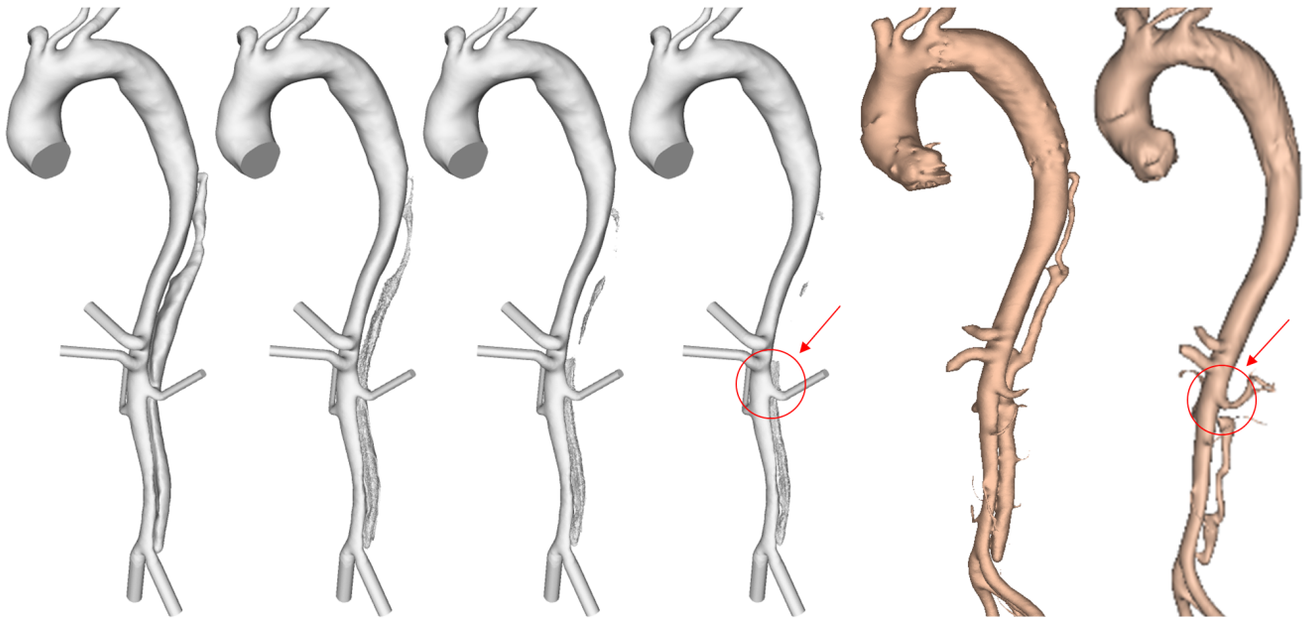

Figure 9.6: Evolution of false lumen (FL) surface in P2 following thrombus growth. (a) Reconstructed lumen surface based on the first post-procedure scan in P2 and predicted FL surface following thrombus growth at (b) 15, (c) 22, and (d) 28 seconds in comparison with the reconstructed lumen surface based on follow-up scans acquired at (e) 1 year and (f) 2 years post-procedure. This simulation shows under-prediction of thrombus growth due to the exclusion of minor branches (Armour et al. 2020).

Figure 9.5D and E), the model over-predicted thrombus growth in the region between the renal arteries and the aortic bifurcation. This was due to the inferior mesenteric artery and one of the intercostal arteries (not included in the computational models) branching off the FL. In P2, the region between the superior mesenteric artery and the right renal artery was predicted to remain patent, while thrombosis was observed during follow-up (highlighted in Figure 9.6D and F). Thrombosis of this region in the computational model was hindered by the presence of a tear at the level of the superior mesenteric artery, which allowed flow into the FL. An intercostal artery can be seen in the CT scan at the same level as the tear. Therefore, most of the flow crossing the tear would have been diverted to the branch, reducing the amount of blood circulating in this region of the FL. A very good agreement was found in P3 (comparing Figure 9.7D and E).

Figure 9.8 shows the final predicted thrombus formation in P1 and P1-mod. It can be seen that moving the tear proximally by 30 mm resulted in reduced thrombus formation in the upper abdominal FL around the region of the left renal artery; overall, the volume of thrombus formed

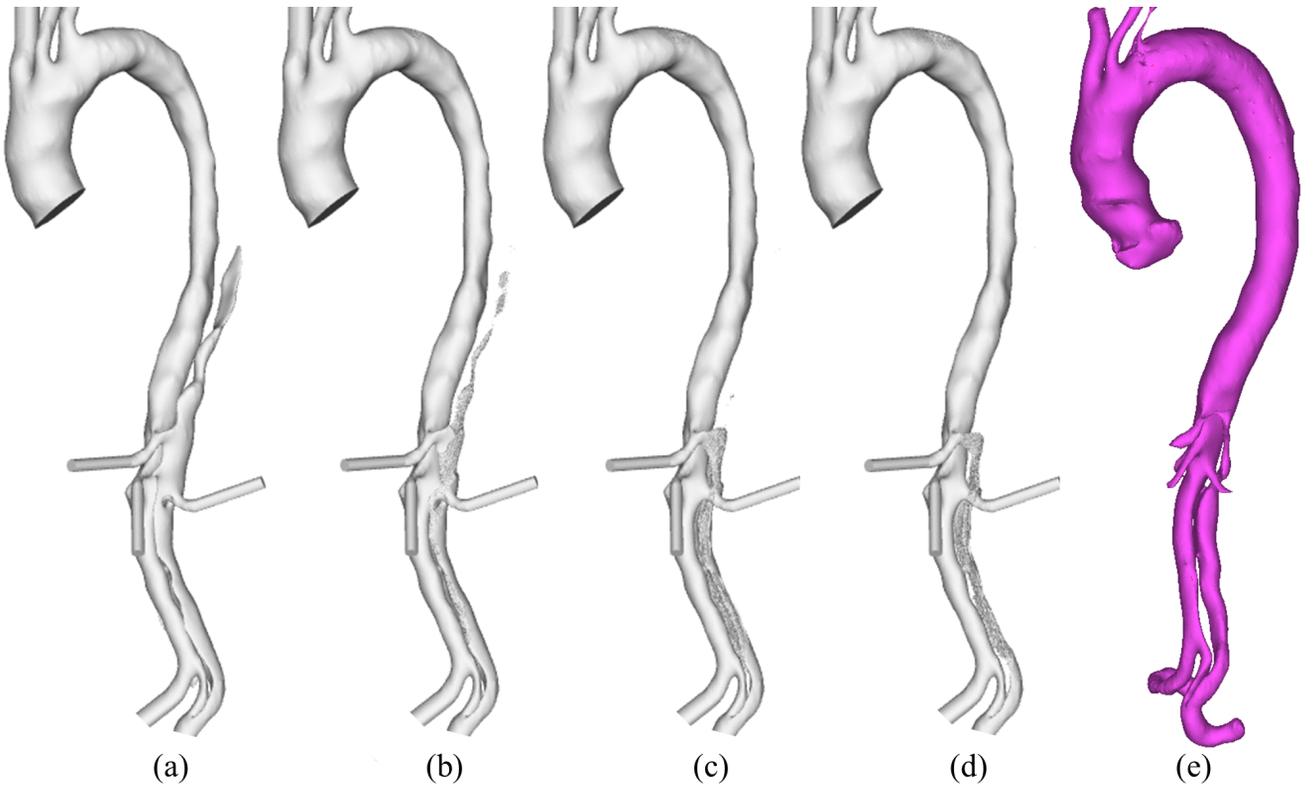

Figure 9.7: Evolution of false lumen (FL) surface in P3 following thrombus growth. (a) Reconstructed lumen surface based on the first post-procedure scan in P3 and predicted FL surface following thrombus growth at (b) 8, (c) 15, and (d) 26 seconds in comparison with (e) the reconstructed lumen surface based on follow-up scans acquired at 1 year post-procedure (Armour et al. 2020).

decreased by 9.6%. This was due to increased flow and TAWSS in this region, as seen in Figure 9.4. Figure 9.9 shows the predicted thrombus formation for P2 and P2-mod, where covering the proximal entry tears resulted in faster thrombosis of the thoracic FL as well as an increase of 4.7% in total thrombus volume. This is due to the substantially reduced thoracic TAWSS, as observed in Figure 9.4.

9.3 Discussion

Although in-hospital survival rates are high for type B aortic dissection patients, the prognosis after discharge remains uncertain, with registry data suggesting a 50% mortality rate at 5 years due to aortic rupture (Nienaber et al. 2005). The key driver for aortic expansion in chronic type B dissection is the presence of blood flow within the FL, and the therapeutic goal of TEVAR

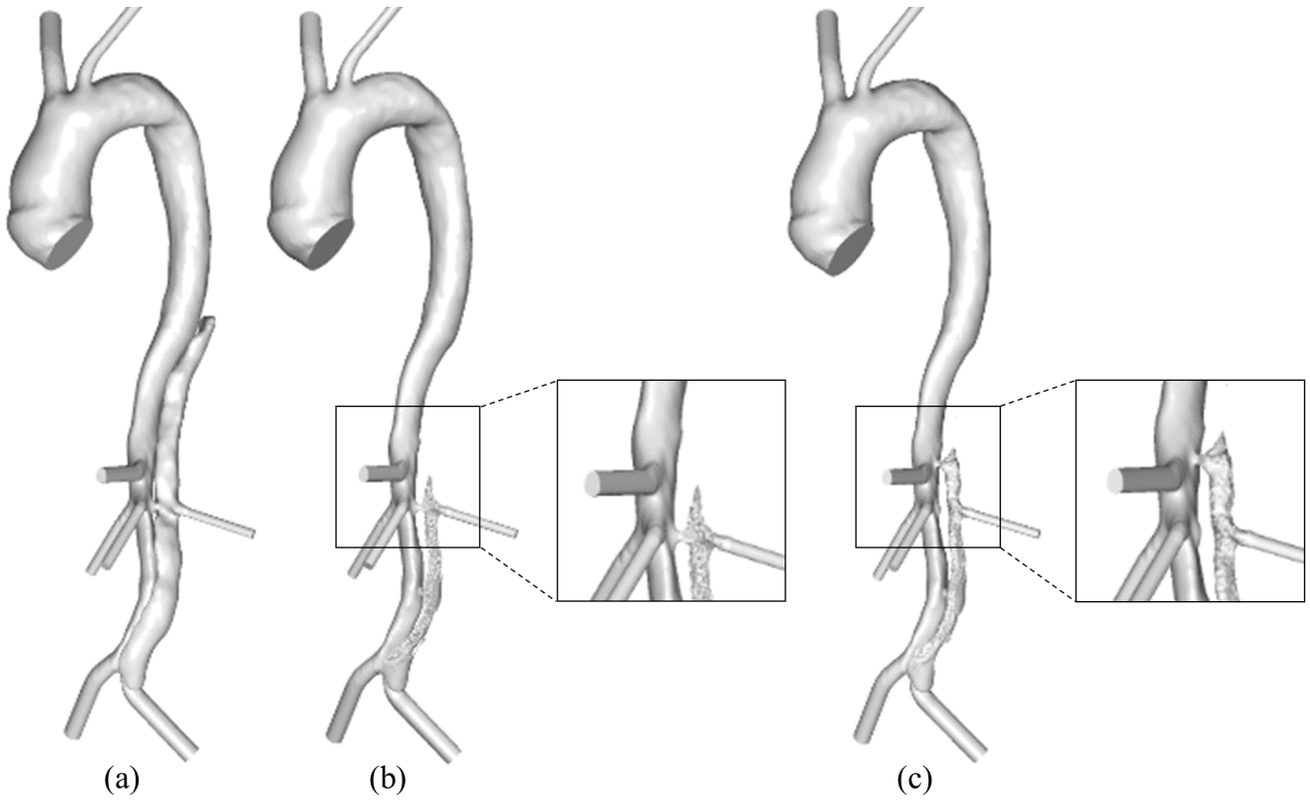

Figure 9.8: (a) Reconstructed postprocedure geometry of P1. Predicted thrombus formation for P1 in (b) the original geometry and (c) the modified geometry. The difference in predictions due to modified reentry tear position is highlighted (Armour et al. 2020).

is to depressurise the FL, resulting in thrombosis.

Extensive studies have been carried out trying to assess the efficacy of TEVAR against medical treatments (Nienaber et al. 2009, Brunkwall et al. 2014, Qin et al. 2016, Li et al. 2018) and to identify parameters that can predict post-TEVAR outcomes (Tolenaar et al. 2014, Qin et al. 2012, Ge et al. 2017, Kamman et al. 2017). Nonetheless, it is still unclear which are the key parameters driving the progression of this disease and determining the outcome of treatments. The main aim of this study was therefore to elucidate the role of certain morphological features, FL thrombosis in particular, in determining patient outcomes post TEVAR. As the presence of patent post-stent reentry tears had been identified as a key predictor of reduced FL thrombosis (Kamman et al. 2017), this parameter was a focus of the current study. Additionally, stent-graft design has been suggested to influence the outcome of TEVAR, either positively by promoting FL thrombosis or negatively by inducing further complications (Sze et al. 2009). Thus, the length of the stent-graft was taken into consideration in combination with the presence of

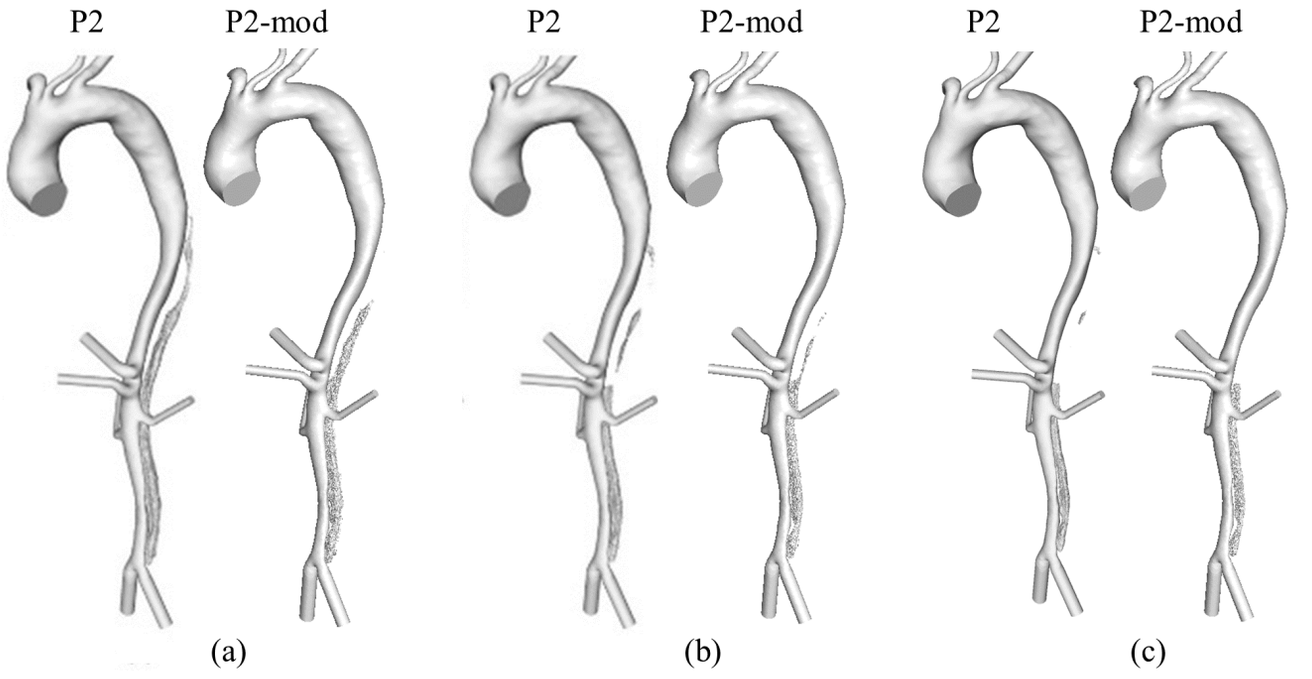

Figure 9.9: Evolution of P2 and P2-mod false lumen surface following thrombus growth compared throughout the simulation at (a) 15, (b) 22, and (c) 28 seconds (Armour et al. 2020)

reentry tears by studying the distance between the SG and FRT.

Comparison of the original patient-specific models showed substantially lower flow and TAWSS in the thoracic FL for P1 and P3 (who had a large SG-FRT distance) compared to P2, initially suggesting that the SG-FRT distance may be a key parameter in determining FL flow and thus FL thrombosis. In order to investigate this parameter while keeping all other morphological parameters constant, modifications were made to P1 and P2. The reduction of the SG-FRT distance in P1, by moving the FRT proximally by 30 mm, resulted in increased FL flow and TAWSS in the region adjacent to the tear and reduced FL thrombosis. The occurrence of a stent-graft–induced new entry tear (SINE) would also drastically decrease the SG-FRT distance. The detrimental influence of SINE on FL thrombosis and aortic remodeling has been highlighted in the literature and is in line with the results of this study showing that a decrease in SG-FRT reduces FL thrombosis (Huang et al. 2018, Menichini et al. 2018).

Increasing the SG-FRT distance in P2 by artificially extending the stent-graft by 30 mm to cover the 2 adjacent reentry tears led to reduced FL flow and TAWSS, as well as faster and increased FL thrombosis. These results indicate that a large distance between the distal end of the stent-graft and the FRT would be favorable for FL thrombosis. Additionally, it was shown

that occluding these tears by extension of the stent-graft had little impact on the flow to the FL-perfused left renal artery. This means a longer stent-graft could have been used for this patient without adversely affecting left renal artery perfusion. In this case the extension of the stent-graft was by only 30 mm, with 100 mm between the distal end of the stent-graft and the celiac trunk remaining uncovered. However, it has been highlighted that extended coverage of the entire thoracic aorta up to the celiac trunk may be linked to an increased risk of spinal cord ischemia (Zipfel et al. 2013). This should be considered when choosing the stent-graft length, and the desire to cover additional tears should be balanced with the increased risk of such a complication. In the case where a longer stent-graft is used to occlude additional reentry tears, reducing the stent-graft length to increase the SG-FRT distance would cause the most distal covered reentry tear to be exposed, resetting the SG-FRT to zero. Therefore, in this scenario, artificially increasing the SG-FRT distance by decreasing stent-graft length would not benefit FL thrombosis.

Following on the previous work of predicting FL thrombosis in TEVAR patients (Menichini et al. 2018), the model complexity was increased to include major side branches. Consistency between simulated thrombus formation and follow-up CT scans further demonstrated the validity of the predictive model. Slight deviations in results were mainly attributed to the presence of minor FL-perfused branches. In regions where small branches were artificially occluded, the model over-predicted thrombus formation. In particular the effect of excluding the inferior mesenteric artery in P1 on thrombus formation was studied in detail in Chapter 5 and the results showed that the over-prediction of thrombus is due to the lack of the FL branch which creates an additional pressure drop that drives flow within the FL and hinders the deposition of platelets and the formation of thrombus. This factor has been highlighted in several anatomical studies for both TEVAR and medical management patients (Tolenaar et al. 2014, Qin et al. 2012, Ge et al. 2017, Kamman et al. 2017).

While it is desirable to compare quantitative volumes of thrombus formation between the CFD simulations and follow-up CT scans, it is difficult to do so from the data available. P1 was utilised in Chapter 5 and quantitative results were discussed, showing that in the abdominal region thrombus volume is inline with the follow-up CT scan when the inferior mesenteric

artery is included in the geometry, however the thoracic region saw higher thrombus volumes in the CFD simulation compared to the CT scan due to expansion of the TL and compression of the FL that could not be modelled in the rigid simulation. For P2 and P3 in the current Chapter, evaluating quantitative thrombus volumes is even more challenging as thrombus was already present at the baseline geometry that was used in the simulation. For both patients, FL thrombosis had already begun in the thoracic region, and the follow-up scans showed that complete thrombosis of this region occurred, which was predicted in simulation. However, the follow-up scans also showed there was expansion of the TL in both P2 and P3, which caused some changes in the volume of the thrombosed FL, therefore measuring the change in thrombus between the baseline and final geometry would require assuming and manually selecting the part of the thrombosed FL that was believed to be initially patent. This is of course not accurate, and for this reason quantitative results are not presented for P2 and P3. The long time period between follow-up scans means such challenges are present with this type of data, as the morphological changes cannot be continuously assessed. The rigid nature of the CFD simulation also means such morphological changes cannot be mimicked and their influence on the thrombosis process is therefore lost. For both of these reasons, only qualitative comparisons can be reliably carried out with the current model. Such qualitative comparisons still provide value results and insight, as seen throughout this thesis, however incorporating wall motion and growth would help to overcome this barrier to quantitative assessment.

Although much work has been done to identify the effects of changing morphological features on the presence of FL thrombosis after TEVAR, little had been done prior to this work to quantify thrombus formation and assess the direct effect of such parameters on changes in FL volume, especially looking at specific regions of the aorta. The aim of this study was to understand the physics behind key morphological parameters related to both the patient and the stent-graft. While there are numerous biological and morphological factors that contribute to FL thrombosis after TEVAR, the focus of this study on one specific parameter highlights the significant influence that a single variable can have on patient outcome. It is hoped that these findings will help elucidate the dynamics driving the progression of type B aortic dissection for endovascularly treated patients, which will further help clinicians develop more effective

treatment strategies for individual patients.

The work presented here has several limitations. First, the number of patients included was small. Dissections can present in a wide range of morphologies and analysis of a larger cohort would provide the opportunity to study morphological parameters in varied cases. Second, all patients included in the present study were treated with a GORE TAG device in the TEVAR procedure. It would be necessary to extend the study to patients treated with different devices in order to elucidate the effect of stent-graft design on the predicted outcome.

With regards to the computational model, while previous work has validated the thrombosis model for predicting clinical outcomes (Menichini & Xu 2016, Menichini et al. 2016, 2018), and the results from this study show good agreement between model predictions and follow-up scans, there is room for further refinement. The patient-specific computational models did not include minor side branches, specifically the exclusion of the FL perfused intercostal artery in P1 resulted in over-prediction of thrombus formation, as discussed previously in this chapter and in Chapter 5. However, the consistency of geometry between P1 and P1-mod means that the interpretation of the results due to the change in tear location is valid.

Patient-specific flow data was not available for these patients, therefore an flat inlet velocity profile taken from literature was applied to all models in this study. As discussed in detail in Chapter 4, using a patient-specific inlet velocity profile is important to accurately predict hemodynamics, however given the focus of this study was to compare modified models any change in hemodynamics can be attributed to the geometric modifications and therefore having a patient-specific inlet velocity profile is not essential. In a similar manner, the outlet 3EWK parameters were taken from literature, but the consistency between models and the evaluation of normalised pressure rather than absolute values means using literature values is reasonable. Additionally, all models in this study assumed rigid wall behaviour. The increase in stiffness of the intimal flap as the disease progresses to the chronic phase (Peterss et al. 2016) could affect predictions of flow and thrombus growth in dissected regions not covered by the stent-graft. Furthermore, the inflexibility of the stent-graft and its relative stiffness compared to the aortic wall may impact aortic hemodynamics and thrombus formation (Qiao et al. 2020). As in all

other chapters, the models will have some degree of error in the segmented volume due to inter and intra-user variability (Section 3.4). However, as this study is drawing conclusions on modified models where the core geometry is the same, with tears either moved or occluded, the results and conclusions are still valid and can be reliably be attributed to these modifications.

9.4 Summary

The results presented in this Chapter demonstrate that the SG-FRT distance can influence FL hemodynamics and thrombus formation, with a large SG-FRT favouring FL thrombosis. These findings could potentially help clinicians select the most appropriate treatments for individual patients and to predict which patients would be most likely to benefit from endovascular treatments. Future studies of a larger cohort of patients will be beneficial to assess the impact of SG-FRT distance on a wide range of dissection morphologies. Additionally, further studies using the methodology of modifying patient-specific geometries will facilitate similar analysis of other key morphological parameters to determine which anatomical factors play the most important role in the progression of aortic dissection.

Chapter 10

Conclusions and Future Work

The primary objective of this thesis was to develop computational methodologies to simulate hemodynamics and thrombus formation in type B aortic dissection, with the aim of the models being applicable in clinical settings. A computational fluid dynamics (CFD) workflow was developed which utilised 4D-flow magnetic resonance imaging (MRI) to incorporate patient-specific flow details. The model was evaluated in detail and was shown to be able to produce high quality and physiologically accurate results. The applicability of the developed methodologies to study clinically important questions was demonstrated through studies on the influence of re-entry tears.

The following section presents a summary of the main contributions of this thesis. Discussion on limitations of the work is then presented alongside suggestions for future work.

10.1 Summary of Main Contributions

1. A fully patient-specific 4D-flow MRI based CFD model for simulation of TBAD has been developed. The model utilised 3D inlet velocity profiles (IVP) derived from 4D-flow MRI, and outlet 3-element Windkessel (3EWK) models were tuned using 4D-flow MRI derived branch flow splits and invasively measured pressures. Patient-specific geometries segmented from CT scans included all major aortic side branches. Detailed quantitative

and qualitative comparison of CFD predicted hemodynamics to *in vivo* data showed the capability of the model to faithfully reproduce aortic dissection hemodynamics (Chapter 6). This is the most physiologically realistic CFD model of TBAD to date.

2. The choice of IVP was studied in great detail (Chapter 4). While a 3D IVP was shown to produce the most physiologically accurate results, a patient-specific 2D or flat IVP did not significantly impact predicted hemodynamics. Evaluation of generic IVPs showed that a non-patient-specific stroke volume, peak systolic flowrate, and flow waveform significantly impacted flow results. These results provide a clear understanding of the implication of generic IVPs, which is important for interpreting results of past and future CFD studies which utilise such non-patient-specific IVPs.

3. The inclusion of major and minor aortic side branches in pre and post-TEVAR models was examined in great depth (Chapter 5). The results showed that the exclusion of any major branches, even with adjustments made to inlet and outlet boundary conditions to account for exclusions, affects the simulation results. The exclusion of minor side branches was shown to have a much smaller impact on both hemodynamic and predicted thrombus results, with the inclusion of FL perfused branches inhibiting thrombus formation. This finding is not only important from a methodological view point, but also gives a mechanistic understanding of the correlation between FL perfused side branches and lack of thrombus formation identified in anatomical studies.

4. Application of the developed 4D-flow MRI based CFD workflow on 5 patients (Chapter 6) produced a large data set of model parameters including branch diameters, 3EWK parameters, and inlet flow waveforms which vary in stroke volume and cycle period. This is valuable data which can be used in future studies where patient-specific flow details are not available. In these cases, researchers can select model parameters that best match any available information.

5. The hemodynamics based thrombus model developed by Menichini & Xu (2016) was simplified to improve computational efficiency (Chapter 7). It was shown that FL thrombosis could be predicted without modelling the transport and reactions of activated and resting

platelets, and computational time was reduced by 52%. This is an important step towards improving clinical applicability of the model.

6. The developed and validated computational workflow was then used to address clinically relevant questions, with a focus on the influence of re-entry tears on pre-TEVAR hemodynamics (Chapter 8) and post-TEVAR hemodynamics and thrombosis (Chapter 9). It was found that increasing the number of re-entry tears in the non-thrombosed pre-TEVAR swine model reduced absolute FL and cross-lumen pressure differences, highlighting the potential benefit of fenestration in similar cases which are experiencing uncontrollable FL expansion. A longer distance between the distal end of the stent-graft and the first post-sent re-entry tear (SG-FRT) was shown to promote FL thrombosis, an important finding which may aid in TEVAR planning procedures.

In summary, a comprehensive 4D-flow MRI based CFD model which can faithfully reproduce TBAD hemodynamics was developed, and the thrombosis model (Menichini & Xu 2016) was further developed to improve its computational efficiency. The methodologies presented in this thesis can also be employed in studies of other aortic and cardiovascular diseases. It is hoped that the work in this thesis can contribute towards the development of computational tools used in the clinical setting to improve patient treatment planning.

10.2 Limitations and Future Work

There are several limitations to the work presented in this thesis. The implication of each limitation and suggested future work are discussed below.

10.2.1 Rigid Wall Assumption

The main limitation of the work in this thesis is the rigid wall assumption. It is known that flap mobility significantly reduces as a TBAD develops and enters the chronic stage (Peterss

et al. 2016) and calcification, commonly observed in dissection flap, also increases flap stiffness (De Jong et al. 2014). Additionally, in order to accurately account for wall motion a 2-way fluid-structure-interaction (FSI) model is required. In such a model there is an exchange of information between the fluid and structural domain at every time step - pressure fields modelled in the fluid domain are applied as a load on the solid domain which leads to deformation, the magnitude of which is sent back to the fluid domain to update the geometry and evaluate forces exerted by the solid wall onto the fluid. This is computationally very expensive and not feasible for clinical applications. Furthermore, material properties for TBAD are rarely available due to the fact that surgical treatment is not common practice and therefore there are few opportunities to collect TBAD tissues for mechanical testing. For all of these reasons, the models in this thesis assumed a rigid wall.

This rigid assumption is of course not physiological given the aorta is a compliant vessel, and previous studies have shown rigid simulations can overestimate pulse pressure (Chong et al. 2020) and cross-lumen pressure differences (Bäumler et al. 2020), and wall motion may be required to capture certain regions of low and oscillatory wall shear stress (Alimohammadi et al. 2015). Discussion in each study of this thesis has also highlighted the rigid wall assumption and indicated the likely impact of this assumption on results. In particular, it is speculated that the discrepancies in simulated and invasively measured pressures in Chapter 6 are due to the rigid wall assumption. Thus, the impact of the rigid wall assumption needs to be assessed.

In order to evaluate the influence of wall compliance, a preliminary 2-way FSI simulation has been performed using P5 from Chapter 6. The fluid domain was modelled in FlowVision (Capvidia NV) and the structural domain was modelled in Abaqus (Dassault Systemes). The intimal flap was segmented from the diagnostic CT scan, meaning the flap had a varying patient-specific thickness throughout, and the wall was modelled as shell elements with a virtual thickness of 1 mm. Both the flap and wall were modelled as linear elastic isotropic materials, with a Young's modulus of 2.7 MPa and a Poisson ratio of 0.475. A rigid CFD simulation was also performed in FlowVision for comparison. In both the rigid and FSI simulation the inlet flowrate derived from the 4D-flow MRI for P5 was applied at the inlet of the fluid domain as a flat IVP, and 3-element windkessel models were applied at all outlets (parameters reported

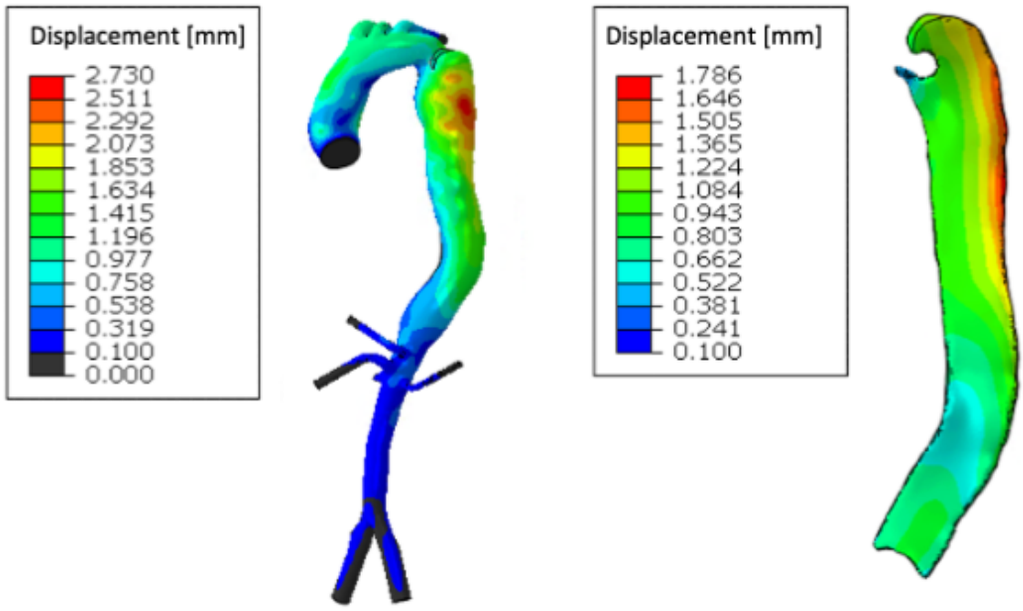

Figure 10.1: Peak systolic displacement contours in the FSI model for the left: wall and right: flap.

for P5 in Table 6.4 in Chapter 6 were used). In the solid domain, the inlet and all outlets were fixed in all three directions and not able to move.

Fluid pressure acts on the wall and serves as the driving force for wall deformation, which can be seen in Figure 10.1. At peak systole, displacement of up to 2.730 mm and 1.786 mm was seen in the wall and flap, respectively. Both the wall and flap saw the highest levels of displacement on the back left side, the point at which the high velocity jet through the primary entry tear would be hitting the wall. Additionally, higher displacement was observed on the posterior wall in the ascending aorta, due to the angle of the aortic root where the inlet was set. The maximum displacement throughout the cardiac cycle was 2.944 mm and occurred in mid-diastole on the upper left back region of the FL wall.

Figure 10.2 shows the peak systolic pressure distributions in the rigid and FSI model, as well as the average aortic pressure plotted over the cardiac cycle for both models. The results clearly show that accounting for wall and flap motion impacts pressure distributions. As can be seen in Figure 10.2C the average pressure is both generally lower than and peaks later than the comparative rigid model. This is due to the mobile wall being able to absorb some of the pressure from the fluid. The distribution of this aortic pressure, shown in Figure 10.2A,

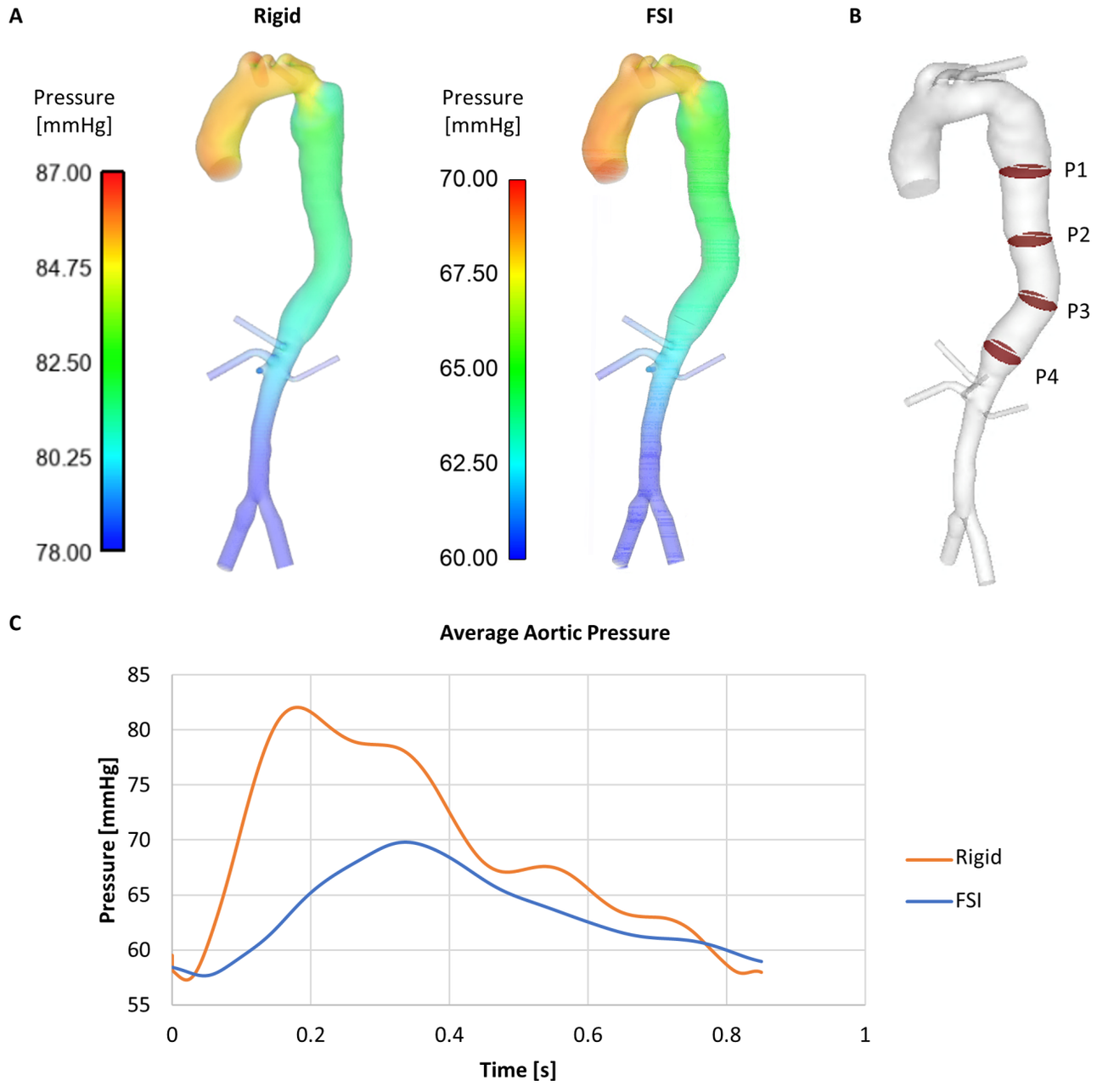

Figure 10.2: A: Peak systolic pressure distributions in the rigid and FSI model. B: Location of analysis planes in the dissection. C: Average aortic pressure over the cardiac cycle in the rigid and FSI model.

was similar between the FSI and rigid model, with the range in peak systolic aortic pressure being approximately 10 mmHg in both models, however absolute values were reduced in the FSI model. The pressure difference between the TL and FL was also measured on four planes within the dissection (the location of which are shown in Figure 10.2B) and the results are reported in Table 10.1. It can be seen that the FSI model predicted slightly higher pressure differences between the TL and FL at all points. The FSI model predicted the TL to have a

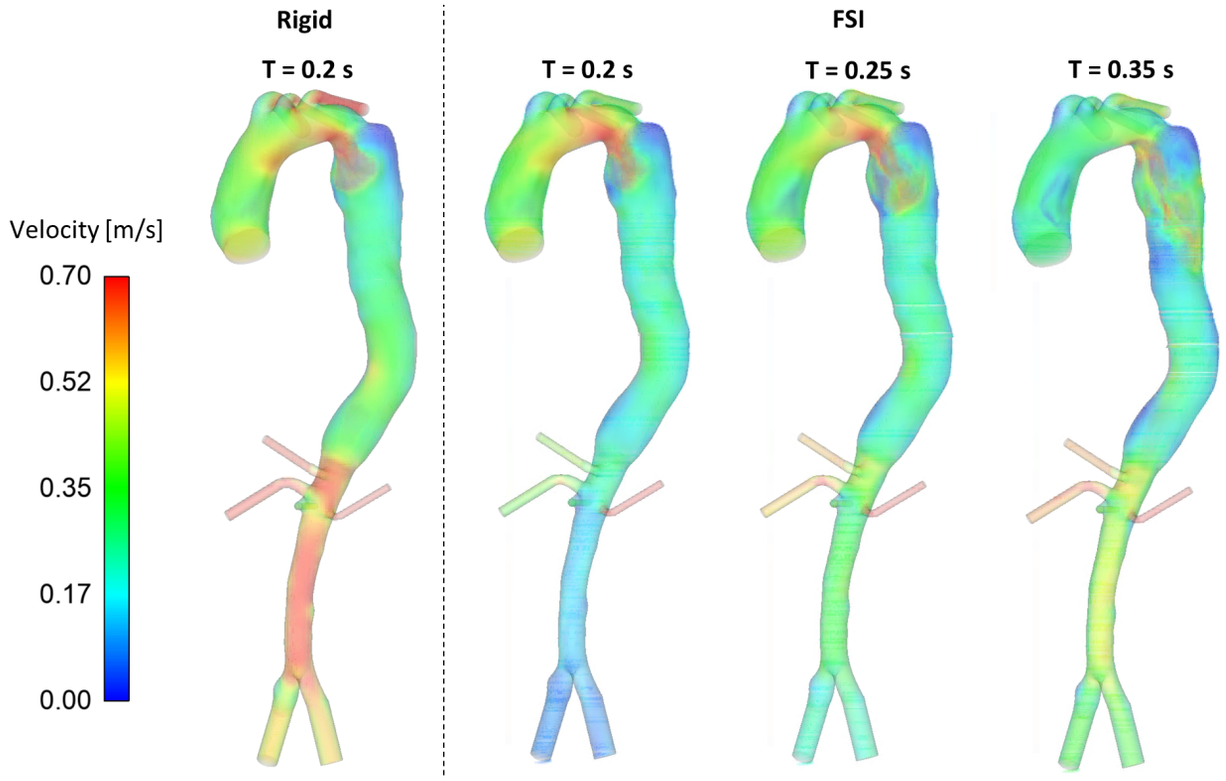

Figure 10.3: Velocity fields at peak systole (T = 0.2 s) in the rigid model, and at peak systole and into systolic deceleration in the FSI model.

higher pressure throughout, however the rigid model predicted a higher FL pressure on plane 4. As seen in Chapter 6, there were discrepancies between predicted pressures and invasively measured Doppler-wire (DW) readings. While still not exactly the same magnitude, the FSI cross-lumen pressure differences are closer in value to the DW readings than the rigid results.

Wall displacement also generally reduced velocities throughout the aorta. Figure 10.3 shows velocity fields at peak systole (T = 0.2 s) in the rigid model, and at peak systole and into systolic deceleration in the FSI model. It can be seen that at peak systole while similar velocity magnitudes are observed in the ascending aorta and in the high velocity jet through the primary entry tear between both models the size of this high velocity jet is reduced with the FSI model. Furthermore, velocities are lower within the dissection at this time point, and significantly lower in the abdominal aorta. Abdominal aorta velocities increased moving into the systolic deceleration but never reached the magnitudes observed in the rigid model. Additionally, at peak systole, the percentage of flow reporting to the FL decreased to 67% in the FSI model from 79% in the rigid model.

Table 10.1: Peak systolic pressure difference between the true (TL) and false lumen (FL) on 4 planes throughout the dissection, the location of which is shown in Figure 10.2B for the rigid and FSI model.

	Pressure difference(TL-FL) [mmHg]			
	P1	**P2**	**P3**	**P4**
Rigid	2.15	1.44	0.77	-0.70
FSI	2.19	1.59	1.71	0.13

This preliminary FSI analysis shows promising results of understanding the impact of the rigid wall assumption. The reduction of systolic pressure and thus reduction of pulse pressure observed in this FSI model is in-line with the findings of Chong et al. (2020). However, the increase in cross-lumen pressure difference and decrease in the percentage of flow reporting to the FL when wall and flap motion was accounted for is opposite to the results of Chong et al. (2020) and Bäumler et al. (2020). This may be due to a range of factors including the use of an idealised geometry in the work of Chong et al. (2020), the varying patient-specific dissection configuration between the current work and the work of Bäumler et al. (2020), and the preliminary nature of the current work. Work is continuing on this FSI model, with pre-stress and varying material properties being incorporated before the model is applied to more patients. Further work should also focus on post-TEVAR cases where the relatively high stiffness of the stent-graft compared to the aortic wall may alter hemodynamics and thrombus formation (Qiao et al. 2019, 2020), with the potential for the mismatch in compliance leading to complications such as stent-graft induced new entry tears (Menichini et al. 2018).

10.2.2 Laminar Flow Assumption

The flow was assumed to be laminar throughout this thesis. In all studies the peak Reynolds number (Re) was calculated and compared to the critical Re for transition to turbulence. All models showed a peak Re below the critical value (with the exception of P5 in Chapter 6 where the peak Re was very close to but slightly above the critical Re), and therefore it is fair to assume that modelling the flow as laminar would not significantly impact results. Furthermore, modelling turbulence adds computational cost, and given the aim of the thesis was to develop

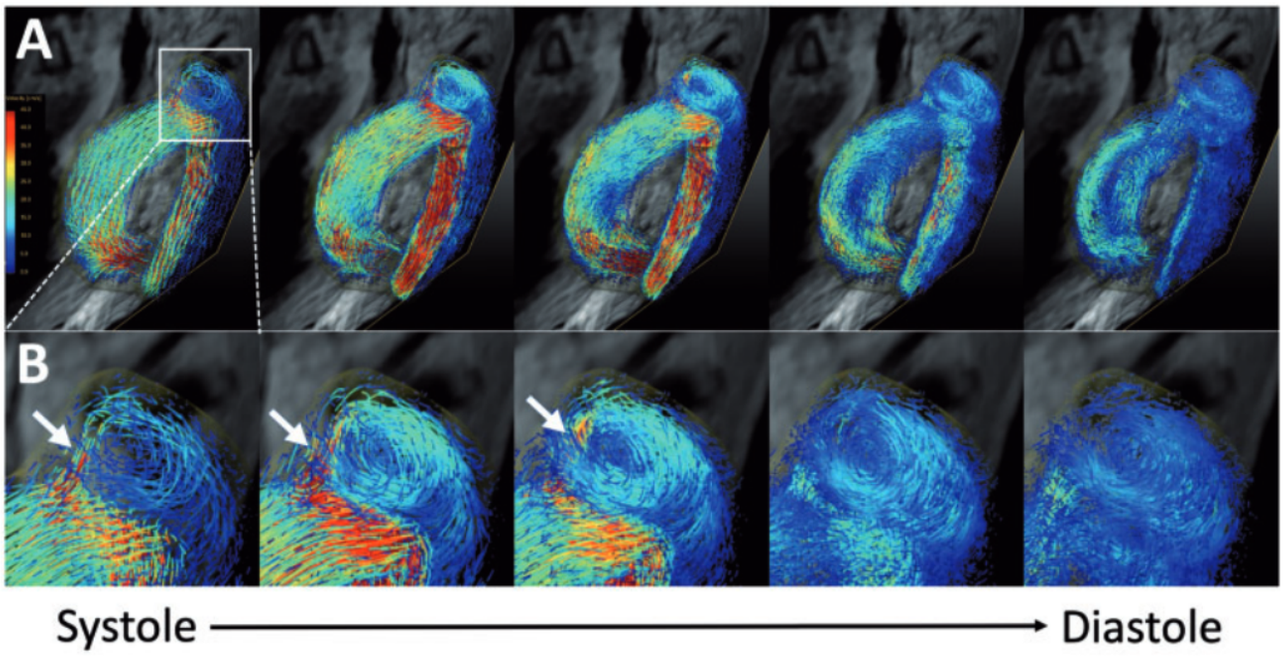

Figure 10.4: A: Helical flow visualised throughout the cardiac cycle. B: Magnified images show a high velocity jet through the entry-tear resulting in turbulence (Takahashi et al. 2021).

clinically applicable methodologies (and therefore keep computational costs to a minimum) the laminar assumption was optimal. However, there may have been regions of turbulent flow in the models. While aortic flow is generally assumed to be laminar, with turbulence more expected for patients with aortic valve diseases (Manchester et al. 2021), turbulence has been observed in healthy patients (Stein & Sabbah 1976). More importantly, a recent TBAD 4D-flow MRI based study by Takahashi et al. (2021) identified regions of turbulence in the FL, dependant on FL volume and velocities, which correlated to an increased risk of complications (Figure 10.4). There are different methods of varying computational cost available to model turbulence. The shear stress transport (SST-Tran) model, which has previously been utilised in CFD TBAD studies (Alimohammadi et al. 2015, Cheng et al. 2014), models transitional flow and is more computationally efficient than a full turbulence model such as large eddy simulations. Future work incorporating the SST-Tran model into the patient-specific CFD workflow will allow for the influence of the laminar assumption to be properly assessed.

10.2.3 Blood Properties

Blood is a non-Newtonian fluid and while the developed CFD workflow modelled such non-Newtonian behaviour through the Quemada model the parameters of this model are not patient-specific. Experimental studies to measure blood viscosity would be the most accurate method but this is not practical on a continuous basis in terms of time and equipment required. However, if blood tests are available for a patient, as is commonly done for patients in hospital undergoing treatment, the correct hematocrit level can be set in the Quemada model, improving the accuracy of the model.

10.2.4 Cohort Size

As discussed throughout the thesis, access to 4D-flow MRI is challenging. The developed 4D-flow MRI based CFD methodology was employed on five patients which presented with a range of morphologies, hemodynamics states, and flow features. This cohort provided a good data set to validate the model and generated a vast range of simulation input parameters. However, application of the model on a larger patient cohort would allow for further analysis of the varying hemodynamics states that can arise in TBAD, potentially leading to statistically significant hemodynamic parameters that are predictive of varying disease progressions. This would be hugely beneficial for clinicians when considering treatment options.

The clinical studies in Chapters 8 and 9 are also limited by the cohort size. While Chapter 8 presents a longitudinal study with multiple scans over a period of time, it is still a single subject study. This means that only one scenario of TBAD, in this case a high pressure patent FL, is studied and the conclusions are limited to this case. The influence of thrombus or varied pressure distributions could not be assessed. A larger cohort would allow for different TBAD forms to be evaluated and the influence of re-entry tears in these varying scenarios to be assessed. Chapter 9 presented three patients and while varying morphological parameters presented between the patients and the results showed that the SG-FRT distance impacted thrombus formation, further study on a larger cohort is again required to fully assess this

parameter in a range of dissections. Overall, while the results of this thesis are important in understand the influence of re-entry tears, larger cohorts are required to draw statistically significant conclusions on which clinical decisions can be based.

Bibliography

Alimohammadi, M., Agu, O., Balabani, S. & Díaz-Zuccarini, V. (2014), 'Development of a patient-specific simulation tool to analyse aortic dissections: Assessment of mixed patient-specific flow and pressure boundary conditions', *Medical Engineering and Physics* **36**(3), 275–284.
URL: *http://dx.doi.org/10.1016/j.medengphy.2013.11.003*

Alimohammadi, M., Pichardo-Almarza, C., Agu, O. & Díaz-Zuccarini, V. (2017), 'A multiscale modelling approach to understand atherosclerosis formation: A patient-specific case study in the aortic bifurcation', *Proceedings of the Institution of Mechanical Engineers, Part H: Journal of Engineering in Medicine* **231**(5), 378–390.

Alimohammadi, M., Sherwood, J. M., Karimpour, M., Agu, O., Balabani, S. & Díaz-Zuccarini, V. (2015), 'Aortic dissection simulation models for clinical support: Fluid-structure interaction vs. rigid wall models', *BioMedical Engineering Online* **14**(1), 1–16.

Allen, B. D., Aouad, P. J., Burris, N. S., Rahsepar, A. A., Jarvis, K. B., François, C. J., Barker, A. J., Malaisrie, S. C., Carr, J. C., Collins, J. D. & Markl, M. (2019), 'Detection and Hemodynamic Evaluation of Flap Fenestrations in Type B Aortic Dissection with 4D Flow MRI: Comparison with Conventional MRI and CT Angiography', *Radiology: Cardiothoracic Imaging* **1**(1), e180009.

Anand, M., Rajagopal, K. & Rajagopal, K. R. (2006), 'A model for the formation and lysis of blood clots', *Pathophysiology of Haemostasis and Thrombosis* .

ANSYS (2006), 'ANSYS CFX Technical Brief - Powerful CFD'.

ANSYS (2014), 'ANSYS Help Viewer: 4.2. Convergence Results and RMS'.

Armour, C., Guo, B., Pirola, S., Saitta, S., Liu, Y., Dong, Z. & Xu, X. Y. (2020), 'The influence of inlet velocity profile on predicted flow in type B aortic dissection', *Biomechanics and Modeling in Mechanobiology* (0123456789).
URL: *https://doi.org/10.1007/s10237-020-01395-4*

Armour, C. H., Menichini, C., Milinis, K., Gibbs, R. G. & Xu, X. Y. (2020), 'Location of Reentry Tears Affects False Lumen Thrombosis in Aortic Dissection Following TEVAR', *Journal of Endovascular Therapy* **27**(3), 396–404.

Austin, S. K. (2013), 'Haemostasis', *Medicine (United Kingdom)* **41**(4), 208–211.

Bäumler, K., Vedula, V., Sailer, A. M., Seo, J., Chiu, P., Mistelbauer, G., Chan, F. P., Fischbein, M. P., Marsden, A. L. & Fleischmann, D. (2020), 'Fluid–structure interaction simulations of patient-specific aortic dissection', *Biomechanics and Modeling in Mechanobiology* (0123456789).
URL: *https://doi.org/10.1007/s10237-020-01294-8*

Ben Ahmed, S., Dillon-Murphy, D. & Figueroa, C. A. (2016), 'Computational Study of Anatomical Risk Factors in Idealized Models of Type B Aortic Dissection', *European Journal of Vascular and Endovascular Surgery* **52**(6), 736–745.

Biasetti, J., Spazzini, P. G., Swedenborg, J. & Christian Gasser, T. (2012), 'An integrated fluid-chemical model toward modeling the formation of intra-luminal thrombus in abdominal aortic aneurysms', *Frontiers in Physiology* **3**.

Birjiniuk, J., Timmins, L. H., Young, M., Leshnower, B. G., Oshinski, J. N., Ku, D. N. & Veeraswamy, R. K. (2017), 'Pulsatile Flow Leads to Intimal Flap Motion and Flow Reversal in an In Vitro Model of Type B Aortic Dissection', *Cardiovascular Engineering and Technology* **8**(3), 378–389.

Birjiniuk, J., Veeraswamy, R. K., Oshinski, J. N. & Ku, D. N. (2019), 'Intermediate fenestrations reduce flow reversal in a silicone model of Stanford Type B aortic dissection', *Journal of*

Biomechanics **93**, 101–110.

URL: *https://doi.org/10.1016/j.jbiomech.2019.06.019*

Bonfanti, M., Balabani, S., Greenwood, J. P., Puppala, S., Homer-Vanniasinkam, S. & Diáz-Zuccarini, V. (2017), 'Computational tools for clinical support: A multi-scale compliant model for haemodynamic simulations in an aortic dissection based on multi-modal imaging data', *Journal of the Royal Society Interface* **14**(136).

Bonfanti, M., Franzetti, G., Maritati, G., Homer-Vanniasinkam, S., Balabani, S. & Díaz-Zuccarini, V. (2019), 'Patient-specific haemodynamic simulations of complex aortic dissections informed by commonly available clinical datasets', *Medical Engineering and Physics* **71**, 45–55.

Bozzi, S., Morbiducci, U., Gallo, D., Ponzini, R., Rizzo, G., Bignardi, C. & Passoni, G. (2017), 'Uncertainty propagation of phase contrast-MRI derived inlet boundary conditions in computational hemodynamics models of thoracic aorta', *Computer Methods in Biomechanics and Biomedical Engineering* **20**(10), 1104–1112.

URL: *https://doi.org/10.1080/10255842.2017.1334770*

Brunkwall, J., Kasprzak, P., Verhoeven, E., Heijmen, R., Taylor, P., Alric, P., Canaud, L., Janotta, M., Raithel, D., Malina, M., Resch, T., Eckstein, H. H., Ockert, S., Larzon, T., Carlsson, F., Schumacher, H., Classen, S., Schaub, P., Lammer, J., Lönn, L., Clough, R. E., Rampoldi, V., Trimarchi, S., Fabiani, J. N., Böckler, D., Kotelis, D., von Tenng-Kobligk, H., Mangialardi, N., Ronchey, S., Dialetto, G. & Matoussevitch, V. (2014), 'Endovascular repair of acute uncomplicated aortic type b dissection promotes aortic remodelling: 1 year results of the ADSORB trial', *European Journal of Vascular and Endovascular Surgery* **48**(3), 285–291.

Burris, N. S., Nordsletten, D. A., Sotelo, J. A., Grogan-Kaylor, R., Houben, I. B., Figueroa, C. A., Uribe, S. & Patel, H. J. (2020), 'False lumen ejection fraction predicts growth in type B aortic dissection: preliminary results', *European journal of cardio-thoracic surgery : official journal of the European Association for Cardio-thoracic Surgery* **57**(5), 896–903.

Burris, N. S., Patel, H. J. & Hope, M. D. (2019), 'Retrograde flow in the false lumen: Marker of

a false lumen under stress?', *Journal of Thoracic and Cardiovascular Surgery* **157**(2), 488–491.
URL: *https://doi.org/10.1016/j.jtcvs.2018.06.092*

Campbell, I. C., Ries, J., Dhawan, S. S., Quyyumi, A. A., Taylor, W. R. & Oshinski, J. N. (2012), 'Effect of inlet velocity profiles on patient-specific computational fluid dynamics simulations of the carotid bifurcation', *Journal of Biomechanical Engineering* **134**(5), 1–8.

Chandra, S., Raut, S. S., Jana, A., Biederman, R. W., Doyle, M., Muluk, S. C. & Finol, E. A. (2013), 'Fluid-structure interaction modeling of abdominal aortic aneurysms: The impact of patient-specific inflow conditions and fluid/solid coupling', *Journal of Biomechanical Engineering* **135**(8).

Chen, D., Müller-Eschner, M., Kotelis, D., Böckler, D., Ventikos, Y. & Von Tengg-Kobligk, H. (2013), 'A longitudinal study of Type-B aortic dissection and endovascular repair scenarios: Computational analyses', *Medical Engineering and Physics* **35**(9), 1321–1330.
URL: *http://dx.doi.org/10.1016/j.medengphy.2013.02.006*

Chen, D., Müller-Eschner, M., von Tengg-Kobligk, H., Barber, D., Böckler, D., Hose, R. & Ventikos, Y. (2013), 'A patient-specific study of type-B aortic dissection: Evaluation of true-false lumen blood exchange', *BioMedical Engineering Online* **12**(1), 1–16.

Chen, I. M., Chen, P. L., Huang, C. Y., Weng, S. H., Chen, W. Y. & Shih, C. C. (2017), 'Factors Affecting Optimal Aortic Remodeling After Thoracic Endovascular Aortic Repair of Type B (IIIb) Aortic Dissection', *CardioVascular and Interventional Radiology* **40**(5), 671–681.

Chen, Z., Yu, H., Shi, Y., Zhu, M., Wang, Y., Hu, X., Zhang, Y., Chang, Y., Xu, M. & Gao, W. (2017), 'Vascular Remodelling Relates to an Elevated Oscillatory Shear Index and Relative Residence Time in Spontaneously Hypertensive Rats', *Scientific Reports* **7**(1), 1–10.

Cheng, Z., Juli, C., Wood, N. B., Gibbs, R. G. J. & Xu, X. Y. (2014), 'Predicting flow in aortic dissection: Comparison of computational model with PC-MRI velocity measurements', *Medical Engineering and Physics* **36**, 1176–1184.

Cheng, Z., Riga, C., Chan, J., Hamady, M., Wood, N. B., Cheshire, N. J., Xu, Y. & Gibbs, R. G. (2013), Initial findings and potential applicability of computational simulation of the aorta in acute type B dissection, *in* 'Journal of Vascular Surgery', Vol. 57, pp. 35S–43S.

Cheng, Z., Tan, F. P. P., Riga, C. V., Bicknell, C. D., Hamady, M. S., Gibbs, R. G. J., Wood, N. B. & Xu, X. Y. (2010), 'Analysis of Flow Patterns in a Patient-Specific Aortic Dissection Model', *Journal of Biomechanical Engineering* .

Cheng, Z., Wood, N. B., Gibbs, R. G. & Xu, X. Y. (2014), 'Geometric and Flow Features of Type B Aortic Dissection: Initial Findings and Comparison of Medically Treated and Stented Cases', *Annals of Biomedical Engineering* **43**(1), 177–189.

Chong, M. Y., Gu, B., Chan, B. T., Ong, Z. C., Xu, X. Y. & Lim, E. (2020), 'Effect of intimal flap motion on flow in acute type B aortic dissection by using fluid-structure interaction', *International Journal for Numerical Methods in Biomedical Engineering* **36**(12), 1–22.

Chung, J. W., Elkins, C., Sakai, T., Kato, N., Vestring, T., Semba, C. P., Slonim, S. M. & Dake, M. D. (2000*a*), 'True-lumen collapse in aortic dissection. Part I. Evaluation of causative factors in phantoms with pulsatile flow', *Radiology* **214**(1), 87–98.

Chung, J. W., Elkins, C., Sakai, T., Kato, N., Vestring, T., Semba, C. P., Slonim, S. M. & Dake, M. D. (2000*b*), 'True-lumen collapse in aortic dissection part II. Evaluation of treatment methods in phantoms with pulsatile flow', *Radiology* **214**(1), 99–106.

Clough, R. E. & Nienaber, C. A. (2015), 'Management of acute aortic syndrome', *Nature Reviews Cardiology* **12**(2), 103–114.

Clough, R. E., Waltham, M., Giese, D., Taylor, P. R. & Schaeffter, T. (2012), 'A new imaging method for assessment of aortic dissection using four-dimensional phase contrast magnetic resonance imaging', *Journal of Vascular Surgery* **55**(4), 914–923.
URL: *http://dx.doi.org/10.1016/j.jvs.2011.11.005*

Concannon, J., Hynes, N., McMullen, M., Smyth, E., Moerman, K., McHugh, P. E., Sultan, S., Karmonik, C. & McGarry, J. P. (2020), 'A Dual-VENC Four-Dimensional Flow MRI

Framework for Analysis of Subject-Specific Heterogeneous Nonlinear Vessel Deformation', *Journal of Biomechanical Engineering* **142**(11), 1–15.

Craven, B. A., Paterson, E. G., Settles, G. S. & Lawson, M. J. (2009), 'Development and verification of a high-fidelity computational fluid dynamics model of canine nasal airflow', *Journal of Biomechanical Engineering* **131**(9), 1–11.

De Jong, P. A., Hellings, W. E., Takx, R. A., Išgum, I., Van Herwaarden, J. A. & Mali, W. P. M. (2014), 'Computed tomography of aortic wall calcifications in aortic dissection patients', *PLoS ONE* **9**(7), 1–5.

Dean, L. (2005), *Blood Groups and Red Cell Antigens*, National Center for Biotechnology Information US, Bethesda.

Desai, C. S. & Kundu, T. (2001), *Introductory Finite Element Method*, CRC Press LLC.

Dillon-Murphy, D., Noorani, A., Nordsletten, D. & Figueroa, C. A. (2016), 'Multi-modality image-based computational analysis of haemodynamics in aortic dissection', *Biomechanics and Modeling in Mechanobiology* **15**(4), 857–876.

Du, T., Hu, D. & Cai, D. (2015), 'Outflow boundary conditions for blood flow in arterial trees', *PLoS ONE* **10**(5), 1–22.

Ethier, C. R. & Simmons, C. A. (2007), The Circulatory System, *in* 'Introductory Biomechanics - From Cells to Organisms', Cambridge University Press, chapter 4, pp. 164–239.

Evangelista, A., Salas, A., Ribera, A., Ferreira-González, I., Cuellar, H., Pineda, V., González-Alujas, T., Bijnens, B., Permanyer-Miralda, G. & Garcia-Dorado, D. (2012), 'Long-term outcome of aortic dissection with patent false lumen: Predictive role of entry tear size and location', *Circulation* **125**, 3133–3141.

Fan, Y., Cheng, S. W.-K., Qing, K.-X. & Chow, K.-W. (2010), 'Endovascular repair of type B aortic dissection: a study by computational fluid dynamics', *Journal of Biomedical Science and Engineering* **03**(09), 900–907.
URL: *http://www.scirp.org/journal/doi.aspx?DOI=10.4236/jbise.2010.39120*

François, C. J., Markl, M., Schiebler, M. L., Niespodzany, E., Landgraf, B. R., Schlensak, C. & Frydrychowicz, A. (2013), 'Four-dimensional, flow-sensitive magnetic resonance imaging of blood flow patterns in thoracic aortic dissections', *Journal of Thoracic and Cardiovascular Surgery* **145**(5), 1359–1366.

Frank J. Criado (2011), 'Aortic Dissection - A 250 Year Prespective', *Texas Heart Institute Journal* **38**(6).

Ge, Y. Y., Guo, W., Cheshire, N., Liu, X. P., Jia, X., Xiong, J., Ma, X. H. & Zhang, H. P. (2017), 'Preoperative thoracic false lumen branches relate to aortic remodeling after thoracic endovascular aortic repair for DeBakey IIIb aortic dissection', *Journal of Vascular Surgery* **65**(3), 659–668.

Girish, A., Padala, M., Kalra, K., McIver, B. V., Veeraswamy, R. K., Chen, E. P. & Leshnower, B. G. (2016), 'The Impact of Intimal Tear Location and Partial False Lumen Thrombosis in Acute Type B Aortic Dissection', *Annals of Thoracic Surgery* **102**(6), 1925–1932.

Goodman, P. D., Barlow, E. T., Crapo, P. M., Mohammad, S. F. & Solen, K. A. (2005), 'Computational model of device-induced thrombosis and thromboembolism', *Annals of Biomedical Engineering* **33**(6), 780–797.

Guo, B., Dong, Z., Pirola, S., Liu, Y., Menichini, C., Xu, X. Y., Guo, D. & Fu, W. (2019), 'Dissection Level Within Aortic Wall Layers is Associated with Propagation of Type B Aortic Dissection: A Swine Model Study', *European Journal of Vascular and Endovascular Surgery* **58**(3), 415–425.
URL: *https://doi.org/10.1016/j.ejvs.2019.02.026*

Ha, H., Kim, G. B., Kweon, J., Kim, Y. H., Kim, N., Yang, D. H. & Lee, S. J. (2016), 'Multi-VENC acquisition of four-dimensional phase-contrast MRI to improve precision of velocity field measurement', *Magnetic Resonance in Medicine* **75**(5), 1909–1919.

Hagan, P. G., Nienaber, C. A., Isselbacher, E. M., Bruckman, D., Karavite, D. J., Russman, P. L., Evangelista, A., Moore, A. G., Malouf, J. F., Pape, L. A., Gaca, C., Armstrong, W. F.,

Deeb, G. M. & Eagle, K. A. (2000), 'The International Registry of Acute Aortic Dissection (IRAD)', *The Journal of the American Medical Association* **283**(7), 897–903.

Hartnell, G. G. & Gates, J. (2005), 'Aortic fenestration: A why, when, and how-to guide', *Radiographics* **25**(1), 175–189.

Huang, C. Y., Hsu, H. L., Chen, P. L., Chen, I. M., Hsu, C. P. & Shih, C. C. (2018), 'The Impact of Distal Stent Graft–Induced New Entry on Aortic Remodeling of Chronic Type B Dissection', *Annals of Thoracic Surgery* **105**(3), 785–793.
URL: *https://doi.org/10.1016/j.athoracsur.2017.08.039*

Institute for Quality and Efficiency in Health Care (2019), 'How does the blood circulatory system work?'.
URL: *https://www.ncbi.nlm.nih.gov/books/NBK279250/*

Jarvis, K., Pruijssen, J. T., Son, A. Y., Allen, B. D., Soulat, G., Vali, A., Barker, A. J., Hoel, A. W., Eskandari, M. K., Malaisrie, S. C., Carr, J. C., Collins, J. D. & Markl, M. (2020), 'Parametric Hemodynamic 4D Flow MRI Maps for the Characterization of Chronic Thoracic Descending Aortic Dissection', *Journal of Magnetic Resonance Imaging* **51**(5), 1357–1368.

Jiang, Y., Qiu, Y., Li, D., Yuan, D., Zheng, T. & Peng, L. (2019), 'Influence of aortic branch arteries on the hemodynamics of patient-specific type B aortic dissection following TEVAR', *Medicine in Novel Technology and Devices* **4**(37), 100028.

Kamman, A. V., Brunkwall, J., Verhoeven, E. L., Heijmen, R. H., Trimarchi, S., Kasprzak, P., Brunkwall, J., Heijmen, R., Alric, P., Verhoeven, E., Schumacher, H., Fabiani, J. N., Eckstein, H. H., Taylor, P., Mailina, M., Mangialardi, N., Larzon, T., Böckler, D., Lönn, L., Dialetto, G., Trimarchi, S. & Lammer, J. (2017), 'Predictors of aortic growth in uncomplicated type B aortic dissection from the Acute Dissection Stent Grafting or Best Medical Treatment (ADSORB) database', *Journal of Vascular Surgery* **65**(4), 964–971.

Karino, T., Goldsmith, H. L., Motomiya, M., Mabuchi, S. & Sohara, Y. (1987), 'Flow Patterns in Vessels of Simple and Complex Geometriesa', *Annals of the New York Academy of Sciences* **516**(1), 422–441.

Karmonik, C., Bismuth, J., Davies, M. G., Shah, D. J., Younes, H. K. & Lumsden, A. B. (2011), 'A computational fluid dynamics study pre-and post-stent graft placement in an acute type B aortic dissection', *Vascular and Endovascular Surgery* **45**(2), 157–164.

Karmonik, C., Bismuth, J., Shah, D. J., Davies, M. G., Purdy, D. & Lumsden, A. B. (2011), 'Computational study of haemodynamic effects of entry- and exit-tear coverage in a DeBakey type III aortic dissection: Technical report', *European Journal of Vascular and Endovascular Surgery* **42**(2), 172–177.
URL: *http://dx.doi.org/10.1016/j.ejvs.2011.04.008*

Karmonik, C., Bismuth, J. X., Davies, M. G. & Lumsden, A. B. (2008), 'Computational hemodynamics in the human aorta: A computational fluid dynamics study of three cases with patient-specific geometries and inflow rates', *Technology and Health Care* **16**(5), 343–354.

Karmonik, C., Müller-Eschner, M., Partovi, S., Geisbüsch, P., Ganten, M. K., Bismuth, J., Davies, M. G., Böckler, D., Loebe, M., Lumsden, A. B. & Tengg-Kobligk, H. V. (2013), 'Computational fluid dynamics investigation of chronic aortic dissection hemodynamics versus normal aorta', *Vascular and Endovascular Surgery* **47**(8), 625–631.

Karmonik, C., Partovi, S., Müller-Eschner, M., Bismuth, J., Davies, M. G., Shah, D. J., Loebe, M., Böckler, D., Lumsden, A. B. & Von Tengg-Kobligk, H. (2012), 'Longitudinal computational fluid dynamics study of aneurysmal dilatation in a chronic DeBakey type III aortic dissection', *Journal of Vascular Surgery* **56**(1), 260–263.
URL: *http://dx.doi.org/10.1016/j.jvs.2012.02.064*

Khan Academy (2014), 'Hematologic system introduction: Coagulation cascade'.
URL: *https://www.khanacademy.org/science/health-and-medicine/advanced-hematologic-system/hematologic-system-introduction/v/coagulation-cascade*

Kim, T.-H., Ko, Y.-G., Kwon, S. W., Choi, D., Lee, D. Y., Shim, W.-H. & Hyon, M. S. (2014), 'Large False Lumen Area Is a Predictor of Failed False Lumen Volume Reduction After Stent-Graft Repair in Type B Aortic Dissection', *Journal of Endovascular Therapy* **21**, 697–706.

Kitamura, T., Torii, S., Oka, N., Horai, T., Itatani, K., Yoshii, T., Nakamura, Y., Shibata, M., Tamura, T., Araki, H., Matsunaga, Y., Sato, H. & Miyaji, K. (2015), 'Impact of the entry site on late outcome in acute Stanford type B aortic dissection', *European Journal of Cardio-thoracic Surgery* **48**(5), 655–661.

Kotelis, D., Grebe, G., Kraus, P., Müller-Eschner, M., Bischoff, M., von Tengg-Kobligk, H. & Böckler, D. (2016), 'Morphologic predictors of aortic expansion in chronic type B aortic dissection', *Vascular* **24**(2), 187–193.

Kousera, C. A., Wood, N. B., Seed, W. A., Torii, R., O'Regan, D. & Xu, X. Y. (2012), 'A Numerical Study of Aortic Flow Stability and Comparison With ¡i¿In Vivo¡/i¿ Flow Measurements', *Journal of Biomechanical Engineering* **135**(1), 011003.
URL: *http://biomechanical.asmedigitalcollection.asme.org/article.aspx?doi=10.1115/1.4023132*

Kreibich, M., Berger, T., Morlock, J., Kondov, S., Scheumann, J., Kari, F. A., Rylski, B., Siepe, M., Beyersdorf, F. & Czerny, M. (2018), 'The frozen elephant trunk technique for the treatment of acute complicated type B aortic dissection', *European Journal of Cardio-thoracic Surgery* **53**(3), 525–530.

Krol, E. & Panneton, J. M. (2017), 'Uncomplicated Acute Type B Aortic Dissection: Selection Guidelines for TEVAR', *Annals of Vascular Diseases* **10**(3), 165–169.

Kuron, M. (2015), '3 Criteria for Assessing CFD Convergence'.
URL: *https://www.engineering.com/DesignSoftware/DesignSoftwareArticles/ArticleID/9296/3-Criteria-for-Assessing-CFD-Convergence.aspx*

Lalkhen, A. G. & McCluskey, A. (2008), 'Clinical tests: Sensitivity and specificity', *Continuing Education in Anaesthesia, Critical Care and Pain* **8**(6), 221–223.

Landenhed, M., Engström, G., Gottsäter, A., Caulfield, M. P., Hedblad, B., Newton-Cheh, C., Melander, O. & Smith, J. G. (2015), 'Risk profiles for aortic dissection and ruptured or surgically treated aneurysms: a prospective cohort study', *Journal of the American Heart Association* **4**(1), e001513.

Leiderman, K. & Fogelson, A. L. (2011), 'Grow with the flow: A spatial-temporal model of platelet deposition and blood coagulation under flow', *Mathematical Medicine and Biology* **28**, 47–84.

Lewis, M. I. & McKenna, R. J. (2010), Disorders of the lung, *in* 'Medical Management of the Thoracic Surgery Patient', pp. 139–146.

Li, F. R., Wu, X., Yuan, J., Wang, J., Mao, C. & Wu, X. (2018), 'Comparison of thoracic endovascular aortic repair, open surgery and best medical treatment for type B aortic dissection: A meta-analysis', *International Journal of Cardiology* **250**, 240–246.
URL: *https://doi.org/10.1016/j.ijcard.2017.10.050*

Liu, F., Ge, Y. Y., Guo, W., Liu, X. P., Jia, X., Xiong, J. & Ma, X. H. (2018), 'Preoperative thoracic false lumen branches are predictors of aortic enlargement after stent grafting for DeBakey IIIb aortic dissection', *Journal of Thoracic and Cardiovascular Surgery* **155**(1), 21–29.
URL: *https://doi.org/10.1016/j.jtcvs.2017.09.010*

Liu, L., Zhang, S., Lu, Q., Jing, Z., Zhang, S. & Xu, B. (2016), 'Impact of oversizing on the risk of retrograde dissection after TEVAR for acute and chronic type B dissection', *Journal of Endovascular Therapy* **23**(4), 620–625.

Maceira, A. M., Prasad, S. K., Khan, M. & Pennell, D. J. (2006), 'Reference right ventricular systolic and diastolic function normalized to age, gender and body surface area from steady-state free precession cardiovascular magnetic resonance', *European Heart Journal* **27**(23), 2879–2888.

Manchester, E. L., Pirola, S., Salmasi, M. Y., O'Regan, D. P., Athanasiou, T. & Xu, X. Y. (2021), 'Analysis of Turbulence Effects in a Patient-Specific Aorta with Aortic Valve Stenosis', *Cardiovascular Engineering and Technology* .

Marui, A., Mochizuki, T., Koyama, T. & Mitsui, N. (2007), 'Degree of fusiform dilatation of the proximal descending aorta in type B acute aortic dissection can predict late aortic events', *Journal of Thoracic and Cardiovascular Surgery* **134**(5), 1163–1170.

Matsuzaki, Y., Yamasaki, T., Hohri, Y. & Hiramatsu, T. (2019), 'Surgical Strategies for Type B Aortic Dissection by Frozen Elephant Trunk', *Annals of Vascular Diseases* **12**(4), 473–479.

McMahon, M. a. & Squirrell, C. a. (2010), 'Multidetector CT of Aortic Dissection: A Pictorial Review', *Radiographics : a review publication of the Radiological Society of North America, Inc* **30**(2), 445–460.

McMichael, M. (2005), 'Primary hemostasis', *Journal of Veterinary Emergency and Critical Care* **15**(1), 1–8.

Menichini, C. (2018), 'Mathematical Modelling of Thrombus Formation in Type B Aortic Dissection', (February).

Menichini, C., Cheng, Z., Gibbs, R. G. J. & Xu, X. Y. (2016), 'Predicting false lumen thrombosis in patient-specific models of aortic dissection', *Journal of The Royal Society Interface* **13**(124), 1–11.

Menichini, C., Cheng, Z., Gibbs, R. G. & Xu, X. Y. (2018), 'A computational model for false lumen thrombosis in type B aortic dissection following thoracic endovascular repair', *Journal of Biomechanics* **66**(36-43).

Menichini, C., Pirola, S., Guo, B., Fu, W., Dong, Z. & Xu, X. Y. (2018), 'High Wall Stress May Predict the Formation of Stent-Graft–Induced New Entries After Thoracic Endovascular Aortic Repair', *Journal of Endovascular Therapy* **25**(5), 571–577.

Menichini, C. & Xu, X. Y. (2016), 'Mathematical modeling of thrombus formation in idealized models of aortic dissection: initial findings and potential applications', *Journal of Mathematical Biology* **73**(5), 1205–1226.

Mimouni, Z. (2016), 'The Rheological Behavior of Human Blood - Comparison of Two Models', *Open Journal of Biophysics* **6**(2), 29–33.

Miyazaki, S., Itatani, K., Furusawa, T., Nishino, T., Sugiyama, M., Takehara, Y. & Yasukochi, S. (2017), 'Validation of numerical simulation methods in aortic arch using 4D Flow MRI', *Heart and Vessels* **32**(8), 1032–1044.

Morbiducci, U., Ponzini, R., Gallo, D., Bignardi, C. & Rizzo, G. (2013), 'Inflow boundary conditions for image-based computational hemodynamics: Impact of idealized versus measured velocity profiles in the human aorta', *Journal of Biomechanics* **46**(1), 102–109.
URL: *http://dx.doi.org/10.1016/j.jbiomech.2012.10.012*

Moyle, K. R., Antiga, L. & Steinman, D. A. (2006), 'Inlet conditions for image-based CFD models of the carotid bifurcation: Is it reasonable to assume fully developed flow?', *Journal of Biomechanical Engineering* **128**(3), 371–379.

Mukaka, M. M. (2012), 'Statistics corner: A guide to appropriate use of correlation coefficient in medical research', *Malawi Medical Journal* **24**(3), 69–71.

Myers, J. G., Moore, J. A., Ojha, M., Johnston, K. W. & Ethier, C. R. (2001), 'Factors influencing blood flow patterns in the human right coronary artery', *Annals of Biomedical Engineering* **29**(2), 109–120.

Nauta, F. J., Lau, K. D., Arthurs, C. J., Eagle, K. A., Williams, D. M., Trimarchi, S., Patel, H. J. & Figueroa, C. A. (2017), 'Computational Fluid Dynamics and Aortic Thrombus Formation Following Thoracic Endovascular Aortic Repair', *Annals of Thoracic Surgery* **103**(6), 1914–1921.
URL: *http://dx.doi.org/10.1016/j.athoracsur.2016.09.067*

Nett, E. J., Johnson, K. M., Frydrychowicz, A., Del Rio, A. M., Schrauben, E., Francois, C. J. & Wieben, O. (2012), 'Four-dimensional phase contrast MRI with accelerated dual velocity encoding', *Journal of Magnetic Resonance Imaging* **35**(6), 1462–1471.

Ngoepe, M. N. & Ventikos, Y. (2016), 'Computational modelling of clot development in patient-specific cerebral aneurysm cases', *Journal of Thrombosis and Haemostasis* **14**(2), 262–272.

Nienaber, C. A., Clough, R. E., Sakalihasan, N., Suzuki, T., Gibbs, R., Mussa, F., Jenkins, M. T., Thompson, M. M., Evangelista, A., Yeh, J. S., Cheshire, N., Rosendahl, U. & Pepper, J. (2016), 'Aortic dissection', *Nature Reviews Disease Primers* **2**.

Nienaber, C. A., Divchev, D., Palisch, H., Clough, R. E. & Richartz, B. (2014), 'Early and late management of type B aortic dissection', *Heart* **100**(19), 1491–1497.

Nienaber, C. A., Rousseau, H., Eggebrecht, H., Kische, S., Fattori, R., Rehders, T. C., Kundt, G., Scheinert, D., Czerny, M., Kleinfeldt, T., Zipfel, B., Labrousse, L. & Ince, H. (2009), 'Randomized comparison of strategies for type B aortic dissection: The INvestigation of STEnt grafts in aortic dissection (INSTEAD) trial', *Circulation* **120**(25), 2519–2528.

Nienaber, C. A., Zannetti, S., Barbieri, B., Kische, S., Schareck, W. & Rehders, T. C. (2005), 'INvestigation of STEnt grafts in patients with type B aortic dissection: Design of the INSTEAD trial - A prospective, multicenter, European randomized trial', *American Heart Journal* **149**(4), 592–599.

Organisation, W. H. (2021), 'Cardiovascular diseases (CVDs)'.
URL: *https://www.who.int/news-room/fact-sheets/detail/cardiovascular-diseases-(cvds)*

Osswald, A., Karmonik, C., Anderson, J. R., Rengier, F., Karck, M., Engelke, J., Kallenbach, K., Kotelis, D., Partovi, S., Böckler, D. & Ruhparwar, A. (2017), 'Elevated Wall Shear Stress in Aortic Type B Dissection May Relate to Retrograde Aortic Type A Dissection: A Computational Fluid Dynamics Pilot Study', *European Journal of Vascular and Endovascular Surgery* **54**(3), 324–330.
URL: *http://dx.doi.org/10.1016/j.ejvs.2017.06.012*

Pape, L. A., Awais, M., Woznicki, E. M., Suzuki, T., Trimarchi, S., Evangelista, A., Myrmel, T., Larsen, M., Harris, K. M., Greason, K., Di Eusanio, M., Bossone, E., Montgomery, D. G., Eagle, K. A., Nienaber, C. A., Isselbacher, E. M. & O'Gara, P. (2015), 'Presentation, diagnosis, and outcomes of acute aortic dissection: 17-year trends from the international registry of acute aortic dissection', *Journal of the American College of Cardiology* **66**(4), 350–358.

Peterss, S., Mansour, A. M., Ross, J. A., Vaitkeviciute, I., Charilaou, P., Dumfarth, J., Fang, H., Ziganshin, B. A., Rizzo, J. A., Adeniran, A. J. & Elefteriades, J. A. (2016), 'Changing Pathology of the Thoracic Aorta From Acute to Chronic Dissection: Literature Review and Insights', *Journal of the American College of Cardiology* **68**(10), 1054–1065.

Pirola, S., Cheng, Z., Jarral, O. A., O'Regan, D. P., Pepper, J. R., Athanasiou, T. & Xu, X. Y.

(2017), 'On the choice of outlet boundary conditions for patient-specific analysis of aortic flow using computational fluid dynamics', *Journal of Biomechanics* **60**, 15–21.

Pirola, S., Guo, B., Menichini, C., Saitta, S., Fu, W., Dong, Z. & Xu, X. Y. (2019), '4-D Flow mri-based computational analysis of blood flow in patient-specific aortic dissection', *IEEE Transactions on Biomedical Engineering* **66**(12), 3411–3419.

Pirola, S., Jarral, O. A., O'Regan, D. P., Asimakopoulos, G., Anderson, J. R., Pepper, J. R., Athanasiou, T. & Xu, X. Y. (2018), 'Computational study of aortic hemodynamics for patients with an abnormal aortic valve: The importance of secondary flow at the ascending aorta inlet', *APL Bioengineering* **2**(2), 026101.

Puiseux, T., Sewonu, A., Meyrignac, O., Rousseau, H., Nicoud, F., Mendez, S. & Moreno, R. (2019), 'Reconciling PC-MRI and CFD: An in-vitro study', *NMR in Biomedicine* **32**(5), 1–14.

Qiao, A., Yin, W. & Chu, B. (2015), 'Numerical simulation of fluid-structure interaction in bypassed DeBakey III aortic dissection', *Computer Methods in Biomechanics and Biomedical Engineering* **18**(11), 1173–1180.

Qiao, Y., Fan, J., Ding, Y., Zhu, T. & Luo, K. (2019), 'A primary computational fluid dynamics study of pre-and post-tevar with intentional left subclavian artery coverage in a type b aortic dissection', *Journal of Biomechanical Engineering* **141**(11).

Qiao, Y., Mao, L., Zhu, T., Fan, J. & Luo, K. (2020), 'Biomechanical implications of the fenestration structure after thoracic endovascular aortic repair', *Journal of Biomechanics* **99**, 109478.
URL: *https://doi.org/10.1016/j.jbiomech.2019.109478*

Qiao, Y., Zeng, Y., Ding, Y., Fan, J., Luo, K. & Zhu, T. (2019), 'Numerical simulation of two-phase non-Newtonian blood flow with fluid-structure interaction in aortic dissection', *Computer Methods in Biomechanics and Biomedical Engineering* **22**(6), 620–630.
URL: *https://doi.org/10.1080/10255842.2019.1577398*

Qin, Y. L., Deng, G., Li, T. X., Jing, R. W. & Teng, G. J. (2012), 'Risk factors of incomplete

thrombosis in the false lumen after endovascular treatment of extensive acute type B aortic dissection', *Journal of Vascular Surgery* **56**(1232-1238).

Qin, Y.-L., Wang, F., Li, T.-X., Ding, W., Deng, G., Xie, B. & Teng, G.-J. (2016), 'Endovascular Repair Compared With Medical Management of Patients With Uncomplicated Type B Acute Aortic Dissection', *Journal of the American College of Cardiology* .

Quemada, D. (1978), 'Rheology of eoncentrated disperse systems II . A model for non-newtonian shear viscosity in steady flows', *Rheologica Acta* **17**, 632–642.

Reymond, P., Merenda, F., Perren, F. & Ru, D. (2009), 'Validation of a One-Dimensional Model of the Systemic Arterial Tree', *American Journal of Physiology - Heart and Circulatory Physiology* **297**, 208–222.

Rinaudo, A., D'Ancona, G., Lee, J. J., Pilato, G., Amaducci, A., Baglini, R., Follis, F., Pilato, M. & Pasta, S. (2014), 'Predicting Outcome of Aortic Dissection with Patent False Lumen by Computational Flow Analysis', *Cardiovascular Engineering and Technology* **5**(2), 176–188.

Roache, P. J. (1994), 'Perspective: A method for uniform reporting of grid refinement studies', *Journal of Fluids Engineering, Transactions of the ASME* **116**(3), 405–413.

Rosentrater, K. A. & Flores, R. A. (1997), 'Physical and rheological properties of slaughterhouse swine blood and blood components', *Transactions of the American Society of Agricultural Engineers* **40**(3), 683–689.

Rudenick, P. A., Bijnens, B. H., García-Dorado, D. & Evangelista, A. (2013), 'An in vitro phantom study on the influence of tear size and configuration on the hemodynamics of the lumina in chronic type B aortic dissections', *Journal of Vascular Surgery* **57**(2), 464–474.
URL: *http://dx.doi.org/10.1016/j.jvs.2012.07.008*

Sailer, A. M., Van Kuijk, S. M., Nelemans, P. J., Chin, A. S., Kino, A., Huininga, M., Schmidt, J., Mistelbauer, G., Bäumler, K., Chiu, P., Fischbein, M. P., Dake, M. D., Miller, D. C., Schurink, G. W. H. & Fleischmann, D. (2017), 'Computed Tomography Imaging Features in Acute Uncomplicated Stanford Type-B Aortic Dissection Predict Late Adverse Events', *Circulation: Cardiovascular Imaging* **10**(4), 1–11.

Saint Luke's (2021), 'What is an aortic dissection?'.

URL: *https://www.saintlukeskc.org/health-library/aortic-dissection-repair*

Saitta, S., Pirola, S., Piatti, F., Votta, E., Lucherini, F., Pluchinotta, F., Carminati, M., Lombardi, M., Geppert, C., Cuomo, F., Figueroa, C. A., Xu, X. Y. & Redaelli, A. (2019), 'Evaluation of 4D flow MRI-based non-invasive pressure assessment in aortic coarctations', *Journal of Biomechanics* **94**, 13–21.

URL: *https://doi.org/10.1016/j.jbiomech.2019.07.004*

Salameh, M. J. & Ratchford, E. V. (2016), 'Aortic Dissection', *Vascular Medicine* **21**(3), 276–280.

Schoephoerster, R. T., Oynes, F., Nunez, G., Kapadvanjwala, M. & Dewanjee, M. K. (1993), 'Effects of local geometry and fluid dynamics on regional platelet deposition on artificial surfaces', *Arteriosclerosis, Thrombosis, and Vascular Biology* **13**(12), 1806–1813.

Shang, E. K., Nathan, D. P., Fairman, R. M., Bavaria, J. E., Gorman, R. C., Gorman, J. H. & Jackson, B. M. (2015), 'Use of computational fluid dynamics studies in predicting aneurysmal degeneration of acute type B aortic dissections', *Journal of Vascular Surgery* **62**(2), 279–284.

URL: *http://dx.doi.org/10.1016/j.jvs.2015.02.048*

Sherrah, A., Callaghan, F., Puranik, R., Jeremy, R., Bannon, P., Vallely, M. & Grieve, S. (2017), 'Multi-Velocity Encoding Four-Dimensional Flow Magnetic Resonance Imaging in the Assessment of Chronic Aortic Dissection', *Aorta* **05**(03), 80–90.

Sorensen, E. N., Burgreen, G. W., Wagner, W. R. & Antaki, J. F. (1999*a*), 'Computational Simulation of Platelet Deposition and Activation: I. Model Development and Properties', *Annals of Biomedical Engineering* **27**, 436–448.

Sorensen, E. N., Burgreen, G. W., Wagner, W. R. & Antaki, J. F. (1999*b*), 'Computational Simulation of Platelet Deposition and Activation: II. Results for Poiseuille Flow over Collagen', *Annals of Biomedical Engineering* **27**(4), 449–458.

Soudah, E., Rudenick, P., Bordone, M., Bijnens, B., García-Dorado, D., Evangelista, A. &

Oñate, E. (2015), 'Validation of numerical flow simulations against in vitro phantom measurements in different type B aortic dissection scenarios', *Computer Methods in Biomechanics and Biomedical Engineering* **18**(8), 805–815.
URL: *https://doi.org/10.1080/10255842.2013.847095*

Stein, P. D. & Sabbah, H. N. (1976), 'Turbulent blood flow in the ascending aorta of humans with normal and diseased aortic valves', *Circulation Research* **39**(1), 58–65.

Sze, D. Y., Van Den Bosch, M. A., Dake, M. D., Miller, D. C., Hofmann, L. V., Varghese, R., Malaisrie, S. C., Van Der Starre, P. J., Rosenberg, J. & Mitchell, R. S. (2009), 'Factors portending endoleak formation after thoracic aortic stent-graft repair of complicated aortic dissection', *Circulation: Cardiovascular Interventions* **2**(2), 105–112.

Takahashi, K., Sekine, T., Miyagi, Y., Shirai, S., Otsuka, T., Kumita, S. & Ishii, Y. (2021), 'Four-dimensional flow analysis reveals mechanism and impact of turbulent flow in the dissected aorta', *European Journal of Cardio-Thoracic Surgery* **00**, 1–9.

Takei, Y., Itatani, K., Miyazaki, S., Shibasaki, I. & Fukuda, H. (2019), 'Four-dimensional flow magnetic resonance imaging analysis before and after thoracic endovascular aortic repair of chronic type B aortic dissection', *Interactive Cardiovascular and Thoracic Surgery* **28**(3), 413–420.

Tang, A., Fan, Y., Cheng, S. & Chow, K. (2012), 'Biomechanical Factors Influencing Type B Thoracic Aortic Dissection: Computational Fluid Dynamics Study', *Engineering Applications of Computational Fluid Mechanics* **6**(4), 622–632.
URL: *http://www.tandfonline.com/doi/abs/10.1080/19942060.2012.11015447*

Tedaldi, E., Montanari, C., Aycock, K. I., Sturla, F., Redaelli, A. & Manning, K. B. (2018), 'An experimental and computational study of the inferior vena cava hemodynamics under respiratory-induced collapse of the infrarenal IVC', *Medical Engineering and Physics* **54**, 44–55.
URL: *https://doi.org/10.1016/j.medengphy.2018.02.003*

The International Registry of Acute Aortic Dissection (n.d.), 'Aortic Dissection: About Dissections'.
URL: *http://www.iradonline.org/about.html*

Thrumurthy, S. G., Karthikesalingam, A., Patterson, B. O., Holt, P. J. E. & Thompson, M. M. (2012), 'The diagnosis and management of aortic dissection', *BMJ* **344**, d8290.

Tolenaar, J. L., Kern, J. A., Jonker, F. H. W., Cherry, K. J., Tracci, M. C., Angle, J. F., Sabri, S., Trimarchi, S., Strider, D., Alaiwaidi, G., Upchurch, G. R. & Upchurch Jr, G. R. (2014), 'Predictors of false lumen thrombosis in type B aortic dissection treated with TEVAR.', *Annals of cardiothoracic surgery* **3**(3), 255–25563.

Tolenaar, J. L., Van Keulen, J. W., Jonker, F. H., Van Herwaarden, J. A., Verhagen, H. J., Moll, F. L., Muhs, B. E. & Trimarchi, S. (2013), 'Morphologic predictors of aortic dilatation in type B aortic dissection', *Journal of Vascular Surgery* **58**(5), 1220–1225.
URL: *http://dx.doi.org/10.1016/j.jvs.2013.05.031*

Tolenaar, J. L., Van Keulen, J. W., Trimarchi, S., Jonker, F. H., Van Herwaarden, J. A., Verhagen, H. J., Moll, F. L. & Muhs, B. E. (2013), 'Number of entry tears is associated with aortic growth in type B dissections', *Annals of Thoracic Surgery* **96**(1), 39–42.
URL: *http://dx.doi.org/10.1016/j.athoracsur.2013.03.087*

Trimarchi, S., Tolenaar, J. L., Jonker, F. H. W., Murray, B., Tsai, T. T., Eagle, K. A., Rampoldi, V., Verhagen, H. J. M., Van Herwaarden, J. A., Moll, F. L., Muhs, B. E. & Elefteriades, J. A. (2013), 'Importance of false lumen thrombosis in type B aortic dissection prognosis', *Journal of Thoracic and Cardiovascular Surgery* **145**, S208–S212.

Tsai, T. T., Evangelista, A., Nienaber, C. A., Myrmel, T., Meinhardt, G., Cooper, J. V., Smith, D. E., Suzuki, T., Fattori, R., Llovet, A., Froehlich, J., Hutchison, S., Distante, A., Sundt, T., Beckman, J., Januzzi, J. L., Isselbacher, E. M. & Eagle, K. A. (2007), 'Partial Thrombosis of the False Lumen in Patients with Acute Type B Aortic Dissection', *New England Journal of Medicine* **357**, 349–359.

Tsai, T. T., Schlicht, M. S., Khanafer, K., Bull, J. L., Valassis, D. T., Williams, D. M., Berguer, R. & Eagle, K. A. (2008), 'Tear size and location impacts false lumen pressure in an ex vivo model of chronic type B aortic dissection', *Journal of Vascular Surgery* **47**(4), 844–851.

Tse, K. M., Chiu, P., Lee, H. P. & Ho, P. (2011), 'Investigation of hemodynamics in the development of dissecting aneurysm within patient-specific dissecting aneurismal aortas using computational fluid dynamics (CFD) simulations', *Journal of Biomechanics* **44**(5), 827–836. **URL:** *http://dx.doi.org/10.1016/j.jbiomech.2010.12.014*

Uberoi, R., Tsetis, D., Shrivastava, V., Morgan, R. & Belli, A. M. (2011), 'Standard of practice for the interventional management of isolated iliac artery aneurysms', *CardioVascular and Interventional Radiology* **34**(1), 3–13.

van Bogerijen, G. H. W., Auricchio, F., Conti, M., Lefieux, A., Reali, A., Veneziani, A., Tolenaar, J. L., Moll, F. L., Rampoldi, V. & Trimarchi, S. (2014), 'Aortic Hemodynamics After Thoracic Endovascular Aortic Repair, With Particular Attention to the Bird-Beak Configuration', *Journal of Endovascular Therapy* .

Versteeg, H. & Malalasekera, W. (2007), *An Introduction to Computational Fluid Dynamics*, Pearson Education M.U.A.

Wake, A. K., Oshinski, J. N., Tannenbaum, A. R. & Giddens, D. P. (2009), 'Choice of in vivo versus idealized velocity boundary conditions influences physiologically relevant flow patterns in a subject-specific simulation of flow in the human carotid bifurcation', *Journal of Biomechanical Engineering* **131**(2), 7–13.

Wan Ab Naim, W. N., Ganesan, P. B., Sun, Z., Lei, J., Jansen, S., Hashim, S. A., Ho, T. K. & Lim, E. (2018), 'Flow pattern analysis in type B aortic dissection patients after stent-grafting repair: Comparison between complete and incomplete false lumen thrombosis', *International Journal for Numerical Methods in Biomedical Engineering* **34**(5), 1–13.

Wan Ab Naim, W. N., Ganesan, P. B., Sun, Z., Liew, Y. M., Qian, Y., Lee, C. J., Jansen, S., Hashim, S. A. & Lim, E. (2016), 'Prediction of thrombus formation using vortical structures

presentation in Stanford type B aortic dissection: A preliminary study using CFD approach', *Applied Mathematical Modelling* **40**(4), 3115–3127.

Wan Ab Naim, W. N., Ganesan, P. B., Sun, Z., Osman, K. & Lim, E. (2014), 'The impact of the number of tears in patient-specific Stanford type b aortic dissecting aneurysm: CFD simulation', *Journal of Mechanics in Medicine and Biology* **14**(2).

Williams, D. M., Andrews, J. C., Victoria Marx, M. & Abrams, G. D. (1993), 'Creation of Reentry Tears in Aortic Dissection by Means of Percutaneous Balloon Fenestration: Gross Anatomic and Histologic Considerations', *Journal of Vascular and Interventional Radiology* **4**(1), 75–83.

Wootton, D. M., Markou, C. P., Hanson, S. R. & Ku, D. N. (2001), 'A mechanistic model of acute platelet accumulation in thrombogenic stenoses', *Annals of Biomedical Engineering* **29**(4), 321–329.

Wuest, W., Goltz, J., Ritter, C., Yildirim, C., Hahn, D. & Kickuth, R. (2011), 'Fenestration of aortic dissection using a fluoroscopy-based needle re-entry catheter system', *CardioVascular and Interventional Radiology* **34**(SUPPL. 2), 44–47.

Youssefi, P., Gomez, A., Arthurs, C., Sharma, R., Jahangiri, M. & Figueroa, C. A. (2018), 'Impact of patient-specific inflow velocity profile on hemodynamics of the thoracic aorta', *Journal of Biomechanical Engineering* **140**(1), 1–14.

Zadrazil, I., Corzo, C., Voulgaropoulos, V., Markides, C. N. & Xu, X. Y. (2020), 'A combined experimental and computational study of the flow characteristics in a Type B aortic dissection: Effect of primary and secondary tear size', *Chemical Engineering Research and Design* **160**, 240–253.
URL: *https://doi.org/10.1016/j.cherd.2020.05.025*

Zhang, Y., Lu, Q., Feng, J., Yu, P., Zhang, S., Teng, Z., Gillard, J. H., Song, R. & Jing, Z. (2014), 'A pilot study exploring the mechanisms involved in the longitudinal propagation of acute aortic dissection through computational fluid dynamic analysis', *Cardiology (Switzerland)* **128**(2), 220–225.

Zilber, Z. A., Boddu, A., Malaisrie, S., Hoel, A., Mehta, C., Vassallo, P., Burris, N., Roldán-Alzate, A., Collins, J., François, C. & Allen, B. (2021), 'Noninvasive Morphologic and Hemodynamic Evaluation of Type B Aortic Dissection : State of the Art and Future Perspectives', *Radiology* **3**(3), e200456.

Zimmermann, J., Baeumler, K., Loecher, M., Cork, T. E., Kolawole, F. O., Gifford, K., Marsden, A. L., Fleischmann, D. & Ennis, D. B. (2021), 'Quantitative Hemodynamics in Aortic Dissection: Comparing in vitro MRI with FSI Simulation in a Compliant Model', pp. 1–8.
URL: *http://arxiv.org/abs/2102.13213*

Zipfel, B., Buz, S., Redlin, M., Hullmeine, D., Hammerschmidt, R. & Hetzer, R. (2013), 'Spinal cord ischemia after thoracic stent-grafting: Causes apart from intercostal artery coverage', *Annals of Thoracic Surgery* **96**(1), 31–38.
URL: *http://dx.doi.org/10.1016/j.athoracsur.2013.03.010*

Appendix A

Mesh Sensitivity Test Results

The results from all mesh sensitivity tests conducted for each study are reported in this Appendix. For each model in all studies three meshes (M1, M2 and M3) were created. Quantitative comparison of mean and maximum velocity and time average wall shear stress (TAWSS) on selected planes between M1/M2 and M2/M3 determined the chosen mesh. Furthermore, the grid convergence index (GCI, decriped in Section 3.5) was calculated for meshes in Chapter 4.

A.1 Chapter 4

Table A.1: Number of elements for three meshes (M1, M2, M3) used for mesh sensitivity analysis for models P1, P2 and P2P in Chapter 4.

	P1	**P2**	**P2P**
M1	3,976,559	3,084,907	1,988,598
M2	6,168,045	5,755,630	4,055,893
M3	9,654,667	10,094,465	6,358,124

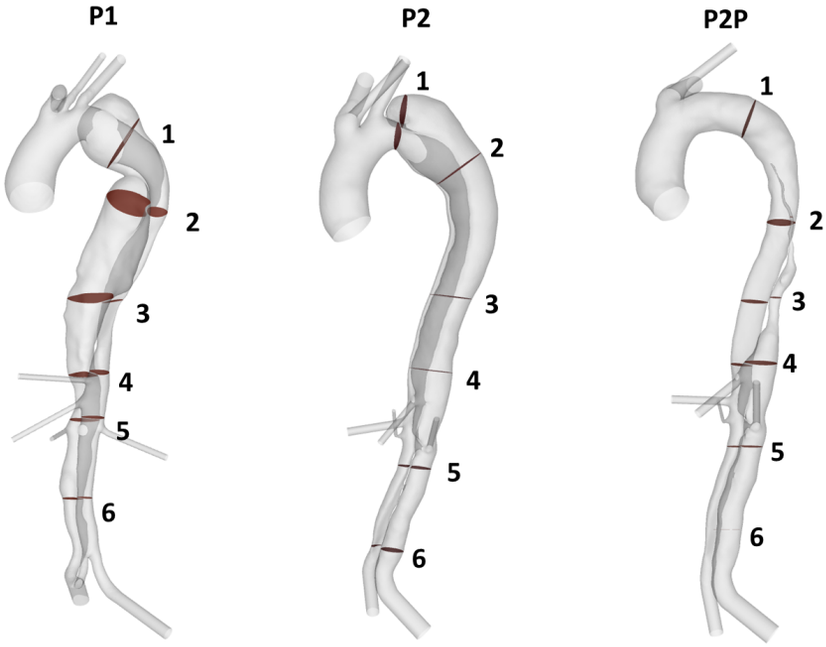

Figure A.1: Analysis planes used for mesh sensitivity tests for models P1, P2 and P2P in Chapter 4.

P1 mesh sensitivity test results

Table A.2: Mean and maximum velocity and time average wall shear stress (TAWSS) on analysis planes (shown in Figure A.1 in each mesh for P1 in Chapter 4. |%E|: Absolute percentage change in value between noted meshes.

Plane	**1**	**2**	**3**	**4**	**5**	**6**
			Mean Velocity [m/s]			
M1	0.090	0.100	0.166	0.240	0.268	0.276
M2	0.090	0.100	0.166	0.241	0.277	0.274
M3	0.090	0.100	0.166	0.241	0.278	0.274
|%E| M2/M1	0.045	0.111	0.124	0.170	3.411	0.669
|%E| M3/M2	0.080	0.180	0.115	0.077	0.259	0.103
$GCI_{2,1}$	0.125	0.363	1.843	0.177	0.352	0.152
$GCI_{3,2}$	0.225	0.589	1.702	0.081	0.028	0.023
			Max Velocity [m/s]			
M1	0.205	0.214	0.671	0.357	0.488	0.447
M2	0.204	0.212	0.668	0.358	0.490	0.445
M3	0.204	0.212	0.667	0.358	0.491	0.445
|%E| M2/M1	0.454	0.525	0.477	0.326	0.521	0.249
|%E| M3/M2	0.359	0.068	0.144	0.089	0.097	0.065
$GCI_{2,1}$	2.113	0.098	0.257	0.153	0.149	0.110
$GCI_{3,2}$	1.670	0.013	0.078	0.042	0.028	0.029
			Mean TAWSS [Pa]			
M1	0.740	0.219	1.088	0.578	0.726	0.786
M2	0.777	0.220	1.081	0.582	0.725	0.790
M3	0.793	0.219	1.085	0.570	0.738	0.799
|%E| M2/M1	4.953	0.081	0.624	0.568	0.080	0.515
|%E| M3/M2	2.110	0.100	0.422	2.031	1.800	1.191
$GCI_{2,1}$	4.772	0.531	1.606	0.978	0.104	1.124
$GCI_{3,2}$	2.090	0.657	1.074	3.590	2.313	2.582
			Max TAWSS [Pa]			
M1	1.536	0.530	3.961	1.208	1.807	1.709
M2	1.568	0.536	3.945	1.198	1.792	1.727
M3	1.589	0.537	3.958	1.160	1.797	1.737
|%E| M2/M1	2.084	1.233	0.405	0.804	0.826	1.033
|%E| M3/M2	1.339	0.153	0.341	3.150	0.307	0.577
$GCI_{2,1}$	4.861	0.219	2.647	1.364	0.607	1.657
$GCI_{3,2}$	3.145	0.027	2.212	5.474	0.223	0.930

Based on the mesh sensitivity results, M2 was chosen for P1.

P2 mesh sensitivity test results

Table A.3: Mean and maximum velocity and time average wall shear stress (TAWSS) on analysis planes (shown in Figure A.1) in each mesh for P2 in Chapter 4. |%E|: Absolute percentage change in value between noted meshes.

Plane	**1**	**2**	**3**	**4**	**5**	**6**
			Mean Velocity [m/s]			
M1	0.089	0.071	0.131	0.121	0.139	0.190
M2	0.089	0.071	0.131	0.121	0.138	0.189
M3	0.089	0.071	0.131	0.121	0.138	0.189
|%E| M2/M1	0.266	0.018	0.063	0.051	0.765	0.753
|%E| M3/M2	0.101	0.012	0.072	0.121	0.173	0.191
$\mathbf{GCI_{2,1}}$	0.077	0.027	0.715	0.262	0.063	0.080
$\mathbf{GCI_{3,2}}$	0.203	0.042	0.626	0.111	0.280	0.319
			Max Velocity [m/s]			
M1	0.318	0.146	0.168	0.185	0.190	0.465
M2	0.315	0.145	0.167	0.183	0.189	0.464
M3	0.316	0.145	0.168	0.182	0.189	0.460
|%E| M2/M1	0.693	0.472	0.770	1.023	0.688	0.140
|%E| M3/M2	0.043	0.059	0.415	0.118	0.115	0.785
$\mathbf{GCI_{2,1}}$	0.003	0.010	0.596	0.019	0.029	1.204
$\mathbf{GCI_{3,2}}$	0.057	0.084	1.118	0.167	0.173	0.213
			Mean TAWSS [Pa]			
M1	0.376	0.149	0.222	0.198	0.323	0.686
M2	0.389	0.149	0.222	0.198	0.323	0.687
M3	0.392	0.149	0.223	0.199	0.324	0.686
|%E| M2/M1	3.616	0.166	0.234	0.043	0.007	0.162
|%E| M3/M2	0.615	0.217	0.644	0.757	0.262	0.115
$\mathbf{GCI_{2,1}}$	0.163	1.160	1.259	0.996	0.336	0.358
$\mathbf{GCI_{3,2}}$	0.932	0.891	0.462	0.057	0.009	0.502
			Max TAWSS [Pa]			
M1	1.152	0.287	0.302	0.330	0.493	2.015
M2	1.191	0.291	0.304	0.328	0.481	2.012
M3	1.203	0.293	0.304	0.334	0.477	1.990
|%E| M2/M1	3.344	1.308	0.508	0.767	2.368	0.111
|%E| M3/M2	1.015	0.687	0.025	2.099	0.859	1.116
$\mathbf{GCI_{2,1}}$	0.575	0.969	0.002	4.066	0.594	1.567
$\mathbf{GCI_{3,2}}$	1.850	1.835	0.032	1.528	1.662	0.155

Based on the mesh sensitivity results, M2 was chosen for P2.

P2P mesh sensitivity test results

Table A.4: Mean and maximum velocity and time average wall shear stress (TAWSS) on analysis planes (shown in Figure A.1) in each mesh for P2P in Chapter 4. |%E|: Absolute percentage change in value between noted meshes.

Plane	**1**	**2**	**3**	**4**	**5**	**6**
			Mean Velocity [m/s]			
M1	0.097	0.222	0.285	0.127	0.091	0.119
M2	0.097	0.223	0.286	0.127	0.091	0.119
M3	0.097	0.223	0.285	0.127	0.091	0.119
|%E| M2/M1	0.337	0.302	0.371	0.636	0.114	0.074
|%E| M3/M2	0.064	0.063	0.116	0.055	0.056	0.025
$GCI_{2,1}$	0.098	0.100	0.212	0.075	0.140	0.048
$GCI_{3,2}$	0.019	0.021	0.067	0.007	0.069	0.016
			Max Velocity [m/s]			
M1	0.147	0.267	0.397	0.507	0.249	0.364
M2	0.148	0.268	0.399	0.506	0.244	0.356
M3	0.148	0.268	0.400	0.506	0.244	0.354
|%E| M2/M1	0.225	0.562	0.462	0.104	2.002	2.262
|%E| M3/M2	0.125	0.124	0.285	0.072	0.020	0.560
$GCI_{2,1}$	0.349	0.200	0.940	0.291	0.025	0.924
$GCI_{3,2}$	0.194	0.044	0.582	0.201	0.000	0.225
			Mean TAWSS [Pa]			
M1	0.153	0.331	0.477	0.381	0.383	0.735
M2	0.153	0.332	0.478	0.384	0.381	0.721
M3	0.153	0.333	0.477	0.387	0.381	0.718
|%E| M2/M1	0.041	0.371	0.227	0.660	0.291	1.880
|%E| M3/M2	0.341	0.288	0.262	0.854	0.025	0.460
$GCI_{2,1}$	0.058	1.623	2.122	3.532	0.035	0.756
$GCI_{3,2}$	0.483	1.260	2.456	4.560	0.003	0.182
			Max TAWSS [Pa]			
M1	0.252	0.513	0.804	1.335	1.165	2.204
M2	0.254	0.521	0.809	1.387	1.173	2.165
M3	0.256	0.521	0.806	1.393	1.187	2.166
|%E| M2/M1	0.946	1.490	0.659	3.863	0.669	1.780
|%E| M3/M2	0.612	0.111	0.342	0.470	1.191	0.045
$GCI_{2,1}$	2.210	0.149	0.893	0.673	1.877	0.057
$GCI_{3,2}$	1.436	0.011	0.468	0.085	3.327	0.001

Based on the mesh sensitivity results, M2 was chosen for P2P.

A.2 Chapter 5

The pre-TEVAR and post-TEVAR models with varying numbers of branches used in Chapter 5 are the same models as P2 and P2P in Chapter 4, without the small region of thrombosis in the upper FL of P2 artificially reconstructed. Therefore, based on previous mesh sensitivity tests the same cell sizes and local refinements were set to mesh the pre and post-TEVAR Chapter 5 models. Cell sizes and local refinements were also kept constant when branches were removed from the model to ensure the same central aortic mesh was used.

Mesh sensitivity information and results for PI and PII used in Chapter 5 are presented here. After meshes were chosen for PI and PII cell sizes and local refinements were kept constant to mesh models PI+ICA and PII+IMA.

Table A.5: Number of elements for three meshes (M1, M2, M3) used for mesh sensitivity analysis for models PI and PII in Chapter 5.

	PI	**PII**
M1	3,703,965	2,541,484
M2	6,194,880	5,471,593
M3	9,778,182	9,630,634

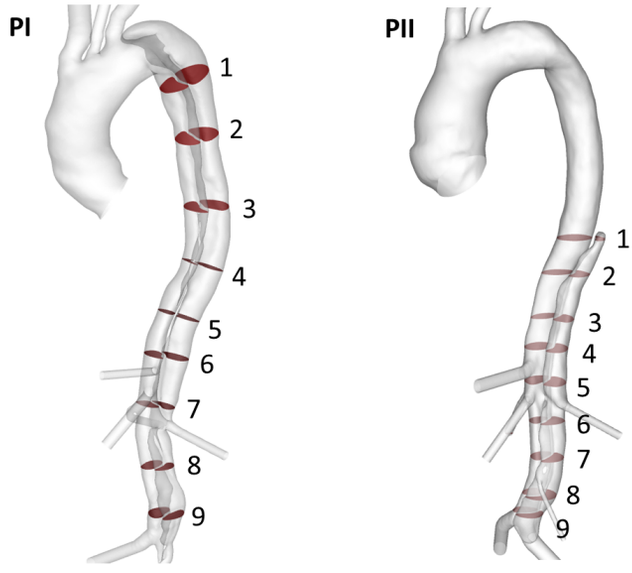

Figure A.2: Analysis planes used for mesh sensitivity tests for models PI and PII in Chapter 5.

PI mesh sensitivity test results

Table A.6: Mean and maximum velocity and time average wall shear stress (TAWSS) on analysis planes (shown in Figure A.2) in each mesh for PI in Chapter 5. |%E|: Absolute percentage change in value between noted meshes.

Plane	**1**	**2**	**3**	**4**	**5**	**6**	**7**	**8**	**9**
					Mean Velocity [m/s]				
M1	0.119	0.145	0.119	0.112	0.096	0.096	0.077	0.043	0.040
M2	0.118	0.146	0.121	0.115	0.098	0.099	0.081	0.045	0.042
M3	0.118	0.145	0.120	0.114	0.098	0.099	0.080	0.045	0.042
|%E| M2/M1	0.856	0.252	1.505	3.042	3.106	3.137	4.175	4.438	4.406
|%E| M3/M2	0.286	0.256	0.352	0.476	0.507	0.460	0.534	1.028	0.803
					Max Velocity [m/s]				
M1	0.187	0.286	0.241	0.350	0.189	0.218	0.137	0.065	0.057
M2	0.186	0.365	0.240	0.355	0.191	0.222	0.145	0.069	0.060
M3	0.186	0.370	0.240	0.353	0.191	0.221	0.144	0.069	0.060
|%E| M2/M1	0.472	27.409	0.549	1.475	1.141	1.856	5.787	6.729	5.762
|%E| M3/M2	0.157	1.245	0.177	0.580	0.249	0.397	0.177	0.885	0.624
					Mean TAWSS [Pa]				
M1	0.316	0.364	0.252	0.480	0.302	0.256	0.229	0.144	0.140
M2	0.308	0.386	0.253	0.484	0.306	0.259	0.242	0.147	0.142
M3	0.310	0.384	0.250	0.486	0.302	0.256	0.243	0.147	0.142
|%E| M2/M1	2.432	6.158	0.333	0.702	1.242	1.012	5.881	2.401	1.785
|%E| M3/M2	0.692	0.554	1.027	0.425	1.295	0.889	0.287	0.067	0.142
					Max TAWSS [Pa]				
M1	0.583	1.103	0.682	1.720	0.896	0.696	0.366	0.263	0.274
M2	0.590	1.205	0.674	1.750	0.894	0.708	0.384	0.266	0.278
M3	0.590	1.189	0.663	1.763	0.866	0.704	0.393	0.267	0.280
|%E| M2/M1	1.244	9.327	1.200	1.749	0.210	1.730	5.009	0.916	1.572
|%E| M3/M2	0.007	1.339	1.676	0.738	3.083	0.608	2.292	0.361	0.891

Based on the mesh sensitivity results, M2 was chosen for PI.

PII mesh sensitivity test results

Table A.7: Mean and maximum velocity and time average wall shear stress (TAWSS) on analysis planes (shown in Figure A.2) in each mesh for PII in Chapter 5. |%E|: Absolute percentage change in value between noted meshes.

Plane	**1**	**2**	**3**	**4**	**5**	**6**	**7**	**8**	**9**
					Mean Velocity [m/s]				
M1	0.412	0.453	0.308	0.239	0.260	0.228	0.287	0.398	0.381
M2	0.411	0.451	0.307	0.234	0.253	0.225	0.284	0.397	0.379
M3	0.410	0.451	0.306	0.234	0.252	0.224	0.284	0.396	0.378
|%E| M2/M1	0.295	0.364	0.410	1.989	2.865	1.061	1.149	0.312	0.380
|%E| M3/M2	0.196	0.200	0.186	0.128	0.309	0.273	0.009	0.250	0.196
					Max Velocity [m/s]				
M1	0.769	0.958	0.794	0.629	0.570	0.618	0.611	0.849	0.574
M2	0.765	0.956	0.798	0.611	0.554	0.653	0.599	0.849	0.571
M3	0.766	0.957	0.801	0.607	0.553	0.659	0.600	0.851	0.569
|%E| M2/M1	0.502	0.162	0.560	3.001	2.762	5.530	1.898	0.076	0.413
|%E| M3/M2	0.093	0.038	0.298	0.516	0.108	0.936	0.138	0.256	0.297
					Mean TAWSS [Pa]				
M1	0.820	0.842	0.526	0.741	0.563	0.945	1.011	0.572	0.588
M2	0.823	0.846	0.524	0.748	0.551	0.950	1.012	0.589	0.589
M3	0.824	0.849	0.521	0.762	0.549	0.958	1.032	0.602	0.593
|%E| M2/M1	0.414	0.565	0.453	1.033	2.260	0.598	0.170	2.916	0.266
|%E| M3/M2	0.111	0.302	0.569	1.869	0.207	0.850	1.939	2.140	0.643
					Max TAWSS [Pa]				
M1	2.148	2.232	2.304	2.283	1.963	3.556	5.279	1.660	1.424
M2	2.157	2.240	2.320	2.327	1.884	3.661	5.339	1.698	1.425
M3	2.182	2.227	2.393	2.439	1.911	3.683	5.384	1.699	1.434
|%E| M2/M1	0.414	0.357	0.666	1.911	4.028	2.964	1.143	2.294	0.100
|%E| M3/M2	1.147	0.587	3.157	4.813	1.428	0.583	0.835	0.095	0.601

Based on the mesh sensitivity results, M2 was chosen for PII.

A.3 Chapter 6

P3 in Chapter 6 is the same model as P2 in Chapter 4, without the small region of thrombosis in the upper FL artificially reconstructed. Therefore, P3 in Chapter 6 was meshed with the same cell sizes and local refinements as the chosen mesh for P2 in Chapter 4 based on the mesh sensitivity results presented in Section A.1. Mesh sensitivity test information and results for patients P1, P2, P4 and P5 in Chapter 6 are presented here.

Table A.8: Number of elements for three meshes (M1, M2, M3) used for mesh sensitivity analysis for models P1, P2, P4 and P5 in Chapter 6.

	P1	**P2**	**P4**	**P5**
M1	2,119,745	2,586,671	2,485,253	2,755,374
M2	3,963,154	4,615,048	4,807,773	5,076,196
M3	6,811,948	7,173,584	10,033,561	9,725,457

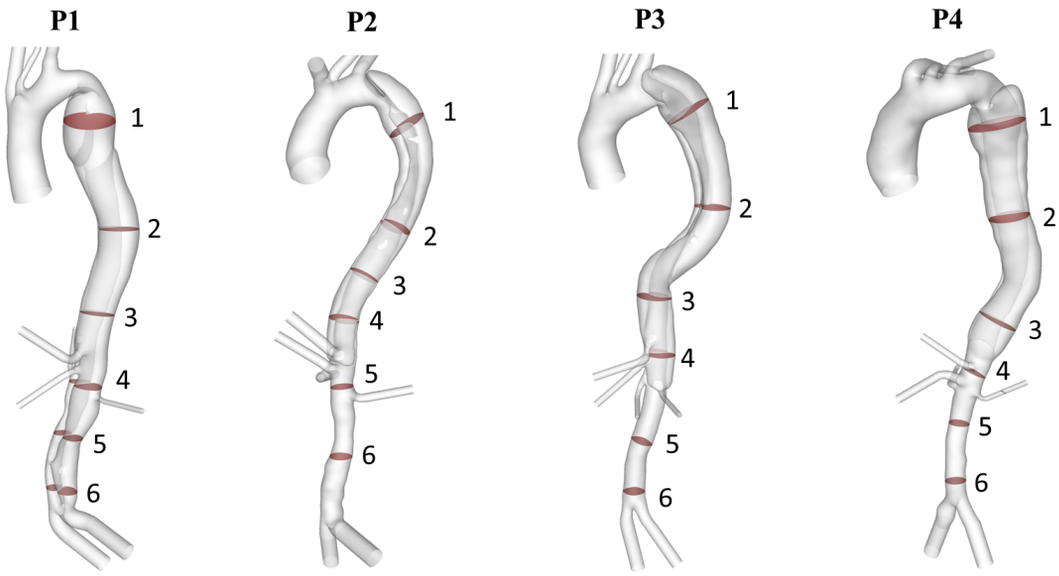

Figure A.3: Analysis planes used for mesh sensitivity tests for models P1, P2, P4 and P5 in Chapter 6.

P1 mesh sensitivity test results

Table A.9: Mean and maximum velocity and time average wall shear stress (TAWSS) on analysis planes (shown in Figure A.3) in each mesh for P1 in Chapter 6. |%E|: Absolute percentage change in value between noted meshes.

Plane	**1**	**2**	**3**	**4**	**5**	**6**
			Mean Velocity [m/s]			
M1	0.087	0.083	0.050	0.059	0.065	0.076
M2	0.100	0.088	0.050	0.060	0.066	0.081
M3	0.098	0.088	0.049	0.059	0.066	0.082
|%E| M2/M1	14.525	6.540	0.182	1.109	1.208	6.135
|%E| M3/M2	1.659	0.569	1.194	1.085	0.322	1.179
			Max Velocity [m/s]			
M1	0.177	0.257	0.268	0.253	0.236	0.190
M2	0.185	0.233	0.262	0.245	0.229	0.194
M3	0.187	0.244	0.249	0.235	0.224	0.189
|%E| M2/M1	4.528	9.230	2.284	3.062	3.005	1.861
|%E| M3/M2	0.720	4.421	4.910	4.165	2.068	2.486
			Mean TAWSS [Pa]			
M1	1.307	0.616	0.600	0.786	0.823	1.298
M2	1.380	0.649	0.595	0.791	0.816	1.379
M3	1.388	0.649	0.582	0.797	0.817	1.372
|%E| M2/M1	5.579	5.247	0.911	0.522	0.859	6.261
|%E| M3/M2	0.593	0.087	2.153	0.760	0.034	0.500
			Max TAWSS [Pa]			
M1	3.590	1.069	1.096	1.950	1.878	3.619
M2	3.717	1.085	1.078	1.977	1.874	5.982
M3	3.870	1.100	1.054	2.018	1.900	6.129
|%E| M2/M1	3.530	1.467	1.678	1.400	0.242	65.297
|%E| M3/M2	4.114	1.399	2.204	2.052	1.418	2.466

Based on the mesh sensitivity results, M2 was chosen for P1.

P2 mesh sensitivity test results

Table A.10: Mean and maximum velocity and time average wall shear stress (TAWSS) on analysis planes (shown in Figure A.3) in each mesh for P2 in Chapter 6. |%E|: Absolute percentage change in value between noted meshes.

Plane	**1**	**2**	**3**	**4**	**5**	**6**
			Mean Velocity [m/s]			
M1	0.099	0.153	0.177	0.121	0.086	0.178
M2	0.099	0.153	0.176	0.120	0.085	0.178
M3	0.099	0.153	0.176	0.120	0.085	0.177
|%E| M2/M1	0.062	0.139	0.220	0.389	0.645	0.101
|%E| M3/M2	0.166	0.216	0.132	0.236	0.391	0.278
			Max Velocity [m/s]			
M1	0.140	0.188	0.235	0.173	0.107	0.226
M2	0.139	0.187	0.235	0.172	0.106	0.226
M3	0.139	0.187	0.235	0.171	0.106	0.225
|%E| M2/M1	0.568	0.166	0.044	0.560	0.763	0.023
|%E| M3/M2	0.031	0.190	0.049	0.608	0.285	0.255
			Mean TAWSS [Pa]			
M1	0.380	0.281	0.355	0.317	0.255	0.378
M2	0.396	0.280	0.355	0.325	0.252	0.379
M3	0.396	0.280	0.354	0.334	0.249	0.380
|%E| M2/M1	4.276	0.139	0.068	2.521	1.247	0.360
|%E| M3/M2	0.040	0.055	0.146	2.898	1.021	0.142
			Max TAWSS [Pa]			
M1	0.669	0.407	0.537	0.488	0.385	0.601
M2	0.655	0.404	0.539	0.502	0.380	0.603
M3	0.647	0.405	0.544	0.506	0.378	0.604
|%E| M2/M1	2.066	0.715	0.400	2.781	1.217	0.293
|%E| M3/M2	1.262	0.329	0.976	0.731	0.523	0.274

Based on the mesh sensitivity results, M2 was chosen for P2.

P4 mesh sensitivity test results

Table A.11: Mean and maximum velocity and time average wall shear stress (TAWSS) on analysis planes (shown in Figure A.3) in each mesh for P4 in Chapter 6. |%E|: Absolute percentage change in value between noted meshes.

Plane	**1**	**2**	**3**	**4**	**5**	**6**
			Mean Velocity [m/s]			
M1	0.298	0.178	0.183	0.189	0.216	0.222
M2	0.298	0.178	0.183	0.189	0.215	0.220
M3	0.297	0.178	0.182	0.188	0.214	0.219
|%E| M2/M1	0.127	0.099	0.002	0.282	0.777	0.849
|%E| M3/M2	0.053	0.138	0.180	0.215	0.543	0.477
			Max Velocity [m/s]			
M1	0.725	0.361	0.257	0.318	0.246	0.265
M2	0.725	0.359	0.256	0.316	0.243	0.262
M3	0.719	0.357	0.256	0.315	0.242	0.261
|%E| M2/M1	0.106	0.709	0.101	0.791	0.857	0.839
|%E| M3/M2	0.930	0.366	0.143	0.251	0.507	0.583
			Mean TAWSS [Pa]			
M1	0.736	0.482	0.439	0.470	0.465	0.497
M2	0.798	0.481	0.441	0.472	0.489	0.498
M3	0.815	0.481	0.443	0.468	0.498	0.497
|%E| M2/M1	8.507	0.283	0.427	0.438	5.173	0.182
|%E| M3/M2	2.100	0.013	0.431	0.917	1.743	0.227
			Max TAWSS [Pa]			
M1	1.558	1.165	0.684	1.036	0.574	0.656
M2	1.814	1.160	0.700	1.009	0.636	0.653
M3	1.857	1.146	0.724	0.987	0.659	0.648
|%E| M2/M1	16.447	0.443	2.308	2.647	10.852	0.382
|%E| M3/M2	2.380	1.179	3.444	2.153	3.611	0.790

Based on the mesh sensitivity results, M2 was chosen for P4.

P5 mesh sensitivity test results

Table A.12: Mean and maximum velocity and time average wall shear stress (TAWSS) on analysis planes (shown in Figure A.3) in each mesh for P5 in Chapter 6. |%E|: Absolute percentage change in value between noted meshes.

Plane	**1**	**2**	**3**	**4**	**5**	**6**
			Mean Velocity [m/s]			
M1	0.215	0.151	0.178	0.330	0.302	0.309
M2	0.215	0.151	0.178	0.329	0.299	0.306
M3	0.215	0.151	0.177	0.328	0.298	0.304
|%E| M2/M1	0.157	0.119	0.247	0.273	0.919	0.922
|%E| M3/M2	0.112	0.234	0.219	0.237	0.420	0.472
			Max Velocity [m/s]			
M1	0.465	0.219	0.396	0.517	0.345	0.373
M2	0.464	0.217	0.393	0.518	0.342	0.369
M3	0.464	0.217	0.393	0.519	0.340	0.367
|%E| M2/M1	0.071	0.766	0.648	0.224	0.859	1.002
|%E| M3/M2	0.079	0.233	0.009	0.202	0.489	0.519
			Mean TAWSS [Pa]			
M1	0.649	0.339	0.478	0.874	0.908	0.750
M2	0.664	0.337	0.472	0.878	0.909	0.748
M3	0.672	0.337	0.471	0.880	0.909	0.748
|%E| M2/M1	2.283	0.702	1.259	0.499	0.112	0.389
|%E| M3/M2	1.209	0.050	0.216	0.254	0.056	0.091
			Max TAWSS [Pa]			
M1	1.269	0.615	1.245	1.246	1.105	0.876
M2	1.297	0.603	1.185	1.249	1.151	0.873
M3	1.303	0.603	1.174	1.247	1.173	0.880
|%E| M2/M1	2.151	2.019	4.862	0.241	4.195	0.371
|%E| M3/M2	0.507	0.146	0.897	0.174	1.884	0.797

Based on the mesh sensitivity results, M2 was chosen for P5.

A.4 Chapter 7

The patient-specific geometry used in Chapter 7 is the same model as PII from Chapter 5 and therefore the mesh was chosen based on the mesh sensitivity results previously presented for PII in Section A.2. Mesh sensitivity information and results for the idealised geometry are presented here.

Table A.13: Number of elements for three meshes (M1, M2, M3) used for mesh sensitivity analysis for the idealised geometry in Chapter 7.

	Idealised Geometry
M1	619,901
M2	1,242,946
M3	2,345,280

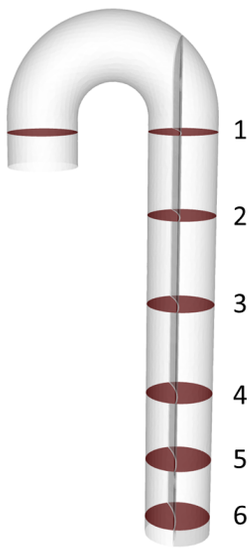

Figure A.4: Analysis planes used for mesh sensitivity tests for idealised geometry in Chapter 7.

Table A.14: Mean and maximum velocity and time average wall shear stress (TAWSS) on analysis planes (shown in Figure A.4) for the idealised geometry used in Chapter 7. |%E|: Absolute percentage change in value between noted meshes.

Plane	**1**	**2**	**3**	**4**	**5**	**6**
			Mean Velocity [m/s]			
M1	0.285	0.271	0.271	0.271	0.270	0.281
M2	0.289	0.270	0.270	0.270	0.270	0.282
M3	0.290	0.270	0.270	0.270	0.270	0.285
|%E| M2/M1	1.687	0.264	0.195	0.174	0.107	0.664
|%E| M3/M2	0.274	0.052	0.108	0.083	0.069	0.838
			Max Velocity [m/s]			
M1	0.702	0.626	0.626	0.626	0.634	0.880
M2	0.726	0.626	0.626	0.625	0.633	0.906
M3	0.739	0.626	0.626	0.626	0.633	0.949
|%E| M2/M1	3.436	0.027	0.084	0.108	0.200	2.927
|%E| M3/M2	1.839	0.018	0.017	0.075	0.136	4.776
			Mean TAWSS [Pa]			
M1	0.502	0.501	0.508	0.505	0.596	0.634
M2	0.519	0.506	0.509	0.508	0.598	0.663
M3	0.531	0.508	0.510	0.509	0.597	0.688
|%E| M2/M1	3.259	1.016	0.220	0.677	0.415	4.561
|%E| M3/M2	2.310	0.387	0.234	0.169	0.094	3.710
			Max TAWSS [Pa]			
M1	0.985	0.945	0.967	0.961	1.101	1.345
M2	0.993	0.963	0.972	0.983	1.089	1.314
M3	1.000	0.952	0.966	0.972	1.103	1.371
|%E| M2/M1	0.779	1.909	0.466	2.281	1.091	2.266
|%E| M3/M2	0.779	1.909	0.466	2.281	1.091	2.266

Based on the mesh sensitivity results, M3 was chosen for the idealised geometry.

A.5 Chapter 8

S2mod is the same geometry as S2 but with one tear artificially occluded. Therefore, S2mod was meshed using the same cell sizes and local refinements of the mesh chosen for S2 based on the mesh sensitivity tests. Mesh sensitivity information and results for S1 and S2 are presented here.

Table A.15: Number of elements for three meshes (M1, M2, M3) used for mesh sensitivity analysis for models S1 and S2 in Chapter 8.

	S1	**S2**
M1	3,822,597	3,189,557
M2	4,995,597	5,649,922
M3	7,522,954	8,043,532

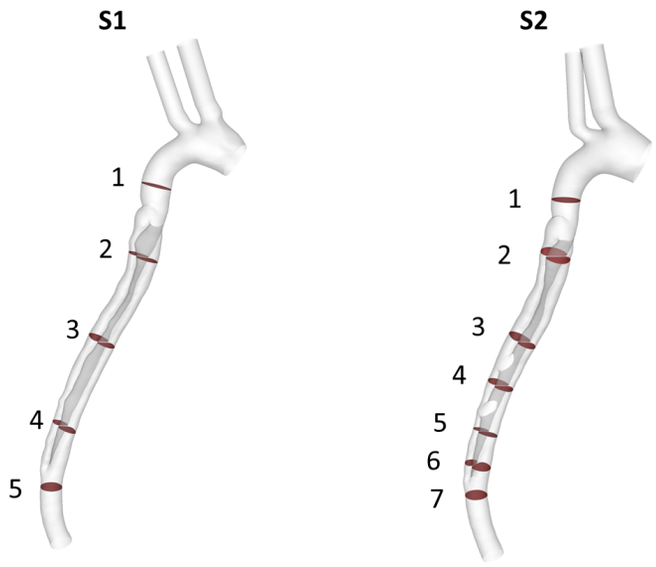

Figure A.5: Analysis planes used for mesh sensitivity tests for models S1 and P2 in Chapter 8.

S1 mesh sensitivity test results

Table A.16: Mean and maximum velocity and wall shear stress (WSS) on analysis planes (shown in Figure A.5) in each mesh for S1 in Chapter 8. |%E|: Absolute percentage change in value between noted meshes.

Plane	**1**	**2**	**3**	**4**	**5**
			Mean Velocity [m/s]		
M1	0.272	0.311	0.258	0.331	0.366
M2	0.273	0.313	0.260	0.333	0.368
M3	0.278	0.310	0.260	0.333	0.367
|%E| M2/M1	0.221	0.842	0.476	0.462	0.470
|%E| M3/M2	1.857	-1.004	0.131	0.041	-0.025
			Max Velocity [m/s]		
M1	0.535	0.951	0.577	0.533	0.955
M2	0.530	0.954	0.601	0.537	0.952
M3	0.539	0.949	0.610	0.547	0.958
|%E| M2/M1	-0.784	0.309	4.150	0.707	-0.310
|%E| M3/M2	1.634	-0.571	1.489	1.935	0.654
			Mean TAWSS [Pa]		
M1	1.748	3.356	1.116	1.186	1.333
M2	1.748	3.376	1.090	1.199	1.296
M3	1.774	3.259	1.054	1.249	1.271
|%E| M2/M1	-0.001	0.593	-2.341	1.018	-2.784
|%E| M3/M2	1.512	-3.450	-3.265	4.174	-1.939
			Max TAWSS [Pa]		
M1	4.011	9.488	3.314	2.173	4.444
M2	3.914	9.131	3.425	2.226	4.507
M3	4.029	8.681	3.514	2.312	4.699
|%E| M2/M1	-2.432	-3.764	3.352	2.481	1.418
|%E| M3/M2	2.930	-4.927	2.577	3.842	4.264

Based on the mesh sensitivity results, M2 was chosen for S1.

S2 mesh sensitivity test results

Table A.17: Mean and maximum velocity and wall shear stress (WSS) on analysis planes (shown in Figure A.5) in each mesh for S2 in Chapter 8. |%E|: Absolute percentage change in value between noted meshes.

Plane	**1**	**2**	**3**	**4**	**5**	**6**	**7**
				Mean Velocity [m/s]			
M1	0.235	0.228	0.224	0.277	0.326	0.319	0.360
M2	0.237	0.227	0.225	0.277	0.325	0.317	0.359
M3	0.239	0.228	0.228	0.278	0.326	0.318	0.361
|%E| M2/M1	0.459	-0.346	0.538	-0.242	-0.417	-0.383	-0.251
|%E| M3/M2	0.889	0.135	1.093	0.504	0.281	0.317	0.713
				Max Velocity [m/s]			
M1	0.358	0.501	0.487	0.415	0.565	0.522	0.638
M2	0.360	0.498	0.504	0.411	0.582	0.510	0.631
M3	0.363	0.500	0.511	0.430	0.593	0.514	0.639
|%E| M2/M1	0.678	-0.617	3.368	-1.029	2.956	-2.303	-0.967
|%E| M3/M2	0.620	0.510	1.379	4.559	1.798	0.832	1.213
				Mean WSS			
M1	0.961	1.241	0.554	1.427	1.799	1.531	1.886
M2	0.949	1.241	0.542	1.420	1.768	1.571	1.928
M3	0.950	1.254	0.547	1.491	1.687	1.510	1.998
|%E| M2/M1	-1.225	0.014	-2.079	-0.464	-1.706	2.607	2.240
|%E| M3/M2	0.043	1.026	0.872	4.986	-4.573	-3.845	3.629
				Max WSS			
M1	1.659	2.931	1.385	2.855	4.681	3.894	4.454
M2	1.656	3.229	1.422	2.894	4.349	4.026	4.337
M3	1.617	3.309	1.455	2.901	4.224	4.122	4.280
|%E| M2/M1	-0.151	10.182	2.692	1.368	-7.092	3.400	-2.631
|%E| M3/M2	-2.369	2.480	2.316	0.250	-2.870	2.390	-1.298

Based on the mesh sensitivity results, M2 was chosen for S2.

A.6 Chapter 9

The mesh for P1 in Chapter 9 was chosen based on the mesh sensitivity results presented in Section A.2 as it is the same model as PII in Chapter 5. P1-mod and P2-mod were meshed with the same cell sizes and local refinements as the chosen meshes of P1 and P2. Mesh sensitivity information and results for P2 and P3 in Chapter 9 and presented here.

Table A.18: Number of elements for three meshes (M1, M2, M3) used for mesh sensitivity analysis for models P2 and P3 in Chapter 9.

	P2	**P3**
M1	2,385,497	2,599,014
M2	5,458,130	5,857,597
M3	8,393,536	9,374,393

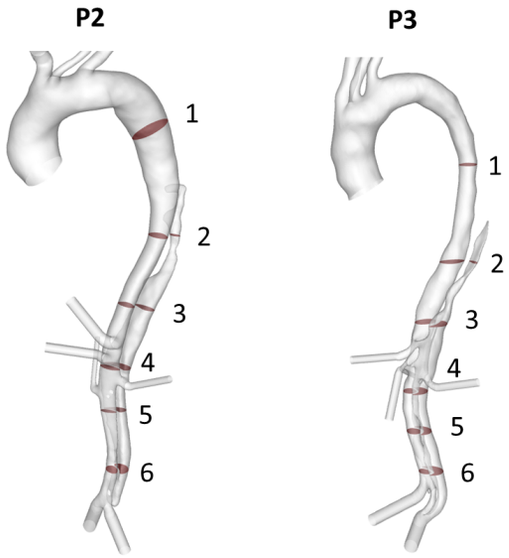

Figure A.6: Analysis planes used for mesh sensitivity tests for models P2 and P3 in Chapter 9.

P2 mesh sensitivity test results

Table A.19: Mean and maximum velocity and time average wall shear stress (TAWSS) on analysis planes (shown in Figure A.6) in each mesh for P2 in Chapter 9. |%E|: Absolute percentage change in value between noted meshes.

Plane	**1**	**2**	**3**	**4**	**5**	**6**
			Mean Velocity [m/s]			
M1	0.167	0.350	0.269	0.105	0.081	0.110
M2	0.168	0.351	0.270	0.105	0.080	0.112
M3	0.168	0.351	0.270	0.105	0.080	0.111
|%E| M2/M1	0.213	0.357	0.375	0.441	0.564	1.316
|%E| M3/M2	0.032	0.127	0.105	0.438	0.147	0.419
			Max Velocity [m/s]			
M1	0.218	0.497	0.618	0.347	0.130	0.394
M2	0.219	0.502	0.622	0.354	0.134	0.445
M3	0.219	0.501	0.622	0.352	0.133	0.439
|%E| M2/M1	0.712	0.875	0.634	1.996	3.165	12.688
|%E| M3/M2	0.137	0.132	0.007	0.533	0.490	1.255
			Mean TAWSS [Pa]			
M1	0.353	0.789	0.596	0.638	0.687	0.570
M2	0.354	0.804	0.602	0.647	0.702	0.568
M3	0.356	0.804	0.603	0.639	0.708	0.580
|%E| M2/M1	0.381	1.834	0.990	1.491	2.200	0.492
|%E| M3/M2	0.361	0.000	0.295	1.296	0.811	2.226
			Max TAWSS [Pa]			
M1	0.547	1.370	1.682	3.069	1.807	1.393
M2	0.564	1.430	1.782	3.102	1.979	1.687
M3	0.570	1.450	1.800	3.130	2.003	1.604
|%E| M2/M1	3.173	4.407	5.945	1.078	9.521	21.136
|%E| M3/M2	0.989	1.389	0.976	0.900	1.214	4.926

Based on the mesh sensitivity results, M2 was chosen for P2.

P3 mesh sensitivity test results

Table A.20: Mean and maximum velocity and time average wall shear stress (TAWSS) on analysis planes (shown in Figure A.6) in each mesh for P3 in Chapter 9. |%E|: Absolute percentage change in value between noted meshes.

Plane	**1**	**2**	**3**	**4**	**5**	**6**
			Mean Velocity [m/s]			
M1	0.230	0.197	0.146	0.069	0.070	0.073
M2	0.229	0.197	0.145	0.068	0.069	0.072
M3	0.229	0.196	0.145	0.067	0.068	0.071
|%E| M2/M1	0.046	0.287	0.172	1.768	1.686	1.775
|%E| M3/M2	0.374	0.212	0.270	1.614	1.563	1.520
			Max Velocity [m/s]			
M1	0.287	0.278	0.279	0.139	0.113	0.168
M2	0.286	0.278	0.278	0.136	0.113	0.167
M3	0.285	0.277	0.276	0.132	0.110	0.161
|%E| M2/M1	0.342	0.241	0.280	2.152	0.428	0.855
|%E| M3/M2	0.671	0.245	0.845	2.906	2.700	3.484
			Mean TAWSS [Pa]			
M1	0.534	0.441	0.283	0.578	0.311	0.406
M2	0.542	0.443	0.284	0.593	0.319	0.425
M3	0.545	0.446	0.289	0.603	0.327	0.429
|%E| M2/M1	1.475	0.428	0.165	2.645	2.641	4.772
|%E| M3/M2	0.673	0.827	1.808	1.720	2.441	0.983
			Max TAWSS [Pa]			
M1	0.629	0.938	0.732	1.797	0.767	1.256
M2	0.642	0.981	0.751	1.927	0.800	1.415
M3	0.634	1.025	0.782	1.997	0.790	1.438
|%E| M2/M1	2.158	4.519	2.606	7.250	4.321	12.658
|%E| M3/M2	1.235	4.459	4.159	3.651	1.201	1.577

Based on the mesh sensitivity results, M2 was chosen for P3.

Appendix B

Chapter 6 supplementary material

Corresponding scatter plots for the Pearson's correlation coefficients reported in Table 6.5 are presented in this Appendix.

P1

Ascending Aorta

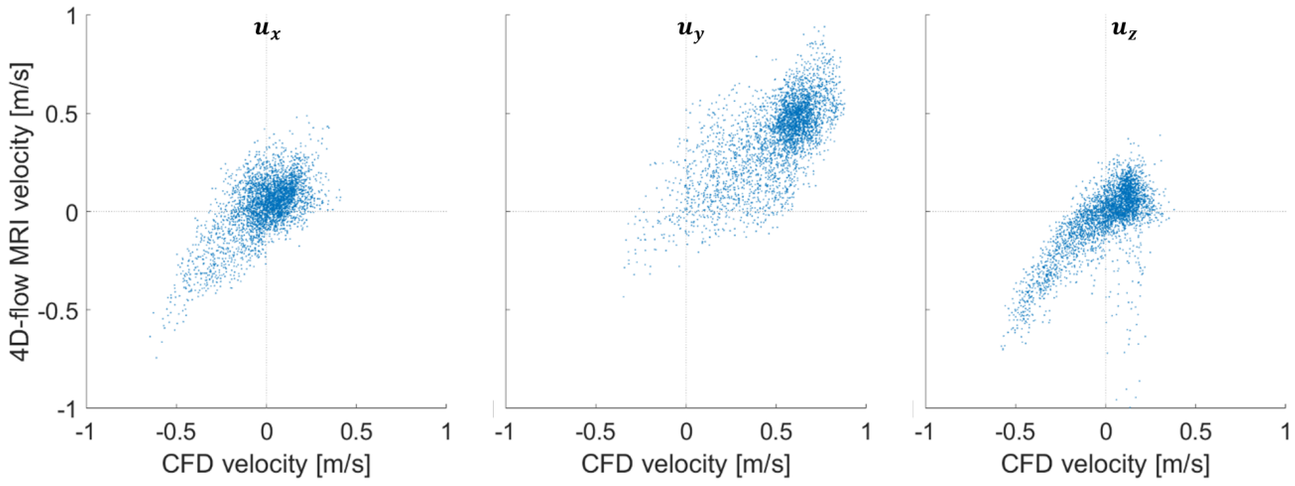

Aortic Arch

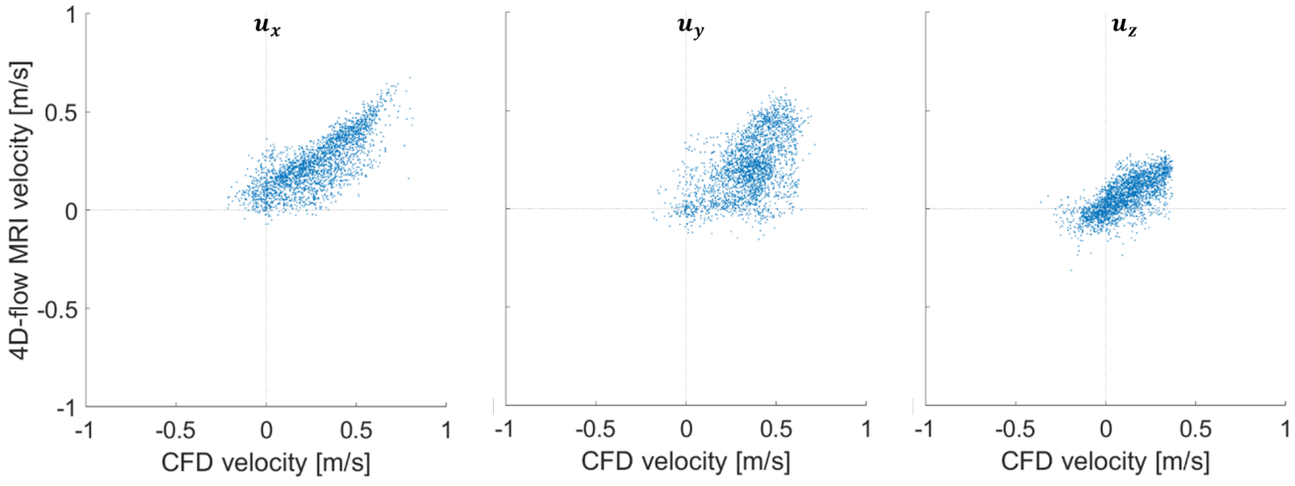

Proximal Descending Aorta

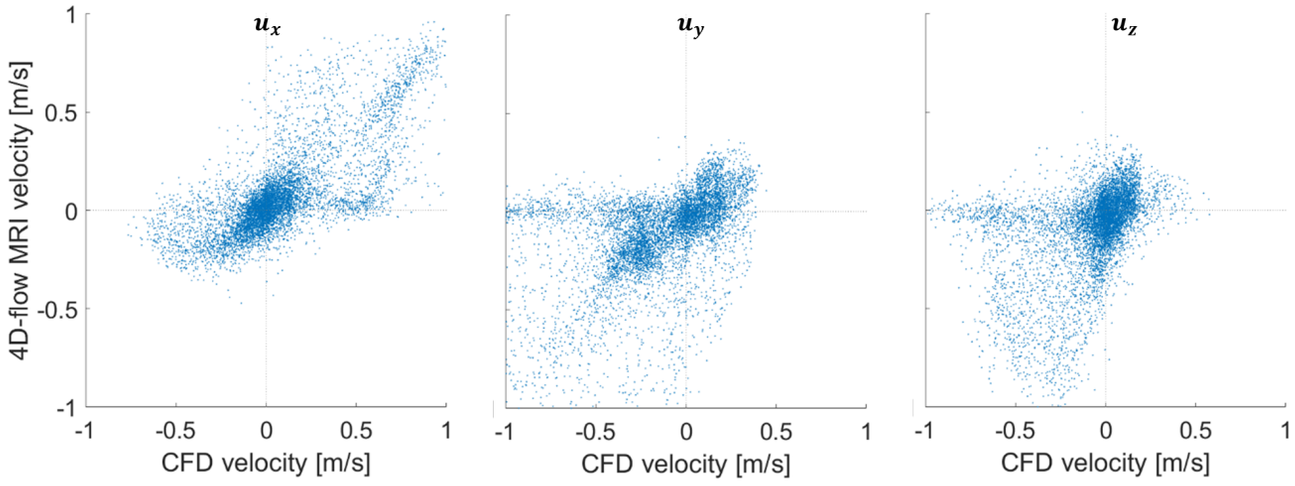

Mid Descending Aorta

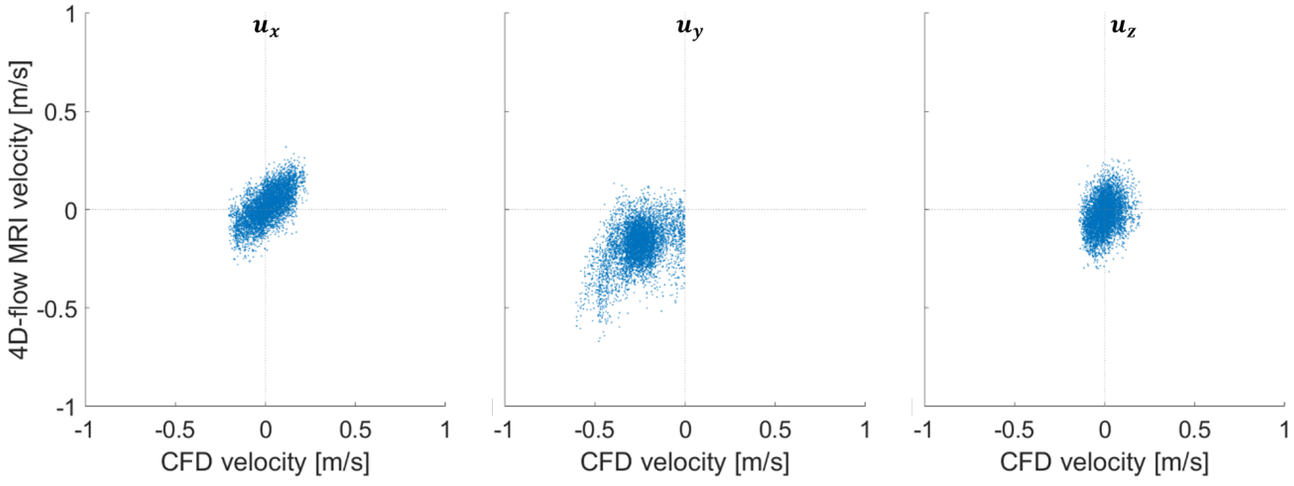

Distal Descending Aorta

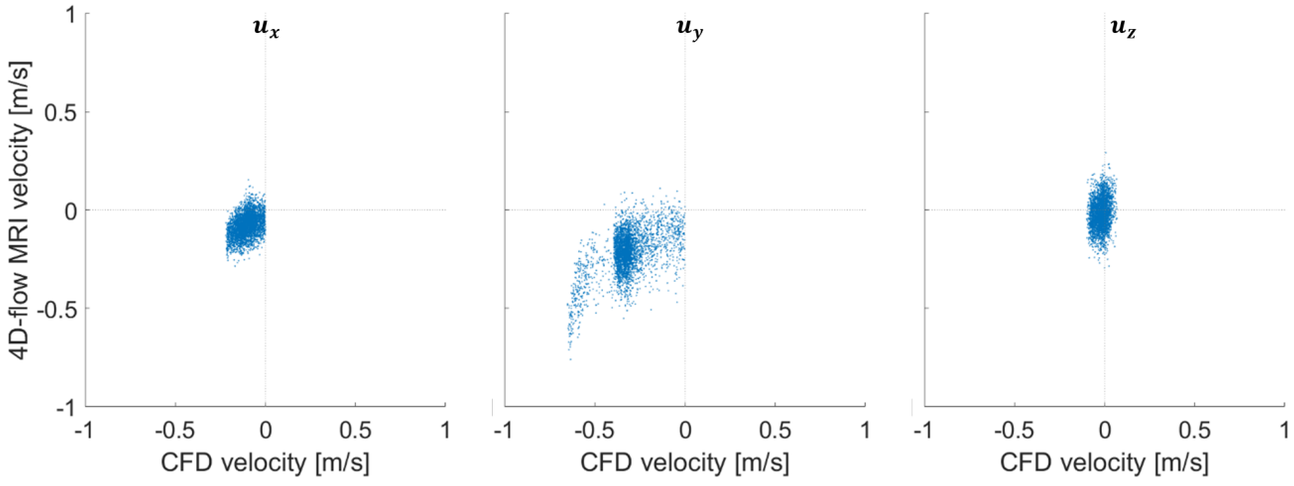

P2

Ascending Aorta

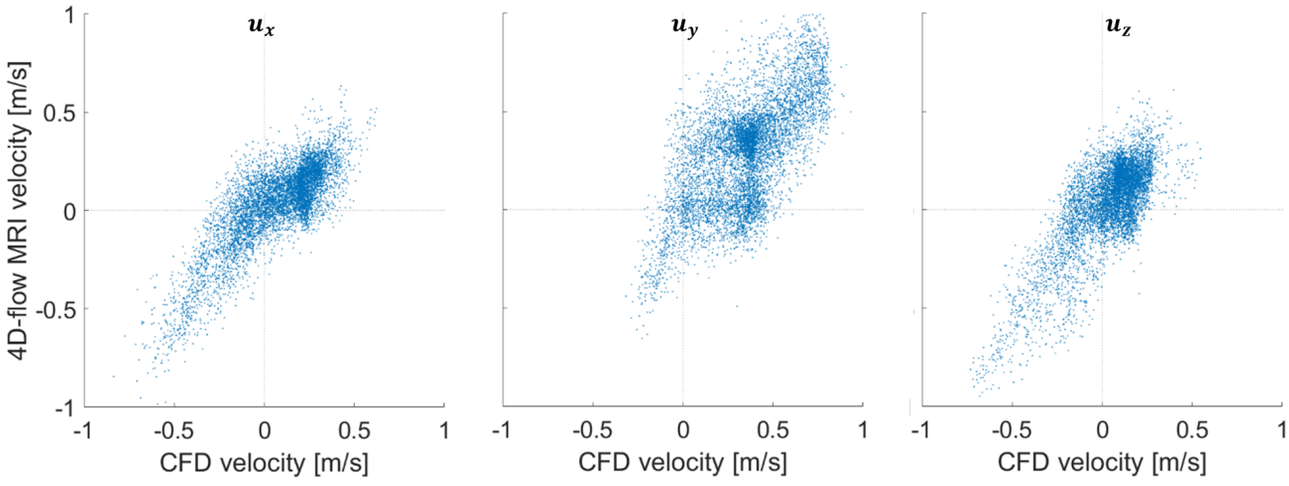

Aortic Arch

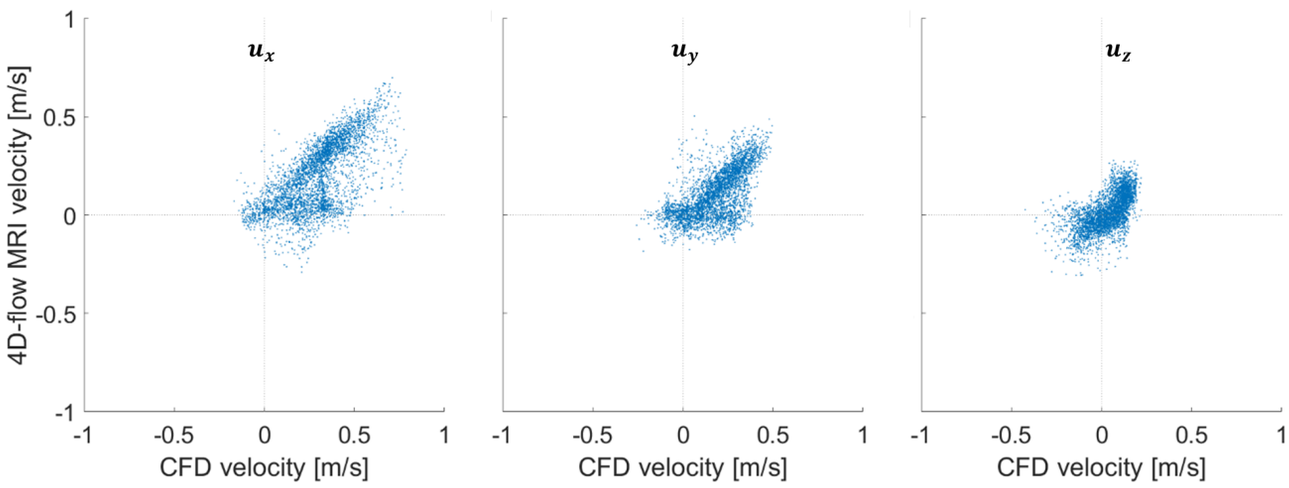

Proximal Descending Aorta

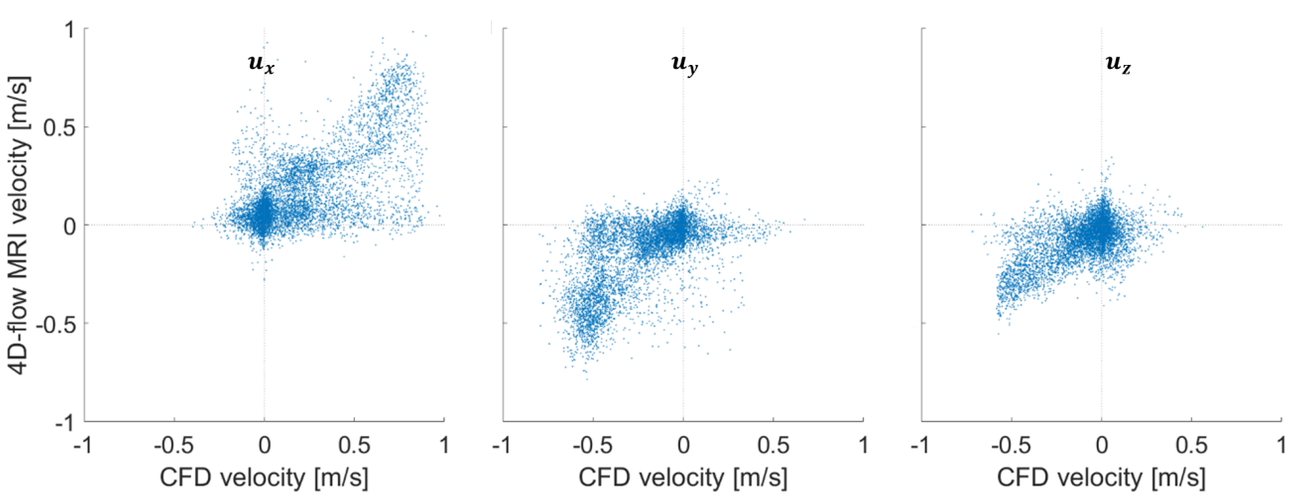

Mid Descending Aorta

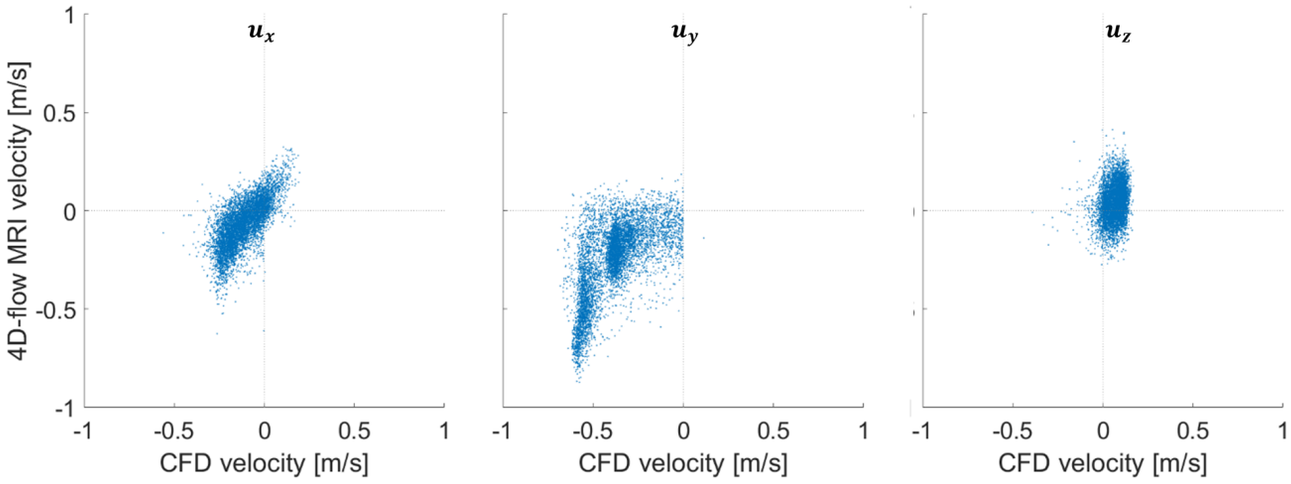

Distal Descending Aorta

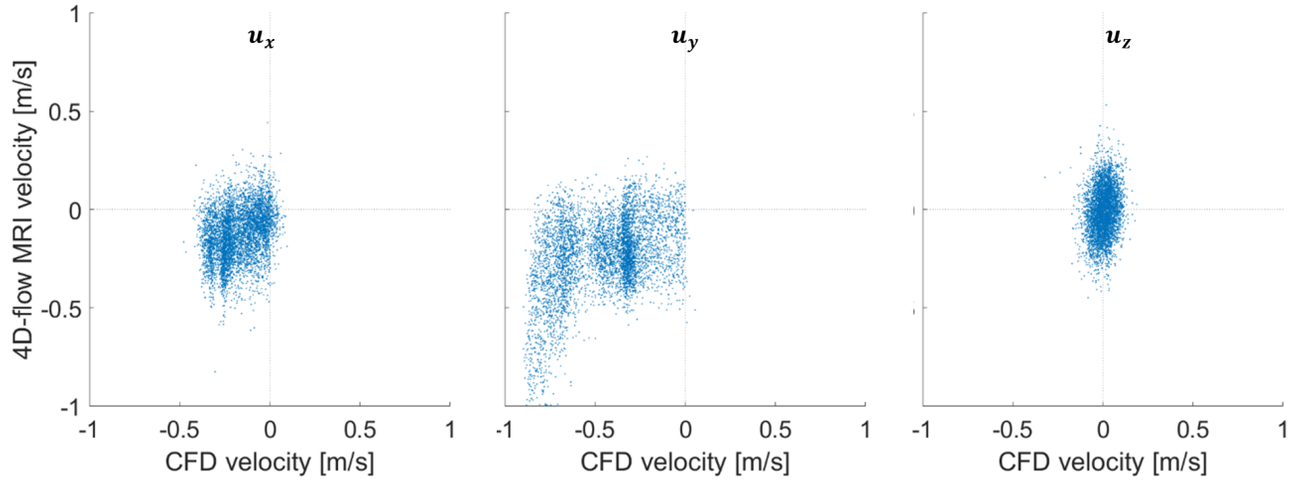

P3

Ascending Aorta

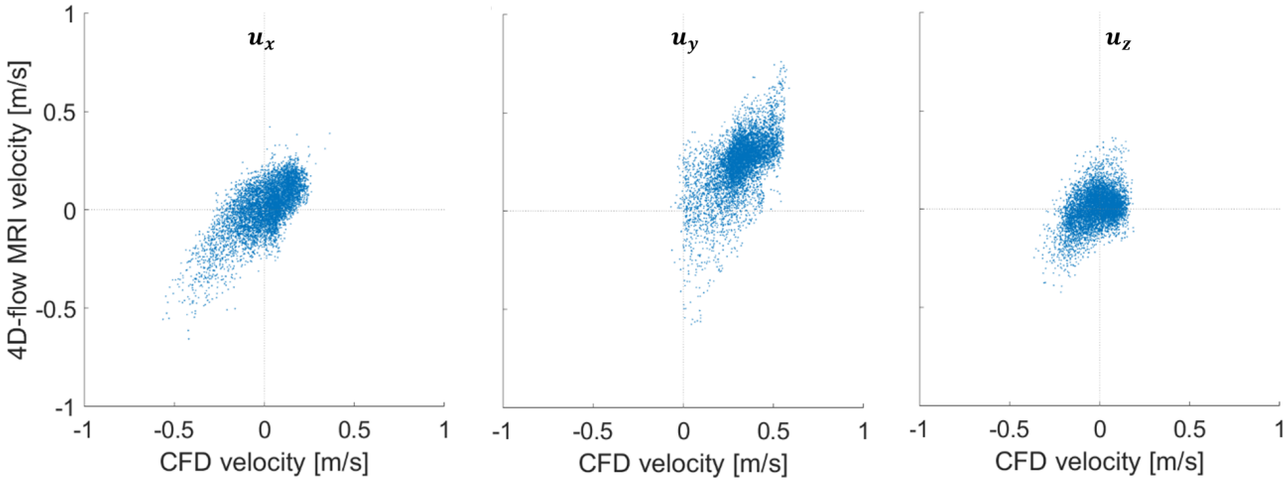

Aortic Arch

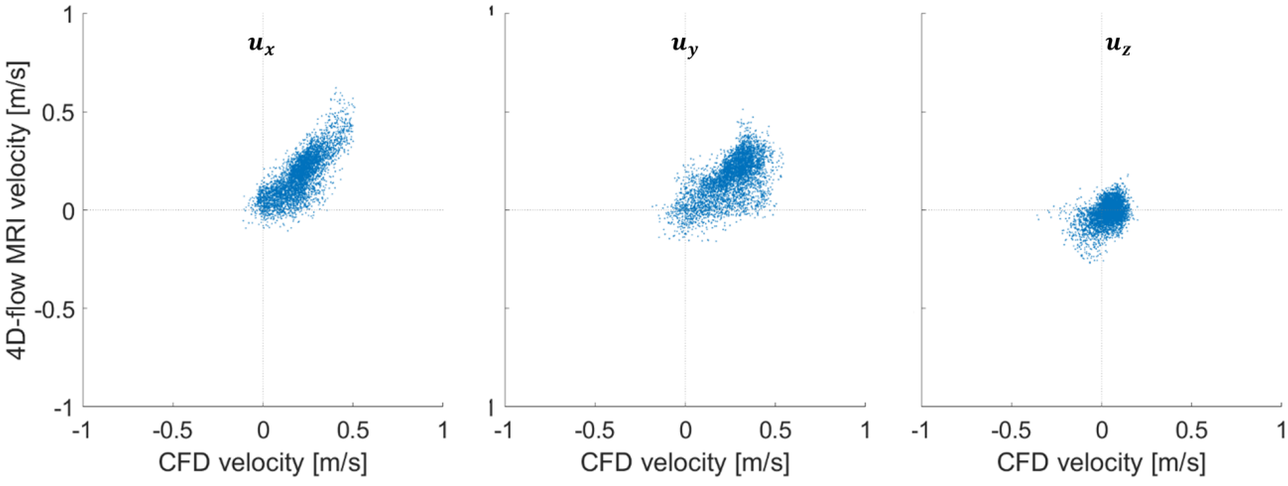

Proximal Descending Aorta

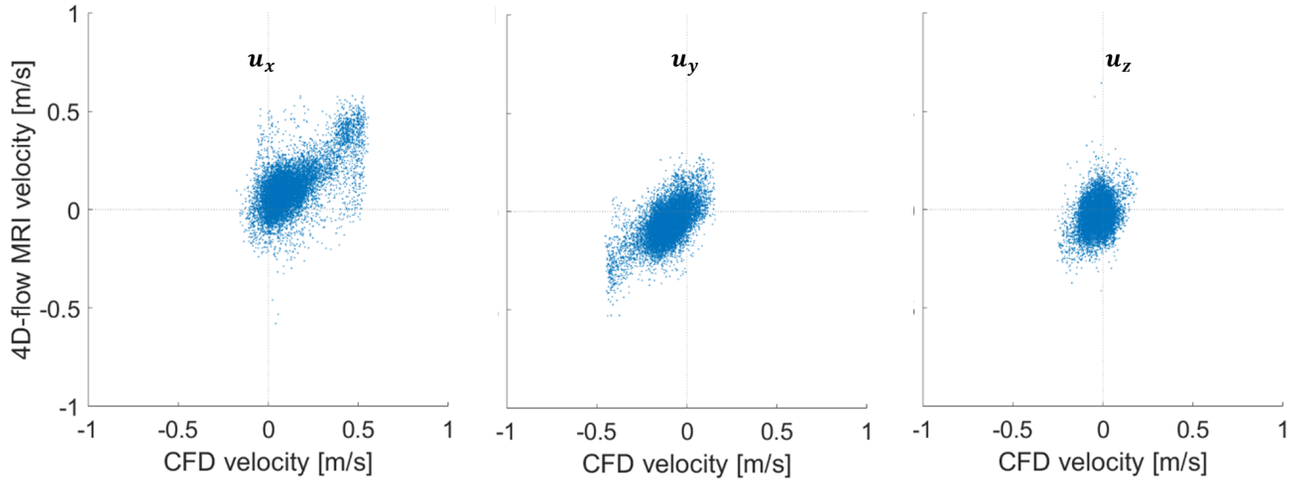

Mid Descending Aorta

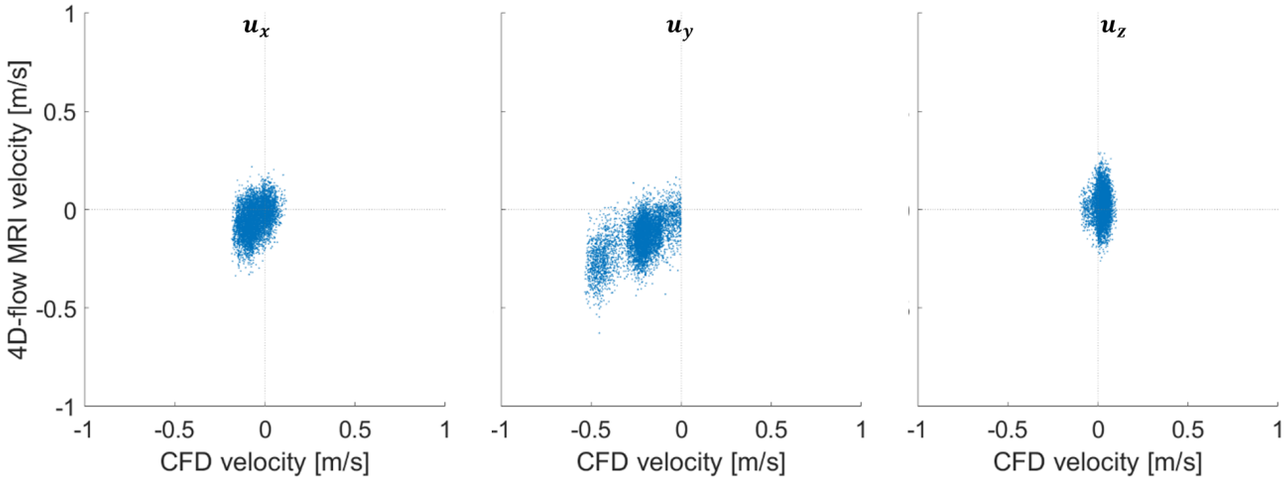

Distal Descending Aorta

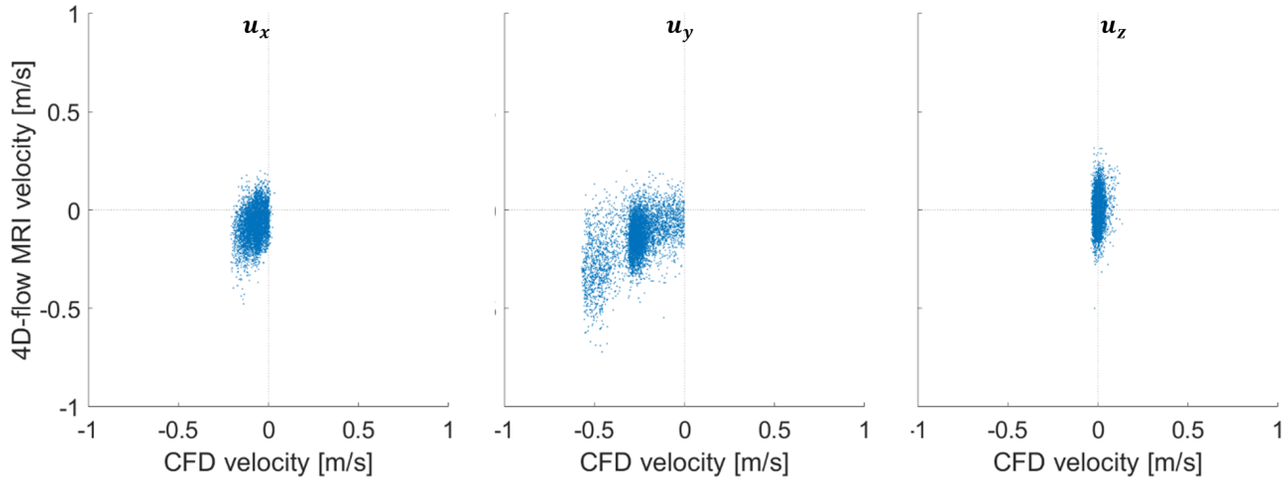

P4

Ascending Aorta

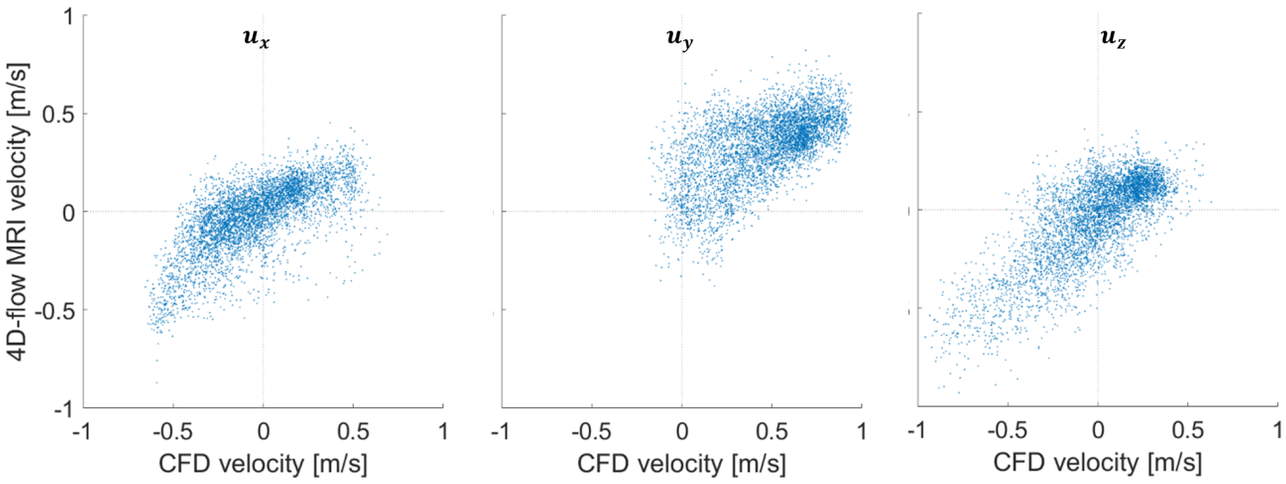

Aortic Arch

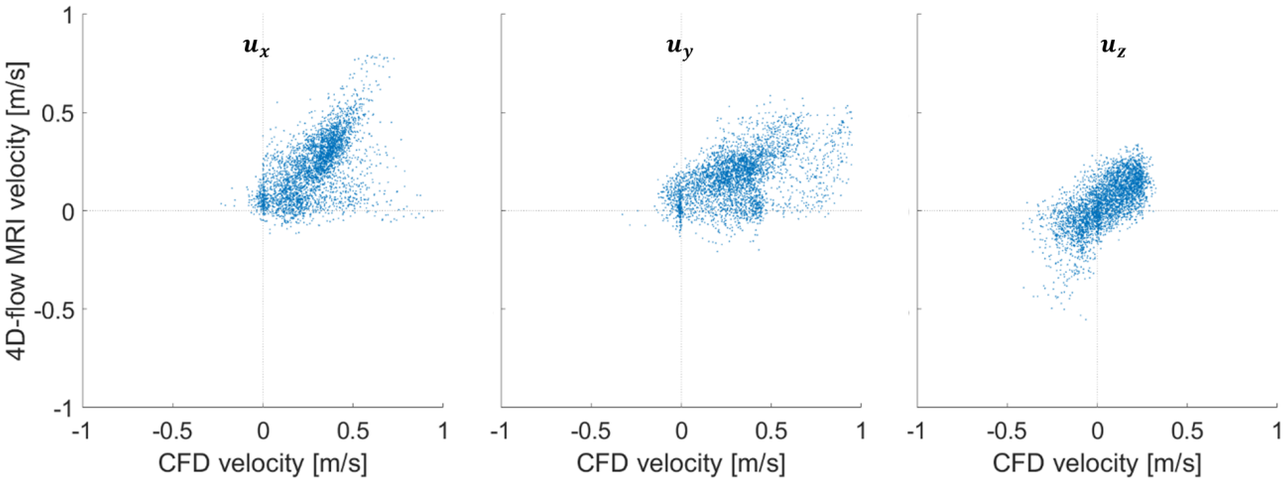

Proximal Descending Aorta

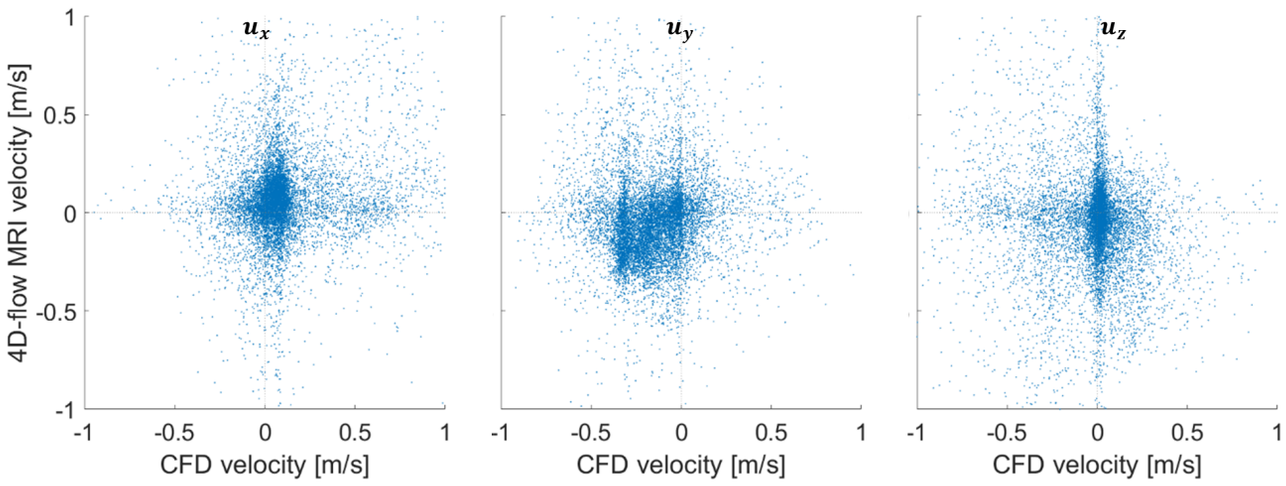

Mid Descending Aorta

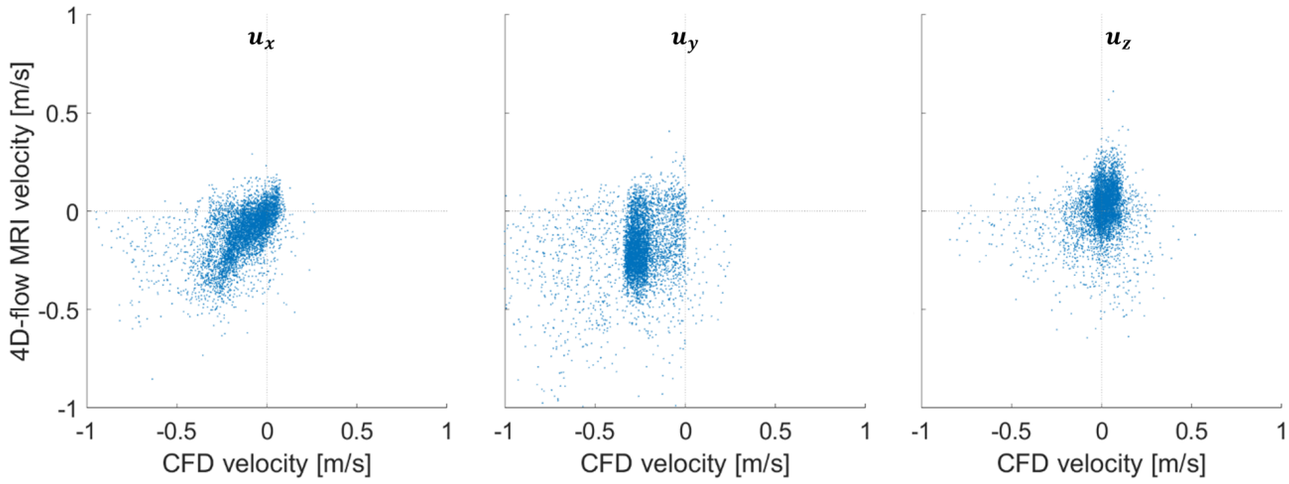

Distal Descending Aorta

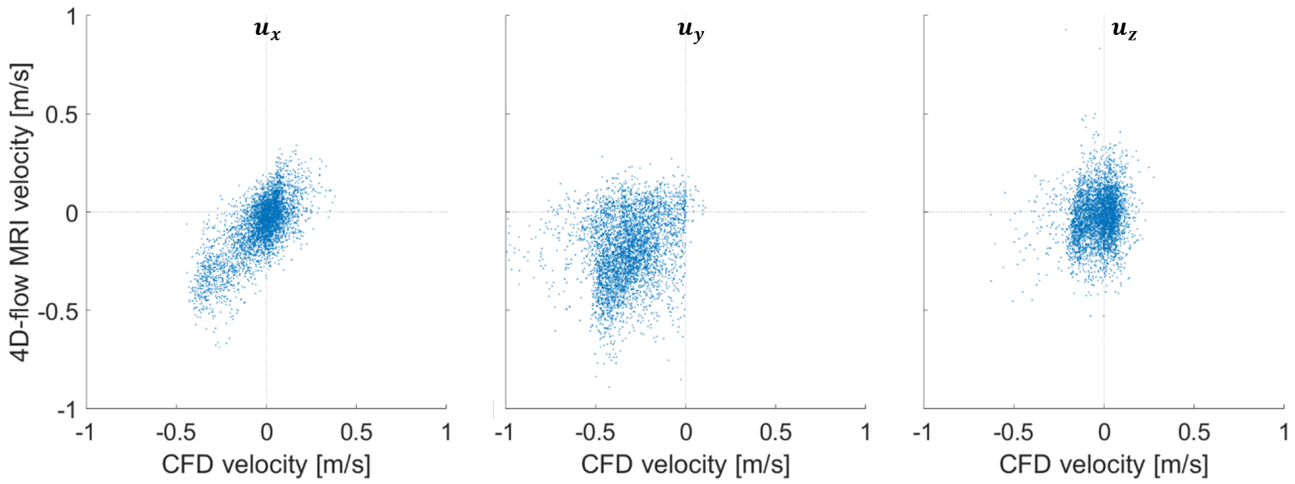

P5

Ascending Aorta

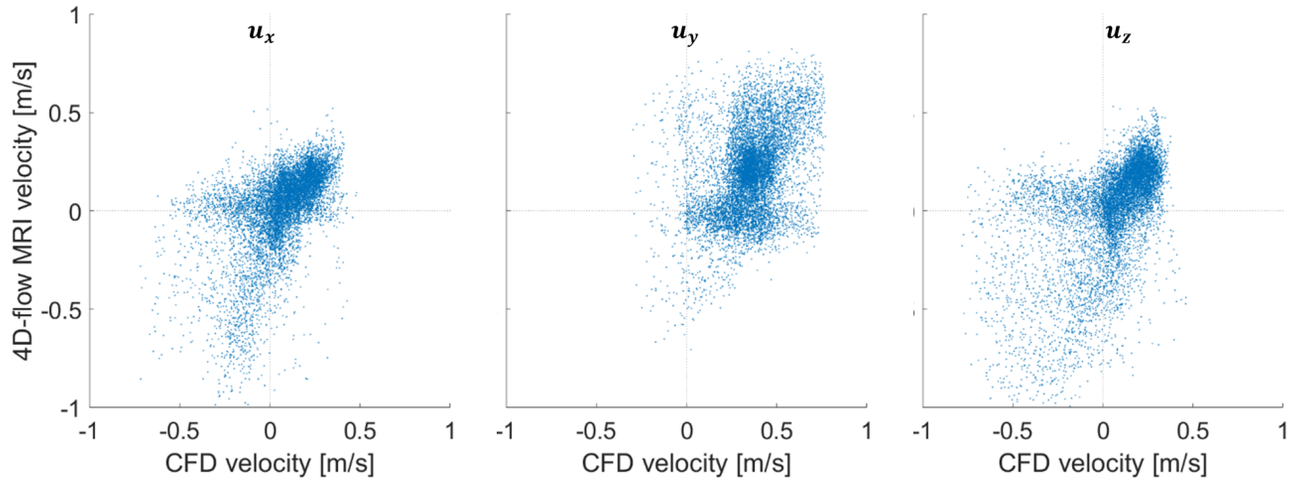

Aortic Arch

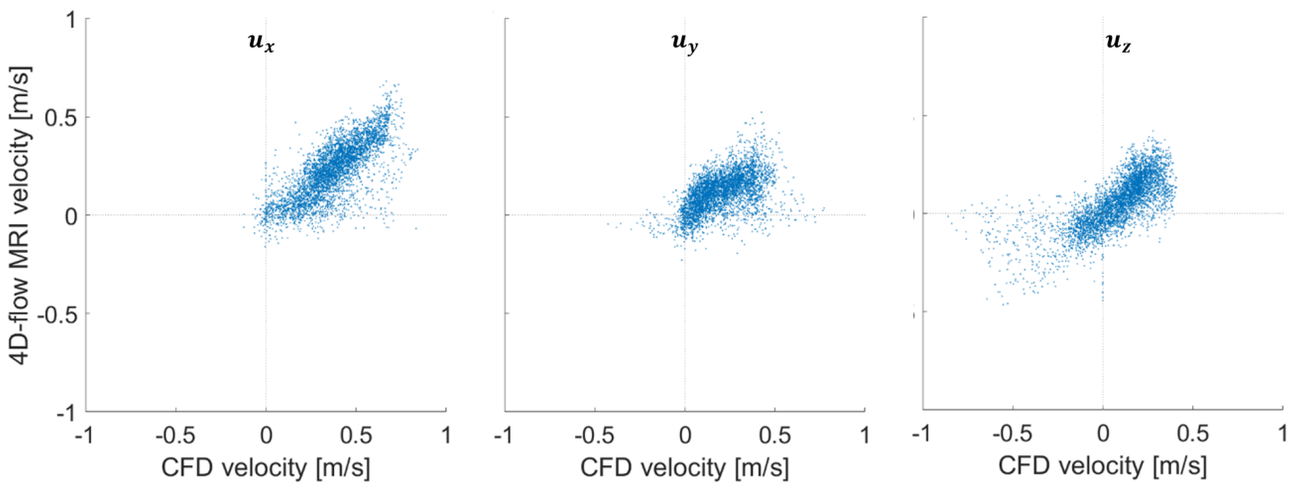

Proximal Descending Aorta

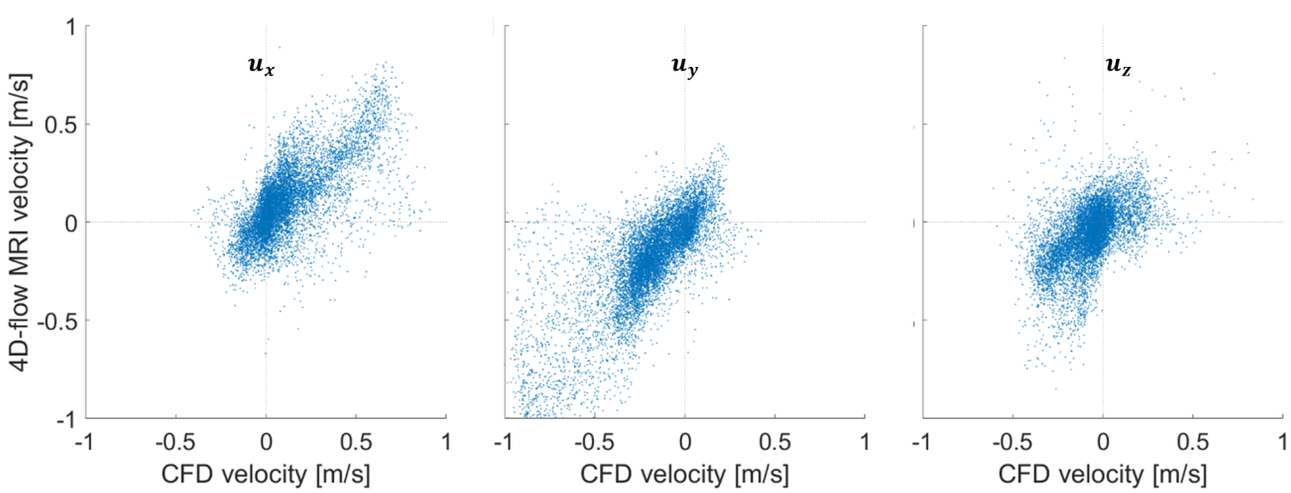

Mid Descending Aorta

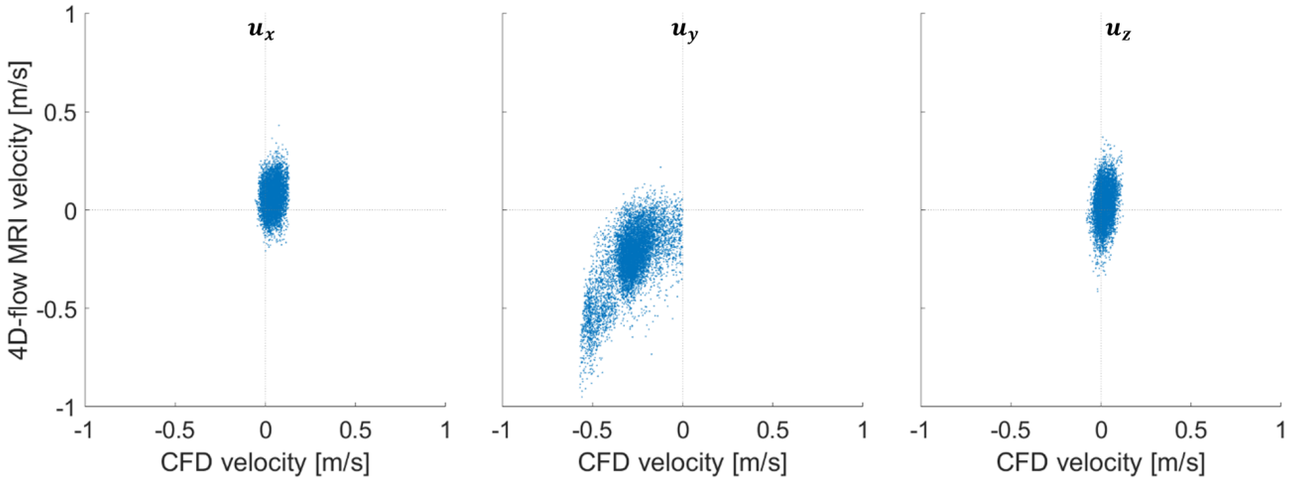

Distal Descending Aorta

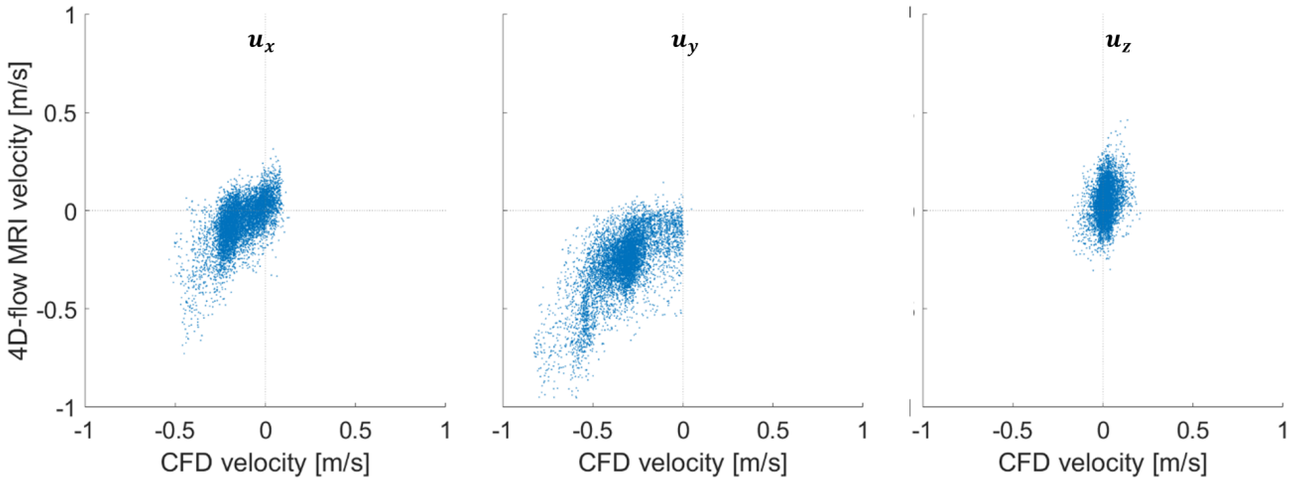

Appendix C

Publications and Presentations

C.1 Peer-Reviewed Publications

Armour, C.H., Menichini, C., Milinis, K, Gibbs, R.G.J., Xu, X.Y. (2020) Location of Reentry Tears Affects False Lumen Thrombosis in Aortic Dissection Following TEVAR. *Journal of Endovascular Therapy* **27**(3), 396-404.

Armour, C.H., Guo, B., Pirola, S., Saitta, S., Liu, Y., Dong, Z., Xu, X.Y. (2020), The influence of inlet velocity profile on predicted flow in type B aortic dissection', *Biomechanics and Modeling in Mechanobiology* **20**, 481-490.

Armour, C.H., Menichini, C., Hanna, L., Gibbs, R.G.J., Xu, X.Y. (2021), Computational Modeling of Flow and Thrombus Formation in Type B Aortic Dissection: The Influence of False Lumen Perfused Side Branches. *Studies in Mechanobiology, Tissue Engineering and Biomaterials*. (Book chapter accepted, due to be published September 2021)

Armour, C.H., Guo, B., Saitta, S., Liu, Y., Dong, Z., Xu, X.Y. (2021) The role of re-entry tears in type B aortic dissection progression: a longitudinal study using a controlled swine model. *Interactive CardioVascular and Thoracic Surgery* (Accepted subject to revisions)

Armour, C.H., Guo, B., Saitta, S., Pirola, S., Liu, Y., Guo, B., Dong, Z., Xu, X.Y. (2021)

Evaluation and Verification of Patient-Specific Modelling of Type B Aortic Dissection. (Manuscript under review)

Chong, M.Y., Gu, B., **Armour, C.H.**, Dokos, S., Ong, Z.C., Xu, Y.X., Lim, E. (2021) Effect of intimal flap motion on thrombus formation and growth over time in acute type B aortic dissection by using fluid-structure interaction. (Manuscript under review)

Xu, H., Xiong, J., Mei, Y., Zhang, Y., **Armour, C.H.**, Chen, D., Xu, X.Y. (2021) The Necessity to Seal the Re-entry Tears of Aortic Dissection after TEVAR: A Hemodynamic Indicator. (Manuscript in preparation)

C.2 Presentations

Armour, C.H., Guo, B., Saitta, S., Pirola, S., Liu, Y., Guo, B., Dong, Z., Xu, X.Y. Validation of Patient-Specific Computational Modelling of Type B Aortic Dissection. 26th Congress of the European Society of Biomechanics. 12th July 2021 - **oral presentation**

Armour, C.H., Menichini, C., Milinis, K., Gibbs, R.G.J., Xu, X.Y. Effect of distal stent to re-entry tear distance on false lumen thrombosis in type B aortic dissection. Challenges in Cardiovascular Flow, IOP, Bath, 24th July 2019 - **oral presentation**

Armour, C.H., Xu X.Y. Predicting the outcome in type B aortic dissection. Imperial Network of Excellence in Vascular Science, Imperial College London, 23rd July 2019 - **oral presentation**

Armour, C.H., Guo, B., Saitta, S., Guo, D., Liu, Y., Fu, W., Dong, Z., Xu, X.Y. The Role of Reentry Tears on Hemodynamics in Type B Aortic Dissection. Annual Project Collaboration Meeting - Fudan Hospital, Shanghai, 19th February 2019 – **oral presentation**

Menichini, C., **Armour, C.H.**, Milinis, K., Gibbs, R.G.J., Xu, X.Y. The Influence of Flase Lumen Side Branch Perfusion on the Progression of type B Aortic Dissection. Frontiers of Simulation and Experimentation for Personalized Cardiovascualur Management and Treatment, University College London, 20th July 2018 - **oral presentation**

Armour, C.H., Menichini, C., Milinis, K., Gibbs, R.G.J., Xu, X.Y. Predicting the Outcome in type B Aortic Dissection: New Insights from the ADSORB Trial. World Congress of Biomechanics, Dublin, 11th July 2018 - **oral presentation**

Appendix D

Copyright Permissions

Permission has been requested to reproduce figures protected by copyright. License numbers are presented in Table D.1. For online images, Open Access journals and figures published elsewhere under a Creative Common License, license numbers have been listed as "Not Available" (N/A).

Permission to adapt the author's own work is as follows:

- Work presented in Chapter 4 is adapted from *Armour CH, Guo B, Pirola S, Saitta S, Liu Y, Dong Z, Xu XY (2020) The influence of inlet velocity profile on predicted flow in type B aortic dissection. Biomechanics and Modeling in Mechanobiology 20:481-490*, published under a Creative Commons Attribibution (CC BY) license (https://creativecommons.org/licenses/by/4.0/legalcode).
- Work presented in Chapter 5 is adapted from *Armour CH, Menichini C, Hanna L, Gibbs RGJ, Xu XY (2021) Computational Modeling of Flow and Thrombus Formation in Type B Aortic Dissection: The Influence of False Lumen Perfused Side Branches*, a book chapter due to be published in the book series 'Studies in Mechanobiology, Tissue Engineering and Biomaterials', published under a publishing agreement with Springer, which gives the author the right of reuse in whole or in part in a 'thesis written by the same Author'.
- Work presented in Chapter 9 is adapted from *Armour CH, Menichini C, Milinis K, Gibbs RGJ, Xu YX (2020) Location of Reentry Tears Affects False Lumen Thrombosis in Aortic*

Dissection Following TEVAR. Journal of Endovascular Therapy 27(3):396-404, published under a Creative Commons Attribibution (CC BY) license (https://creativecommons.org/licenses/by/4.0/legalcode).

Table D.1: Figure copyright permissions.

Figure No.	Page No.	Source	Copyright Holder	License Number/Link
1.1, 2.2, 2.3	2, 10, 12	The International Registry of Acute Aortic Dissection (n.d.)	The International Registry of Acute Aortic Dissection	N/A
2.1	8	Institute for Quality and Efficiency in Health Care (2019)	Institute for Quality and Efficiency in Health Care	N/A
2.3	12	Salameh & Ratchford (2016)	SAGE Publications	N/A
2.4	15	Saint Luke's	Saint Luke's	N/A
2.4	15	Krol & Panneton (2017)	Krol & Panneton (2017)	N/A https://creativecommons.org/licenses/by-nc-sa/4.0
2.5	18	McMichael (2005)	John Wiley and Sons	5114260940919
2.7, 3.1	23, 45	Menichini et al. (2016)	The Royal Society	N/A https://creativecommons.org/licenses/by/4.0
2.8	26	Cheng et al. (2014)	Elsevier	5112000413350
2.9	30	François et al. (2013)	Elsevier	5111461066189
2.10	34	Marui et al. (2007)	Elsevier	5114270270929
2.11	35	Sailer et al. (2017)	Wolters Kluwer Health, Inc.	5114950279880
10.4	189	Takahashi et al. (2021)	Oxford University Press	5115490874529